Politecnico di Torino

Department of Electronics and Telecommunication

Laurea Magistrale in Electronic Engineering

Metal-dielectric nanostructures

Synthesis and characterization for SERS analysis

Supervisor: Prof. F. Giorgis

Advisor: Dr. A. Chiadò

Dr. C. Novara

Giuliano Caruso

October 2018

Se decidi di tornare a Itaca,
augurati che sia lunga la tua strada,
piena di avventure, piena di cose da scoprire.
Non temere i Lestrigoni e i Ciclopi,
e neppure la collera di Posidone:
sulla tua strada non troverai nulla del genere
se alto manterrai il pensiero, se un'emozione
scelta ti toccherà l'anima e il corpo.
I Lestrigoni e i Ciclopi,
il feroce Posidone, non li incontrerai,
se non li porti con te nella tua anima,
se la tua anima non te li pone innanzi.

Augurati che sia lunga la tua strada.
Che siano molte le mattinate estive
in cui, con chissà quanta soddisfazione, e quanta gioia
entrerai in porti mai visti prima.
Fai scalo nei mercati fenici
e acquista merci pregiate,
madreperla e corallo, ambra ed ebano,
e profumi voluttuosi di ogni tipo,
quanti più puoi profumi voluttuosi.
Attracca in molte città d'Egitto,
per imparare tanto dai sapienti.

Nella mente, dovrai sempre avere Itaca.
È lei la meta tua, è là che devi giungere.
Ma non affrettare il viaggio.
Meglio che duri molti anni;
e che tu arrivi all'isola ormai vecchio,
ricco di tutto quel che hai guadagnato in viaggio,
senza aspettarti che le ricchezze te le dia Itaca.

Itaca ti ha dato il viaggio bello.
Senza di lei non ti saresti messo in strada.
E non ha altro da darti.

E se la troverai povera, non è Itaca che ti ha ingannato.
Ora sei diventato sapiente, e hai tanta esperienza
che avrai capito, ormai, cosa significano le tante Itache.

Konstantinos Kavafis

A chi ha dimora nel mio cuore...

Abstract

Surface-enhanced Raman scattering (SERS) spectroscopy can lead to the fabrication of high-sensitivity label-free sensors for detection purposes in many fields, such as biomedical diagnostics and therapy monitoring, but also agricultural and environmental monitoring.
The electromagnetic enhancement plays an important role in the SERS effect, which is featured by a huge amplification of the Raman scattering intensity. Actually, the resonant excitation of Localized Surface Plasmons (LSPs) of noble metal nanoparticles (NPs) – in the regions close to their surface – is the main reason of the scattered light enhancement, also if a moderate contribution can be ascribed to charge transfer processes. The electromagnetic enhancement is strongly dependent on the type, size, shape, inter-particle distance and aggregation state of the NPs. Full control of size and shape of the NPs can be obtained with approaches based on lithographic techniques, with the drawbacks of high costs and complexity, along with the time-consuming fabrication. Recently, the fabrication of tuneable plasmonic nanostructures constituted by Ag-NPs on flexible elastomeric polydimethylsiloxane (PDMS) matrices has been reported.
This kind of substrates can potentially fulfil the need of flexible and wearable devices, able to constantly monitor people's health, by checking their physiological and biochemical parameters. Unfortunately, the poor compatibility of these substrates with the buffers used for bioassays, which results in a reduced SERS efficiency, limits their practical bio-application.

The main aim of this work was to investigate low-cost methods for the synthesis of sensitive and stable substrates, based on silver NPs (Ag-NPs) immobilized on PDMS membranes, to be used for biosensing applications. Indeed, the optimization of this SERS substrate was ultimately aimed to the development of a flexible multi-chamber microfluidic chip, for fast and low-cost detection of cancer biomarkers.

As first attempt, the optimization of Ag-coated PDMS membranes, obtained by means of DC-sputtering, was performed by varying the synthesis parameters (current, deposition time and distance from target). The analysis of these substrates showed very low reproducibility and very low stability. For this reason, two main approaches have been followed in

order to increase the stability of the NPs on the PDMS substrates.
In the first case the PDMS membranes were activated with a piranha-like solution or with a plasma treatment and finally functionalized by means of (3-mercaptopropyl)trimethoxysilane (MPTMS) and (3-Aminopropyl)triethoxysilane (APTES), in order to promote the adhesion between the sputtered-Ag and the PDMS. The second strategy was, instead, based on the static incubation of the PDMS samples in a AgNO3 solution in different conditions.
Different characterizations techniques have been carried out to have a deep insight into the Raman response of all the synthetized substrates. UV-Vis transmittance analysis and Raman mapping of mercaptobenzoic acid (MBA) have been used to provide information respectively on the correlation between the synthesis parameters and the SERS signal intensity and homogeneity of the samples. A Field Emission Scanning Electron Microscopy (FESEM) characterization has been used to investigate the morphology of the NPs. To extract information useful to link the Raman response of the samples and the Ag-NPs geometrical characteristics, an image analysis on the FESEM micrographs has been carried out. MATLAB and ImageJ have been used for this purpose and a comparison between the results obtained with the two programs has been performed to investigate the accuracy of both methods. Finally, the samples have been incubated in water or Tris EDTA buffer supplemented with 1 M NaCl to verify the retention of the NPs on the PDMS substrate, by using UV-Vis transmittance spectroscopy at different times of incubation.

For what concerns the functionalized PDMS substrates, the stability tests showed that the best performances where attained in the case of the MPTMS-functionalized Ag-coated PDMS membrane. However, despite of the high stability, these substrates also showed the lowest Raman efficiency and intra-sample repeatability, compared to Ag-coated PDMS and APTES functionalized Ag-PDMS. For what concerns the APTES functionalized sample, it was found a higher Raman efficiency with respect to both the other two specimens, but still a lower stability compared to the MPTMS sample typology. For this reason, we have investigated a different method for the synthesis of the Ag-NPs based on the static incubation of the sample in silver nitrate: the synthesis parameters (monomer to curing ratio, thickness of the substrate, incubation temperature, cross-linking degree, precursor concentration, presence of ethanol in the solution) have been deeply analysed one-by-one to find the best conditions. The incubated SERS samples showed better properties (high Raman efficiency, high intra-sample repeatability and high stability) than the Ag-sputtered PDMS substrates.

Finally, an assay for the detection of miRNA222, a known cancer biomarker, was performed both by SERS and Enzyme-Linked ImmunoSorbent assay (ELISA) on the best

sample obtained from each fabrication technique. The bioassay was implemented using different concentrations of miRNA222-R6G, along with two "negative control" to measure the nonspecific binding. The results revealed that the best performances (high sensitivity, low nonspecific binding) are obtained in the case of the SERS substrate synthesised by means of static incubation. As a consequence, the best sample obtained by static incubation (5:1 monomer to curing-agent ratio, totally cross-linked 1 mm thick PDMS membranes, incubated at 40 °C for 24 h), were chosen for the development of an all-PDMS multi-chamber microfluidic chip. This revealed that the SERS analysis works also in the case of the multi-chamber chip, showing a good sensitivity for the highest concentrations, along with a low nonspecific binding.

In conclusion, these results suggest that the fabricated chip is a good candidate in the view of an effective implementation for biosensing applications, such as label-free detection of cancer biomarkers.

Table of contents

Introduction

With the discovery of the so-called Raman scattering effect – from Chandrasekhara Venkata Raman in 1928 – the investigation of matter has gained a new powerful tool, with many perspectives for diverse applications. Raman spectroscopy focuses on the analysis of the optical spectrum generated by a sample interacting with light, that results in the excitation of the molecular vibrational states of molecules or group of atoms. Raman signals from molecules can then be isolated by means of complex detection instrumentation (filters, gratings and detectors). Unfortunately, the main limitation of Raman spectroscopy is related to its weak or very weak effect.

At the beginning of the 70s, main efforts were put on sensing single-monolayers of molecules. Good results were obtained by Fleischmann [1], whose aim was to observe pyridine on the surfaces of electro-chemical roughened silver electrodes, by Raman spectroscopy. The intense pyridine signals were erroneously justified by the increment of the effective area, due to the roughness of the surfaces of the electrodes, but this simple explanation could not legitimize the high amplification. It became clear later that the effect was due to a direct action of the nanostructured metal surface on the Raman scattering efficiency of the molecules. In fact, the enhancement of the Raman signals in Surface Enhanced Raman Spectroscopy (SERS) is mainly responsibility of the interaction of light with metals, which produces an amplification of the field, due to the Localized Surface Plasmons (LSPs) of the metal nanostructure [2].

The successive implementation to the metal electrodes was oriented to the synthesis of metallic nanoparticles in solution, i.e., metallic colloids [3] for SERS spectroscopy. This type of SERS substrates has been lately substituted by '2D planar' substrates, such as metallic nano particles synthesized on planar substrates. Metal-dielectric nanostructures seem to meet the expectations for the production of flexible and wearable devices, for *in vivo* measurements [4]. However, standardization, uniformity and in particular reproducibility, are the main challenging issues to be controlled in the production of novel SERS substrates. Full control can be reached with lithographic techniques, but with the drawback of high costs and complexity. Hence, a satisfactory response to the need of low cost techniques – but still

capable to ensure a good degree of reproducibility and sensitivity – is demanded.

SERS substrates are highly appealing thanks to their quality to preserve the vibrational 'fingerprint' of the analyte with a much higher sensitivity than usual Raman spectroscopy. SERS spectroscopy paves the way for many applications, ranging from analytical chemistry and biochemistry, tracing and analysis of drugs and bio-fluids [5–8]

The main properties of SERS substrates are presented, starting from the Raman spectroscopy (Chapter 1) – which is the foundation of SERS spectroscopy – all the way to the description of the main enhancement effects at the root of the SERS spectroscopy (Chapter 2). Afterwards, some of the novel solutions for SERS substrates for bio applications are discussed (Chapter 3). Aim and objectives of the work are explained in Chapter 4. Finally, in Chapter 5 materials and methods that were used in the synthesis of the metal-dielectric SERS nanostructures are presented, while in Chapter 6 results are discussed, focusing on the growth and characterization of an optimized substrate based on the synthesis of silver nanoparticles (Ag-NPs) on PDMS membranes, for the final aim of its integration in a multi-chamber microfluidic chip.

Chapter 1

Raman spectroscopy

1.1 Introduction

The interaction between an electromagnetic field and a molecule produces a transfer of energy from the field to the molecule. According to Quantum Theory, such a transfer can occur only in the condition

$$\Delta E = h\nu = h\frac{c}{\lambda} = hc\tilde{\nu}, \tag{1.1}$$

with ΔE the energy from a quantized state to the next one, h the Planck's constant, c the speed of light and λ the wavelength of the electromagnetic field. In vibrational spectroscopy it is also very common to find the parameter $\tilde{\nu}$, which refers to the so-called wavenumber, different from the frequency ν. In fact, while the first has dimension of s^{-1}, the second usually refers to cm^{-1}, as unit of measurement.

Raman and IR spectroscopy are two techniques, used for the investigation of the vibrational transitions of molecules, occurring in the range $10^4 - 10^2\ cm^{-1}$, and applied to acquire information about the structure of the analysed sample. IR and Raman spectrum analysis are actually based on two different processes. In the first case, the sample is exposed to infra-red light and absorption and/or reflection is measured as a function of the frequency; this means that the energy in equation 1.1 is absorbed by the sample for each vibrational transition. Instead, in Raman spectroscopy the sample is irradiated by intense laser beams with a frequency in the UV-Vis-NIR range and the components of the scattered light are eventually collected and observed. In short, in Raman spectroscopy the vibrational frequency is measured as a shift from the incident light frequency.

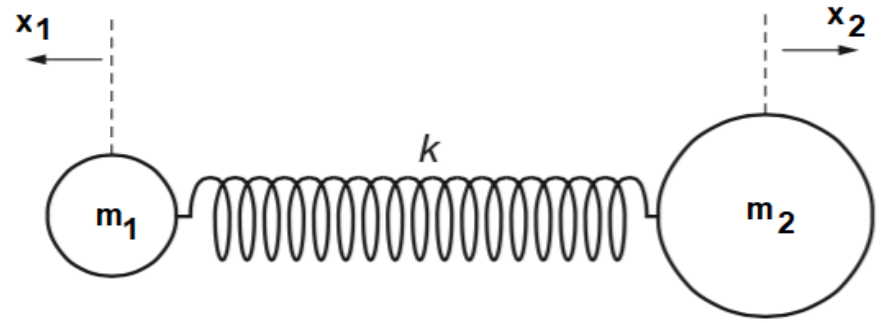

Fig. 1.1 Diatomic molecule model.

In the next sections a brief explanation of the vibrational theory of molecules is presented, since Raman spectroscopy lays the foundations for the SERS spectra analysis. In Section 1.2, the elementary diatomic molecule will be studied with the harmonic oscillator model. In Section 1.3 it will be gained an insight into the origin of Raman spectra, while IR and Raman spectra will be compared in Section 1.4.

1.2 Diatomic Molecule model for vibration

Let's start considering a molecule constituted of two atoms – with masses m_1 and m_2 – connected one to the other by mean of a chemical bond; this is called a diatomic molecule (see Figure 1.1).

The chemical bond can be treated as a spring connecting the two atoms, obeying the usual Hooke's Law. From the First Newton's Law, the forces acting on the single atoms can be expressed as

$$F_{12} = m_1 \frac{dv_1}{dt} \qquad \text{and} \qquad F_{21} = m_2 \frac{dv_2}{dt}. \tag{1.2}$$

Since $F_{12} = -F_{21}$, it's possible to write from 1.2

$$\frac{F_{12}}{m_1} - \frac{F_{21}}{m_2} = \frac{dv_1}{dt} - \frac{dv_2}{dt}$$

$$\frac{m_2 + m_1}{m_2\, m_1} F_{12} = -\frac{dv_{21}}{dt}. \tag{1.3}$$

From the Hooke's law the single force acting on the single atom can be rewritten as

$$F_{12} = -k(x_1 - x_2) \tag{1.4}$$

with k the spring constant of the bond and x_1 and x_2 the displacements of the two atoms. Combining equations 1.3 and 1.4, the following differential equation is obtained

$$\frac{d^2q}{dt^2} = -\frac{k}{\mu}q \tag{1.5}$$

with μ the effective mass of the system and q the total displacement. The solution of such a differential equation is

$$q(t) = q_0\, sin(2\pi\nu_0 t + \varphi) \tag{1.6}$$

with q_0 the maximum displacement, $\nu_0 = \frac{1}{2\pi}\sqrt{\frac{k}{\mu}}$ the vibration frequency of the diatomic molecule and φ the phase constant.
Eventually, the potential energy (V) and the kinetic energy (T) of the system can be found, so to obtain the total energy E

$$\begin{aligned} V &= \frac{1}{2}kq^2 \\ T &= \frac{1}{2}\mu\left(\frac{dq}{dt}\right)^2 \\ E = T + V &= 2\pi^2\nu_0^2\mu q_0^2 = const. \end{aligned} \tag{1.7}$$

Potential energy V of a harmonic oscillator is parabolic with q. It is clear that when $q = 0$ the potential energy is zero and the total energy consists only of the kinetic component; in the same way, when $q = \pm q_0$, the kinetic energy is zero and the total energy is only made of the potential component. Such a behaviour is the classical way to represent a diatomic molecule, but still deeply incorrect.

To overcome the limitations of such a model, vibration of a diatomic molecule is studied from the quantum mechanics point of view. The Schröedinger equation is here solved in the approximations of a system of equivalent mass μ. Once the eigenvalues are found, it is possible to notice that the quantum-mechanical frequency is the same of the classical model. Differently from the classical solution, the potential energy V results not being zero when $q = 0$ – but it takes minimum value $\frac{1}{2}h\nu$ – and it doesn't change continuously with q, but with steps of width $h\nu$.

Such results are reached for the simplifications of a harmonic oscillator; in the real case of a real molecule, the transition from a level to the next is not constant. Real behaviour can be described by the Morse potential function, shown in Figure 1.2. In brief, this function states

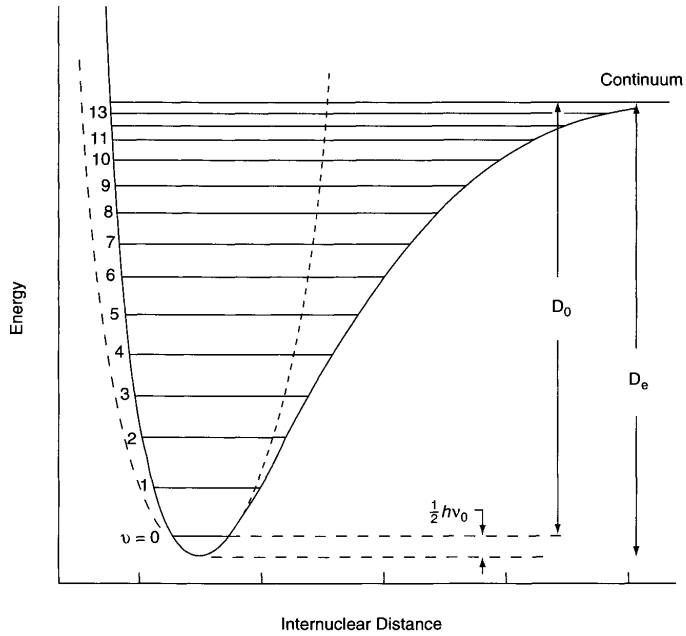

Fig. 1.2 Potential Energy Curves for diatomic molecule. Solid line is the Morse potential approximation of the actual potential. Broken line is the parabolic potential of the harmonic oscillator. [9]

that the energy levels of a diatomic molecule are not equidistant, but that their distance is decreasing as a function of v. In addition to this, from the Maxwell-Boltzmann distribution, it is possible to derive the population ratio of two energy levels:

$$\frac{P_j}{P_i} = e^{-\frac{\Delta E}{k_b T}} \tag{1.8}$$

where ΔE is the energy between the i^{th} and the j^{th} states, k_b the Boltzmann's constant and T the absolute temperature. As it can be seen, the higher the distance between the two states, the smaller the ratio. Then, at fixed temperature, if the energy difference between the two states is very large, it is more probable to find molecules in the i^{th} state, than in the j^{th}. This means that transitions from the j^{th} state to the near ones are less probable to happen. On the other side, for a smaller energy difference, more molecules are found in the j^{th} energy level. If the j^{th} level has more molecules, then also more transitions from this state to the nearer ones can occur. This translates in a higher intensity with which these transitions are observed.

Raman and IR spectroscopy take advantage of these properties to gain an insight on the

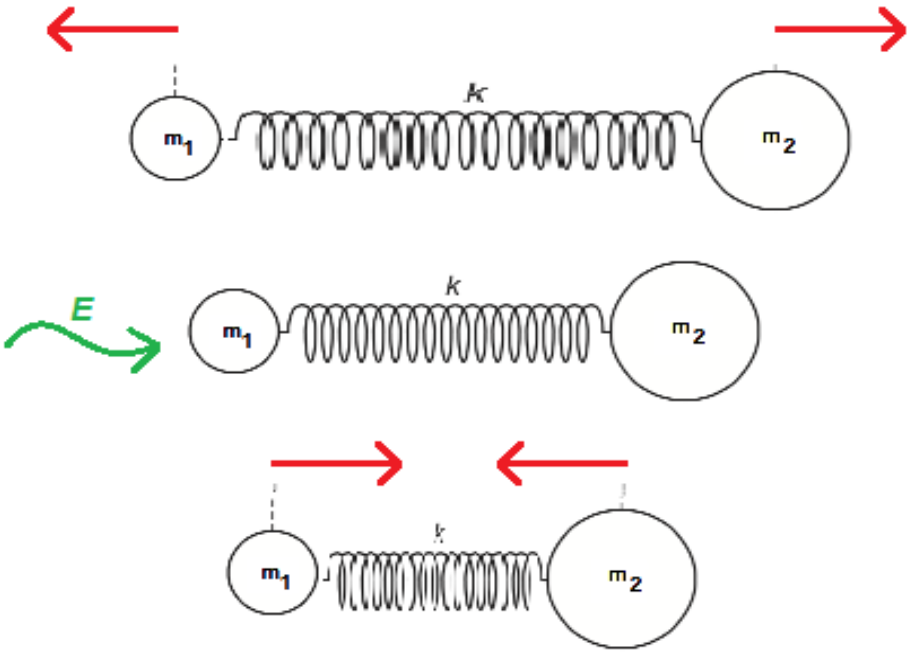

Fig. 1.3 Vibration of a diatomic model irradiated by an electric field **E** directed along the bond.

structure of the analysed molecules. In the following, a better explanation on the origin of the Raman spectra is given.

1.3 Origin of Raman Spectra

As already said, Raman spectra are originated by the interaction of a laser light beam and a molecule. As first approximation let's consider the system presented in Fig. 1.3, irradiated by an electromagnetic field – the laser beam – with an electric field **E** of magnitude

$$E = E_0 cos(2\pi\nu_0 t). \tag{1.9}$$

where the E_0 is the field amplitude and ν_0 the frequency of the oscillation. In the classical approximation, the induced oscillating dipole moment **P** of an anisotropic medium can be written as

$$\mathbf{P} = \underline{\alpha}\mathbf{E} = \begin{bmatrix} \alpha_{xx} & \alpha_{xy} & \alpha_{xz} \\ \alpha_{yx} & \alpha_{yy} & \alpha_{yz} \\ \alpha_{zx} & \alpha_{zy} & \alpha_{zz} \end{bmatrix} \cdot \begin{bmatrix} E_x\hat{\mathrm{x}} \\ E_y\hat{\mathrm{y}} \\ E_z\hat{\mathrm{z}} \end{bmatrix} \tag{1.10}$$

with $\underline{\alpha}$ the polarizability tensor, describing the chemical and physical properties of the sample. For simplicity, the electric field will be supposed directed along the bond of the molecule, so to have $E_y, E_z = 0$ (if the x-axis is taken along the bond). The vibration of the molecule can also be described by the nuclear displacement

$$q = q_0 \cos(2\pi \nu_m t). \tag{1.11}$$

with q_0 the amplitude of the vibration and ν_m the vibrational frequency of the molecule. In this approximation, the polarizability is just a proportionality constant, function of the displacement q. For small variations of q, the polarizability can be linearised by its Taylor series, obtaining

$$\alpha = \alpha_0 + \left(\frac{\partial \alpha}{\partial q}\right)_0 q + \ldots \approx \alpha_0 + \left(\frac{\partial \alpha}{\partial q}\right)_0 q_0 \cos(2\pi \nu_m t) + \ldots. \tag{1.12}$$

Finally, substituting equations 1.12 and 1.9 in 1.10, the induced dipole moment can be rewritten as follows

$$\begin{aligned} P &\approx \alpha_0 E_0 \cos(2\pi \nu_0 t) + \left(\frac{\partial \alpha}{\partial q}\right)_0 q E_0 \cos(2\pi \nu_0 t) = \\ &= \alpha_0 E_0 \cos(2\pi \nu_0 t) + \left(\frac{\partial \alpha}{\partial q}\right)_0 q_0 E_0 \cos(2\pi \nu_m t) \cos(2\pi \nu_0 t) = \\ &= \underbrace{\alpha_0 E_0 \cos(2\pi \nu_0 t)}_{\text{Raylieigh scattering}} + \underbrace{\left(\frac{\partial \alpha}{\partial q}\right)_0 \frac{q_0 E_0}{2} \{\underbrace{\cos[2\pi(\nu_0 + \nu_m)t]}_{Stokes} + \underbrace{\cos[2\pi(\nu_0 - \nu_m)t]}_{Anti-Stokes}\}}_{\text{Raman scattering}}. \end{aligned} \tag{1.13}$$

The induced dipole moment is made of two components; the former radiates light with same frequency ν_0 of the incident beam (Rayleigh scattering); the latter is the result of the modulation of the input field, due to the vibrational response of the molecule (Raman scattering). Beside this, Raman scattering is given by two frequencies; $v_0 - v_m$ (Stokes frequency) and $v_0 + v_m$ (Anti-Stokes frequency).

From a semi-classical approach, the appearance of the Normal Raman bands (see Figure 1.4a) can be explained as follows. When a photon of energy $h\nu_0$ hits a molecule at the ground state E_0, this reaches a "virtual state" – an energy level E_n below the first excited vibrational state of the molecule. In this condition, three cases may arise. In the first case the molecule decades again to the original ground state E_0 and the Rayleigh band forms. In the second occurrence, the excited molecule decades from the virtual state to a higher vibrational energy level than the original one, emitting a light with frequency $(v_0 - v_m)$. The remaining energy

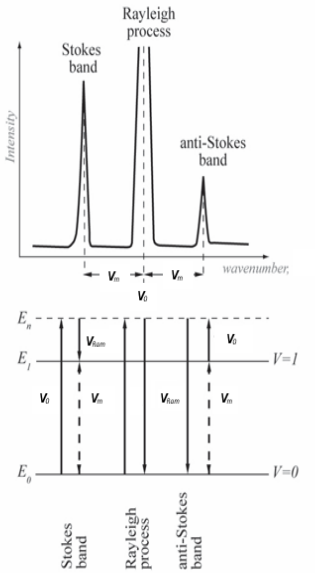

(a) Normal Raman energy levels for Stokes, Rayleigh and anti-Stokes bands

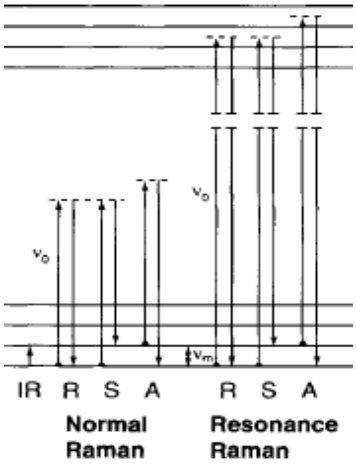

(b) Normal Raman and Resonance Raman energy levels [9]

Fig. 1.4 Normal Raman and Raman Resonance energy levels

is converted into vibration of the molecule, at a frequency v_m; this gives origin to the Stokes band. Since the probability of molecules to go to a higher energy level is lower, also the corresponding Raman band will have a lower intensity. Finally, the anti-Stoke process occurs when a state lower than the initial is reached, so that the scattered light will have a frequency of $(v_0 + v_m)$, higher than the one of the incident beam. This is the least probable occurrence and the corresponding peak will be the weakest.

In Raman spectroscopy the Stokes and anti-Stokes bands give the same information about the vibration of the molecule, so that just one of them is measured as a frequency shift from the Rayleigh band.

Moreover, when the energy of the laser is chosen exactly with an energy able to excite the molecule to an electronic excited state, the Raman spectrum presents a very high enhancement, justified by this peculiar transition; this occurrence gives origin to the Resonance Raman Spectra, an optimum condition to obtain high intensity Raman signals (see Figure 1.4b).

Finally, it is important to underline from equation 1.13 that in order to have Raman-activity, the polarizability α_0 at equilibrium position can also be zero, but the condition $\left(\frac{\partial \alpha}{\partial q}\right)_0 \neq 0$ is necessary. In other words, even if the molecule has no intrinsic dipole moment – for example in the case of homonuclear molecules – it is enough that the polarizability

changes, due to vibrational activity, to have Raman scattering. In the following section it will be explained why this phenomenon makes IR and Raman spectroscopy two complementary techniques.

1.4 Vibrations of Polyatomic Molecules

So far, only the vibration of diatomic molecules has been analysed. In this simple case, the vibration occurs only in the direction of the chemical bond between the nuclei of the molecule. In complex polyatomic molecules each single nucleus vibrates of its own harmonic oscillations. It can be shown that these complex vibrations can be considered as the superposition of many "normal vibrations", each independent from any other [9] .

Consideration can be given to a N-atoms polyatomic molecule. Since each atom can freely move in three directions, $3N$ degrees of freedom must be taken. Included in these $3N$ degrees of freedom of motion, 3 are the ones for a translation of the molecule in the main axes directions and other 3 include the rotational motions around the three main axes passing through the centre of gravity. Ultimately, only $3N-6$ are the net vibrational degrees of freedom (in case of linear molecules they become $3N-5$, since rotation around the molecular axis can't occur). These vibrations become the normal modes to describe complex vibration motions of the molecule.

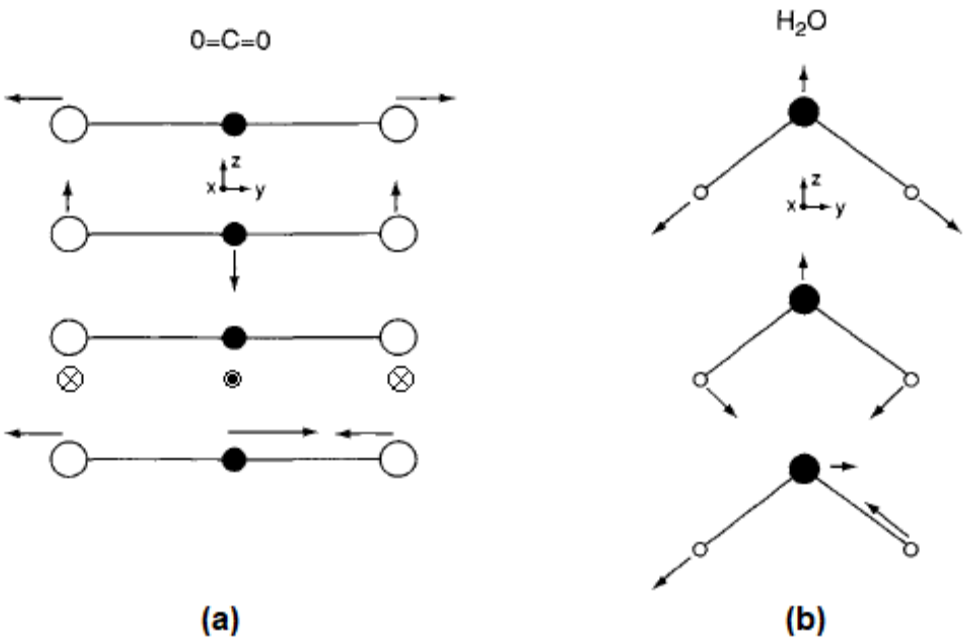

Fig. 1.5 Normal modes of vibration of CO_2 (a) and H_2O (b) [9]

As an example, the CO_2 and the H_2O molecules are considered (see Figure 1.5). The former is a linear molecule, so that the total number of normal modes is equal to 4. In fact, the rotation around the molecule axis (the *y-axis* in the Figure) doesn't give any important variation of the geometry of the structure. The same thing can't be said for the H_2O molecule: as a result, 3 normal vibrations must be considered. In both cases, all the vibrations can be written as superimposition of their normal vibrational modes.

1.4.1 Mutual Exclusion Principle

Normal vibrations can be IR-active or Raman-active, or both. As already said IR-spectra are related to the absorption of an incident infra-red light. Then, according to quantum mechanics a vibration is IR-active when the dipole moment changes. This means that a heteropolar diatomic molecule can't ever be IR-active.
As already underlined from equation 1.13 – Raman-activity is satisfied when at least one of the components of the polarizability tensor changes with the vibration.

Selection rules allow to determine whether the vibration is IR-active or Raman-active. After an accurate inspection of the normal modes, the *Mutual Exclusion Principle* can be derived; for simple structures it can be stated that; vibrations symmetric with respect to the molecule centre of symmetry are Raman-active, but not IR-active, whereas those antisymmetric with respect to the centre of symmetry are IR-active but not Raman-active. The Mutual Exclusion Principle works also for the molecules with more complex structures. In fact, studying the molecule symmetry in its equilibrium structure, it is possible to predict whether its normal vibrational modes are IR or Raman active.
Mutual Exclusion Principle is clear comparing the IR and Raman spectra of the same sample: typically, bands of high Raman-activity correspond to weak bands in the IR spectra, and vice versa.

Chapter 2

SERS spectroscopy

2.1 Introduction

The origin of the Raman spectra was explained in the previous chapter. In a nutshell, when an intense laser beam hits a molecule, this radiates light, which is made mainly of two components; the former with the same frequency of the incident beam (Rayleigh scattering); and the latter with a frequency which is the result of the modulation of the input field, due to the vibrational response of the molecule (Raman scattering). The Raman scattering is actually a rare event – compared to the Rayleigh scattering – so that, generally, Raman signals are extremely weak.
By the way, Raman signals can be amplified in particular conditions. In fact, when an electromagnetic field interacts with metals, an amplification of the near-field concerning the metal surface is observed, thanks to specific optical excitations known as plasmon resonances [2]. SERS effect takes advantage of this phenomenon to boost the Raman signals. In fact, when a molecule is adsorbed on the metal surface (or when it is at least very close to it) these plasmon resonances can be exploited to obtain the Raman signal amplification, mainly due to the so-called electromagnetic enhancement.
In spite of this, SERS effect may also introduce some differences in the spectra of the molecules. In fact, the enhancement of the Raman spectra, is not equal for all the wavelengths, so that the different characteristic peaks may undergo also different intensity amplification. In addition to this, also a shift of the Raman modes can be observed. These last effect is due to the so-called chemical enhancement, caused by the interaction between the metal surface and the adsorbed molecule.

Since the plasmonic resonance mechanisms play a big role in the SERS effect, in Section 2.2 a review of the optical properties of metals will be presented, in order to introduce

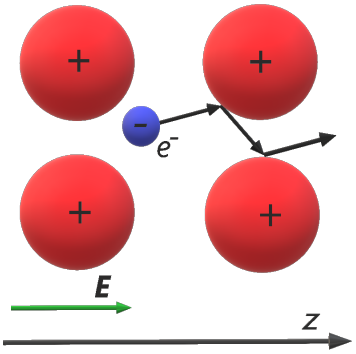

Fig. 2.1 Microscopic model of a metal immersed in an electric field as described by the Drude model: the electric field forces the electrons to move; these interact with the positive ions of the lattice of the metal and slow down.

the definition of plasmons and Localized Surface Plasmons (LSP). Hence, electromagnetic and chemical enhancement effects will be analysed respectively in Sections 2.3 and 2.4, to understand how to act on the substrates to have more optimized nanostructures for a high enhancement.

2.2 Basics for SERS spectroscopy

2.2.1 The Drude model and the optical properties of metals

The Drude model is a simple way to describe the interaction between an electromagnetic field and a metal. The electrons of a metal are free to move in a background of positive ions, forming by definition the so called free-electron plasma, or solid-state plasma. The optical response of the solid-state plasma is, at first approximation, the one that governs the overall optical response of the metal.

Let's suppose for simplicity that a metal is irradiated by a planar and linearly polarized electric field $\mathbf{E}$ oriented along $\hat{z}$. To model the optical response of the metal, all the forces acting on the electrons and the ions – and between these – should be considered.

Considering the difficulty of such a task, as first approximation, we'll suppose that the vibrations of the ions (the so-called phonons) and that the electron-electron and phonon-electron interactions are negligible. Moreover, since the conduction electrons in a metal are not bound, no attractive force (long range interaction) is supposed to exist between them. Hence, two forces are supposed to act on a single electron of the metal: the former is the force of the electric field, the latter a linear-damping term. The latter is justified by the instantaneous interaction of the electrons with the positive ions: indeed, during their motion, electrons are slowed down by the collisions with the positive ions forming the lattice (see

Figure 2.1), resulting in a modelled energy-dissipative force, describing the dissipation of part of the kinetic energy of the electrons into heat (phonons). The equation of motion governing the single electron can finally be written as follows

$$\begin{aligned} m_e \frac{d^2}{dt^2} z(t,\omega) &= -eE - b\frac{d}{dt} z(t,\omega) \\ \frac{d^2}{dt^2} z(t,\omega) + \gamma \frac{d}{dt} z(t,\omega) &= -\frac{e}{m_e} E \end{aligned} \tag{2.1}$$

where m_e [kg] is the mass of a single electron, γ [rad s^{-1}] the rate of collisions of electrons with the crystal or the impurities and e [C] the electric charge of a single electron. Applying the Fourier transform to both the terms of equation 2.1, the dependency on ω can be found

$$Z(\omega,t) = \frac{e}{m_e} \frac{1}{\omega(\omega + i\gamma)} E(\omega,t). \tag{2.2}$$

From equation 2.2 it is possible finally to find the Drude relative dielectric function of the metal, i.e.:

$$\varepsilon(\omega) = 1 - \frac{ne^2}{m_e \varepsilon_0} \frac{1}{\omega(\omega + i\gamma)}. \tag{2.3}$$

The response of the positive ions in the crystal has been neglected so far. This is true only in case of long wavelengths, but not for higher frequencies. For this reason, their contribution is added and modelled as a constant background real dielectric function $\varepsilon_\infty \geq 1$. Finally, including this contribute in 2.3, the final expression of $\varepsilon(\omega)$ is obtained:

$$\varepsilon(\omega) = \varepsilon_\infty \left(1 - \frac{{\omega_p}^2}{\omega(\omega + i\gamma)} \right) \tag{2.4}$$

with $\omega_p = \sqrt{\dfrac{ne^2}{m_e \varepsilon_0 \varepsilon_\infty}}$ the plasma frequency of the metal, corresponding to the natural oscillation of the solid-state plasma charge density. Finally, from equation 2.4, and supposing negligible the magnetic response of the medium, the refractive index of the metal is found, i.e.:

$$n(\omega) = \sqrt{\varepsilon_\infty \left(1 - \frac{{\omega_p}^2}{\omega^2 + \gamma^2} + i\frac{{\omega_p}^2 \gamma}{\omega\,(\omega^2 + \gamma^2)} \right)}. \tag{2.5}$$

From equation 2.5 the optical response of a metal can be derived. In fact, in the event that $\omega < \gamma$, the refractive index $n(\omega)$ has non-negligible real and imaginary parts. This means that both the dispersion and absorption phenomena occur. Important results are obtained at high frequencies, i.e. in the range where the condition $\omega > \gamma$ is satisfied. In this range (which still contains visible wavelengths) and in the condition $\omega^2 > {\omega_p}^2$, absorption becomes negligible and only the dispersion phenomenon is detectable. Nevertheless, the range of the most interesting optical effects of metals (including plasmon resonances), is still the one in high frequency range, but with $\omega^2 < {\omega_p}^2$. In this peculiar range, the dispersion becomes negligible and the absorption is still really small. Here the refractive index can be rewritten as follows:

$$n(\omega) \approx \sqrt{\varepsilon_\infty \left(1 - \frac{{\omega_p}^2}{\omega^2}\right)} \approx i\frac{\sqrt{\varepsilon_\infty}\omega_p}{\omega}. \tag{2.6}$$

For the case of Ag it has been verified experimentally a value of $\sqrt{\varepsilon_\infty}\omega_p = 1.4 \times 10^{16}\, rad\, s^{-1}$ [10], resulting in a very small refracting index, a very low absorption and a reflection coefficient close to one.

The Drude model gives a very simple description of the optical behaviour of a metal, but it is still a starting point for our aim to describe the plasmonic resonances. In real metals, other optical processes should be taken into account, such as the inter-band transitions and non-local properties (for example with the ε not depending only on the frequency ω, but also on the position through $\mathbf{k}$).

2.2.2 Plasmons and Localized Surface Plasmons (LSPs)

2.2.2.1 Definition of Plasmons

As already explained, when light interacts with a metal (and with the nanostructured features of a metal in the case of SERS), certain excitations are produced, known as plasmonic resonances. The solid-state charge plasma density of a metal, described in simple words by the Drude model, plays an important role in the origin of these plasmonic resonances.
Although this, before talking about the plasmonic excitations, plasmons must be defined. These are described as "the quantum of elementary excitation associated with the high-frequency valence electron collective oscillations"[11]. To better understand this definition, plasmons can be compared to photons; a photon is in fact the quantum particle that describes the elementary excitations of the free electromagnetic field oscillations. At the same way, plasmons can be described in a classical way as plasma charge density oscillations, or

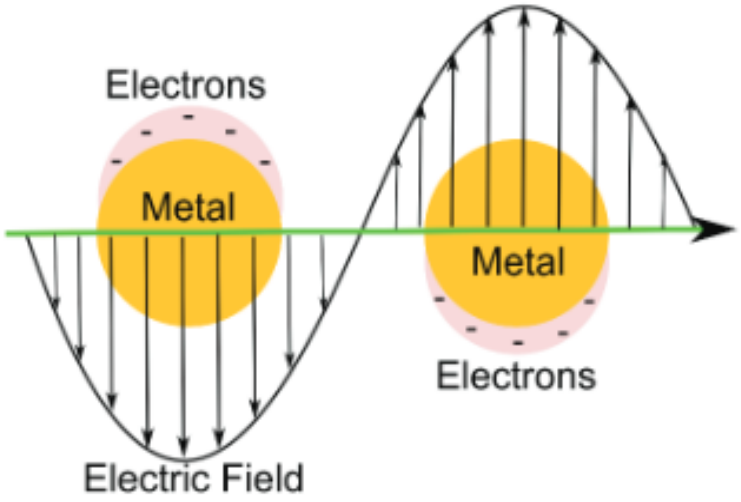

Fig. 2.2 The coupling between the EM field and the metallic spheres induces the oscillations of the electrons in the spheres. The interaction between the field and the free-electron plasma of a metal is known as plasmon-polariton. [12]

defined purely as 'plasmons'when dealing with quantum aspects of the plasma charge density oscillations. This permits a full description of the plasmonic-effects as electromagnetic effects, coupling the description of the problem only to the optical properties and to the geometry of the specific case.

Let's suppose now to consider an electromagnetic field propagating in an optically responsive medium – meaning that at least one of the relative dielectric function ε or the relative magnetic permittivity μ must be different from one. The electromagnetic field oscillations excite the internal degrees of freedom of the medium (i.e., bound electrons in a dielectric and free-electron plasma in a metal at infra-red and visible ranges) and, from a classical point of view, this interaction is perfectly described by the Maxwell's equations in a medium. In fact, the polarization field **P** and the magnetization field **M** fully describe the internal excitations of the medium, as response to the EM field oscillations. The same problem can also be depicted as the interaction between the photons and the microscopic structure of the medium. Energy is exchanged between the EM field oscillations and the internal excitations of the medium [2], so that the quantum particle that describes this interaction is not a photon any more, but a quasi-particle that is called polariton.
Moreover, as already said, the optical response of a metal is dominated by the interaction of the photons with the free-electron plasma, at least in the visible and infra-red ranges. This peculiar interaction between a photon and the free-electron plasma of a metal will be

specifically named plasmon-polariton (see Figure 2.2).
Resuming, a plasmon represents the quasi-particle describing the collective charge density oscillations not interacting with light, while plasmon-polaritons are specifically a mixture of plasmons and photons, in the infra-red and visible ranges, and they can't exist without the interaction with a photon. An important family of plasmon-polaritons for the explanation of the SERS effect is the one of the so-called Surface Plasmon-Polaritons (SPPs). These correspond to a mix of longitudinal charge density wave (plasmon) in metal thin films and a transverse electromagnetic wave (photon).

Despite the apparent complexity of such definitions, plasmon effects can be fully described without any consideration on the free electron dynamics of the charge oscillations. In fact, the dynamic of the charge density is strictly related to the optical properties of the material – for example, as seen for the case of the metal in the Drude model. For this reason, the only complexity occurs in studying the SERS and plasmonic phenomena knowing the optical response of the metal, described by its relative dielectric function $\varepsilon(\omega, \mathbf{k})$. With this approach, plasmon-polaritons – and especially SPPs – can be studied as electromagnetic modes of the system under test.

2.2.2.2 Localized Surface Plasmons

Surface Plasmon Polaritons (SPPs) have been defined as electromagnetic surface modes of the system, associated with surface charge oscillations. In SERS spectroscopy only some of these modes play an important role for the desired enhancement effect. With a view to understanding how to manipulate a SERS substrate to optimize the enhancement, such modes must be studied.

For this reason the first ideal system to take into account is the one of a planar interface between a semi-infinite non-absorbing dielectric (i.e. with a real and constant dielectric function $\varepsilon_M \geq 1$) in the $z < 0$ half-plane and a semi-infinite metal with a dielectric function $\varepsilon(\omega)$, occupying the $z > 0$ half-plane (see Figure 2.3a). As shown by Le Ru and Etchegoin [2], surface modes exist for this system only in the assumption of TM polarization, and never for TE one. Hence, in the assumption of a TM polarized field, with wavevector $\mathbf{k}$ laying on the $xz-plane$, and imposing the boundary conditions on the fields at the discontinuity, the dispersion relation for the existence of the surface modes is found as follows:

$$k_x{}^2 = \frac{\omega^2}{c^2} \frac{\varepsilon\, \varepsilon_M}{\varepsilon + \varepsilon_M}. \tag{2.7}$$

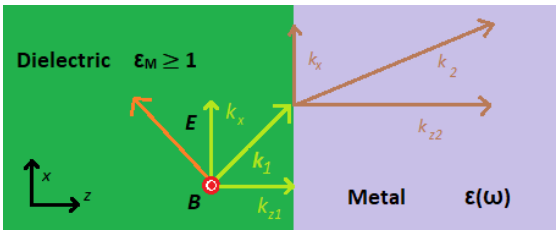

(a)

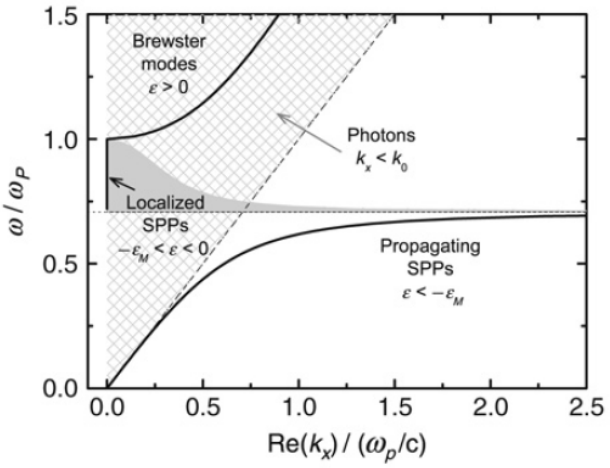

(b)

Fig. 2.3 Figure (a): Schematic view of an EM field, with wavevector **k** approaching the interface between a non-absorbing dielectric and a metal. The EM field is supposed with TM polarization.
Figure (b): Dispersion relation for an interface of air ($\varepsilon = 1$) and an ideal metal following the Drude model (2.3); with $\varepsilon_\infty = 1$, a plasma frequency ω_p and no absorption ($Im(\varepsilon) = 0$). [2]

Knowing the frequency dependency of the invariant component k_x of the wave-number **k**, the transversal component k_{z1} at the dielectric side and the transversal component k_{z2} at the metal side can be found. Different modes are characterized by different values of the real and imaginary parts of each component.
In Figure 2.3b the dispersion relation for an ideal Drude metal with ω_p plasma frequency is plotted and three different types of modes can be visualized;

- for $\omega > \omega_p$, Bulk Plasmon modes are obtained. These modes are not generally useful for plasmonic and SERS applications and are differentiated from the Surface Plasmon modes:
- for $\omega_{sp} < \omega < \omega_p$, Localized Surface Plasmons (LSPs) are obtained. The frequency ω_{sp} is known as the surface plasmon frequency. These modes are not propagating, meaning that the component k_x along the discontinuity is purely imaginary, and thus

evanescent. This characteristic is clearly visible in Figure 2.3b, where the real component of k_x results zero for all the interval of frequencies from ω_{sp} and ω_p. Nevertheless, the transversal components of the wave-numbers are both real, making them radiative, i.e. with waves propagating from the surface. Such modes are the most important in the case of SERS applications, being the ones that make the electromagnetic enhancement possible:

- and finally for $\omega < \omega_{sp}$ the Propagating Surface Plasmons (PSPs) are obtained. Such modes are still surface plasmons, but propagating along the surface and non-radiative. These are fundamental for plasmonic applications, but negligible for the explanation of the SERS effect, where LSPs take a major role.

The previous case gives a first explanation on the origin of the LSPs. In any case, when talking about SERS spectroscopy the geometries to be investigated are different. In the previous example, indeed, the planar approximation could be used since dealing with features of the boundaries bigger than the wavelength, so that the Geometrical Optics approximation was valid.

However, when dealing with the SERS effects, small metallic objects – comparable or smaller than the used wavelengths of impinging radiation – are involved. In this case, electromagnetic modes exist for discrete values of ω, and not as continuous modes, like in the dispersion relation of equation 2.7. The study of such LSPs modes becomes very important for the SERS applications. The final aim of such a study is to understand which are the main radiative LSP modes that contribute significantly to the electromagnetic enhancement. In fact, coupling to LSP modes will result in a resonant optical response at the LSP frequency. The nature of such modes guarantees an enhancement of the field on the surface and nearby the small metallic object.
Next paragraph will seek to give information of the LSP resonances of nanoparticles, trying to understand the reasons of the electromagnetic enhancement of the SERS effect and how size, shape and morphological characteristics of nano-particles in general influence the enhancement and then the final SERS effect.

2.3 The Electromagnetic Enhancement

The SERS effect is given by two main enhancement contributions: the electromagnetic (EM) enhancement and the chemical enhancement. A molecule near a SERS substrate is influenced by these effects when analysed by means of Raman spectroscopy. In fact, the EM SERS

enhancement effects contribute with a Local Field enhancement nearby the metallic surface. In addition to this, the chemical enhancement is observed in the variation of the Raman polarizability of the molecule.
Metallic nanoparticles play a central role in SERS spectroscopy. In the following subsections, the effects influencing the EM enhancement are studied, starting from simple systems and generalizing the results for more complex cases.

2.3.1 LSP resonances and Local Field Effects

As an initial step, the LSPs resonances of a single metal particle are computed and the variation of the local field nearby the surface analysed, starting from certain required approximations for analytical results.

2.3.1.1 The Electrostatic Approximation solution: Mie theory

The first simple case to take into account is that of a metallic particle with a spherical geometry (see Figure 2.2), a diameter a and with dielectric function $\varepsilon(\omega)$, completely immersed in a non-absorbing infinite dielectric medium with dielectric function ε_M. Such a problem is analytically soluble applying the Mie theory, to find an analytical solution for the scattering of a spherical metallic particle in the so-called Electrostatic Approximation (ESA). This means that the solution is accepted as valid in the assumption that the maximum size of the object is much smaller than the wavelength of the approaching field, i.e. retardation effects are initially supposed negligible.

The ESA involves an incident uniform electrostatic field $\mathbf{E_{Inc}}$. The solution of such a problem is known (see for example Ref. [2]) and the internal electric field to the metallic sphere found:

$$\mathbf{E_{Int}} = \frac{3\,\varepsilon_M}{\varepsilon + 2\,\varepsilon_M}\mathbf{E_{Inc}} = \tag{2.8}$$

$$= (1-\beta_s)\mathbf{E_{Inc}} \tag{2.9}$$

where

$$\beta_s = \frac{\varepsilon(\omega) - \varepsilon_M}{\varepsilon(\omega) + 2\,\varepsilon_M}, \tag{2.10}$$

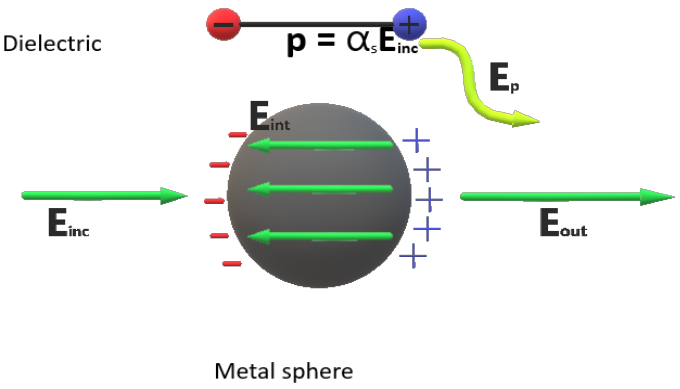

Fig. 2.4 Schematic view of a metallic sphere immersed in an infinite dielectric medium. The sphere behaves as an equivalent dipole, with charges oscillating under the action of the incident field $\mathbf{E_{inc}}$. The oscillation produces a field $\mathbf{E_p}$ that adds to the incident one, hence resulting in an external field, in the vicinity of the sphere surface, equal to $\mathbf{E_{out}}$.

with β_s the non-dimensional polarizability of the sphere.
The electric field inside the sphere is then constant and uniform, and the internal electric polarization can be easily found out. In fact, reminding that the electric displacement field is equal to $\mathbf{D} = \varepsilon_0 \varepsilon_M \mathbf{E_{int}} + \mathbf{P}$ – with the usual constitutive relation $\mathbf{D} = \varepsilon_0 \varepsilon \mathbf{E_{int}}$ – the electric polarization inside the sphere (but relative to the medium, and not to the vacuum, usually done) is obtained, using equation 2.8:

$$\mathbf{P} = 3\varepsilon_0 \varepsilon_M \beta_s \mathbf{E_{Inc}}. \tag{2.11}$$

Finally, since the polarization field is uniform inside the sphere, it is possible to integrate over the volume of the sphere, hence obtaining an equivalent dipole $\mathbf{p} = \alpha_s \mathbf{E_{Inc}}$.
These results tell that the incident field $\mathbf{E_{Inc}}$ induces a polarization $\mathbf{P}$ inside the volume of the sphere, which is equivalent to an induced dipole $\mathbf{p}$, centred at the centre of the sphere. This induced dipole creates a field $\mathbf{E_p}$ that adds to the incident field outside the sphere, giving a total electric field as the following:

$$\mathbf{E_{Out}} = \mathbf{E_{Inc}} + \mathbf{E_p}. \tag{2.12}$$

In Figure 2.4 a schematic view of the all process is shown. From equations 2.10 and 2.11, it becomes clear that no size dependency is taken into account in the ES approximation. In fact, such approximation is valid only for the spheres with diameters much smaller than visible wavelengths (smaller than $10\,nm$). For this reason, in the Mie theory a correction

is required to consider the size dependency, which is included in the β_s formula. Besides this, with the Mie theory also non-uniform incident fields can be considered, with solutions that are similar to the previous case. The main difference is that the total electric field outside the sphere will be considered as a sum of spherical harmonics, each described by the polarizability α_l, with l the index of the harmonic.

2.3.1.2 Localised Surface Plasmon Resonances (LSPRs)

The first resonance frequency – corresponding to the so-called dipolar localised surface plasmon resonance – is the most important for the EM enhancement effects. This is found maximizing the magnitude of the polarization **P** (see equation 2.11), which is equivalent to imposing a maximum non-dimensional polarizability β_s. In fact, reminding that the dielectric function $\varepsilon(\omega)$ of a metal is generally complex, in the ESA the resonance condition is found when the value of the module of β_s (see equation 2.10) tend ideally to infinity, with the square of the module of β_s equal to the following:

$$|\beta_s(\omega)|^2 = \frac{|(\varepsilon'(\omega) - \varepsilon_M)^2 + \varepsilon''^2(\omega)|}{|(\varepsilon'(\omega) + 2\varepsilon_M)^2 + \varepsilon''^2(\omega)|}. \tag{2.13}$$

In the ideal case, resonance is found when the real part of the dielectric function of the metal satisfies the condition $\varepsilon'(\lambda_{res}) = -2\varepsilon_M$, coupled with a non-absorbing behaviour of the metal ($\varepsilon''(\lambda_{res}) = 0$). For a real metal the condition on the imaginary part of the dispersion function is impossible, since a metal always presents absorption, hence an ε'' always different from zero. Yet despite this, strong resonances can still be obtained for metals with low absorption in the resonance range. An example is the case of silver, for which the strongest resonances are obtained in this region, which is the one already seen in the Drude model of the metal, which takes an important role also in SERS spectroscopy, as already stated.
Higher resonances can also be found outside the ESA, for non-uniform incident electric fields. As already said above, in this case a polarizability α_l is taken into account and the conditions on the dispersion function imposed.

Finally, Mie theory gives the dependency of the resonances on the size of the metallic sphere. It is found (see for example Le Rue et. al ref. [2]) that the dipolar LSP resonance is the one with the longest wavelength, undergoing a shift towards longer wavelengths when increasing the size of the sphere. For what concerns higher-order LSP resonances, it is found that they are negligible for the smaller spheres, but become more and more significant with the increase of the size.

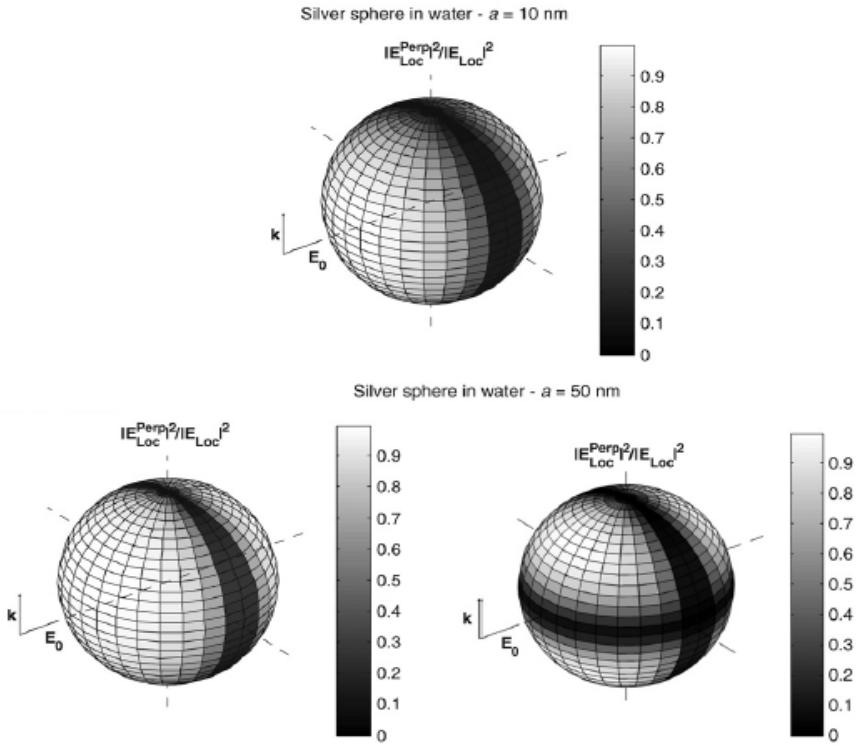

Fig. 2.5 Normal component $|\mathbf{E}^{\perp}|\backslash|\mathbf{E_{Loc}}|$ computed at the main dipolar LSP resonance (top) for a 10 nm radius silver sphere in water at $\lambda = 392nm$, and (bottom left) for a 50 nm radius silver sphere in water at $\lambda = 492nm$. Normal component $|\mathbf{E}^{\perp}|\backslash|\mathbf{E_{Loc}}|$ computed at the quadrupolar LSP resonance (bottom right) for a 50 nm radius silver sphere in water at $\lambda = 393nm$ [2]

2.3.1.3 Local field enhancement and size effect

As already said, the Raman spectrum of a molecule is affected by the EM enhancement; these effects are attributed to the local fields effects. In order to understand how they act on a molecule on or nearby the surface of the metallic particle, the local field enhancement distribution can be computed, in the assumption of an incident plane wave with a wave-vector along the $z-axis$ and a polarization along the $x-axis$.

From Figure 2.5 it is clear that the local field enhancement is stronger at points perpendicular to the electric field of the incident wave, but minimum for points tangential to the electric field. Moreover, for what concerns the dipolar LSPR, the local field enhancement is more uniform on the surface of smaller spheres, while the variation changes more quickly for bigger spheres.

From the field distribution, it is also clear why first resonance is called dipolar LSP resonance; for example, looking at the distribution shown in Figure 2.5 (top and bottom left spheres), it is possible to find similarities to the distribution that would be originated by a dipole,

centred at the centre of the sphere and oriented along the incident field $\mathbf{E_{Inc}}$. At the same way, the quadrupolar resonance resembles the distribution that would be given by a quadrupolar source at the centre of the sphere.
Finally, a molecule at distance d from the surface is effected by an electric field, which has undergone a decay inversely proportional to $(a+d)^3$.

In conclusion, the SERS effect is stronger near the surface of the metallic particle, preferentially at certain points, depending on how the incident wave excites the surface charge density (i.e., coupling into LSP polaritons). Moreover, the enhancement has a decay that is function of the distance from the surface and such decay is faster for higher-order resonances.

2.3.2 Shape effect on EM enhancement

The real shape of the metal nano-particle strongly influences the LSP resonances and then the local field, too. With the aim of finding results for the general case of a nano-particle with any shape, a simplified model is first studied.

For this reason, at first stage, an ellipsoidal metal nano-particle, surrounded by an infinite dielectric with real dielectric function ε_M is taken as sample of study in the assumption of ES approximation. Results are very similar to the one obtained for the sphere, with the difference that three non-dimensional polarizability functions are obtained, each for one of the main axes of the ellipsoid, with the i^{th} being as follows:

$$\beta_i(\omega) = \frac{\varepsilon(\omega) - \varepsilon_M}{3L_i\,\varepsilon(\omega) + (3-3L_i)\varepsilon_M}, \quad i = 1, 2, 3, \tag{2.14}$$

with L_i the geometrical factor of index i.
As in the simple case of the sphere, also here the resonance condition is imposed on the non-dimensional polarizability β_i, with the result of three LSP resonance wavelengths, each associated to one of the main axes. In a nutshell, when these resonances are compared to the dipolar resonance of a sphere, the following results are found: the axes featured by surfaces with smaller curvatures, if compared to the one of the sphere, present smaller resonance wavelengths; at the same time, axes with pointy curvatures, if compared to the one of the sphere, show resonances with wavelengths longer than the one of the sphere. These results are shown in the graph of figure 2.6. Here the resonance wavelengths of different spheroids (i.e. ellipsoids with two equal semi-axes length) are shown as a function of the Aspect Ratio (A.R.). More precisely, an oblate ellipsoid and a prolate one are chosen as example to understand how the A.R. affects the LSPRs and the Local Field effects.

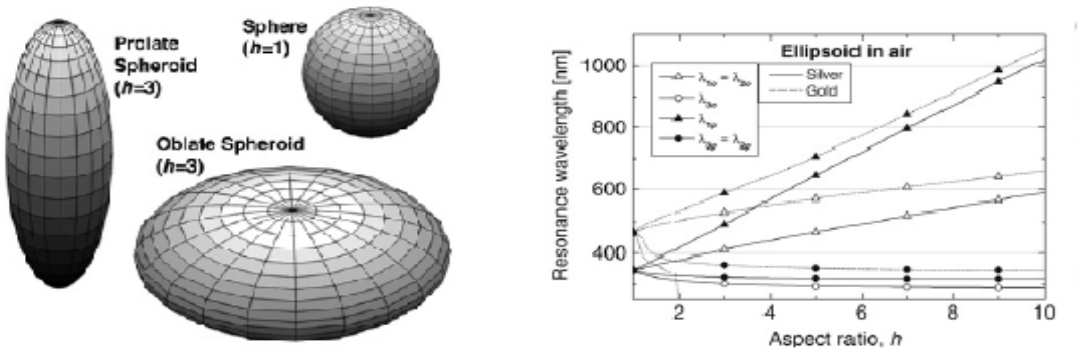

Fig. 2.6 Resonance wavelengths for silver and gold ellipsoid embedded in air, for different A.R.s, for prolate and oblate ellipsoids [2]

These results translate of course also in different enhancements for each axis. In fact, it is found out that flat curvatures (i.e. smaller A.R.s) give rise to damped resonances and damped EM enhancement as well; on the other side, pointy curvatures (i.e. higher A.R.s) result in enhanced resonances and enhanced EM effects too, of course in comparison to the one of a spherical metal particle.

Previous considerations can finally be extended to more complex shapes. This means that LSP resonances depend strongly on shape and size of the nano-particle. It is possible to state that in general LSPRs shift to longer wavelengths with the increase of the size of the nano-particle and with the increase of the sharpness of the curvature of the surface, with stronger enhancement for sharper surfaces.

2.3.3 Coupled-LSPRs and hot-spot localization

The Mie theory is a powerful tool for the analysis of simple, but fundamental geometries to understand EM enhancement effects for single particles. Nonetheless, it ignores the interaction between two objects in the vicinity of each other. For this reason, another simple case can be studied by means of the so-called Generalized Mie theory, that investigates the interaction between two metal spherical nano-particles separated by the gap g. Even if this is just a simple case, it can later be further generalized by extending the results for particles with any shape and size (thanks to the previously found results).

The system is made of two identical metallic spheres of diameters a and dispersion function $\varepsilon(\omega)$, separated by the gap g, and immersed in an infinite non-absorbing dielectric

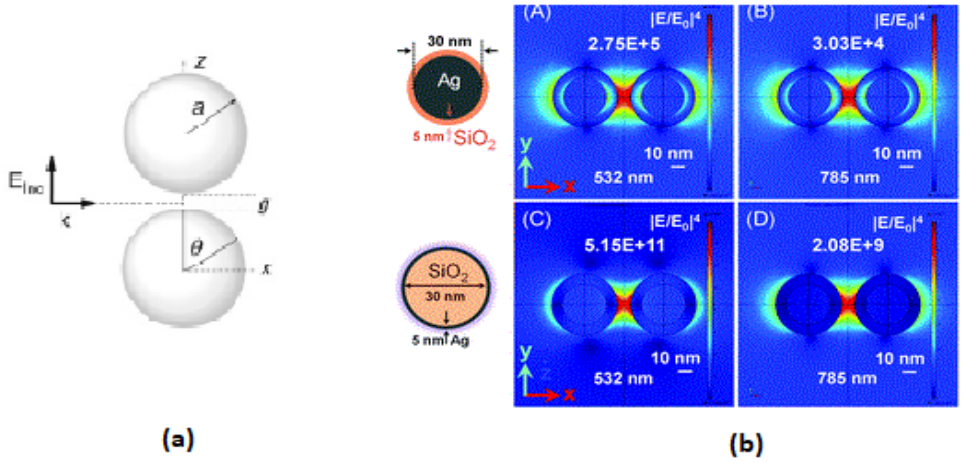

Fig. 2.7 Figure (a): Schematic configuration of a dimer (along z) formed by two spheres of radii a and separated by a gap g. The incoming wave is polarized along z (axis of the dimer) and with wave-vector **k** along x. [2]
Figure (b): "Calculated electromagnetic field distribution in the dimers consisting of two types of nanoparticles: (A)–(D) silver nanoparticles (30 nm) with a thin silica layer (5 nm) and silica nanoparticles (30 nm) with a thin silver layer (5 nm) at two excitation wavelengths (532 nm and 785 nm)." The hot-spot region exhibits high EM field intensities. [13]

with dielectric constant ε_M. As shown in Figure 2.7a the incident electric field is supposed having a wave-vector **k** perpendicular to the dimer axis, and a polarization that lays on it.

From the coupling of the two objects, new LSP resonances are created; these are different from the ones of the isolated particles; to underline this fact, they are called coupled-LSP resonances. Also the dipolar LSP resonances of the single particles couple, giving rise to the so-called main coupled-LSP resonance of the dimer, that – taking into account the molecular orbital theory – presents a longer resonance wavelength, if compared to the one of the single separated objects. Of course, also other new resonances form, due to the coupling of the single LSP resonances of the single objects, but like the single particle case, the most important resonance results being the main one.

Such interaction promotes the EM enhancement, that can be much stronger than the one due to the single particle. It's easy to presume that stronger enhancement effects will be obtained as well in the gap-region between the two particles; this region plays a very important role in the SERS enhancement effect and for this reason is named the hot-spot of the dimer, underling the strong EM enhancement that here originates (see for example Figure 2.7b). Moreover, the EM enhancement turns out to be stronger for smaller gaps, but also more spatially localised. This means that, for a single molecule in the hot-spot position, the electromagnetic effect

will be stronger, but less distributed in the gap region, so to disadvantage the average effect for the other molecules near the hot-spot.

In conclusion, for the general case of two nanoparticles it's easy to understand that the SERS effect is advantaged by the presence of the hot-spots, whose effect would be even stronger for sharper nanoparticles and small gaps. It is worth to underline that within the above-mentioned Raman hot-spots, exploiting the electromagnetic enhancement, the Raman signal can be boosted by 10-12 order of magnitudes.

2.3.4 Other effects: supporting substrates and roughness effects

The importance of the surrounding dielectric around the nano-particles on the resonances is clear; thus, the SERS effect can be affected from the spectral point of view. This is for example the case of metallic nanoparticles supported by a silicon substrate. In this case the single nano-particle is not completely surrounded just by a single dielectric, but it is usually partially embedded in the substrate. This translates into more boundaries and more dielectric functions.
Actually, by simplifying the issue and supposing that the particles are half-stuck in the dielectric, it's possible to assume that the nano-particle is surrounded by a material with an effective dielectric function ε_{eff}, whose value is halfway between the one of the dielectric and the one of the external environment. Briefly, a shift of the LSPRs occurs in these conditions, due to the new effective dielectric function of the model.

Moreover, also the roughness of the metallic surfaces of the nanoparticles introduces a shift of the LSPRs. In such a case, also a moderate increase of the EM enhancement is registered, but it is still just a secondary effect.

2.4 The Chemical Enhancement

In spite of its name, chemical enhancement is more related to the modification of the polarizability of the analyte – due to the adsorption of the molecule onto the metal surface – than to its contribute to the total enhancement, which is actually just one or two orders of magnitude.

Chemical enhancement reveals itself especially in the different enhancement for different Raman modes of the spectra of the analyte, or in the shift of the Raman modes. These effects are due to the interaction between the metal surface and the adsorbed molecule.

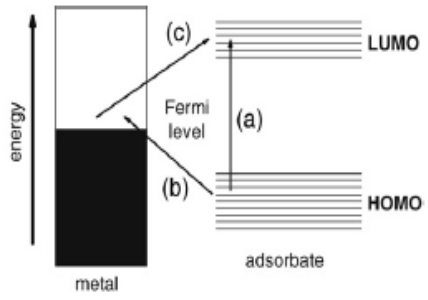

Fig. 2.8 Schematic representation of a charge-transfer mechanism. [2, page 259]

Actually, different explanations have been given, including the so-called charge-transfer mechanism.

Chemical enhancement can occur at different levels, depending on how the analyte interacts with the metal surface. For example, when the molecule doesn't bind to the metal, this acts on the electronic distribution of the molecule only as a perturbation. This phenomenon can affect the polarizability and then also the Raman efficiency of the mode, but only mildly. Another situation is the case of direct or indirect binding of the analyte to the metal (for example with a covalent binding for the former case, or by means of an electrolyte in the latter). It must be first underlined that the polarizability is strongly dependant on the availability of optical transitions. When the molecule-metal complex forms, new indirect transitions may appear – due to the overlap of the molecular orbitals. This means that in certain conditions the laser can be resonant with these new electronic transitions, with a consequent improve of the Raman enhancement for that particular frequency (see Fig. 2.8, (a)).
Another possible situation arises when the Fermi level of the metal is located in between the HOMO and the LUMO of the adsorbate. If the energy of the laser is matched with the charge-transfer energies between HOMO and an occupied state above the Fermi level (see Fig. 2.8, (b)), or between the LUMO and an unoccupied state below the Fermi level (Fig. 2.8, (c)), a further contribution to the enhancement is given to the Raman spectrum.

In conclusion, chemical enhancement is to be taken into account when using SERS spectroscopy, since the spectrum on the adsorbate usually presents differences, compared to the one of the isolated molecule; whereas the main contribute to the enhancement is instead given by the EM effects.

Chapter 3

SERS for bio-applications

3.1 Introduction

In the previous chapters main concepts of Raman and SERS spectroscopy have been investigated. These basic notions help to correctly design and optimize SERS substrates. High hot-spot density and matching between the excitation wavelength and one plasmonic resonance are needed to achieve good efficiencies and sensitivities. Good SERS substrates must also provide high stability and reproducibility, along with good uniformity and low-cost fabrication.
Furthermore, since SERS substrates are often employed for biological applications [3, 6–8, 14], stability in diverse physiological conditions and bio-compatibility can be also demanded.
For this reason, a brief comment on the diverse SERS substrates' fabrication techniques and their bio-applications is made hereafter.

3.2 State of the art of SERS substrates

Fabrication of SERS substrates can be obtained following different techniques. The first SERS substrates were obtained by Fleischmann [1] in 1974, when electro-chemically roughened silver electrodes were used for the detection of pyridine in a $0.1\ M, KCl$ solution. The enhancement of the Raman spectra was only later attributed to the SERS effect, and to the EM enhancement and chemical enhancement effects. Metal electrodes exploit surface protrusions of $25 - 500\ nm$, with the drawback of low enhancements factors. For this reason, these substrates are nowadays mostly used specifically for electro-chemistry applications (e.g. monitoring of specific electro-chemical reactions)[15, 16]. At present, other two classes

of SERS substrates occupy a pre-eminence in SERS spectroscopy applications; the former is the one of metallic particles in solution, for instance colloidal SERS substrates, while the latter corresponds to planar metallic structures, i.e. nano-particles on a planar substrate, among which metal-dielectric nanostructures play a role of primary importance.

3.2.1 Colloidal SERS substrates

Colloidal substrates are suspensions of metal nanoparticles and can be used as SERS active substrates. These are usually obtained by two main methods: physical or chemical synthesis [17].

An example of a physical method is given by ablation of a noble metal target in a liquid medium (usually water or an organic solvent), by means of a pulsed laser [18]. The laser is focused on the metal target, generating a plasma that expands in the liquid. The material that is exported from the target interacts with the species in the liquid, so allowing the nucleation, the growth and finally the formation of the NPs [17]. A drawback of this method is given by the formation of large NPs, that may lead to sedimentation and thus to undesired time dependency of the optical properties of the colloids. A way to optimize this method was obtained with the addition of a fragmentation of the larger particles by means of a further irradiation of the fabricated colloids, which results in a higher uniformity of the size distribution of the colloids [19]. The ablation method guarantees the advantage of NPs free of organic and ionic species [20].

The second method is given by the wet chemical synthesis of colloids. Reduction reactions in solution allow the production of Au and Ag colloids, obtained by reduction of a metal precursor, co-precipitated in a solution with the presence of a reducing agent and a stabilizing agent, this last added to achieve repulsion among the particles. A first nucleation process triggers the growth of the metallic nanoparticles to a certain size and shape, and the reaction continues until the amount of metal or reducing agent is extinguished – if not stopped before by means of chemical or physical processes [17].
One of the most used type of colloids is represented by the so-called Lee-&-Meisel colloids, where an aqueous solution of silver nitrate or chloroauric acid (the precursor) – respectively used for Ag and Au colloids – is added to a solution of sodium citrate (which plays both the role of reducing and stabilizing agents) [21]. Other reducing agents (e.g., sodium borohydride, hydrazine, or hydroxylamine hydrochloride [22]) can be used in place of citrate to obtain different sizes or/and shapes, and thus different absorption maxima. As an example,

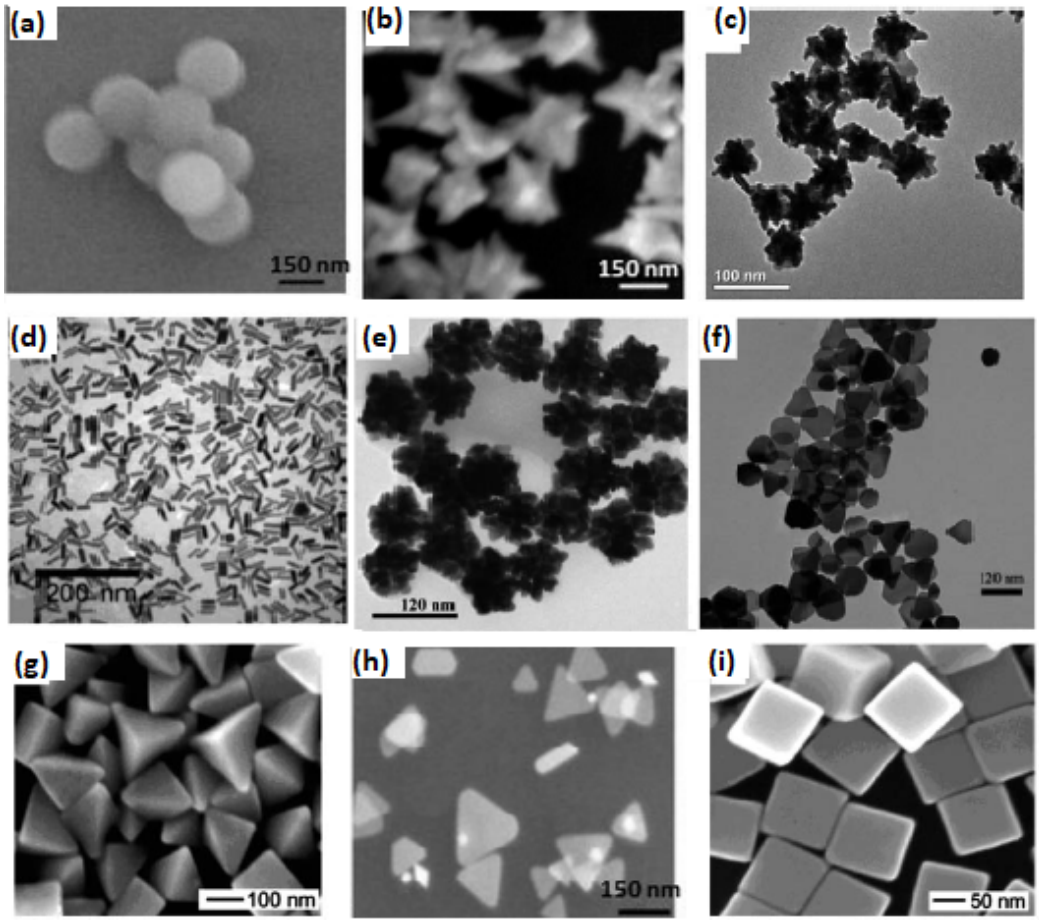

Fig. 3.1 SEM images of different colloids NPs: nanospheres (a), nanostars (b-c), nanorods (d), nanoflowers (e), nanoplates (f), nanoprisms (g), nanotriangles (h) and nanocubes (i) (from ref. [24–30].

borohydride, in the form of sodium borohydride ($NaBH_4$), is used as reducing agent, but with the inconvenience of the latter not working as stabilizer [23].

Despite being commonly used, Lee-&-Meisel colloids show a low size uniformity, which can be still achieved with a two-step synthesis [31, 32]. In this approach, a first reduction is used for the synthesis of very small particles, which behave as seeds for a second step reduction, i.e. a more controlled and slower reduction process, where larger particles are eventually grown with a higher control over the process and a better homogeneity. In order to control the shape of the NPs of the colloids, surfactants are added to the solution during the synthesis process. As an example, in Figure 3.1 different NPs with various shapes are reported (i.e., nanospheres, nanostars, nanorods, nonoflowers, nanoplates, nanoprisms, nanotriangles and nanocubes), all prepared by means of the two-steps method. Some of these shapes guarantee intense SERS signals, like the nanocubes, thanks to their sharp edges [33],

or nanostars [17]. This is of course explained by the presence of more sharp regions in the morphology of the NPs that, as explained previously, increase also the SERS enhancement and the probability of hot-spots.

Colloidal solutions are generally used in SERS applications for their high enhancements and versatility, but unfortunately, they also present poor reproducibility and low stability over time, thus leading to unwanted time-dependent and unreproducible results [17]. For this reason, and since higher SERS enhancements are obtained for the smaller colloidal clusters, different strategies have been applied to control the aggregation of colloidal nanoparticles, so avoiding coagulation of colloids and time-dependent results [34, 35].

3.2.2 Planar SERS substrates

A second family of SERS substrate is the one of planar substrates. Also in this case, large enhancements and reproducibility are desired properties. For this purpose, different techniques are nowadays used for their fabrication, which may be subdivided in three main categories; nano-lithographic techniques, template-based techniques and nanoparticles immobilization [36–39]

The nano-lithography approach guarantees a structure of the substrate that is carefully controlled, with the result of a high uniformity and reproducibility of the nano-structures, but with the disadvantage of high costs [40].
Electron Beam Lithography (EBM), for example, can be used for the fabrication of metal nano-particles arrays with well-defined shape and size and carefully-controlled inter-particle gaps. Usual resolution of the geometric features can be pushed down to $10-20\,nm$, with smaller gaps of $5\,nm$ [36]. In this case, a focused beam of electrons is used to expose a radiation-sensitive resist, which works as photo-mask to protect the substrate from successive processes. Usually a positive photo-mask of polymethylmethacrylate (PMMA) is first developed and then the pattern is transferred onto the substrate.

Finally, to deposit the metal, two different ways can be followed: in the first case, a Reactive Ion Etching (RIE) process is performed, followed by a metal deposition, after the removal of the mask; in the other case, the metal is first deposited and then the mask is removed by means of a lift-off process [41] (see Figure 3.2).
It was shown, that generally nanostructures fabricated by means of lift-off process exhibit higher SERS enhancement, if compared to the ones fabricated through etching process [42]. Indeed, the former ones show also less sharp edges, resulting in smaller enhancements [43].
UV-laser irradiation and Focused Ion Beam (FIB) can also be used to pattern the wanted

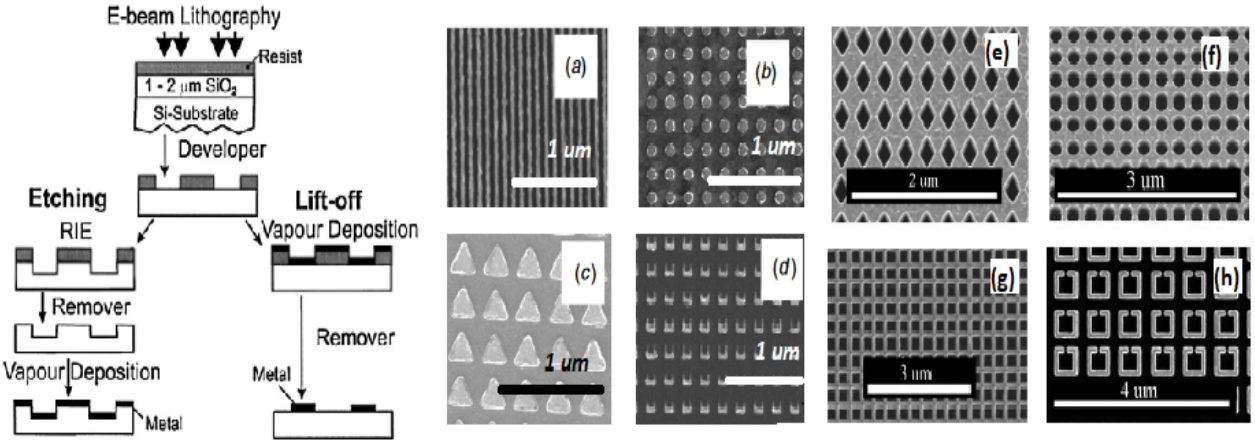

Fig. 3.2 Left: the EBL is schematically represented. After the exposition of the resist with a beam of electrons, two ways are followed. In the first case (left) a RIE process is used to first transfer the pattern onto the substrate. Then, after the removal of the mask, the deposition of metal is performed. In this way all the surface is covered by the metal. In the second case (right), the metal is first deposited after the EBL and a lift-off process is then made follow, so that a series of isolated NPs form on the substrate. [41]
Right: SEM images of SERS substrates with NPs fabricated by means of EBL with lift-off process (a-d) and by means of EBL followed by a Plasma Ion Etching process (e-h) [42]

geometry on the photo-resist, with the drawback of a lower resolution, but also with lower costs and shorter exposure times [37, 44, 45].
Two other approaches are the thermal-assisted nano-imprinting lithography (T-NIL) and the UV nano-imprinting lithography (UV-NIL), which overcome the limitations imposed by light diffraction and beam scattering of the usual lithographic techniques [46]. In this case, a hard mould (generally obtained by means of EBL) is pressed onto the resist film, at high temperature and pressure, to transfer the features; then the metal is eventually deposited onto the patterned substrate. In addition, a resist can be first deposited on the substrate and patterned by same procedure: the difference with the previous case is that, in this case, after the deposition process, a lift-off is performed to obtain the nanostructures (see Figure 3.3).

This technique can be very useful when the pattern is to be transferred onto a silicone-like substrate for SERS applications, for example PDMS [48]. Furthermore, it allows a high throughput with high resolution, which is highly convenient for large-scale patterning, along with high reproducibility of the results, thanks to the use of the same mould for all the samples.

EBL and FIB can give the assurance of a very high reproducibility of the nanostructured substrates, but they are difficult to use for mass production [40]. For this reason, template-based techniques can be used to obtain ordered nanostructures for SERS applications, with a good

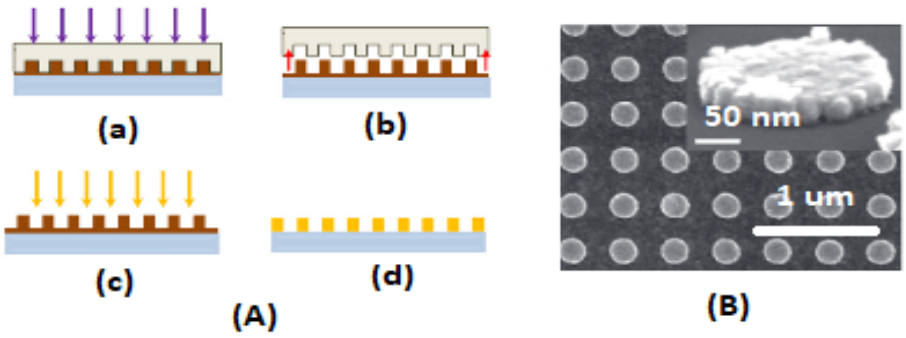

Fig. 3.3 Figure (A). Schematic view of NIL with lift-off: the mould is pressed onto the resist to transfer the features (a) and the hard-mask ripped-off (b). After the deposition of the metal (c), a lift-off of the resist follows and the nanostructures are obtained (d).
Figure (B). SEM images of nanocylinders obtained by NIL [47].

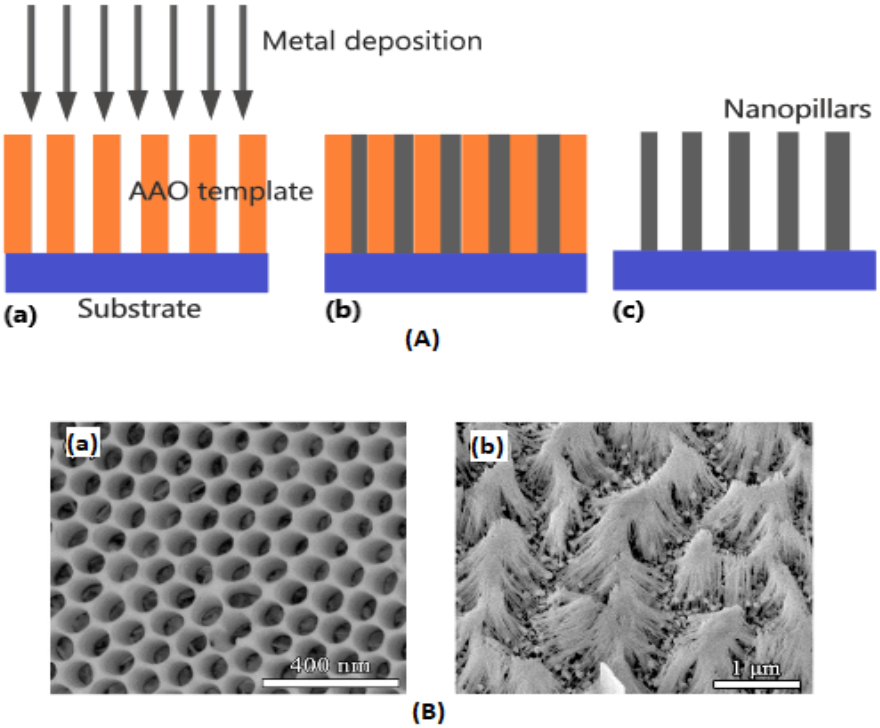

Fig. 3.4 Figure (A). Schematic view of AAO template-based procedure for nano-wires fabrication: metal deposition by electroplating or vapor deposition (a-b), AAO template electrochemical etching (c).
Figure (B). SEM images: AAO template (a) and bundles of nano-wires (b) [38].

control on the morphology, along with lower costs and production time [49]. In this case, the metal is deposited into or onto a template with a pre-patterned geometry, using different deposition strategies.

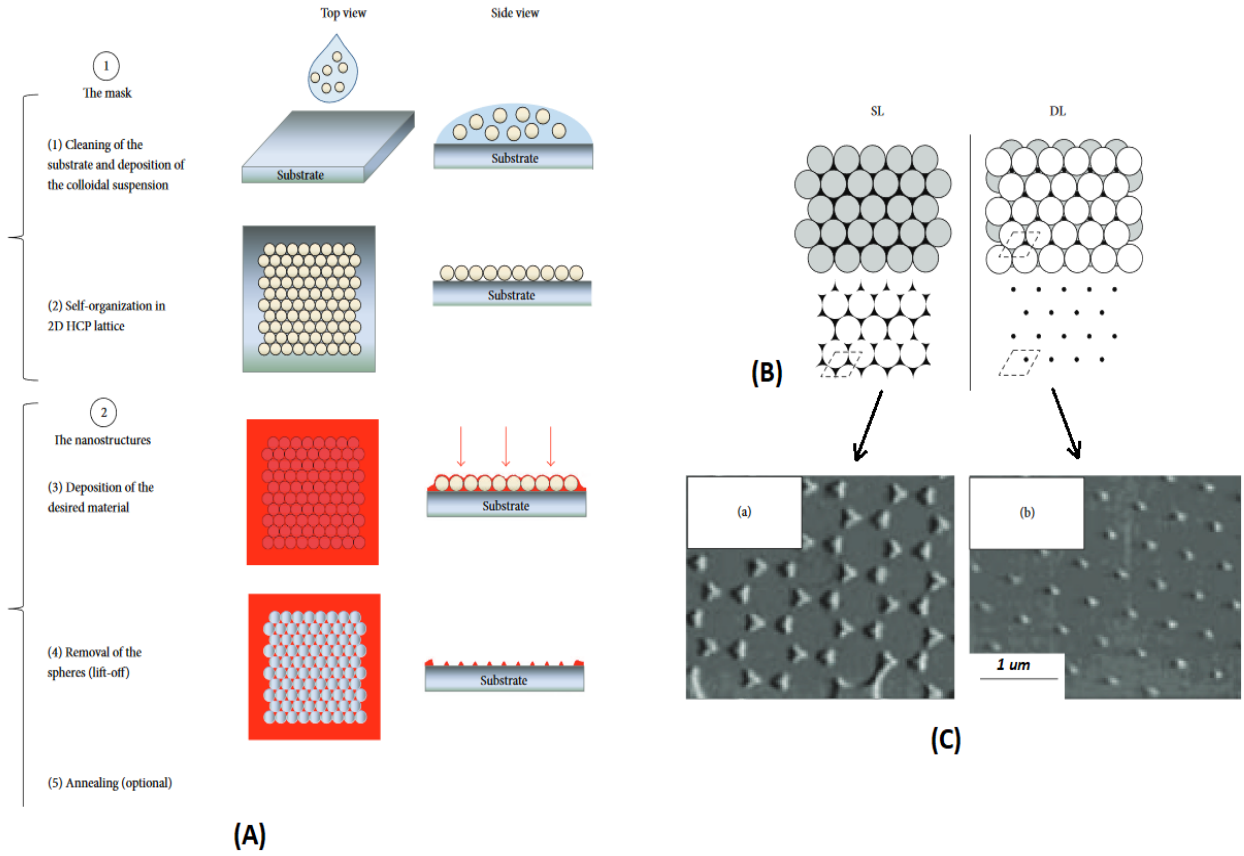

Fig. 3.5 Figure A: Nanosphere Lithography process steps with a hexagonal-close-packed monolayer of monodisperse spherical colloids [51].
Figure (B): schemes of the single- and double-layer nanosphere masks (on top) and scheme of the nanoparticles pattern after deposition and lift-off processes (on bottom) [52].
Figure (C): SEM micrograph of Ag triangular nanoparticles made with a single-layered colloidal mask (a). SEM micrograph of Ag nanoparticles made with a double-layered colloidal mask (b). [53]

For the case of Anodic Alumina Oxide (AAO) substrates, alumina templates are obtained by electrochemical etching in acid conditions. These are characterized by a regular pattern of pores, with controlled pore density and diameter (usually varying in a range from about *10* to *400 nm* [38]), into which the metal is deposited by regular electroplating or vapor deposition techniques. Finally, the template is totally or partially dissolved to obtain nano-wire or nano-tube arrays. Moreover, if the AAO template is etched for a long enough time, the nano-wires collapse, forming a bundle with a high density of hot-spots [38]. As it can be seen from Figure 3.4, the pillars collapse, touching each other by the edges and allowing the formation of the hot-spots. Despite the low cost and reproducibility, the main drawback of this technique is given by the gap sizes, hardly lower than $5\,nm$ [50].

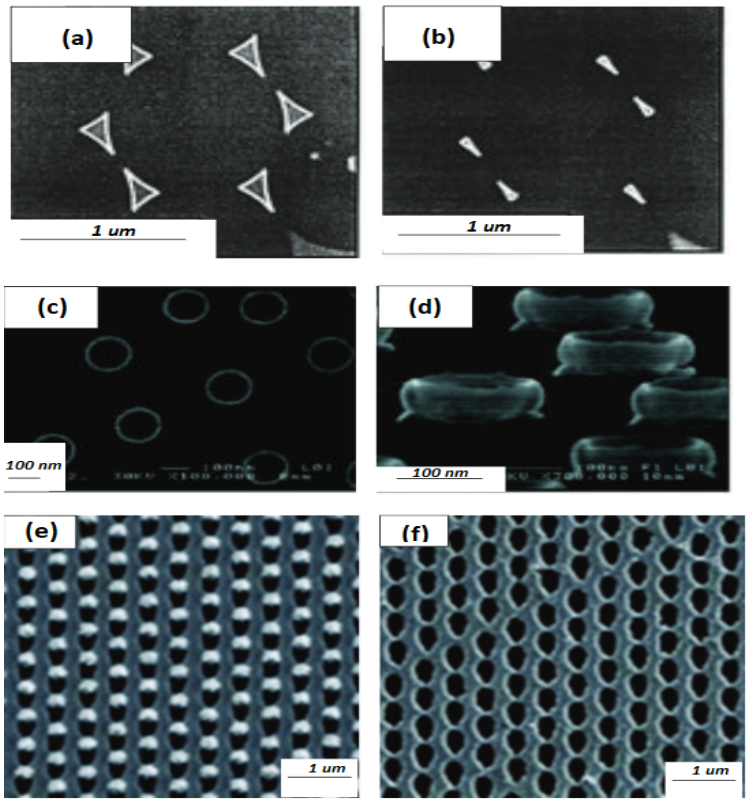

Fig. 3.6 SEM micrograph of SERS substrates obtained by means of NSL: nanodots obtained by angle-resolved colloidal lithography with $\Theta = 20°$ and $\Theta = 40°$ (a-b) [56]; Au nanorings (c-d) [57]; elliptical Ag porous ordered arrays before the NS lift-off (e) and after the lift-off (f) [58]

Another interesting method for the fabrication of template-based nanostructured SERS-active substrates is the one presented by the Van Duyne group [53–55]. Nanosphere Lithography (NSL) is a template-based technique that takes advantage of monodisperse spherical colloids (e.g., polystyrene) in a suspension [51]. The substrate is coated by this suspension, which is let dry, allowing the formation of a mono- or bi-layer nano-spheres, that take on the role of a mask for the following metal deposition process. Finally, a lift-off process is used to allow the removal of the spheres, with the formation of the metallic pattern. In Figure 3.5A an example is given, with the spheres forming a monolayer, giving origin to a hexagonal-close-packed (HCP) pattern [51]. In Figure 3.5B the pattern is shown both for the mono- and bi-layer cases: as it can be seen from Figure 3.5C, after the deposition of the metal on the colloidal mask, triangular nanodots (a) or circular nanodots (b) form.

Although NSL appears to be an easier and cheaper method, if compared to the usual lithographic techniques, it has the disadvantage of its resulting patterns, mostly limited to triangular structures [51]. For this reason, different strategies have been proposed to

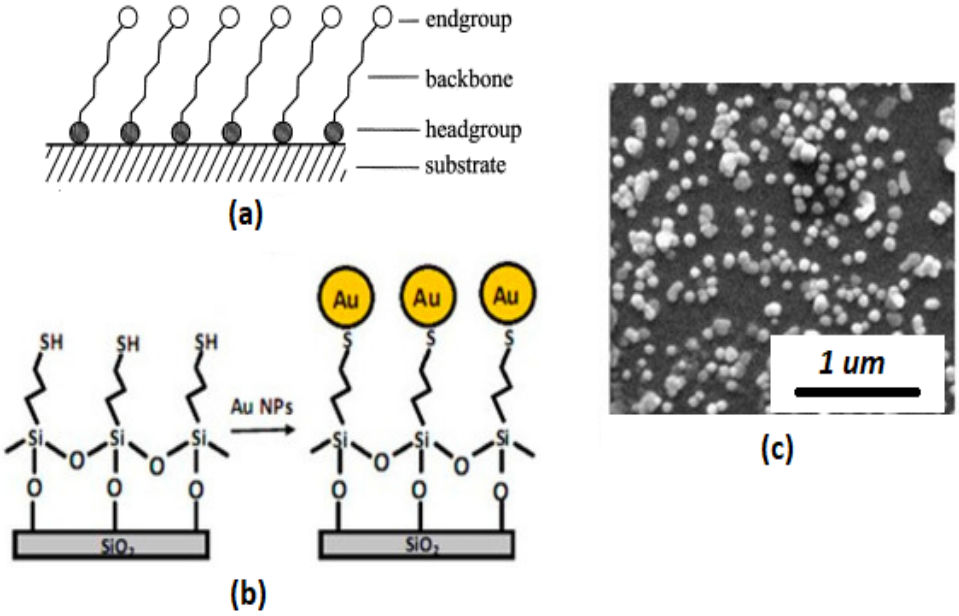

Fig. 3.7 Figure (a): scheme of a general functionalised substrate by means of a bi-functional ligand [62]
Figure (b): scheme of a quartz substrate functionalised by means of MPTMS and covered by Au-NPs [63]
Figure (c): SEM micrograph of Au-NPs on a quartz substrate functionalised through MPTMS [63]

overcome this limitation [56, 57, 59–61]. With a monolayer HCP pattern, triangular metal nanostructures are obtained, in the assumption of a zero-incident angle to the substrate (Θ) of a Psychical Vapor Deposition (PVD) beam. Nevertheless, when a tilting of the substrate is performed, i.e. when, a non-zero Θ is selected, different sizes and shapes are obtained [56]; this result can be seen in Figure 3.6a-b, where the angle Θ was chosen equal to 20° and 40° respectively. Other geometries (e.g., nanorings [57, 61] and nanoholes [58–60]) can be obtained also with other techniques. The SEM micrograph of some of these nanostructures are shown in Figure 3.6 from (c) to (f).

It has been previously shown that one limiting characteristic of colloidal substrates is its poor stability over time [34, 35]. In order to overcome this, different strategies, such as immobilization, have been applied. The immobilization approach includes a set of techniques that were originated to overcome this limitation in planar structures. Two different types of immobilization methods can be distinguished, depending on whether the nanoparticles are pre-synthesized or directly grown on the substrate.
Two main approaches fall within the former case; chemical or electrostatic methods. In

the case of the chemical approach, a bi-functional ligand is generally used for the purpose [39, 62, 64]. Typically, the functional group of one of these molecules is anchored to the activated surface, whereas the other (i.e., a thiol or an amine group) is let free to bind to the metal NPs. In Figure 3.7a the scheme of a general bi-functional ligand on a substrate is shown. An example is reported in Figure 3.7: in this case a quartz substrate is treated by means of MPTMS, allowing the immobilization of Au NPs by the interaction of the thiol with the gold surface [63]. The final Au-NPs on the functionalised quartz substrate are shown in Figure 3.7c.
For what concerns the electrostatic approach, the immobilization on the surface of the support is performed by interactions with polymers [65–68] or biomolecules [69, 70]. There is another possibility to immobilize pre-synthesized NPs, that takes advantage of capillarity [71–73], for example allowing the self-assembling into layers of NPs contained in a droplet on the surface, being careful to prevent their aggregation.
With the second approach, the NPs are directly synthesized on the substrate. A possible way is to immerse the substrate into a solution of a metal precursor and a reducing agent, in order to have the growth of NPs at the interface between the solution and the substrate [74–78]. This is the case, for example, of porous silicon-based SERS substrates, onto which copper, silver and gold nanoparticles have been grown thanks to the reducing properties of its freshly etched substrate [79]. With a similar approach, PDMS substrates have been used in place of porous silicon to directly grow Au-NPs [75].
Since these techniques have been exploited in the framework of this thesis, metal-dielectric nanostructures will be briefly focused in the next subsection, discussed on PDMS substrates covered by silver nanoparticles.

3.2.2.1 SERS-Active Ag Nanoparticles on PDMS substrates

Polydimethylsiloxane (PDMS) is one of the most used material in the framework of nanotechnological applications, thanks to its properties: it is cheap, easy to fabricate, bio-compatible, optically transparent and flexible [80–83]. Moreover, thanks to its chemical structure, this material exhibits high thermal stability, along with chemical and biological inertness [84]. Among these properties, optical transparency is necessary for microfluidic integration in elastomeric microfluidic chips [85].
PDMS is cross-linked into an elastomer via a hydrosilylation process, in which the vinyl groups of prepolymer react with the hydrosilane groups of the curing agent, in a platinum catalysed reaction [84]. It has been shown how the variation of the weight ratio of the elastomer precursor and the curing agent influences the surface properties of the substrate [86]. Different attempts have been made to synthesize metal NPs using PDMS films [75, 87–90].

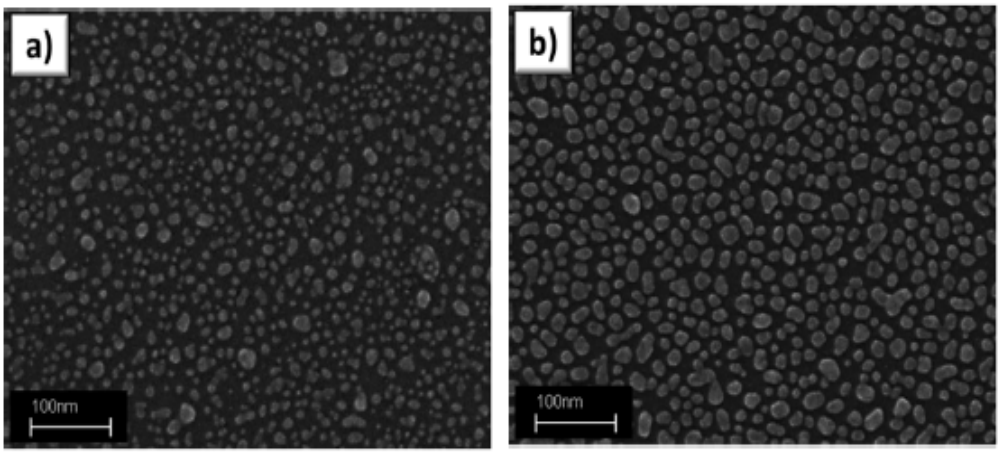

Fig. 3.8 "FESEM micrographs of Ag nanoparticles obtained by DC sputtering at *20* (a) and *40 mA* (b)" [84]

A first method to grow Ag-NPs on a PDMS substrate is presented by Lamberti et al. In this case a deposition by means of a sputtering process is used to build a SERS-active substrate, constituted of Ag-NPs on the elastomeric matrices [84, 87], integrated in a microfluidic device, used for on-chip label-free detection purposes. To this aim, a sputtering deposition of silver can be used, along with a fine-tuning of all the influencing parameters, i.e., sputtering current, distance of surface from target, deposition time [87], in order to prevent the formation of a continuous film, but allowing the nucleation and formation of the Ag-NPs. With this process an average size of 12 *nm* of the Ag-NPs was recorded, along with an inter-particle gap tuned in the range $1 - 30$ *nm*, obtained through the modulation of the external uniaxial strain on the elastomer substrate, thanks to the flexibility of the PDMS [91, 92]. In Figure 3.8 the Ag-NPs are shown in the case of a sputtering current of *20 mA* (a) and *40 mA* (b).
This technique is effective in terms of cost and time of fabrication, but it presents some inconveniences mostly related to the stability of the substrate over time [93]. In fact, a simple deposition of the metal onto untreated PDMS surfaces doesn't assure the complete adhesion of the NPs to the substrates, because of the weak interactions between the NPs and the PDMS. This is limiting in cases of flexible microfluidic chips, where robustness and reliability would be strongly compromised, or in case of bio-applications, where SERS-active substrates are often exposed to harsh environments, that could damage the NPs layers [94].

functionalisation of the PDMS substrate can be helpful for the immobilization of pre-synthesised metal NPs [95] onto PDMS surface. Different ways can be followed for the functionalisation of a PDMS substrate [95–100] in perspective of immobilization of the

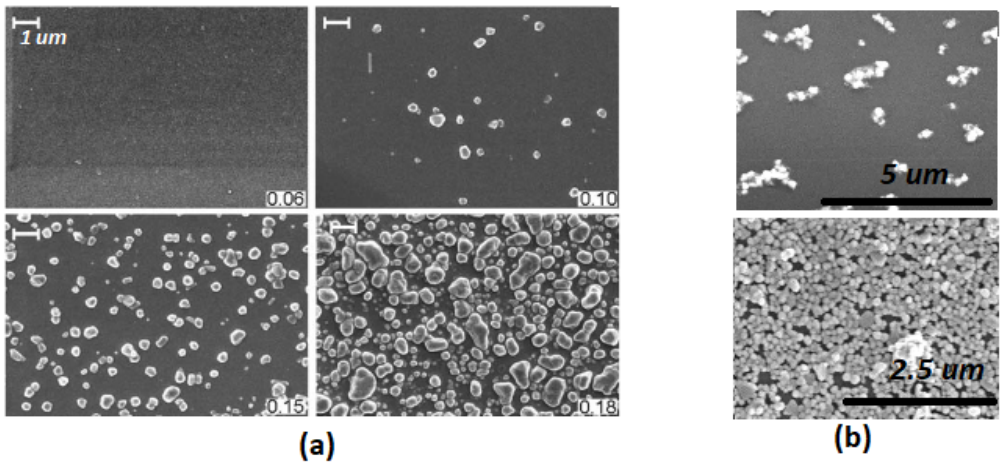

Fig. 3.9 Figure (a): SEM images of Au-NPs on PDMS membranes synthesized by using the method proposed by Zhang et al. [90]. The different substrates are obtained for different values of curing-to-monomer ratio (value on bottom-right for each image) [90]
Fig (b): SEM images of Au-NPs fabricated using the method of Ahmed et al [75], for hydrophilic and hydrophobic PDMS membranes (respectively on top and on bottom) [75]

NPs. Major focus was given to amino- silanes [95, 97–99] and mercapto- silanes [99, 100], that can be used to provide amine and thiol functionalities on PDMS, helpful for the immobilization of the metal NPs or to immobilize biomolecules on the surface. For example, colloidal Ag-NPs were immobilized on PDMS substrates using a functionalisation though 3-aminopropyletriethoxy silane (APTES), followed by plasma treatment [95].

Another possibility is to exploit wet-chemical approach for PDMS substrates [75, 88–90]. Synthesis of gold nanoparticles was for example accomplished by incubation of PDMS membranes in a solution of tetrachloroauric acid ($HAuCl_4$) and chitosan [89]. PDMS membranes were first coated by the chitosan biopolymer, working as reducing and stabilizing agent for the reduction of the gold nanoparticles on the membranes [89]. Finally, the chitosan-treated PDMS films were immersed in the $HAuCl_4$ solution for the synthesis of the Au-NPs on the films surface. Following the same trail, Zhang et al. [90] presented a simple *in-situ* fabrication technique for the synthesis of Ag-NPs without the need of additional reducing agents [90]. Here the residual curing agent used for the PDMS fabrication was used to reduce $HAuCl_4$: by controlling the curing agent and monomer mass-ratio different coverages, inter-particle gaps and NP size were obtained (see Figure 3.9a). Using the same method, Ahmed et al. [75] used a one-step procedure for the synthesis of Au-NPs, by immersing PDMS membranes in a solution of sodium formate and $HAuCl_4$. In this study, a portion of the membranes was treated by O_2 plasma, in order to make them more hydrophilic, so to

study the deposition of the Au-NPs on the different substrates. Higher density Au-NPs was obtained in case of hydrophobic substrate, as it can be seen from Figure 3.9b.

3.3 SERS for bio-sensing applications

SERS substrates have demonstrated excellent sensing performances, mixed with the power of structural and chemical information, that make them good candidates for biosensing applications [101–108]. Among these, biosensing platforms of challenging biological analytes are of primary interest. SERS substrates have been widely used for label-free detection and identification of pathogens [101], like viruses [109, 110] or bacteria [111, 112], proteins [113–116] and other biomolecules [108], such as DNA [117–119] or RNA [120, 121], for early-diagnosis application. In the following, some biosensing applications are shown.

3.3.1 SERS for biological detection and identification

SERS substrates have recently taken an increasingly important role in the framework of diagnostics and therapy monitoring [5, 104, 105, 121], thanks to their ability in the detection of different types of molecules involved in biological processes. In the following sub-sections some application for biological detection are shown.

3.3.1.1 Proteins and biomolecules

Detection of proteins through SERS substrates can be a difficult task. This is mainly due to the complex chemical composition of proteins, along with the need of high concentration to obtain intense SERS signals [7]. For this reason, in order to perform a reliable analysis, purification from biological fluids is needed, since other species, with higher concentrations and adsorbing behaviour, would dominate the SERS spectra [7]. In addition to this, spectra of proteins are often low reproducible as a consequence of the denaturation and adsorption on the substrate [122].

The low SERS signals of proteins can be a limiting factor when these take the role of biomarkers (i.e. molecules that help to distinguish between normal and cancerous conditions [123]), whose quantitative detection plays a key role in disease diagnosis and cancers monitoring [124]. A possible solution to this problem is given by Ahn et al., who proposed a multiple protein biomarker approach, instead of a single protein biomarker detection, used for lung cancer diagnosis [123]. The main idea is based on the fact that various protein biomarkers are found in blood samples of individuals at high risk for lung cancer, including Cytokeratin-19

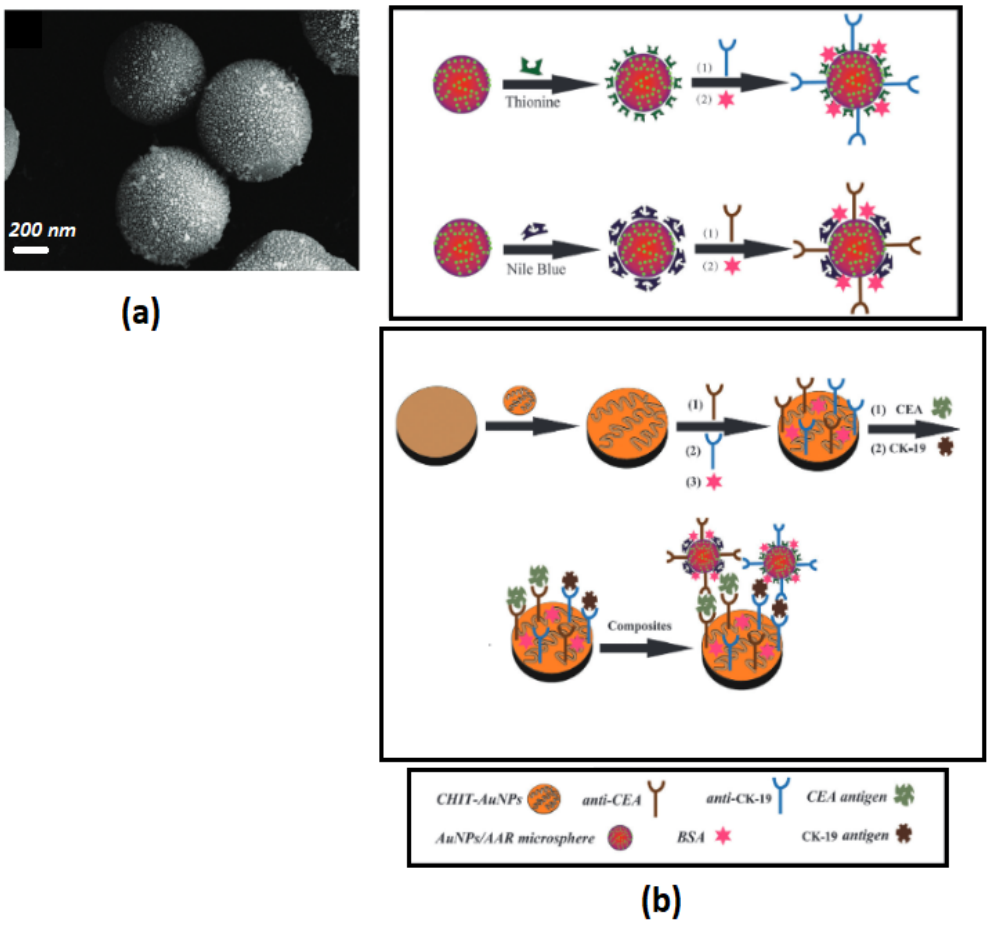

Fig. 3.10 Figure (a): SEM images of AAR microspheres coated by Au-NPs [115] Figure (b): schematic immobilization of the first antibodies on the Raman dye-labelled AuNPs-coated microspheres (top image); schematic illustration of the sandwiched structure due to the interaction of the electrode coated with the second antibodies and the AuNPs coated with the first ones (bottom) [115]

fragments (CYFRA 21-1), carcinoembryonic antigens (CEA), cancer antigen-125 (CA-125) and neuron-specific enolase (NSE) [123]. This approach gives higher sensitivity than single biomarker approach, thus making it easier to distinguish individuals with high risk for lung cancer from those to keep under control [123]. The multi-marker approach for lung cancer diagnosis was implemented by Wenbo et al., with the fabrication of a SERS immunosensor for the simultaneous detection of carcinoembryonic antigen (CEA) and cytokeratin-19 (CK-19) [115]. To this aim, aminosalicylic acid-based resin (AAR) microspheres were synthesized and coated by AuNPs (see Figure 3.10a). To have the simultaneous detection of both the CEA and CK-19 antigens, two Raman dyes (Thionine and Nile blue A) were used to label the AuNPs-coated microspheres. The scheme of the structure of the immunosensor for the

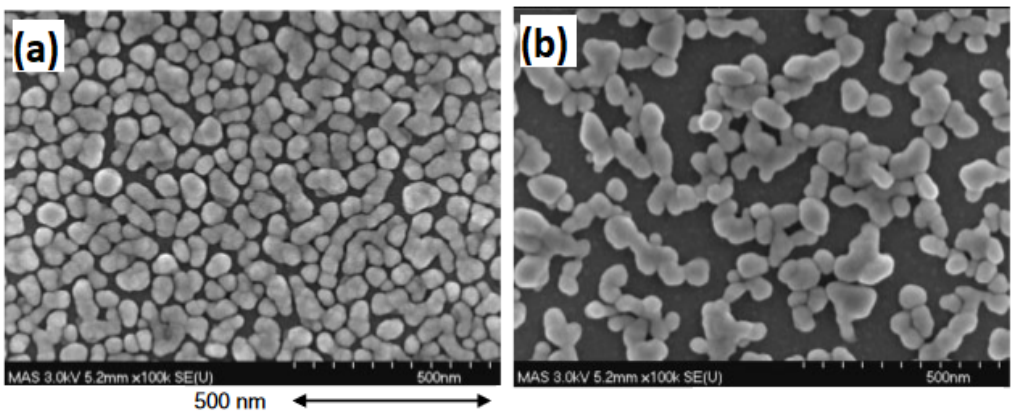

Fig. 3.11 FESEM images of ASF inside the spot before (a) and after (b) the deposition of the protein and washing [125]

detection of the antigens is shown in Figure 3.10b. As it can be seen, a sandwich structure used for the detection, is formed by three main components: i) the Raman dye-labelled Au-NPs-coated microsphere, which also presents antibodies on its surface; ii) a second antibody, previously immobilized on the surface of an Au-NPs-coated Glassy Carbon Electrode and iii) the antigen, which binds the two parts together, through an antibody-antigen-antibody interaction. Finally, since the used label dyes present different characteristic peaks of their Raman signals [115], the simultaneous multiplex detection of both antigens can be performed.

The problem of the change of the conformational state of adsorbed protein on SERS substrates is also an important issue [7, 122]. It was shown that vacuum evaporated or sputtered semi-continuous metal films on insulating substrates permit the rearrangement of their structure under protein deposition [125–128], along with large SERS enhancement. Such structures are referred as *adaptive* substrates, since they seem to preserve the functionality of the biomolecules by the change of the structure of the metal nanoparticles on the substrate [125]. Drachel et al. fabricated a SERS substrate by vacuum evaporation of silver on a dielectric substrate, to exploit the high enhancement guaranteed by silver [125–128], referring to these as Adaptive Silver Films (ASFs). FESEM images of an ASF before and after the analyte deposition are shown in Figure 3.11. The redistribution of the evaporated metal films guarantees a better match with the different analytes, providing better SERS enhancements depending on the different size of the biomolecule, without significant structural changes of the analyte (soft adsorption) [125]. In addition to this, it also seems that the biomolecule-metal combination, after the restructuring of the substrate, stabilizes the silver film, increasing the nanoparticles adhesion to the substrate [125].

3.3.1.2 Nucleic acids

Nucleic acids detection and identification have become an important case study, due to its relation with the identification of pathogens [101], mutations caused by cancers [121, 129] and inherited genetic diseases [130]. The detection of Raman signals of labels attached on oligonucleotides is already possible [131], nevertheless a label-free SERS detection would guarantee faster and simpler options [7], along with the possibility to study the characteristics of the oligonucleotides.
However, as in the case of protein detection, this can be an issue, due to the conformation changes of free DNA adsorbed on the SERS substrates, due to problems correlated to spectral reproducibility [132, 133]. In addition to this, only four bases make up the various sequences, becoming a challenging issue for the identification aim [7].

Barhoumi et al. reported a protocol that dramatically increases the reproducibility of the SERS spectra of single-stranded DNA (ssDNA) and double-stranded DNA (dsDNA) [117]. This is based on a gentle thermal cycling pretreatment of the analyte before the adsorption onto an Au-nanoshells substrate, resulting in a relaxation of the ssDNS and dsDNA molecules into a linear conformation. A spectral correlation function was used by the group to prove

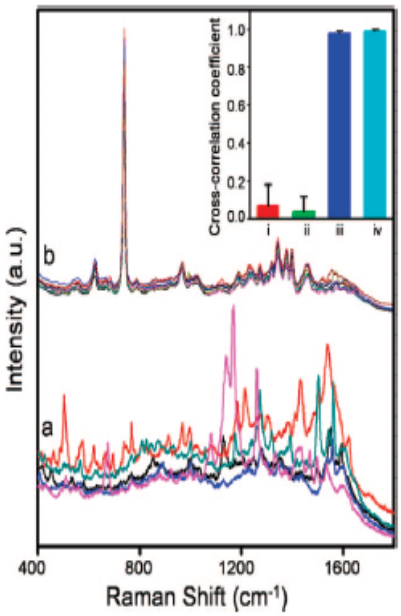

Fig. 3.12 SERS spectra of untreated ssDNA (a) and thermal pretreated ssDNA (b). In the inset, the cross-correlation coefficient is shown for 8 SERS spectra of: i) untreated ssDNA, ii) untreated ssDNS with its complement (untreated), iii) thermally pretreated ssDNA and iv) thermally pretreated dsDNA [117]

the improvement of the reproducibility thanks to the thermal pretreatment protocol. The results are clear, by looking at the spectra of untreated (a) and thermally pretreated (b) SERS spectra of ssDNA, reported in Figure 3.12. The spectra of pretreated ssDNA show also higher correlation than untreated samples, suggesting the effective operation of the pretreatment protocol.

An alternative solution to minimize irreproducibility issues due to conformational changes is to analyse smaller nucleotide sequences [7] like miRNAs, consisting in a family of small non-coding RNAs, composed by 20-22 nucleotides [134]. These short sequences are responsible for the control of gene expression via either transitional repression or mRNA turnover. Since they are involved in various biological processes (i.e., cell proliferation, differentiation, development), their aberrant expression is associated with different diseases, genetic disorders and oncogenesis [94]. Usually, the detection methods for miRNA re-quire complex instrumentations and expensive chemicals, like for example the microarray technology or the quantitative Polymerase Chain Reaction (qPCR). For this reason, the SERS substrates are potential solutions for miRNA detection. The reported applications are often related to colloidal SERS substrates, with the usual inconvenient of very low stability and reproducibility. Oblique Angle Vapor Deposition (OAD) was used by Driskell et al. for the production of aligned silver nanorods arrays applied for SERS-active substrates for the detection of miRNA [120]. The miRNA SERS spectra showed high reproducibility thanks to the use of the OAD-fabricated SERS substrates. The reproducibility was measured collecting a fixed number of spectra from various equally-fabricated substrates and from different points for each substrate. From this study similar band position and shape, and only very slight differences in relative intensities were observed for each measurement [120]. The reproducibility of this fabrication technique suggests that these substrates can be used to confidently identify

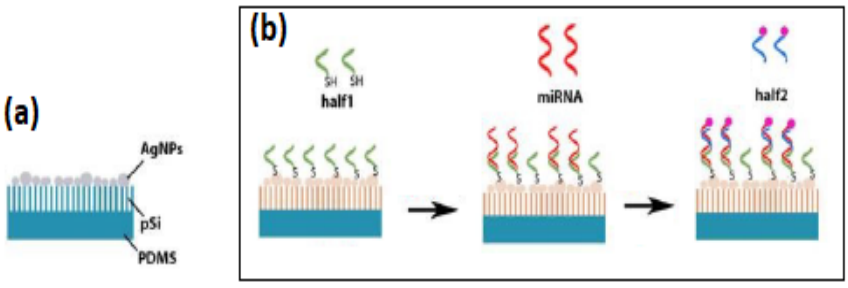

Fig. 3.13 Figure (a): schematic view of silver-decorated porous silicon (pSi) membrane, supported on an elastomeric PDMS matrix. Figure (b): two-step hybridization assay for miRNA detection [134]

spectral differences among different miRNAs resulting from sequence-dependent structural differences [120].

Novara et al. proposed a method for the detection of miRNAs [134], based on the use of a two-step bioassay. In this case a thiol-capped DNA probe is halved in two strands. The first strand is immobilized on a silver-decorated porous silicon (pSi) membrane, supported on a elastomeric PDMS matrix and is responsible for capturing the miRNA in the sample. The second strand is hybridised and labelled with a Raman dye, so to assist the SERS detection, after the capturing of the miRNAs. The two-step label-free bioassay is described in Figure 3.13. This protocol was compared to typical methods based on single hybridization. SERS enhancement and uniformity has been tested in both cases, with good results, raising the expectations of improvements in terms of specificity and limit of detection.

3.3.1.3 Pathogens

Detection and identification of dangerous pathogens at early stages with fast and accurate techniques for disease monitoring systems have been lately drawn attention for new solutions [135, 136]. Already available methods, such as approaches based on Polymerase Chain Reaction (PCR) [137, 138] are hardly exploited for on-site rapid detection [109]. Different

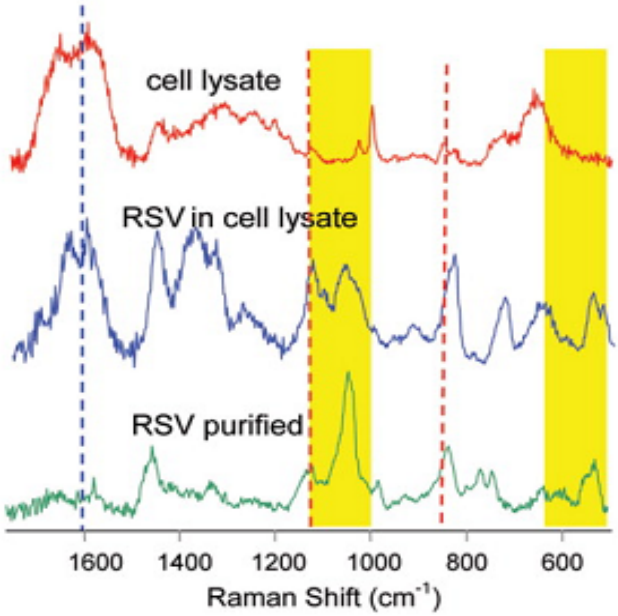

Fig. 3.14 "SERS spectra of Vero cell lysate before and after infection with RSV, top and middle spectra, respectively. The SERS spectrum of purified RSV is shown at the bottom for comparison" [101]

solutions have been proposed during the years (i.e., microcantilevers [139, 140], evanescent wave biosensors [141, 142] and atomic force microscopy [143, 144]), but all unable to discriminate between types of pathogens [101]. It has become a necessity to find new methods for the detection and discrimination of pathogens with reproducible results, along with a reduction or elimination of the sample preparation or amplification procedures [101].

Tripp et al. have demonstrated the advantages obtained by SERS pathogen biosensing through Ag-nanorod arrays, obtained by means of OAD [101]. A direct configuration was used, with the analyte directly applied to the nanostructured surface. The Tripp group showed the possibility to rapidly and sensitively distinguish different viruses by their SERS spectra, also in the presence of a complex background [101]. This aim was reached thanks to the observation and comparison of the SERS spectra of: i) uninfected Vero cell lysate, ii) respiratory syncytial virus (RSV) infected cell lysate and iii) purified RSV. As it can be seen from Figure 3.14, the Vero cell lysate after the infection shows peaks unambiguously identified in its SERS spectrum.
A similar approach was proposed by Durmanov et al., who presented a SERS substrate made of a silver film, obtained by Electron Beam PVD (EBPVD), on a roughened surface with pore-like indentations and folds [109]. Also these substrates have demonstrated the capability to differentiate between different virus species, exploiting the identification of the differences of the chemical structure of the various viral particles.

For what concerns the bacterial identification, a main issue is given by the complexity of SERS signals obtained by bacterial cells. For this reason, it is necessary to build a data reduction protocol for an accurate identification of the different specimen [145, 146]. A Principal Component Analysis (PCA) can be used to reduce the complexity of the spectra, maximizing also the variance and guaranteeing a basis for a more accurate identification [112]. Patel et al. proposed a SERS-based methodology for bacterial identification [112]. In this approach, bacterial cells are placed on an *in situ* grown Au-NPs-coated SiO_2 substrate [147, 148], which was shown to exhibit high SERS enhancement and good reproducibility [112]. An identification algorithm was developed using a PCA for the collected SERS signals as a diagnostic method for bacterial pathogens.

Chapter 4

Aim of the work

Surface Enhanced Raman Scattering (SERS) is a ground-breaking technique for the fabrication of label-free sensors, relevant in the framework of early-diagnostics and therapy monitoring. In particular, recent works on tunable plasmonic metal-dielectric nanostructures for SERS applications have raised hope that this kind of substrates can potentially fulfil the need of flexible and wearable devices.

The main aim of this work is to investigate recent low-cost methods for the synthesis of efficient and stable substrates, based on Ag-NPs immobilized on PDMS membranes. The optimization of the Ag-NPs substrate is ultimately aimed to the development of a flexible multi-chamber microfluidic chip, for fast and low-cost detection, oriented to biosensing applications.

In order to achieve these aims, a first approach was used for the synthesis and the optimization of a reference SERS-active substrate, based on sputtered Ag-NPs on untreated PDMS membranes [84, 87]. Sputtering current, deposition time and distance of the PDMS membranes from the metal target were finely adjusted to obtain the best conditions for this type of substrates. In order to overcome the limitations of the previous type of substrates (i.e., small SERS enhancement, low reproducibility and low stability over time) two other approaches were then followed. The first is based on the synthesis of Ag-NPs, through a sputtering deposition process on functionalised PDMS membranes; a chemical functionalisation with MPTMS or APTES was tested in order to promote the adhesion of Ag-NPs to the PDMS membranes, and therefore also to increase the substrate stability. The second synthesis method was, instead, based on the static-incubation of PDMS membranes in a solution of silver nitrate ($AgNO_3$). In both cases, different synthesis conditions were used to study the influence of the synthesis parameters (monomer-to-curing ratio, incubation time,

thickness of the PDMS substrate, incubation temperature, cross-linking degree, presence of ethanol in the incubation solution and concentration of silver nitrate in the solution) on the final properties of the substrates.
To this end, various characterisation methods were used, in order to find out the best conditions for the synthesis. UV-Vis transmittance analysis and Raman mapping of MBA were used to get information regarding respectively the plasmonic resonances of the substrates and their homogeneity. A FESEM characterization was used to investigate the correlation between synthesis parameters and Ag-NPs morphology; moreover, in order to have accurate results, an image analysis of the obtained FESEM micrographs was carried out by means of MATLAB and ImageJ tools. Finally, the stability of the substrates was studied using UV-Vis transmittance spectroscopy of the samples immersed in water and Tris-EDTA buffer at different incubation times.

After an accurate analysis, one best sample – in terms of stability, SERS efficiency, sensitivity and reproducibility – was chosen for each synthesis method and used for the development of miRNAs cancer biomarker bioassays, implemented both by SERS and ELISA techniques, following the optimized protocols already suggested by Chiadò et al. [94]. Finally, the best conditions of synthesis were used for the development of a flexible multi-chamber microfluidic chip, whose properties were again probed though SERS bioassays, in order to achieve the final application.

Chapter 5

Materials and methods

Experimental materials and methods that have been used are introduced in this chapter.
In Section 5.1 the protocol for PDMS preparation is provided, while in Section 5.2 the methods for the synthesis of silver nanoparticles are described. The sections from 5.3 to 5.5 deal with the characterization methods that have been used. Finally, Section 5.6 introduces the biofunctionalisation protocol, used for the detection of the microRNAs.

5.1 Substrate synthesis

5.1.1 PDMS preparation

Polydimethylsiloxane (PDMS) was prepared starting from the prepolymer and the curing agent, mixed with different weight ratios, depending on the application. Starting from the results of previous researches, the ratio was chosen differently for the different processes of synthesis of silver nanoparticles. A 20:1 curing-ratio was chosen for SERS substrates obtained by DC sputtering deposition of Ag nanoparticles (AgNPs). Instead, 3:1 and 5:1 were used for the PDMS membranes used for the synthesis in static incubation conditions. The thickness of the PDMS substrates was *1 mm*, unless differently stated. The mixture of the prepolymer and curing agent was poured into a mould ($50 \times 50\,mm$) and degassed at room temperature for $5\,min$ and finally cured in an oven for $1\,h$ at *60 °C* to obtain samples with a total cross-linking degree and for $30\,min$ for those with partial cross-linking degree.

5.1.2 PDMS functionalisation protocol

The functionalisation of the PDMS membranes was carried out both with (3-Aminopropyl)triethoxysilane (APTES) and (3-Mercaptopropyl)trimethoxysilane (MPTMS). First, the PDMS membranes

(20:1, cured 1 h at 60°C) were either treated with a piranha-like solution [H_2O: H_2O_2: HCl; 5: 1: 1] for 5 min, at room temperature or pretreated with Ar plasma for *120 s* and *30 mA* sputtering current in the case of a plasma-activation approach, to increase the reactivity of the PDMS surface. The PDMS was then rinsed in deionized water for three times and dried in a stream of N_2 gas. The PDMS membranes thus obtained were finally immersed in a solution of ethanol (at *60 °C*), with 1% of APTES or MPTMS, for 10 min, at room temperature. Finally, the membranes were rinsed at room temperature in ethanol for three times and dried under a N_2 stream.

5.2 Silver nanoparticles synthesis

5.2.1 Ag-Nanoparticles sputtering

The Ag nanoparticles were deposited on the PDMS by DC sputtering in Ar atmosphere of 10^{-4} bar (Q150T ES, Quorum Technologies), at room temperature. The target was cleaned before each deposition using a current of 150 mA for 30 s, to prevent the deposition of contaminants on the membranes. In order to optimize the synthesis of the sputtered Ag-NPs, different control parameters were inquired concurrently; sputtering currents were changed in the range $40-50$ mA, for a time interval in the range $2-5$ s, with a distance of the membranes from the Ag target from 3 to 5 cm.

5.2.2 Static incubation of substrates

The static incubation of the PDMS membranes in $AgNO_3$ solution was carried out in different conditions, to examine the influence of the synthesis parameters on the growth of the Ag-NPs. The monomer to curing agent ratio was fixed at 3:1 and 5:1 for all the experiments, with 3 different samples for each condition – corresponding to 24 h, 48 h and 72 h of incubation. The different experiments were carried out by changing the synthesis parameters one-by-one (thickness of the PDMS membrane, incubation temperature, cross-linking degree of the membrane, presence of ethanol in the incubation solution, concentration of the silver nitrate in the incubation solution), while fixing the others (an accurate description of all the synthesis conditions for each experiment is reported in Table 5.1).
The PDMS was prepared following the procedure described at Section 5.1.1. In order to obtain a different thickness, the mixture of pre-polymer and curing agent was poured into a 5×5 cm^2 square mould. Knowing the PDMS mixture density (0.965 g/cm^3), and the desired thickness, the right amount of PDMS was poured into the mould. Each 5×5 cm^2 PDMS sample was then cut into 4 (2.5×2.5) cm^2 equal pieces. After the incubation in 4 mL of a

Experiment	Thickness	incubation temperature	Cross-linking degree	Concentration of ethanol	Concentration of silver nitrate
Thickness	0.5, 1, 2 mm	20 °C	Totally cross-linked (1 h in oven)	0 %	100 mM
Incubation temperature	1 mm	20, 30, 40 °C	Totally cross-linked (1 h in oven)	0 %	100 mM
Cross-linking degree	1 mm	30 °C	Totally and partially cross-linked (1 h and 30 min in oven)	0 %	100 mM
Presence of ethanol	1 mm	30 °C	Totally cross-linked (1 h in oven)	0, 5, 10, 20 %	100 mM
Concentration of silver nitrate	1 mm	30 °C	Totally cross-linked (1 h in oven)	0 %	10, 100, 1000 mM

Fig. 5.1 Synthesis conditions for each experiment. The monomer-to-curing agent ratio was fixed to 3:1 and 5:1, whereas the incubation time was always fixed at *24, 48 and 72 h*.

100 mM $AgNO_3$ solution (unless differently stated), the samples were washed with $4\,mL$ of deionized water on a shaker at $240\,rpm$, for $5\,min$ at room temperature. Finally, the samples were dried in a N_2 stream and their back sides eventually wiped clean of Ag traces, by using of ethanol.

5.3 Optical contact angle characterization

Contact Angle characterization was performed by a OCA H200 (Dataphisycs), equipped with two motorized syringes. The sample under test was mounted on a stage, on which the two syringes nozzles could be set. First, three water (H_2O) drops of $1\,\mu L$ each were dispensed on the sample surface and the images of their profiles acquired. The drop profiles were fitted through an ellipsoid shape and the minimum, the maximum and the mean Contact Angles (CAs) collected, along with the Standard Deviation for each set of data. Same procedure was then repeated with the use of diiodomethane (CH_2I_2).

5.4 Optical characterization

Information regarding the plasmonic resonance behaviour of the fabricated nanostructures were collected with a CARY5000 UV-Vis-NIR spectrometer. The optical response of the SERS substrates was checked acquiring transmittance spectra in the range $300 - 800\,nm$.

5.5 Morphological characterization and image analysis

5.5.1 Morphological characterization

Morphological characterization was performed using a SUPRA 40 FESEM system. PDMS membranes with sputtered Ag-NPs were covered with a copper grid, connected to the FESEM stub, to ease the electrons discharging. Instead, SERS substrates that had gone through the static incubation synthesis were covered by a deposited Pt film. This was obtained by a DC sputtering process in Ar operational atmosphere of $10^{-4}\,bar$ (Q150T ES, Quorum Technologies), with a sputtering current of $40\,mA$, for $20\,s$, at a distance of the samples from the Pt target of $5\,cm$. Typical imaging parameters for conductive samples were an acceleration tension of $5\,kV$, a working distance of $4\,mm$ and an aperture size of $20\,\mu m$. For each sample, at least a $50\,kx$ and a $100\,kx$ magnification images were taken (other magnifications were used when required).

5.5.2 Image analysis for morphological characterization

Inter-particle distance and size of the NPs play a pivotal role in the SERS enhancement effect. A MATLAB routine for FESEM images analysis (introduced by Novara et al., 2014 [149]) was modified and used for the purpose of getting an insight on the morphological structure of the synthesized SERS substrates. FESEM images with $50\,kx$ magnification were used as input for the analysis. The script was modified to distinguish between dense particles and spread ones. Different MATLAB functions were then used to semi-automatically adjust contrast, to remove the background noise, to separate connected nanoparticles and finally to fill the bigger ones. Eventually the properly corrected images were converted to black and white. Final images were then used to obtain the distribution of the gaps between the neighbouring NPs and the one of the equivalent NPs' diameters. For the first purpose, a MATLAB operator was used to measure the distance between each NP to the nearest one. For the second, each NP was substituted by a circular disk with same size, so to have an equivalent diameter. ImageJ was then used on the same FESEM images in order to have a cross-check of the results. By means of this tool the images were manually adjusted and finally the gap and equivalent

diameters retrieved. ImageJ could guarantee a higher controllability of the adjustment of the images, whose accuracy could be observed in real-time.

5.6 Raman characterization

5.6.1 4-Mercapobenzoic acid Raman mapping

4-mercaptobenzoic (4-MBA) acid was used as probe molecule to investigate the properties of the SERS substrates.

For the incubation of the 4-MBA the following protocol was used for each tested sample. A solution of $10\,mM$ of 4-MBA in ethanol was first prepared. An aqueous 4-MBA solution, with a concentration of $10\,\mu M$, was then prepared by dilution in water of the previously prepared solution. A $(0.5 \times 0.5)\,cm^2$ piece of the sample under test was obtained and incubated for $10\,min$ in $300\,\mu L$ of the aqueous 4-MBA solution. All the samples under test were put in wells of the same dimensions, to control the concentration of 4-MBA per unit of surface. Finally, the wells were emptied from the 4-MBA solution and the samples cleaned by pouring $300\,\mu L$ of water for three times into the wells. Eventually, the samples were dried under the stream of N_2 gas.

A Renishaw InVia Reflex Raman Microscope was used for the Raman measurements in a backscattering configuration. The samples were excited by a $514.5\,nm$ laser source (Cobolt, $100\,mW$). Mapping measurements were used as a tool to have information about the uniformity of the SERS substrates. A $10x$ objective was used for the map acquisition. Raman imaging was performed using $2\,s$ as exposure time and 2 accumulations, with a laser power on the sample reduced by filters to the 0.5% of the original one. Acquisition of the map was performed on a $(450 \times 450)\ \mu m^2$ area, with a $50\,\mu m$ step, resulting in 80 collected spectra.

5.7 Biofunctionalisation protocol

In this section the biofunctionalisation protocol is described (Sub-section 5.7.2). In detail, in the sub-section 5.7.1 the procedure followed for the characterization of the stability of the SERS substrates in buffers is given. ELISA and Raman characterizations are finally presented in Sub-sections 5.7.3 and 5.7.4 respectively.

5.7.1 Stability of SERS substrates in buffer

In order to measure the retention of the Ag-NPs on the SERS substrates, all the samples were incubated in $3\,mL$ of deionized water or in an aqueous Tris-EDTA buffer solution, $1\,mM$ of EDTA and $10\,mM$ Tris with $pH\,7.5$ (TE), supplemented with $1\,M$ of $NaCl$ (TE-NaCl). The Varian CARY5000 UV-Vis-NIR spectrometer was used to check the optical response variation over-time of the SERS substrates. The spectra were measured at the beginning of the incubation (time 0), after $1\,h$, after $24\,h$ and finally after 1 *week*.

5.7.2 Bioassay protocol

SERS substrates pretreatment

All the samples were pretreated to reduce the non-specific binding of the probe and of the target on the surface of the SERS substrate. To this end, samples were incubated for $1\,h$ in a 1% BSA sodium acetate buffer $pH\,4.0$ (NaAc). They were then washed in TE buffer to remove the excess protein.

Probe reduction

A 5'-alkylthiol-capped DNA probe (probe222, 5'-C6SHACCCAGTAGCCAGATGTAGCT-3'), corresponding to the antisense sequence of miRNA222 was immobilized on the Ag-NPs by following a previously reported method [94]. In detail, the probe was reduced for *1 h* with *100 mM* DL-dithiothreitol (DTT), and separated from the reductant by size-exclusion with the help of Illustra MicroSpin G-25 columns, and finally quantified by means of a UV-Vis-NIR Cary5000 spectrophotometer (Agilent Technologies Italia S.p.A., Milan, Italy), equipped with a TrayCell (Hellma GmbH & Co., Müllheim, Germany).The reduced probe was finally diluted to the working concentrations ($1-100\,\mu M$) in TE-NaCl buffer and incubated overnight on the substrates.

5.7.3 ELISA-Like Bioassay on Metal-Dielectric Substrates.

A 5'-biotinylated miRNA222 (5'-biotin-AGCUACAUCUGGCUACUGGGU-3') was used to check the hybridization by Enzyme Linked Immuno Sorbent Assay (ELISA). Pretreated samples were cut into $5\times 5\,mm^2$ pieces and incubated overnight at room temperature in $25\,\mu L$ of probe222 diluted in TE-NaCl, in order to allow the probe immobilization. Negative controls were also incubated overnight in TE-NaCl without the probe (no-probe control). The samples were finally washed three times in TE-t (TE, 0.05% Tween20, pH 7.5) for $5\,min$

to remove nonspecific binding and blocked with 1% BSA in TE for $1\,h$. Afterwards, 25 μL of miRNA222 in SSC 4x (from stock 20x, 0.1% SDS, pH 7.5) was incubated for 1 h. The substrates were washed three times in SSC 1x (diluted SSC 4x) and incubated with 25 μL of 0.5 $\mu g/mL$ Streptavidin protein covalently conjugated to the Horse Radish Peroxide enzyme (Str-HRP) in SSC 1x, washed three times with SSC 1x, and developed by ELISA.
In this case, the TMB substrate solution was added onto the samples to initiate the colorimetric reaction and stopped after 2 min by the addition of H_2SO4_4 (*0.5 M*), with a 1:1 TMB:H_2SO4_4 ratio. The optical density (OD) of the solution was measured at 450 nm and at *630 nm* with the use of a 2100-C microplate reader (Ivymen Optic System), and the results analysed as reported previously [94].

5.7.4 SERS Analyses on Metal-Dielectric Substrates

A 3'-R6G-modified miRNA222 (5'-AGCUACAUCUGGCUACUGGGU-R6G-3') was used for SERS analysis. The same protocol applied for the ELISA was used also for the SERS substrates exploited for the Raman analysis, unless that the substrates were not incubated with the Str-HRP. The substrates were analysed after the immobilization of the probe and after the miRNA incubation. To this end, samples were dried under a nitrogen stream and analysed with a Renishaw InVia Reflex micro-Raman spectrometer (Renishaw plc, Wotton-under-Edge, UK) with a *514.5 nm* laser excitation in backscattering light collection under a *10*× objective. Mapping measurements were used as a tool to have information about the uniformity of the SERS substrates. A $10x$ objective was used for the map acquisition. Raman imaging was performed using $2\,s$ as exposure time and 2 accumulations, with a laser power on the sample reduced by filters to the 0.5% of the original one. Acquisition of the map was performed on a $(450 \times 450)\ \mu m^2$ area, with a $50\,\mu m$ step, resulting in 80 collected spectra.

Chapter 6

Results and discussion

6.1 Introduction

In this work, the experimental activity has been focused on the synthesis of metal-dielectric nanostructures for SERS application. Two different synthesis methods for Ag-NPs on PDMS membranes were exploited. The first is based on the sputtering of silver on PDMS membranes, the second deals with the static incubation of PDMS substrates in a solution of silver nitrate. In both cases, the synthesis conditions were varied to find out their influence on the performances and characteristics of the substrates (i.e., sensitivity, enhancement uniformity, stability). To this aim, different characterization techniques were performed on the samples, i.e. UV-Vis transmittance analysis, FESEM characterization, Raman spectroscopy and stability analysis. It was chosen, at first instance, to present and discuss the results separately for each experiment (see the table of Figure 5.1). Moreover, the best set of synthesis conditions for each method were chosen in view of the final part of the work, concerning a bioassay for the detection of miRNA222, which was then developed for the selected samples. Finally, the substrate showing the best performances was chosen for the integration in an all-PDMS multi-chamber microfluidic chip and the bioassay repeated on the fabricated device, in order to assess its performance with a view to a practical implementation.

6.2 Sputtered Ag-NPs on PDMS membranes for SERS substrates synthesis

A first approach to the fabrication of planar SERS-active PDMS substrates is given by the sputter deposition of Ag-NPs on PDMS membranes. Previous results on the same nanostructures, done by Chiadò et al., have brought to light the difficulty to use such substrates for

bio-compatible applications, due to the weak interaction between the synthesised nanoparticles and the PDMS substrate [94]. In fact, the low adherence of the sputtered Ag-NPs on the surface of the PDMS does not allow the protracted incubation of the substrates in harsh environments (e.g. high ionic strength of buffer used for biosensing) without a strong variation of the morphology of the nanostructures, and thus also of the properties of the SERS substrate. For this reason, a first preliminary study was aimed to understand the limitations of these substrates, and finally to find a methodology – based on a functionalisation of the PDMS membranes trough APTES and MPTMS – aimed to solve the main issues related to the stability of the substrates.

6.2.1 Synthesis of Ag-NPs on PDMS membranes via sputter deposition

A metal deposition process was first employed for the fabrication of SERS-active nanostructures. This was based on the DC sputtering of silver NPs onto totally cross-linked PDMS membranes, with monomer-to-curing ratio equal to 20:1. This choice was justified by previous similar studies, carried out by Lamberti et al. [84, 87]. As first step, a large number of samples was fabricated, with the aim of finding how the synthesis parameters affect the reproducibility and the stability of these substrates. A systematic approach to the problem was used: the sputtering current, the deposition time and the PDMS membrane-to-target distance, were varied one by one and each sample was characterized by means of UV-Vis transmittance analysis and FESEM imaging.

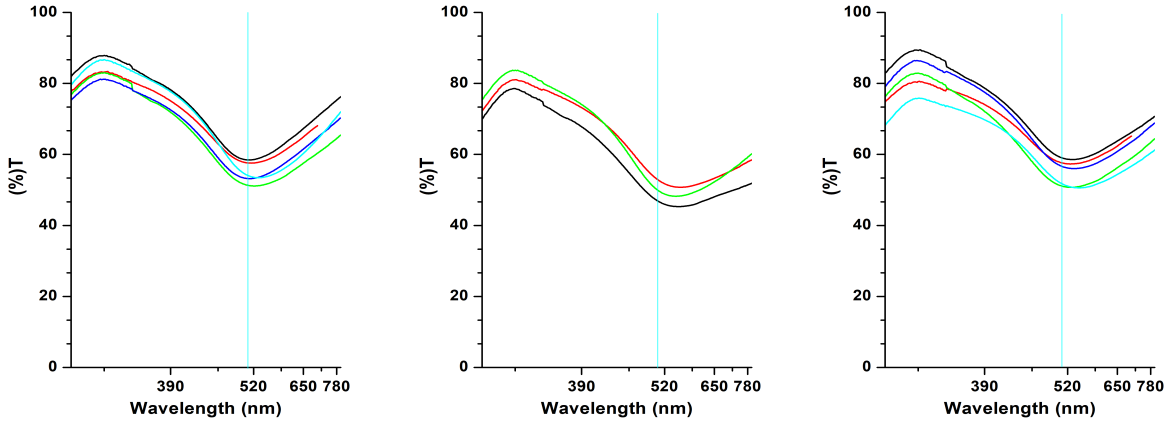

(a) $40\,mA$, $3\,s$, $4.5\,cm$ (b) $40\,mA$, $5\,s$, $5\,cm$ (c) $50\,mA$, $3\,s$, $5\,cm$

Fig. 6.1 UV-Vis transmittance spectra in air for $1\,mm$ PDMS membranes (20:1 curing ratio) with sputtered Ag-NPs in different synthesis conditions. Different curves for the same condition correspond to different samples, fabricated with the same synthesis parameters.

Optical and morphology analysis

The optical behaviour of the fabricated samples is first discussed. The transmittance spectra of these substrates usually present a dip due to enhanced absorption and scattering related to the Localized Surface Plasmon Resonances (LSPRs) of the metallic nanostructures, which for optimized substrates need to be tuned to the wavelength of the laser source used in the Raman experiment, namely, 514.5 nm. Indeed, when the dip is in the vicinity of this wavelength, also good SERS enhancement is more likely to be encountered, due to the resonant excitation of the LSPRs. In fact, the dip is strongly related to the plasmonic resonances of the nanostructure, meaning that when it is centred around the laser wavelength (in this case 514.5 nm), the plasmonic resonances of the substrates are excited, thus providing stronger enhancement effects. As an example, UV-Vis transmittance spectra of some of the fabricated samples are shown in Figure 6.1 (see Appendix A.1 for all the spectra).

In Figure 6.2a the results are resumed in a single graph, which shows the dip transmittance versus the absolute value of the difference between the dip wavelength and the source wavelength. For the sake of simplicity this latter quantity will be now on called $\Delta\lambda$ [nm]. These two quantities give important information about the nanostructures: the first one is an empirical estimation of the enhancement of the optical processes, but it is also affected by Ag

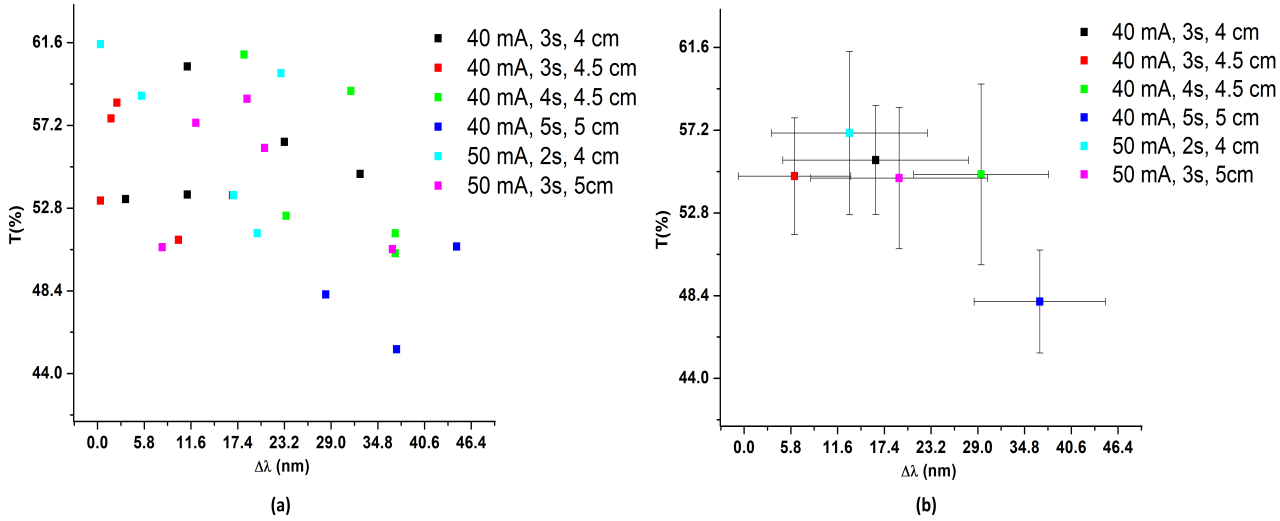

Fig. 6.2 Dip transmittance vs. $\Delta\lambda$, for samples prepared with different sputtering conditions. Different points with the same colour (a) represent different replicates fabricated in the same synthesis conditions; (b) the different points represent the mean values of the replicates reported in (a). The bars are the standard deviation values of the transmittance (vertical bar) and $\Delta\lambda$ (horizontal bars).

surface coverage, while the second one is used to evaluate the contribution of the resonant excitation of the LSPs. This means that, samples represented in Figure 6.2a, which have low transmittance and low $\Delta\lambda$, also have high probability to produce a high SERS enhancement. It is already clear from the graph of Figure 6.2a, that these substrates are affected by a very low reproducibility: different samples, fabricated in the same conditions present variable optical properties. Moreover, while fabricating the samples it was also noticed that different results were obtained for the same conditions (whose symbol is featured by the same colour) also during the same deposition session. The substrates seem to reach a fixed morphology increasing the number of processes, according to a stabilization of the sputtering conditions over time. In agreement with this, after about ten depositions from the initial one, the samples begin to present more predictable results and less differences one to the other. In Figure 6.2b it was chosen to graph each set of synthesis conditions as a single point, corresponding to the mean transmittance of the dip vs. $\Delta\lambda$; vertical and horizontal bars for each point represent the standard deviations, respectively of the transmittance and of the distance from the excitation wavelength, of all the samples that were synthesised in the same deposition conditions. In conclusion, it is easy to state that these samples are characterized by unpredictable properties for the same synthesis conditions, which make them unreproducible.

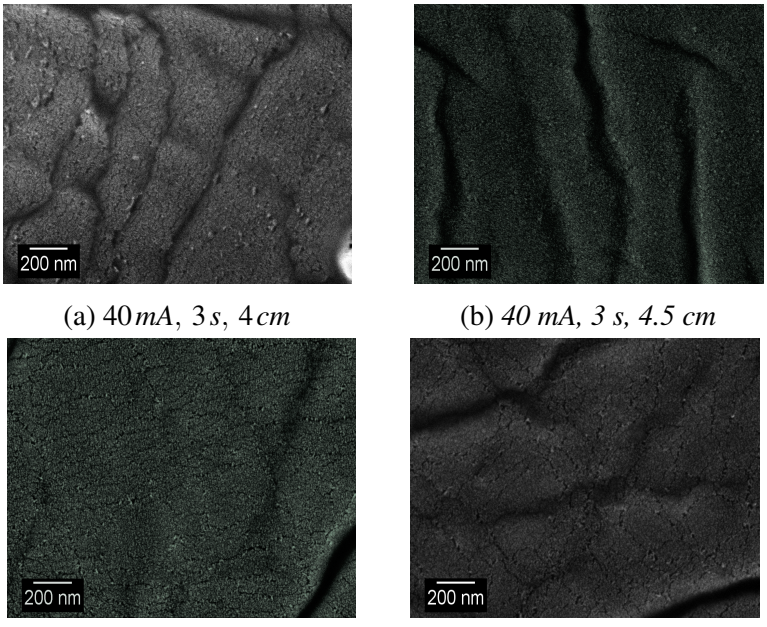

(a) $40\,mA$, $3\,s$, $4\,cm$ (b) *40 mA, 3 s, 4.5 cm*

(c) *40 mA, 4s, 4.5 cm* (d) *40 mA, 5s, 5 cm*

Fig. 6.3 FESEM images of samples with $1\,mm$ PDMS membranes (20:1 curing ratio) and sputtered Ag-NPs under different synthesis conditions. Images are taken with $150\,kx$ magnification.

A FESEM analysis was carried out on the samples, in order to link the morphology to the obtained characteristics of the transmittance spectra. In Figure 6.3 FESEM images of some of the samples are shown (see Appendix A.1 for all the FESEM images). As it can be seen, the nanoparticles that are fabricated by sputter deposition on PDMS membranes are very small (average diameter around 10 *nm*). Comparing the samples shown in Figures 6.3a and 6.3b, it looks that the second, that was sputtered at longer distance from the target, has smaller and more uniform nanoparticles. This could be explained by the fact that for the same sputtering current and deposition time, but at lower distances, silver particles that are sputtered from the target and reached the PMDS surface, are more energetic, so that their aggregation on the surface is easier. Whereas, for longer distances, silver nanoparticles on the substrate tend to be smaller, since particles sputtered from the target are less energetic when they reach the surface and their nucleation into bigger nanoparticles is made slower [150].
In the same way, looking at Figures 6.3b and 6.3c, it seems that the longer the time of the deposition, the bigger the obtained NPs. This can be explained by the fact that for longer depositions more material is sputtered from the target, so that the aggregation into bigger NPs is favoured. This effect is translated into a red-shift of the wavelength of the dip, which changes – as already seen – with the size and the inter-particle distance of the Ag-NPs, since it is related to the LSPRs of the substrate. This can be seen from Figure 6.2b: indeed longer-time deposition produces samples with bigger $\Delta\lambda$, if compared to the ones sputtered for smaller times.

In conclusion, this type of substrates requires a very fine tuning of all the synthesis parameters for the fabrication of SERS substrates with resonant behaviour with respect to the used source. This high complexity is to be added to their low reproducibility, both in the same deposition session and in different ones, making these substrates very hard to be used for large scale fabrication.

6.2.2 Synthesis of Ag-NPs on functionalised PDMS membranes via sputter deposition

The PDMS substrates can be treated before the deposition of Ag-NPs to promote their adhesion to the surface, and thus also the stability of the nanostructures. A possible pretreatment process consists in a functionalisation of the PDMS membranes, which improves the retention of the deposited Ag-NPs on the PDMS substrates. In the following, the methods that were used for the Ag-NPs sputtered on PDMS substrates are explained and the results discussed.

Properties of differently functionalised PDMS membranes

The first step to a functionalisation of the substrates is given by the activation process. This process favours the exposure of the silanol groups on the PDMS surface, which temporary increases the wettability of the substrates. Two different activations were tested: a) the first corresponds to an activation of the PDMS membranes by means of a piranha-like solution; b) in the second case an Argon plasma was used to physically etch the PDMS membrane to favour its activation. The activation was finally followed by the functionalisation of the membranes with an organosilane. Two ways were followed, using (3-mercaptoproyl)trimethoxysilane (MPTMS) and (3-aminopropryl)triethoxysilane (APTES) as adhesive layers. Practically, the methoxy or the ethoxy terminal groups of MPTMS or APTES break, while the silane is attacked by the silanol moieties on the PDMS surface and finally methanol or ethanol is released; on the other side, the thiol or the amino group is free and available to bind the metal, thus providing a more stable interaction between the PDMS surface and the Ag-NPs. The wettability of the activated and functionalised substrates was measured by means of optical contact angle characterization. Water and diiodomethane (CH_2I_2) were used as standard liquids to study the hydrophobicity of the substrates. A higher hydrophobicity is related to a higher roughness of the substrates, theoretically helping the formation of more Ag-NPs per unit area [75], i.e., ensuring also a possible increase of the SERS enhancement.

In Table 6.1 the values of the Contact Angles are shown for all the cases. As it can be clearly seen, both the activation methods lead to an increased hydrophilic behaviour of the surface of the PDMS membranes. In fact, activated membranes show lower CAs, in comparison to the non-activated ones. A very high water CA of 131.44° is obtained for the

Table 6.1 Values of Contact Angle (in degree) for water and diiodomethane drops of 1 μL on PDMS substrates

Drop	Piranha			Plasma		
	No Funct.	APTES	MPTMS	No Funct.	APTES	MPTMS
H_2O	118.86 ± 4.98	130.99 ± 3.53	116.73 ± 6.53	83.67 ± 3.37	123.58 ± 5.16	127.62 ± 6.39
CH_2I_2	85.33 ± 3.62	61.63 ± 4.01	67.55 ± 4.06	70.77 ± 3.52	60.39 ± 4.57	81.04 ± 4.6

Drop	No Activation		
	No Funct.	APTES	MPTMS
H_2O	131.44 ± 3.57	125.49 ± 3.48	119.92 ± 3.15
CH_2I_2	103.80 ± 3.34	90.96 ± 4.6	69.45 ± 4.76

not treated PDMS membrane. Lower CAs are obtained for diiodomethane, whose surface tension is characterized by a stronger non-polar contribution [50].

It can be stated that, for APTES functionalisation method, the membranes activated by a piranha-like solution are more hydrophobic, in comparison to the ones activated by Ar-Plasma. On the contrary, the MPTMS-treated membranes result more hydrophobic when pre-treated by plasma activation. All the results are compared in a single histogram in Figure 6.4a: as it can be easily seen, the higher hydrophobicity of the functionalised substrates is observed in piranha activated substrates in case of APTES functionalisation, and in plasma activated substrates in the case of MPTMS. In Figure 6.4b the standard deviation (SD) of the CA measurements vs. the respective CA values are shown. MPTMS functionalised substrates show high SDs both for plasma and piranha activation (for water drops), even if with high hydrophobicity. From this it can be inferred that MPTMS functionalised samples have a lower homogeneity. On the contrary, the piranha activated PDMS, functionalised by means of APTES shows high CA along with a low value of SD.

After the study of the CA, a FESEM characterization was carried out to understand if it exists a correlation between the morphology of the substrates and their wettability. In Figure 6.5 some of the Ag-coated substrates are shown. As it can be noticed, MPTMS-

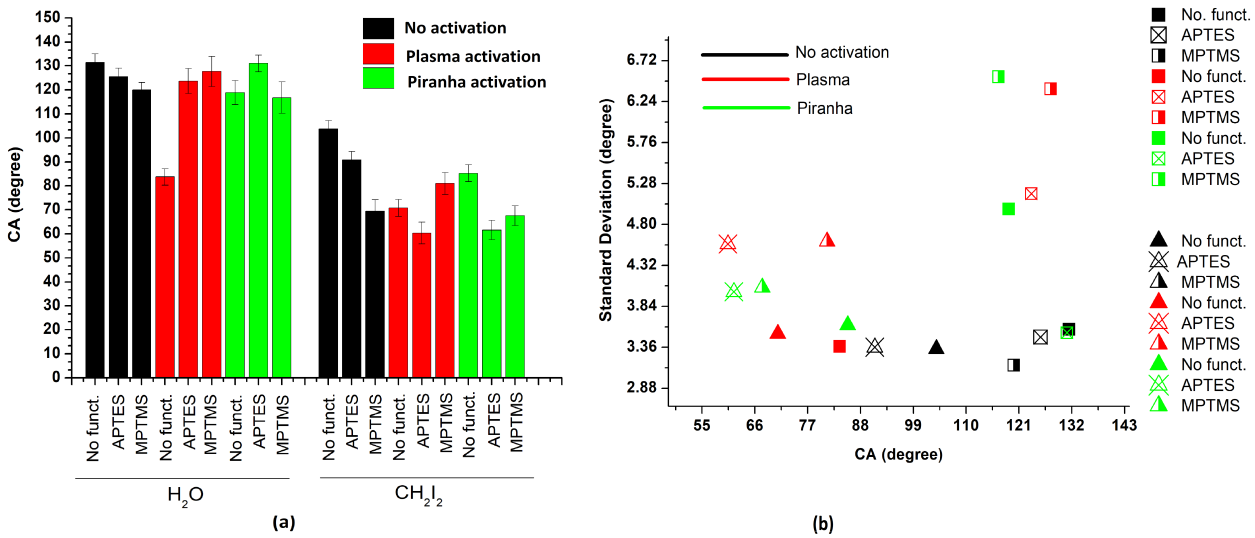

Fig. 6.4 Graph of: (a) Values of Contact Angle (in degree) for water and diiodomethane drops of 1 μL on PDMS substrates with the respective Standard Deviation (SD) bars; (b) SD vs. CA values for the different samples: square points are measurements with water drops and triangle points are measurements with diiodomethane drops.

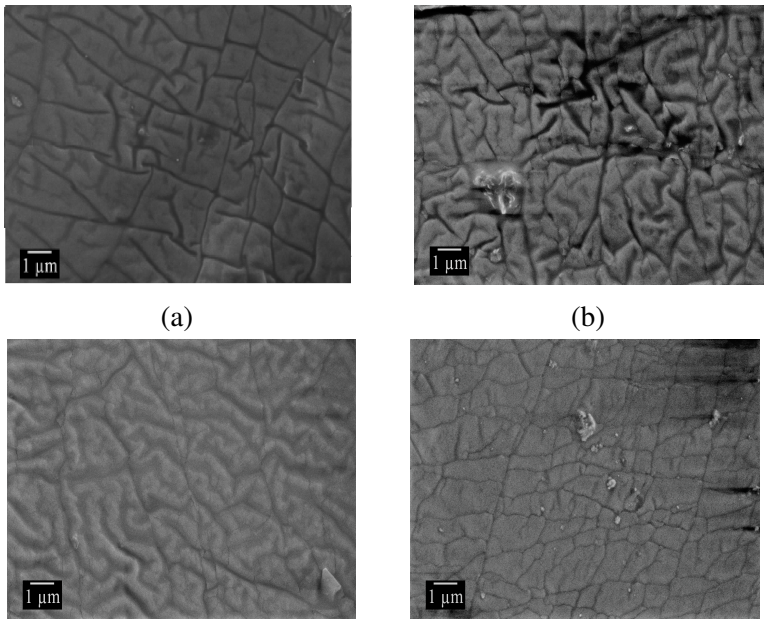

Fig. 6.5 FESEM images of Ag-NPs on untreated PDMS membrane (a), plasma-activated PDMS membrane and treated with MPTMS (b), piranha-activated PDMS membrane and treated with MPTMS (c) and plasma-activated PDMS membrane and treated with APTES (d)

functionalised PDMS substrates have a different morphology if compared to the PDMS functionalised by means of APTES, so that it can be assumed that the morphology is related to the used functionalisation. In addition to this, the higher hydrophobicity of the MPTMS-functionalised plasma-activated PDMS membranes – in comparison to the piranha-activated one – seems to be supported by the higher roughness of the surface.

Optical analysis

functionalised PDMS membranes and untreated PDMS were finally coated with Ag-NPs. The starting PDMS was fabricated with a 20:1 monomer-to-curing agent ratio and eventually coated at sputter conditions of $40\,mA$, $5\,s$, $5\,cm$. In Figure 6.6a the UV-Vis transmittance spectra of the samples are shown, while in Figure 6.6b it is shown the minimum transmittance of the UV-Vis spectra vs. $\Delta\lambda$. It can be noticed that the untreated Ag-coated PDMS substrate shows a dip around *514.5 nm*, in resonant condition with the laser source used for the Raman measurements. This result can also be seen in Figure 6.6b; the untreated PDMS matches better the resonance condition than the other substrates, but at the same time it shows a relatively-high transmittance. Moreover, the plasma-activated substrates (full squares points), both for APTES and MPTMS, show higher transmittances, if compared to PDMS membranes

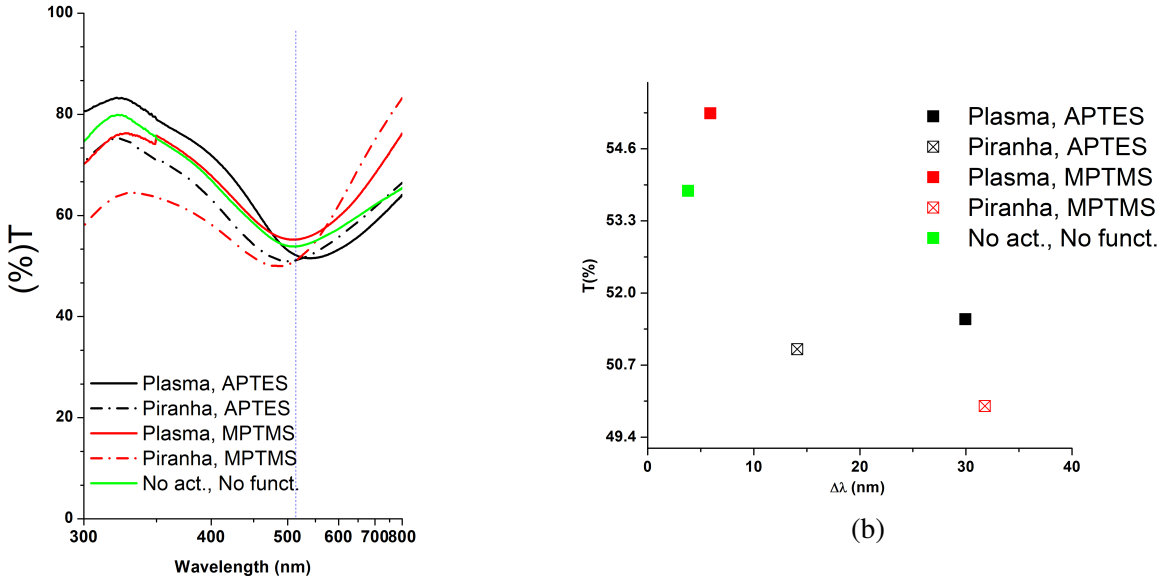

(a) (b)

Fig. 6.6 UV-Vis transmittance spectra in air for *1 mm* PDMS membranes with sputtered Ag-NPs, with different activation and functionalisation processes (a) and graph of dip transmittance vs. $\Delta\lambda$ (b). The sputtering conditions are 40 mA, 5 s, 5 cm

activated by means of piranha-like solution (crossed empty squares points). This means that piranha-activated APTES-functionalised membranes are theoretically the ones that should show the strongest enhancement.

Raman efficiency and uniformity

For the study of the Raman efficiency and of the uniformity of the samples, 4-mercaptobenzoic acid (4-MBA) was used as SERS probe molecule. The MBA does not present electronic resonant behaviour for the used excitation source, so that the results are easily related to label-free detection applications. This behaviour is an excellent starting point for the comparison of the enhancement efficiencies of SERS nanostructures, since only the response of the SERS substrate is responsible for the enhancement, at the most usually employed excitation sources. Moreover, 4-MBA strongly binds to noble metal particles through its thiol group, thus allowing the formation of stable monolayers suitable for the evaluation of the SERS enhancement uniformity.

In Figure 6.7 the typical SERS spectra of 4-MBA acquired on Ag coated PDMS and APTES are shown. The spectrum is dominated by two intense bands: the most intense centred at 1584 cm^{-1}, and the second at 1075 cm^{-1}. For the sake of completeness, the main vibrational bands of the 4-MBA are also shown in the table of Figure 6.8. In order to compare

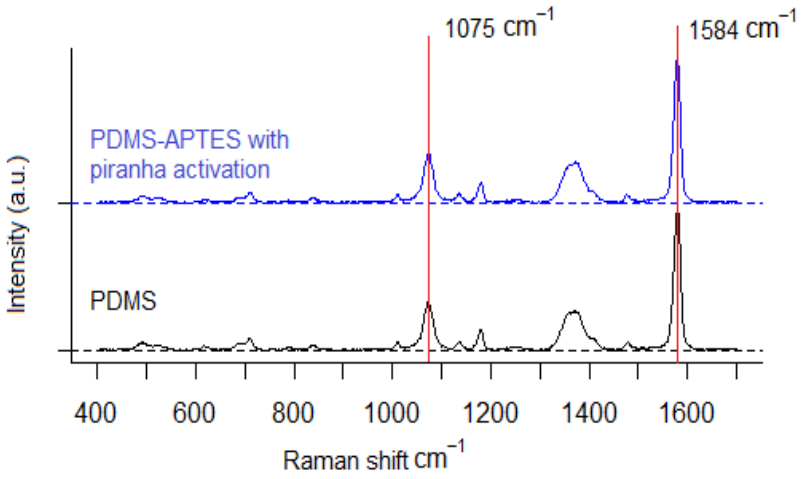

Fig. 6.7 SERS spectrum of 4-MBA at the concentration of $10^{-5}\,M$, acquired at 514.5 *nm*, on an Ag-coated SERS substrates, with piranha-like solution activation and APTES functionalisation (blue spectrum) and on Ag-coated SERS substrate with untreated PDMS substrate.

4-MBA

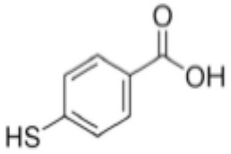

Raman shift (cm^{-1})	Assignment
1075	ring breathing (ν_{12}, a_1) +ν C-S
1137	δC-H (ν_{15}, b_2)
1180	δC-H (ν_9, b_1)
1380	COO^- stretching
1584	ring breathing (ν_{8a}, a_1)

Fig. 6.8 Band assignments for 4-MBA spectrum [50]

the SERS performances of the prepared substrates, an integration of the intensity over the area of the latter peak was performed for all the spectra. The spectra were acquired by mapping the surface of each sample, so to obtain an average intensity for the single substrate, along with the RSD to acquire the information about the uniformity of the sample.

The results of the Raman characterization of the functionalised samples are reported in the following. In Figure 6.9 the average intensities of SERS signals measured for the dif-

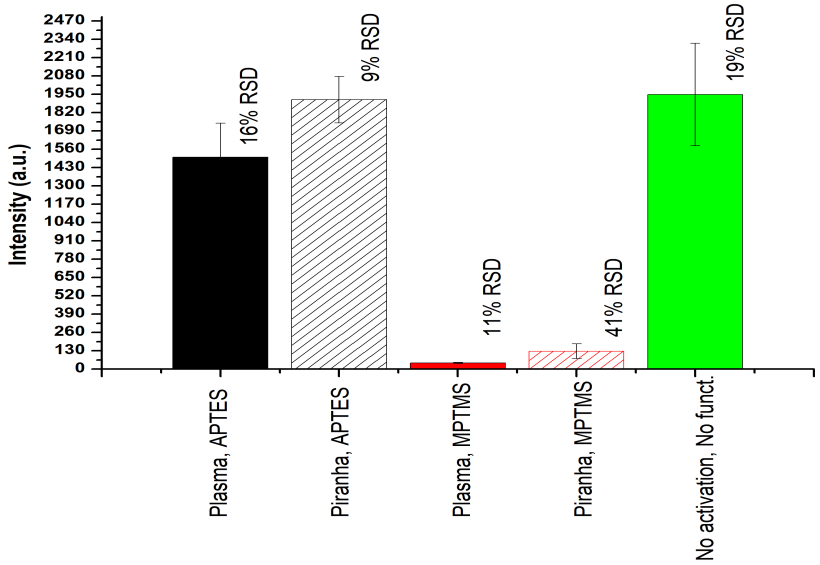

Fig. 6.9 Average intensities of the different Ag-coated substrates, with different activation and functionalisation processes. Relative Standard Deviations are also shown on top of each column of the histogram.

ferent Ag-coated substrates are shown. As it is clearly seen, the substrates that underwent a functionalisation with APTES show the highest average SERS intensities. In particular, the substrate that was activated by means of a piranha-like solution and functionalised with APTES is the one showing better properties. This outcome agrees with the results obtained by the optical analysis (see Figure 6.6b), in which this sample exhibits a low dip transmittance and a good plasmonic resonant behaviour. Furthermore, also a low RSD is obtained (*8.6 %*), meaning that the substrate is uniform and guarantees a good intra-sample repeatability. On the contrary, for what concerns MPTMS functionalised substrates, nothing can be inferred. Indeed, the results don't match with the ones expected from the optical response. Very low SERS intensities are indeed revealed and then the spectra are not shown in Figure 6.7.

6.2.3 Stability tests

To study the stability, the samples (Ag-coated PDMS, Ag-coated APTES and MPTMS functionalised PDMS, *20:1, 1 mm, 40 mA, 5 s, 5 cm*) were incubated in TE-NaCl solution and the variation over time of the transmittance spectra was measured by acquiring UV-Vis spectra at the beginning of the test (T0) and after *1 h* (T1) *24 h* (T24) and *1 week* (Tw).
As it can be seen from the transmittance spectra shown in Figure 6.10(a-c), this test showed a very low retention of the Ag-NPs on non-pretreated PDMS membranes and APTES-functionalised PDMS membranes pretreated by a piranha-like solution, with a variation of

the optical behaviour already after *1 h* of incubation. In fact, the weak forces that fix the Ag-NPs to the PDMS substrates are not sufficient to strongly bind them to the surface, so that the NPs redistribute into different morphologies when incubated in liquid solutions, especially increasing the ionic strength of the used buffer. This redistribution of the NPs translates into a variation of the Plasmon Resonances of the nanostructures that are strongly related to their geometry and arrangement, changing their SERS activity. This makes these substrates almost impossible to be used for bioapplications, which usually require high stability. On the other side, MPTMS-functionalised membranes showed a more stable behaviour. In fact, the

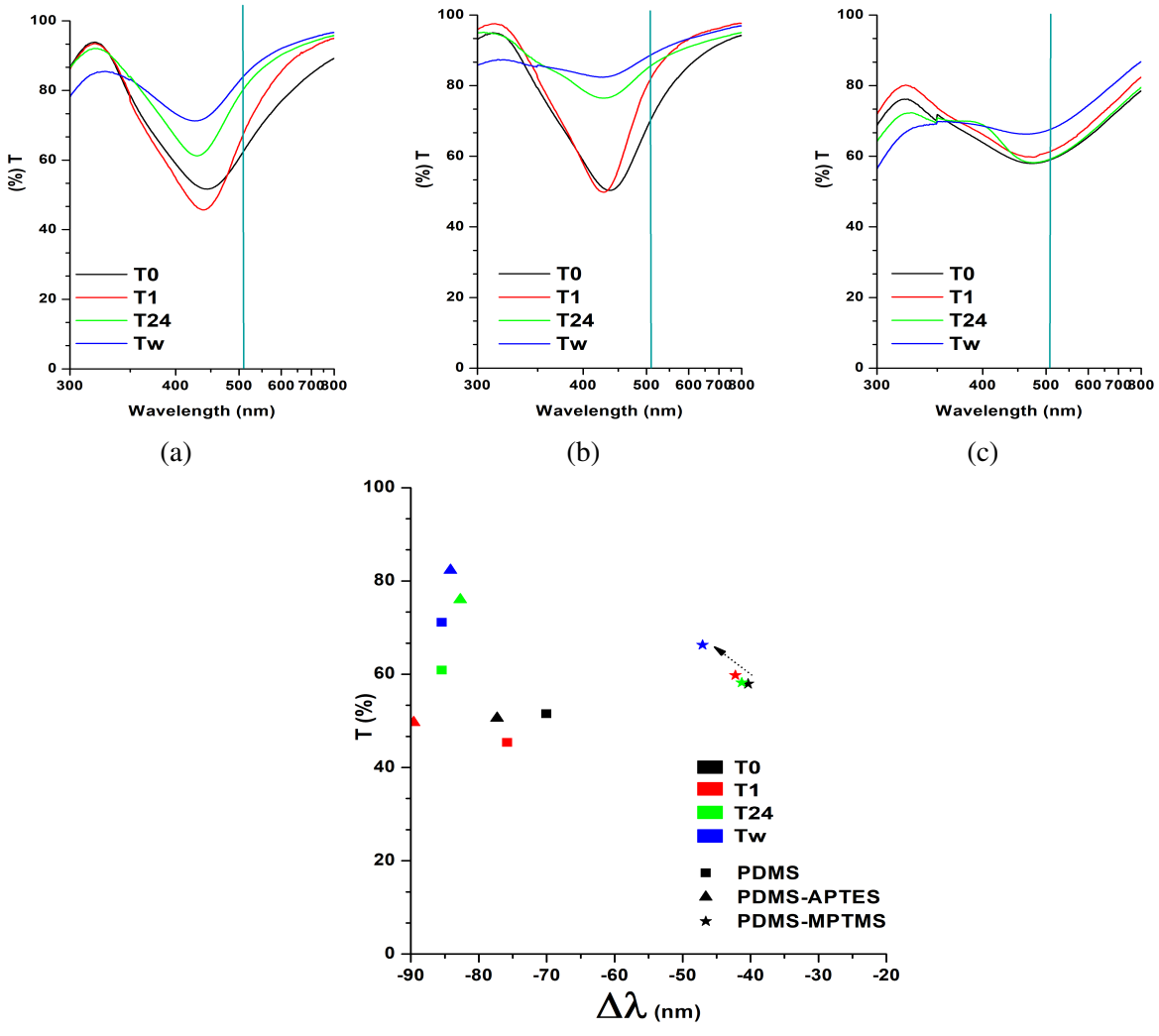

Fig. 6.10 UV-Vis transmittance spectra in TE-NaCl buffer for Ag-coated PDMS (a) and Ag-coated piranha-activated APTES (b) and MPTMS (c) PDMS substrates. Graph of the dip transmittance vs. relative $\Delta\lambda$ for different the sputtered samples.

interactions between the sputtered metal and the thiol group of the MPTMS are more stable, since between Ag and the sulfur atom of the thiol group a semi-covalent bond forms. On the other side, the interactions between the sputtered Ag and the amino group of the APTES are of electrostatic nature, i.e. weaker than the semi-covalent Ag-S bond.
A fast comparison between the variations of the optical properties of the samples can be done using the Figure 6.10d, in which the dip transmittance vs. the distance of the dip wavelength from the source wavelength is plotted. It is first important to underline that in the *x-axis* the shift of the dip wavelength (due to the incubation) with respect to the source is represented. This means that the value in the *x-axis* is to be interpreted as the quantity $\Delta\lambda$, but with the particularity that: when its value is negative, a blue-shift is registered, instead, when positive, a red-shift is registered. As it can be easily seen, the MPTMS-functionalised PDMS result stable, with the dip transmittance and the dip wavelength almost fixed, showing only a small shift also after *1 week* in incubation, thus agreeing with the explanation of a stronger bond between the Ag-NPs and the surface.

6.2.4 Conclusions

Sputtered Ag-NPs on PDMS membranes are still difficult to be used in the framework of bio-applications. More precisely, not functionalised nanostructures show low reproducibility and stability, incompatible characteristics for SERS applications. A solution to the low stability is given by the functionalisation of the PDMS surface before the deposition of silver: thanks to the addition of an adhesive layer, a higher retention on the surface of the Ag-NPs is possible. As result of the stability tests the MPTMS-functionalised PDMS Ag-coated substrates showed higher stability in TE-NaCl buffer, if compared to the other samples (non-treated Ag-coated PDMS and APTES-functionalised Ag-coated PDMS).
The best SERS enhancement was instead observed for the SERS-active substrates, obtained by means of a pre-treatment with piranha-like solution and followed by a functionalisation with APTES. Moreover, these samples also showed good intra-sample repeatability. On the contrary, the MPTMS-functionalised Ag-coated samples, despite their good stability, didn't exhibit a good SERS enhancement, showing a sensitivity which is much lower than the other Ag-coated PDMS membranes.
For this reason, other synthesis methods were investigated to obtain PDMS substrates with higher Raman enhancement and a higher reproducibility if compared to those fabricated up to now. The next paragraph deals with the synthesis of SERS-active nanostructures by means of static incubation of PDMS membranes in a solution of silver nitrate

6.3 Static incubation of PDMS membranes for SERS substrates synthesis

A second approach was used for the *in-situ* synthesis of silver nanoparticles on PDMS membranes. In this case, the PDMS membranes were incubated in a solution of silver nitrate. The synthesis parameters (monomer-to-curing agent ratio, incubation time, thickness of the membranes, incubation temperature, cross-linking degree, presence of different concentration of ethanol, concentration of silver nitrate) were tested separately and all the samples were characterized by means of UV-Vis transmittance analysis, FESEM characterization (along with an image analysis) and Raman characterization, using also in this case MBA as analyte for a mapping of the samples.
Two different values of monomer-to-curing agent ratio (3:1 and 5:1) were chosen for all the experiments, so that for any other varying parameter, two sets of samples were fabricated. Moreover, for each condition three different samples were fabricated, one for each of the three different incubation times, corresponding to 24h, 48h and 72h, that were chosen in order to analyse the influence of the incubation time on the synthesis.
The results are first presented separately for each experiment. A comparison is finally performed and the best conditions chosen for the bio-assay. The complete list of all the measurements is in Appendix A.

6.3.1 Thickness of PDMS membranes

Optical and morphological analysis

The UV-Vis transmittance spectra of the fabricated samples are reported in the corresponding section of the Appendix A.2. In Figure 6.11a the graphs for the *1 mm* thickness case are plotted, along with the correspondent FESEM images, in order to show the general shape of the spectra of this type of samples. On the other side, Figure 6.11(b,c) collect respectively the 3:1 and the 5:1 samples for different thickness.
From Figure 6.11a it is possible to notice a trend with time of the transmittance spectra. In fact, with the increase of the time of incubation, also the available time for the reaction increases. This manifests itself in the decrease of the transmittance from 24h to 72h, for all the chosen thickness of the PDMS membranes. This means that, with the increase of the incubation time also a higher coverage of the PDMS membranes is expected, with a higher density of Ag-NPs for a longer incubation of the samples. This agrees with the FESEM images shown in Figure A.10 (Appendix A.2), in which all the FESEM images of the samples are shown. As it can be seen (e.g., from the FESEM images of *1 mm* substrates of Figure

6.11a), the highest coverage is obtained for longer times of incubation.

From Figures 6.11b and 6.11c a comparison between 3:1 and 5:1 samples can be seen

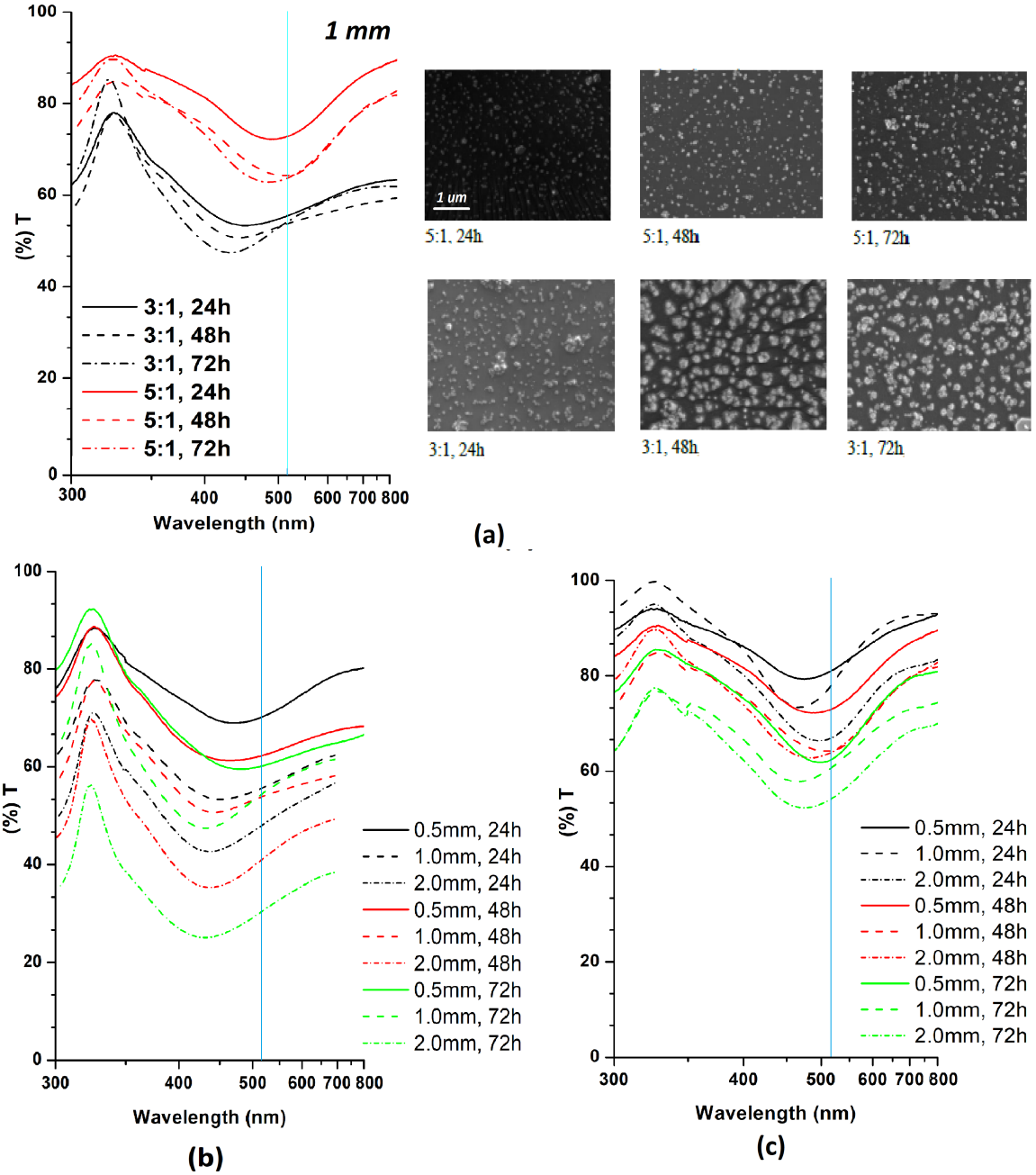

Fig. 6.11 UV-Vis measurements in air and FESEM images for PDMS thickness of 1 *mm* prepared with different curing ratio and incubation times (a), UV-Vis measurements in air for curing ratio of 3:1 (b) and 5:1 (c) at different substrate thickness. The FESEM images were taken at *50 kx* magnification.

as well. First of all, the 5:1 samples present on the average higher transmittances, which is explained by the lower coverage of 5:1 samples, if compared to 3:1 samples. It is worth to notice that the 5:1 samples exhibit a dip that is more tuned to the excitation wavelength, along with a higher sharpness of the curve around the dip. Indeed, 3:1 samples are characterized by flatter spectra, and dips that are shifted to lower wavelengths. The flatness of the spectra of the 3:1 samples must be attributed to a lower homogeneity of the NPs morphological characteristics, corresponding to a broader distribution of the NPs sizes and inter-particle gaps, in comparison to the 5:1 samples, which present more uniform distributions of these features.

An image analysis was carried out to have more precise information about the morphology of the samples. The results obtained by means of the MATLAB script and ImageJ were compared. It was noticed that the MATLAB script was more efficient in the case of smaller particles with fewer clusters, giving accurate results in short time. Unfortunately, the script is not completely optimized for the identification of the nanoparticles in big agglomerates. The division of the NPs collected in big clusters was instead manageable (even if with longer times) by means of the ImageJ software. For this reason, it was chosen to use ImageJ for those samples with a big amount of compact clusters of Ag-NPs (usually 3:1 samples) and to use the MATLAB automatic script for samples with smaller and sparser NPs (usually 5:1). Average sizes and gaps for all the samples are plotted in the graph of Figure 6.12a. As it can be seen, 5:1 samples (labelled in the Figure with numbers from 10 to 18) own smaller NPs with smaller inter-particle gaps. More importantly, from the image analysis a study on the distribution of the NPs was also executed, so to evaluate the variation of the size and the inter-particle gap within the same sample, along with the coverage of the surface. From these results it was confirmed that 3:1 samples have higher coverage indexes (with an average value of 8% for 5:1 samples and 20% for 3:1 ones), which justify the lower transmittance of their spectra, along with a higher variability of the gap size, compared to the one of 5:1 samples. These results agree with the UV-Vis spectra and justify also the broader linewidth of 3:1 samples dips.
In Figure 6.12b a final graph is reported, showing the dip transmittance vs. the distance of the dip wavelength from the excitation wavelength. Also here it is easy to notice that 5:1 samples (triangular points) show a more resonant behaviour. More importantly, it can be seen that the transmittance decreases with the increase of the thickness (thinner samples showed higher transmittance values). In fact, the silver nitrate reacts with the PDMS to form Ag-NPs. Thicker substrates then would allow the production of more silver in the form of NPs, that translates into a higher coverage. Despite of this, it is also important to underline that the

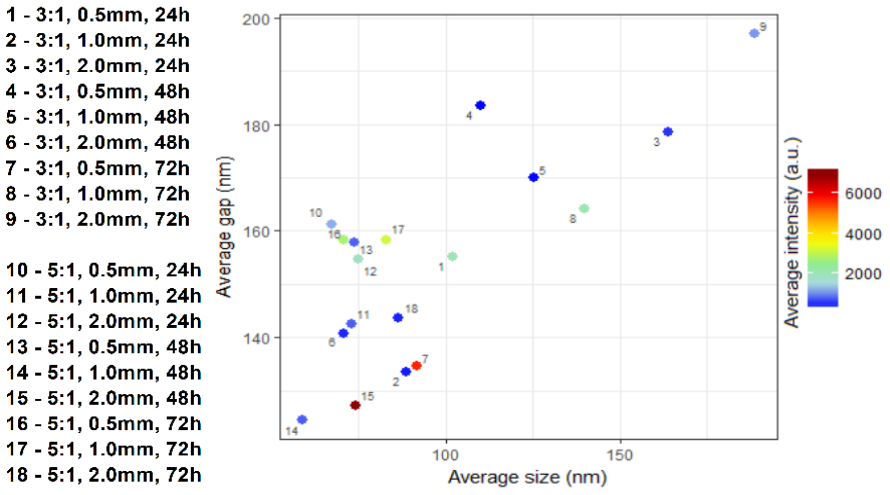

(a)

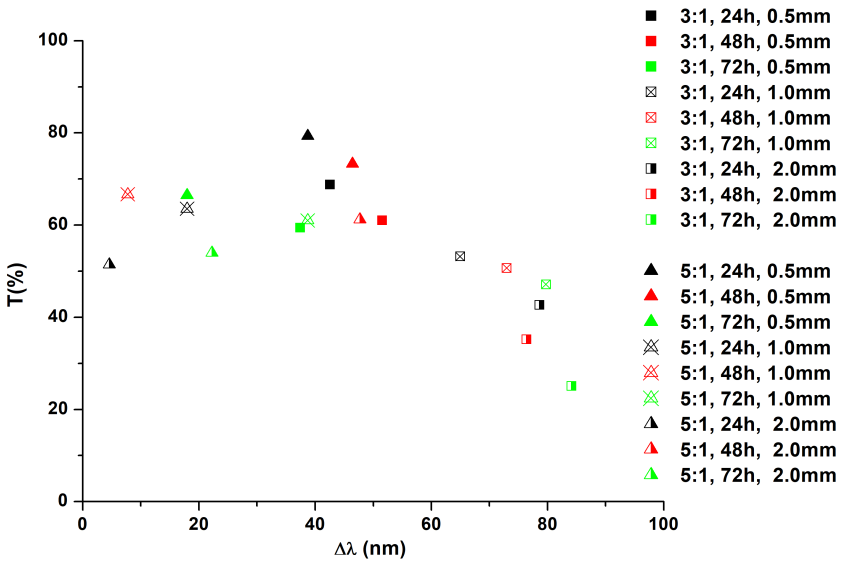

(b)

Fig. 6.12 Figure (a): each point represents a sample: the colour represents the Average SERS intensity in arbitrary unit, while in the y- and x-axis, the average size of the Ag-NPs and their Average Inter-Gap distance are used respectively; (b): dip transmittance vs. $\Delta\lambda$ for samples with different substrate thickness.

higher thickness itself is a possible cause for the lower transmittance of thicker substrates. It is also interesting to notice that the dip of samples with 3:1 monomer-to-curing agent ratio is blue-shifted when increasing the thickness of the PDMS membrane. Moreover, also the sharpness of the spectra around the dip increases with the thickness (see Figure A.6 from (a) to (c)). This behaviour is justified by the image analysis on the samples. In fact, the increase

of the thickness comes with a decrease of the gap variance, that would mean a more uniform family of Ag-NPs on the thicker substrates.

Raman efficiency and uniformity

The average intensity calculated from the Raman analysis of the substrates, using MBA as analyte, is shown for all the samples in the histogram of Figure 6.13a. It can be seen that on an average, the 5:1 samples exhibit higher Raman intensities, agreeing with the more resonant behaviour shown by these samples. In Figure 6.13b the Relative Standard Deviation (RSD) versus the mean intensity is plotted. Looking at this, it is clear that 5:1 samples (triangular points) have smaller RSD, again in accordance with the optical and morphological characterizations, which underlined the higher homogeneity of the 5:1 substrates, with smaller gap and size variances.

In Figure 6.12a the mean gap versus the mean equivalent diameter of the Ag-NPs of each sample is plotted, along with the average Raman intensity. As it can be seen, on average, low Raman intensities are registered. The samples showing the highest Raman intensities (respectively labelled in the Figure with number 7 and 15) have also lower gap size, which could explain their higher Raman efficiency, related to a higher density of hot-spots on the substrates. In conclusion, the best samples are the 3:1, $0.5\,mm$, $72h$ and the 5:1, $2\,mm$, $48h$, with the latter showing the lowest RSD (see figure 6.13b).

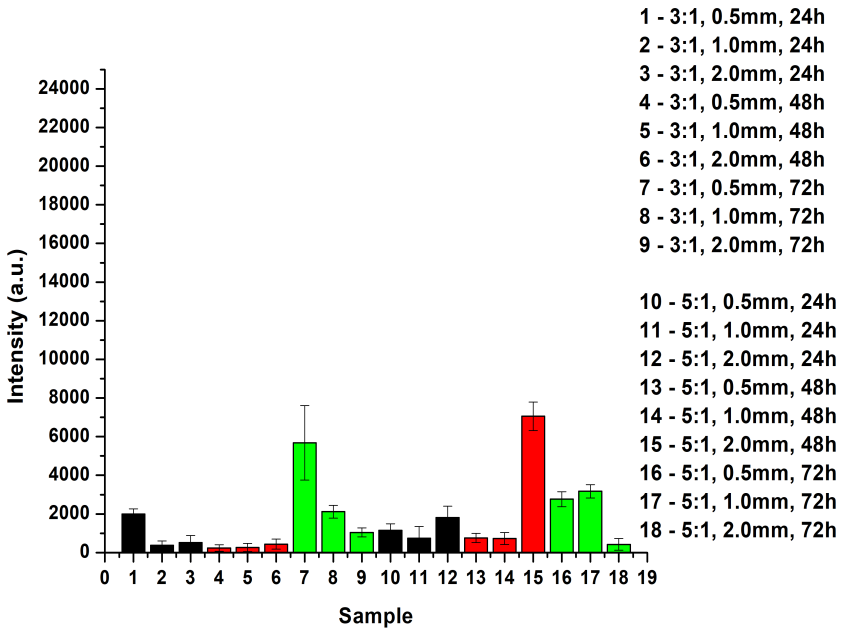

(a)

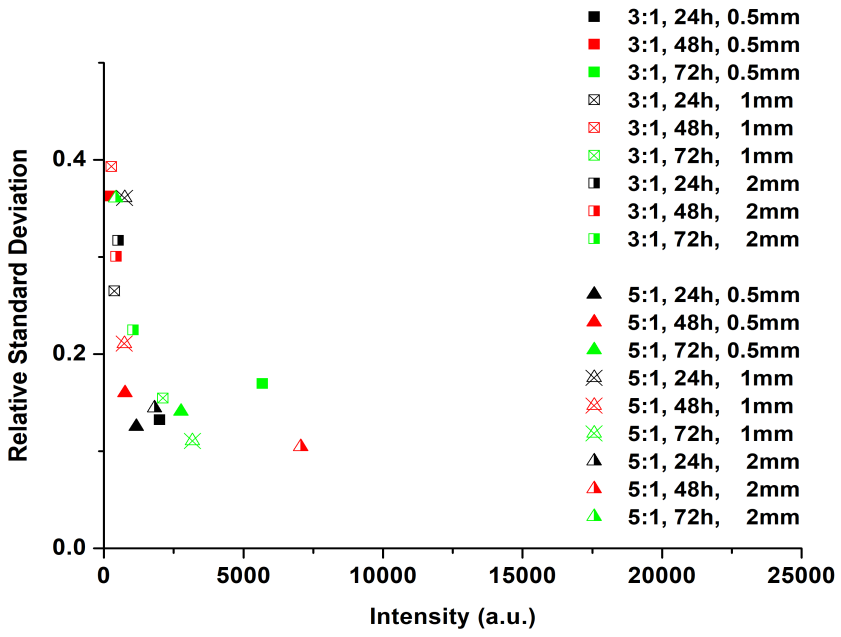

(b)

Fig. 6.13 Figure (a): Average intensities of the SERS substrates synthesised for different thickness of the PDMS membranes; (b): RSD vs. average intensity of the SERS substrates synthesised for different thickness of the PDMS membranes.

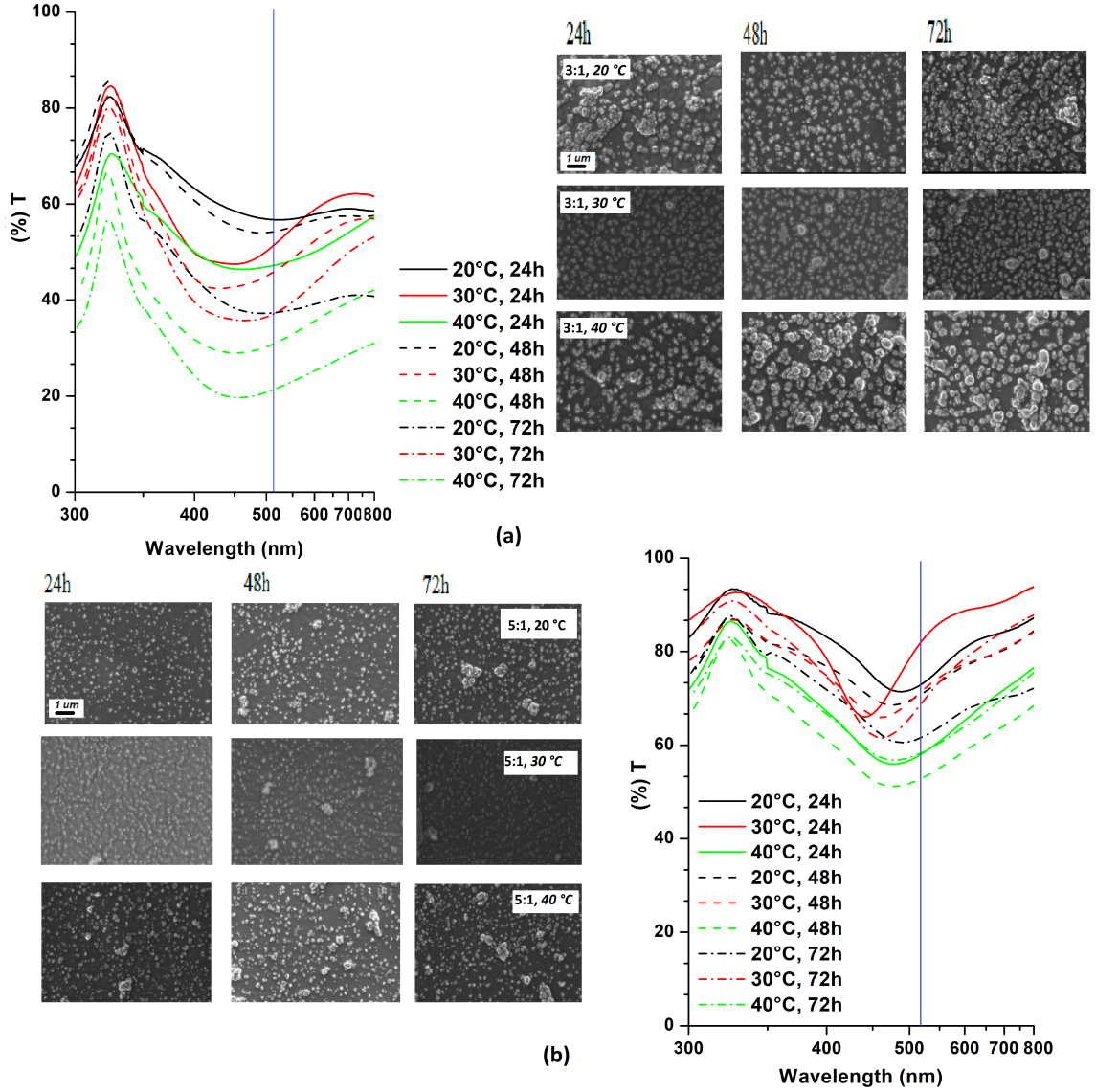

Fig. 6.14 UV-Vis measurements in air and FESEM images for curing ratio of 3:1 (a) and 5:1 (b) at different incubation temperature. FESEM images have been taken at magnification of *50 kx*

6.3.2 Incubation temperature of PDMS membranes

Optical and morphology analysis

In order to evaluate the effect of temperature on the synthesis of the Ag-NPs, the PDMS membranes with 3:1 and 5:1 monomer-to-curing agent ratio were incubated at *20, 30* or *40* $^{\circ}C$. In Figure 6.14a and 6.14b the UV-Vis spectra and the FESEM images of all the samples are reported. As in the case of the variation of the thickness of the PDMS membranes, it

can be seen that longer incubation times allow a higher coverage of the PDMS membranes, resulting in the decrease of the transmittance.
Moreover, also in this experiment it was seen that the 5:1 samples have dips more centred around the 514.5 nm source wavelength, along with a higher sharpness of the spectra in the vicinity of this wavelength if compared to the 3:1 samples. A quick look through the FESEM images of the samples is sufficient to relate this behaviour to a higher variability of the NPs size and inter-particle distances of the 3:1 samples. The image analysis on the samples confirmed this hypothesis; indeed, 3:1 samples exhibit higher size and gap variances, which is also the reason for their flatter transmittance spectra.

The temperature of incubation acts on the speed of the reaction, so that a higher temperature leads to a higher coverage of the PDMS membranes. This agrees with the decrease of the transmittance with the increase of the incubation temperature. Results are confirmed by the analysis of the FESEM images, which revealed a higher coverage for samples incubated at 40 $^{\circ}C$. Figure 6.15a shows all the main optical characteristics of the samples (transmittance of the dip and dip wavelength) in a single graph. As it can be seen, samples synthesised at 40 $^{\circ}C$ fall in the lower region of the graph along the transmittance-axis (both for the cases of 3:1 and 5:1 monomer-to-curing agent ration), if compared to the same ones incubated at 20 $^{\circ}C$. Moreover, samples incubated at 30 $^{\circ}C$ lay between the two previous sets of samples, that agrees with the increase of the coverage with the increase of the temperature.
The dip wavelength of the samples is now analysed. Samples prepared with 3:1 PDMS membranes (square points) and incubated at the temperature of 20 $^{\circ}C$ show a dip, whose minimum is nearer to the wavelength of the source, if compared to the ones incubated at 30 $^{\circ}C$ and 40 $^{\circ}C$. Figure 6.15b shows the average inter-particle gap vs. the average size of the samples. As it can be seen for the graph, the 3:1 samples incubated at 20 $^{\circ}C$ (labelled with numbers 1, 4 and 7) showed smaller sizes than those obtained at 30 $^{\circ}C$ (labelled with numbers 2, 5 and 8) and at 40 $^{\circ}C$ (3, 6 and 9). For what concerns the samples with 5:1 ratio it can be seen that the bigger $\Delta\lambda$ values are obtained for the samples incubated at 30 $^{\circ}C$. Looking at Figure 6.15b, it can be seen that 5:1 samples have particles with almost equal average size. It is interesting to notice that, having almost the same size, these samples have a coverage, and then also a transmittance, that depend mostly on the gap dimension; indeed, at same size, larger gaps would mean also a lower coverage. This is easy to be seen in the graph of Figure 6.15b, where 5:1 substrates incubated at the temperature of 20 $^{\circ}C$ (labelled with numbers 10, 13 and 16) are on average in the upper part of the plot, with respect to the ones incubated at 30 $^{\circ}C$ (labelled in figure with numbers 11, 14 and 17) and those incubated at 40 $^{\circ}C$ (samples labelled with numbers 12, 15 and 18).

In conclusion, it is expected that: samples with 3:1 PDMS substrates and incubated at $20°C$ exhibit higher SERS enhancement, whereas for what concerns 5:1 PDMS substrates, the higher SERS enhancements are expected from the ones incubated at $40°C$.

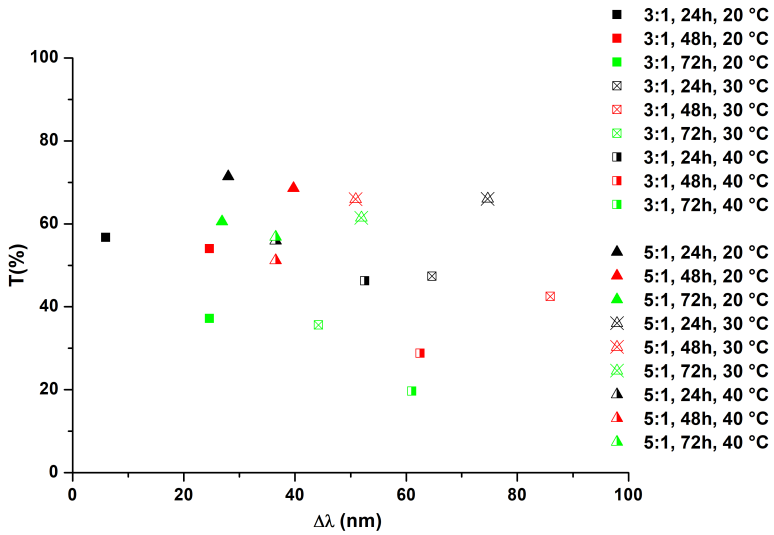

(a)

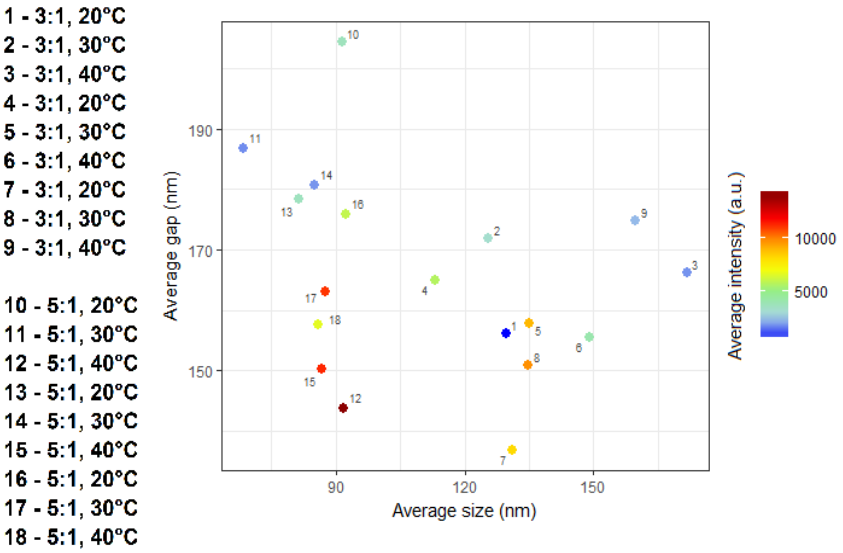

(b)

Fig. 6.15 Figure (a): dip transmittance vs. $\Delta\lambda$, for samples with different incubation temperature; (b): each point represents a sample: the colour represents the Average intensity in arbitrary unit, while in the y- and x-axis, the average size of the Ag-NPs and their average inter-gap distance are used respectively.

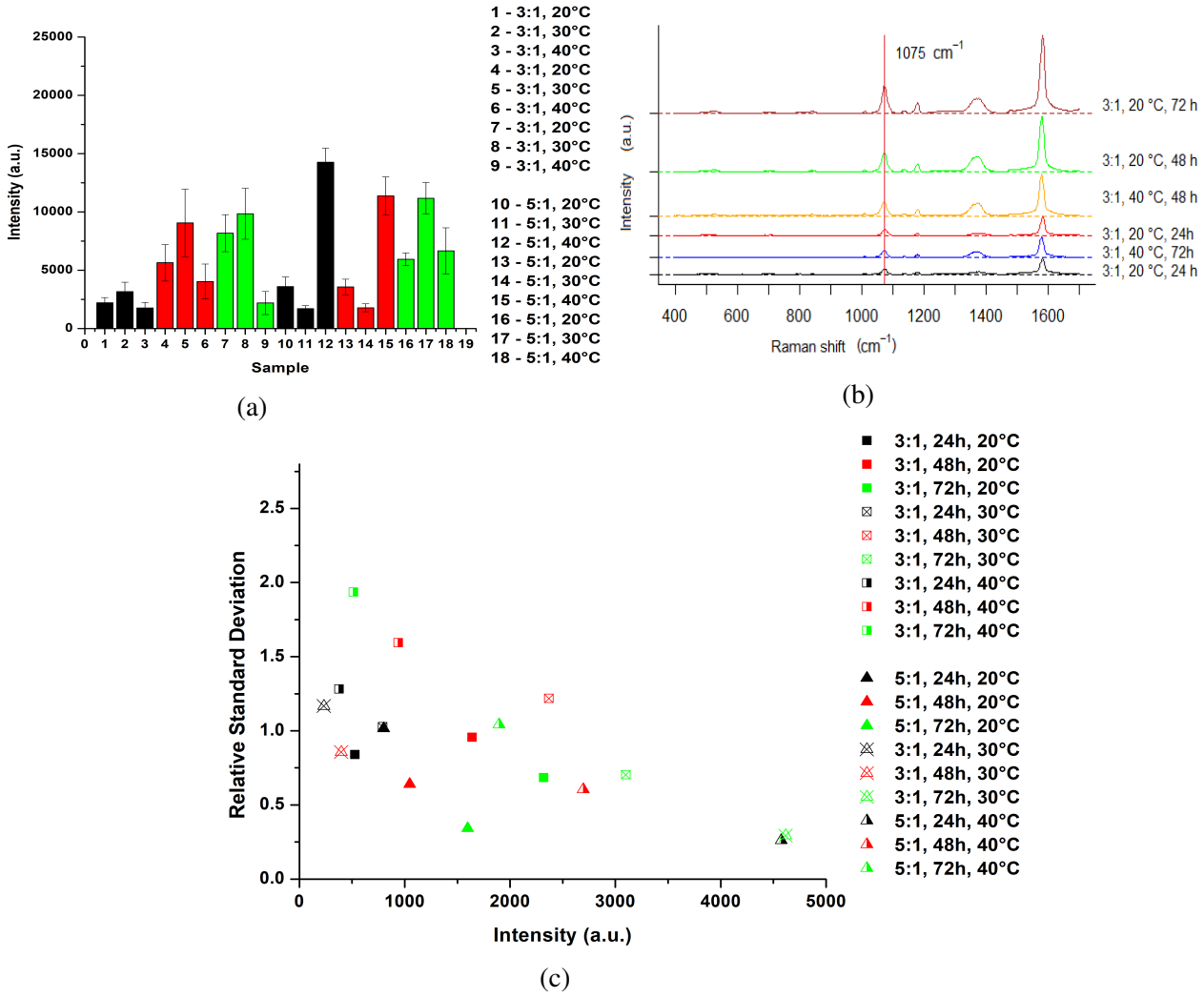

Fig. 6.16 Figure (a): Average intensities of the SERS substrates synthesised for different incubation temperatures of the PDMS membranes. Figure (b): as it can be seen, the peak at 1075 cm^{-1} is present. The enhancement changes depending on the substrate and on the enhancement is produces. Figure (c): RSD vs. average intensity of the SERS substrates synthesised for different incubation temperature.

Raman efficiency and uniformity

Results of Raman analysis is now discussed. All the average Raman intensities are collected in the histogram of Figure 6.16a, while SERS spectra of 3:1 samples are shown in Figure 6.16b. The highest Raman intensities are obtained by samples with 5:1 monomer-to-curing agent ratio. The graph in Figure 6.16c also shows that 5:1 substrates (triangular points) provide not only higher Raman signal intensities, but generally also smaller RSD, with respect to the 3:1 ones. The higher intra-sample repeatability of Raman measures can be associated

to the higher homogeneity of the nanostructures, built using the 5:1 PDMS membranes, in comparison to those based on the 3:1 ratio.

Referring to Figure 6.16c, two different trends are noticed for 3:1 and 5:1 samples. The former ones have increasing Raman intensities going from incubation temperature of 20 $°C$ to 30 $°C$, but low values for the 40 $°C$ case. In addition to this, samples incubated at 20 $°C$ and 30 $°C$ are also more uniform, if compared to the ones whose synthesis was performed at the temperature of 40$°C$. These results agree with the results obtained in the optical and morphological analysis. It is also interesting to notice that, an increase of the enhancement is obtained when a higher incubation time is chosen, at least for the incubation at 20 $°C$ and 30 $°C$. On the other side, samples incubated at 40 $°C$ have better Raman efficiency in the case of 5:1 samples, along with better intra-sample repeatability. This is true only for 5:1 samples incubated for *24 h* and *48 h*, but not for those incubated at *72 h*, which instead exhibit the highest efficiency when incubated at the temperature of 30 $°C$.

In conclusion, the best samples are the ones with a 5:1, incubated at 40 $°$, with incubation times of 24h and 48h respectively.

6.3.3 Cross-linking degree of PDMS membranes

Optical and morphology analysis

The effect of different cross-linking degrees was then evaluated by fixing the temperature at *30 °C*. This temperature was chosen since it revealed being the best for the synthesis of the 3:1 samples. Figure 6.17 shows the UV-Vis transmittance spectra and the FESEM images of samples divided by cross-linking degree. Again, 3:1 samples are characterised by spectra with lower transmittances. Also in this case, this phenomenon is confirmed by a higher coverage index for these samples compared to the 5:1 ones. This is actually easy to be visualized from the FESEM images and it is supported by the results of their analysis. In addition to this, 3:1 samples are characterised by flatter spectra, again reconfirming that this latter property is related to a bigger size variation of the silver nanoparticles, also keeping in mind that this result is also given by a better coupling between NPs. Finally, like in the previous cases, samples with smaller monomer-to-curing ratio also show a dip with a minimum, which is more blue-shifted with respect to the excitation wavelength. In fact, also for this experiment, the image analysis confirmed that the 3:1 sample have bigger nanoparticles. This can be visualized more easily in Figure 6.18b.

Differences between partially and totally cross-linked SERS substrates were found as well. Partially cross-linked substrates (black curves of Figures 6.17a and 6.17b) have lower values of transmittance, when compared to the corresponding substrates built on totally cross-linked PDMS membranes (red curves). This behaviour is again related to the fact that partially cross-linked substrates are more covered by Ag-NPs. In fact, it can be inferred that partially cross-linked PDMS membranes allow a higher production of silver during the reaction of the formation of the nanoparticles, at equal incubation time. Indeed, silver nitrate in the solution

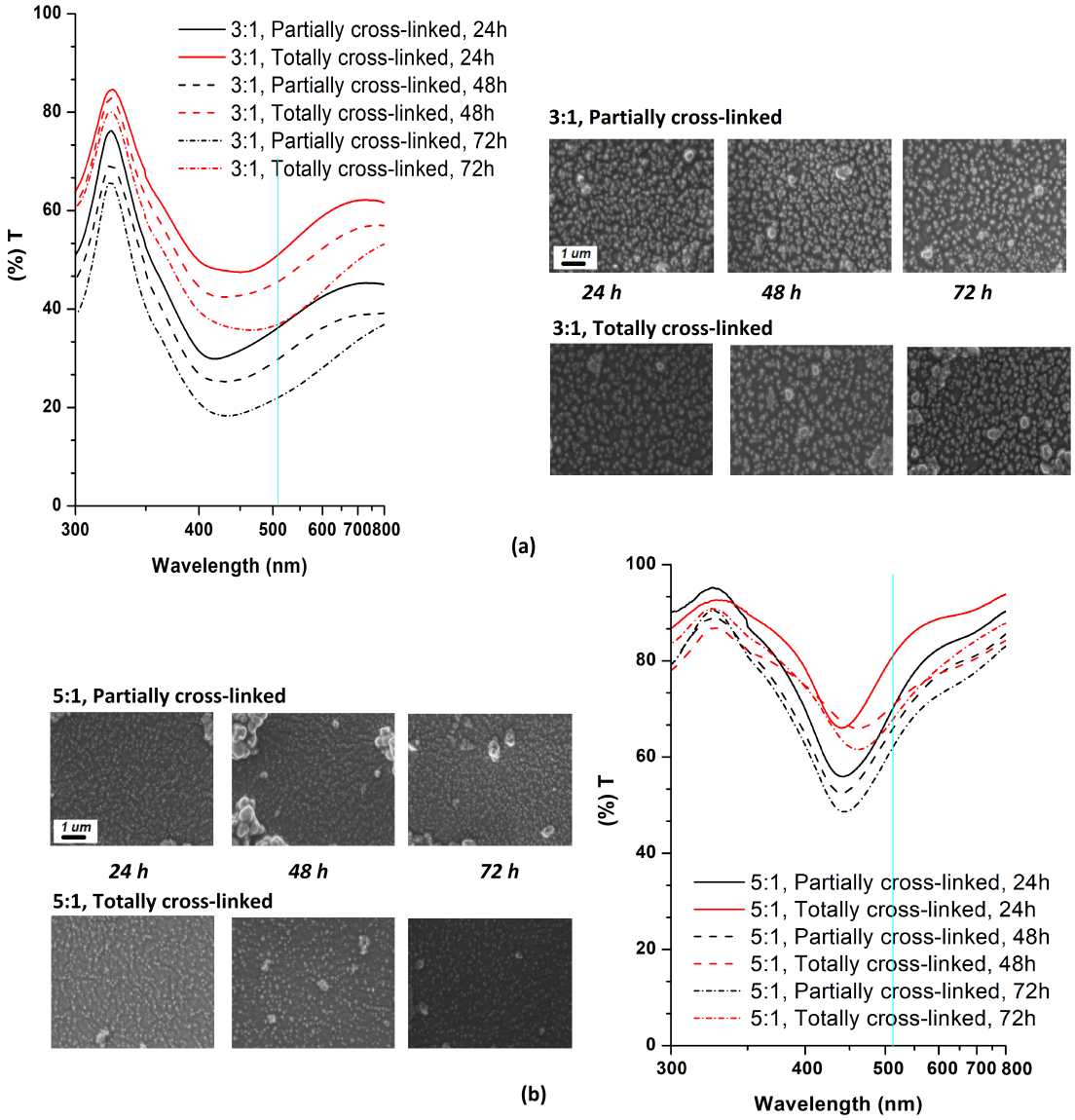

Fig. 6.17 UV-Vis measurements in air and FESEM images for *3:1, 1 mm, 30 °C* (a) and *5:1, 1 mm, 30 °C* (b) at different PDMS cross-linking degree. FESEM images were taken with a magnification of 50*kx*.

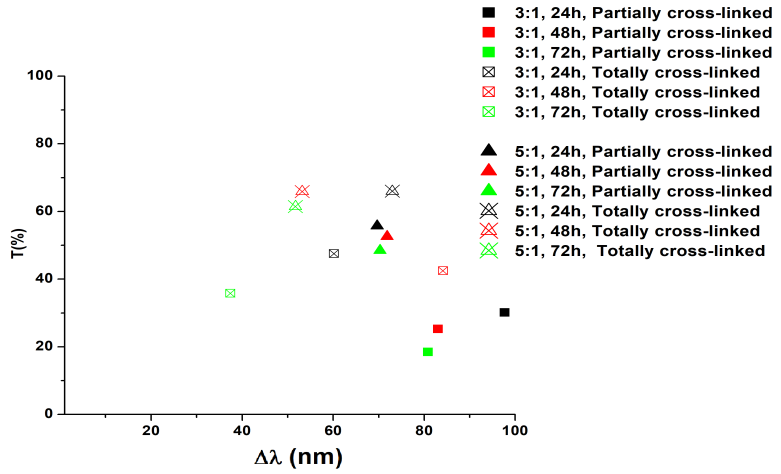

(a)

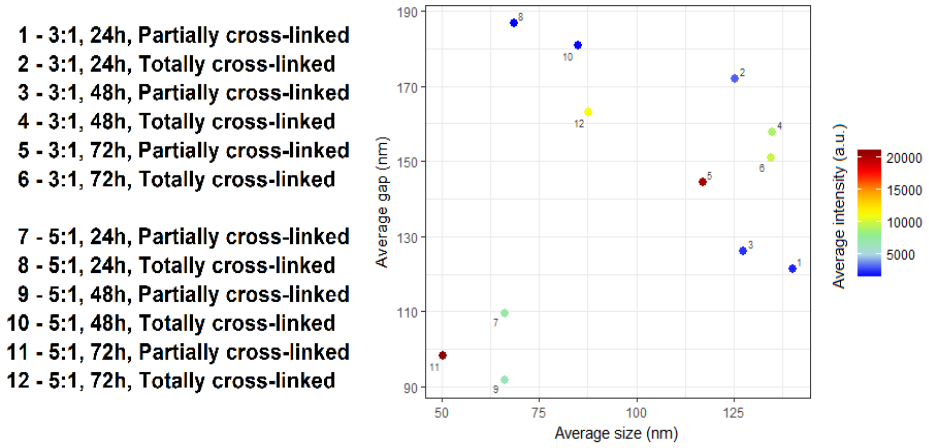

(b)

Fig. 6.18 Figure (a): dip transmittance vs. $\Delta\lambda$ for samples with different cross-linking degree. Figure (b): each point represents a sample: the colour represents the Average intensity in arbitrary unit, while in the y- and x-axis, the average size of the Ag-NPs and their average inter-gap distance are used respectively.

reacts with the curing agent of the PDMS membranes resulting in metallic silver. A partial cross-linking means also a higher amount of non-reacted curing-agent in the PDMS, which will be free react with silver nitrate, when immersed in the incubation solution.

However, the partially cross-linked substrates also show a longer distance of the dip wavelength from the 514.5 *nm* line. This behaviour is easily highlighted in the graph of Figure 6.18a, which shows the dip transmittance vs. the $\Delta\lambda$. Figure 6.18b shows the average gap vs. the average size of the NPs of the samples. The following fact is observed: partially cross-

linked substrates have, on average, Ag-NPs with smaller gaps, both for 3:1 and 5:1 PDMS membrane. This behaviour could be correlated to the increased presence of curing-agent of these membranes, which makes the particles nearer to each other due to an increased number of nucleation sites. It's also interesting to notice that a better tuning seems to be obtained for a ratio between size and gap of around 0.5 (this same behaviour was also encountered in the previous experiments). However, this result seems opposite to the theoretical knowledge concerning the SERS effect, which would attribute bigger enhancements in the case of smaller gaps (usually gaps smaller than the radius of the NPs). To explain this inconsistency, it must be kept in mind that the algorithms used for the image analysis are not completely accurate and optimized for these SERS substrates. In fact, both the tools have some limitations in the identification of the particles agglomerated into clusters. This translates in a low accuracy of the measured average gap, especially in the case of substrates with numerous and big clusters. Indeed, since the algorithms are not always capable to identify sensitively the particles in the clusters, the smaller gaps between the particles in the same cluster are not taken into account. As a result, the inter-particle gaps are bigger than reality.

Raman efficiency and uniformity

From the optical and morphological analysis of the sample it appears easy to expect better Raman signals from totally cross-linked substrates, since more tuned with the excitation of the source. Actually, this behaviour is encountered in the 3:1 samples, with 24h and 48h incubation time (see Figure 6.19a). On the other side, opposite trend is discovered for all the other samples. However, it must be underlined that all the samples are still with a dip wavelength far from the source wavelength, making them weakly resonant. If this trend remains unjustified for the 3:1 samples, it can be explained for 5:1 samples, looking at the graph of Figure 6.18b: it can be noticed that partially crossed linked substrates have slightly smaller Ag-NPs, but this along with much smaller gaps, that could make increase the density of hot-spots per area.

Finally, the samples showing the highest Raman efficiencies are the partially cross-linked substrates, incubated for 72h, both for 3:1 and 5:1 PDMS substrates. Nevertheless, despite these samples show the highest Raman signals, it is clear looking at Figure 6.19a that they also show high variability. For this reason, it was chosen to continue to use totally cross-linked PDMS membranes for the fabrication of the SERS substrates, since these show smaller variability, in spite of the lower Raman efficiency.

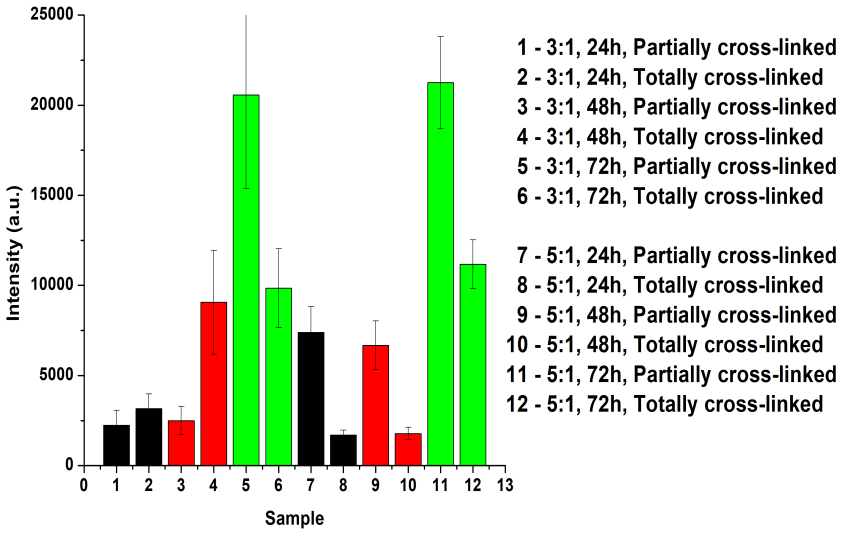

(a)

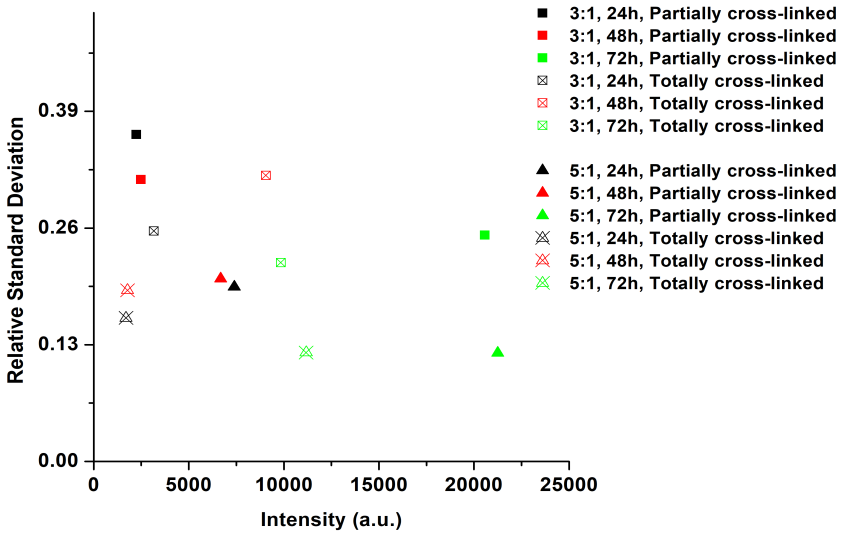

(b)

Fig. 6.19 Figure (a): Average intensities of the SERS substrates synthesised for different cross-linking degrees of the PDMS membranes. Figure (b): RSD vs. average intensity of the SERS substrates synthesised for different cross-linking degree.

6.3.4 Concentration of ethanol in the incubation solution

Optical and morphology analysis

In the previous experiments it was always used an aqueous solution of $AgNO_3$, but no other solvent apart from water, was tested before. For this reason, it was chosen to test the influence of different percentage of ethanol in the incubation solution, in order to understand how it acts on the growth of the Ag-NPs. As in the previous cases, an optical and morphological

analysis was performed on the obtained samples. Transmittance spectra of all the sample are collected in Appendix A.5. Differences are found when comparing substrates immersed in solution without ethanol and the ones immersed in a solution with various percentage of ethanol. Focusing on 5:1 substrates, it can be seen that samples incubated without ethanol are less transparent to light. Looking at the FESEM images of the 5:1 samples (see Appendix A.5) it is clearly visible that substrates incubated with ethanol in the silver nitrate solution have lower coverage. In fact, the ones incubated with 0% of ethanol in the solution, have also bigger Ag-NPs sizes and smaller gaps (see image 6.20a: samples labelled by the numbers 13, 21 and 17 are located more to the right part of the graph if compared to the other 5:1 samples).

In addition to this, also in this case the results confirm what already found for the previous experiments when comparing 3:1 and 5:1 samples. In fact, samples with a monomer-to-curing agent of 3:1 show lower transmittances, agreeing again with the higher coverage shown by these samples and confirmed through the image analysis. This behaviour is clearly noticeable in Figure 6.20b, where the dip transmittance is represented as a function of the $\Delta\lambda$: the 3:1 samples (square points) occupy the lower region of the graph, underling their lower transparency to the UV-Vis light. Again, 3:1 are also less tuned to the excitation source (see Figure 6.20b: 3:1 samples are more shifted, if compared to the 5:1 ones). This behaviour is again confirming that there is a strict relation that links the morphology of the substrate to its optical response. Indeed, looking at the graph of Figure 6.20a it can be noticed that 3:1 samples (samples from 1 to 12) exhibit bigger NPs, compared to the ones of the substrates with a ratio of 5:1 (samples labelled with numbers from 13 to 24). Finally, the 5:1 substrates feature a narrower dip. The image analysis was again carried out, showing also in this case a higher variance of the particles sizes of the 3:1 samples, finally linking this property to the steepness of the transmittance curve around the plasmonic dip.

From this optical analysis it is expected that best Raman signals would be obtained for samples incubated in a solution of silver nitrate with no ethanol, with better performances for the 5:1 samples.

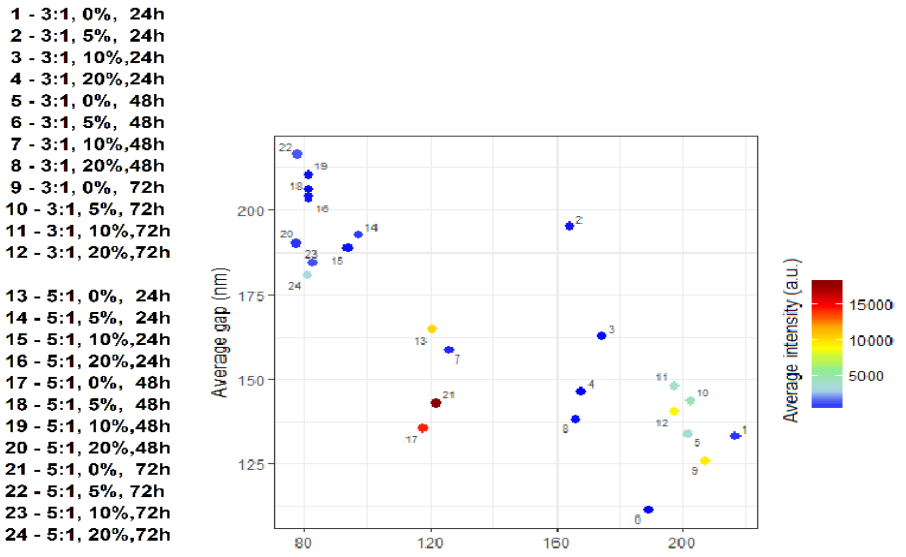

(a)

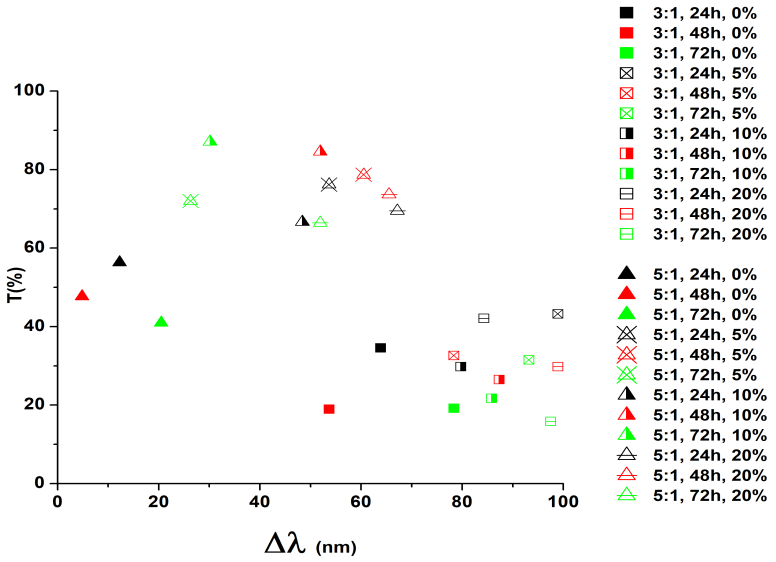

(b)

Fig. 6.20 Figure (a): each point represents a sample: the colour represents the Average intensity in arbitrary unit, while in the y- and x-axis, the average size of the Ag-NPs and their average inter-gap distance are used respectively. Figure (b): dip transmittance vs. $\Delta\lambda$ for samples with different percentage of ethanol in incubation solution.

Raman efficiency and uniformity

The results obtained by the Raman analysis confirmed what expected from the optical and morphological analysis of the samples. In fact, the substrates incubated in a solution of silver nitrate, with no ethanol, show better Raman signals, as it can be seen from the histogram in

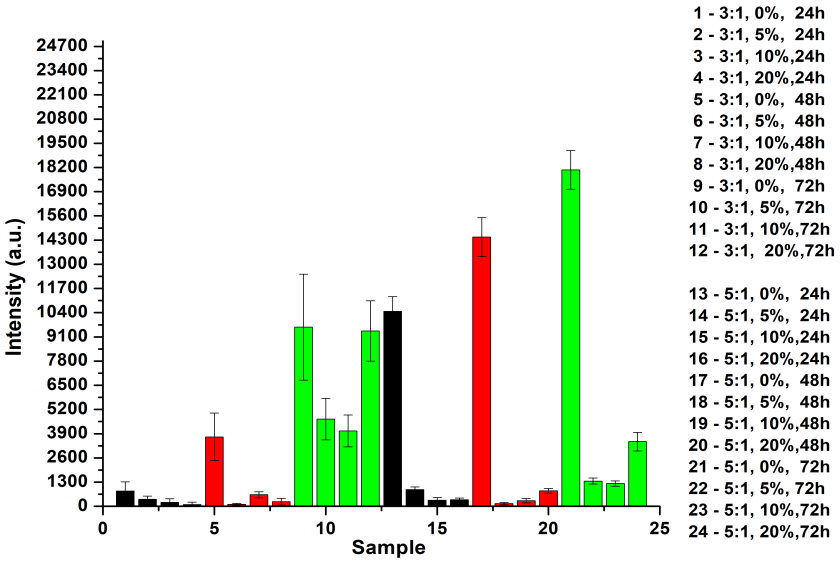

(a)

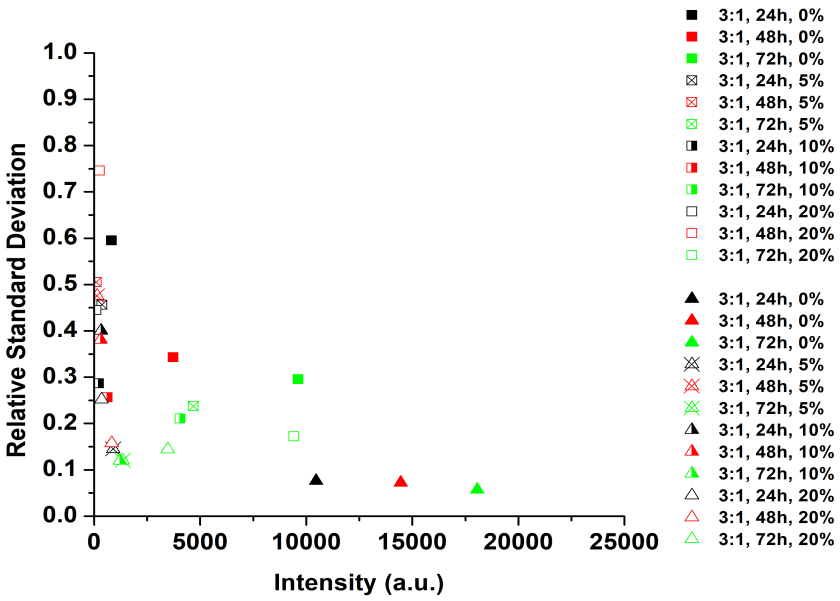

(b)

Fig. 6.21 Figure (a): Average intensities of the SERS substrates synthesised for different percentage of ethanol in the incubation solution. Figure (b): RSD vs. average intensity of the SERS substrates synthesised for different percentage of ethanol in the incubation solution.

Figure 6.21a, which collects the average SERS intensities for all the samples. In addition to this, the samples incubated without ethanol have also smaller RSDs, that make them also the samples with the higher intra-sample repeatability for this experiment (see Figure 6.21b).

Finally, an important property is to be underlined. Also in this case, the highest Raman signals have been observed for samples with certain dimension of the nanoparticles, coupled with specific inter-particle gaps. More precisely, also in this case it was found out that the best behaviour is shown by those substrates with Ag-NPs with size of around $100\,nm$, and gap about $150\,nm$. A similar behaviour was found also in the previous experiments, so that it makes it probable that, in order to have high plasmonic resonances for the used excitation source, the size-gap ratio of 0.5 is required. Anyway, as already explained, the used image analysis tools defect in the evaluation of the gaps between the particles in the clusters, making this result less reliable.

In conclusion, the presence of the ethanol in the incubation solution worsen the properties of the SERS substrates.

6.3.5 Concentration of silver nitrate

Optical and morphology analysis

Finally, the concentration of silver nitrate in the incubation solution (with no ethanol) was varied to study its influence on the synthesis of the silver NPs. The UV-Vis transmittance spectra are shown in Figure 6.22. In this case, a difference from the previous results is found. Focusing on the spectra of the samples incubated in a solution with 10 *mM* of silver nitrate,

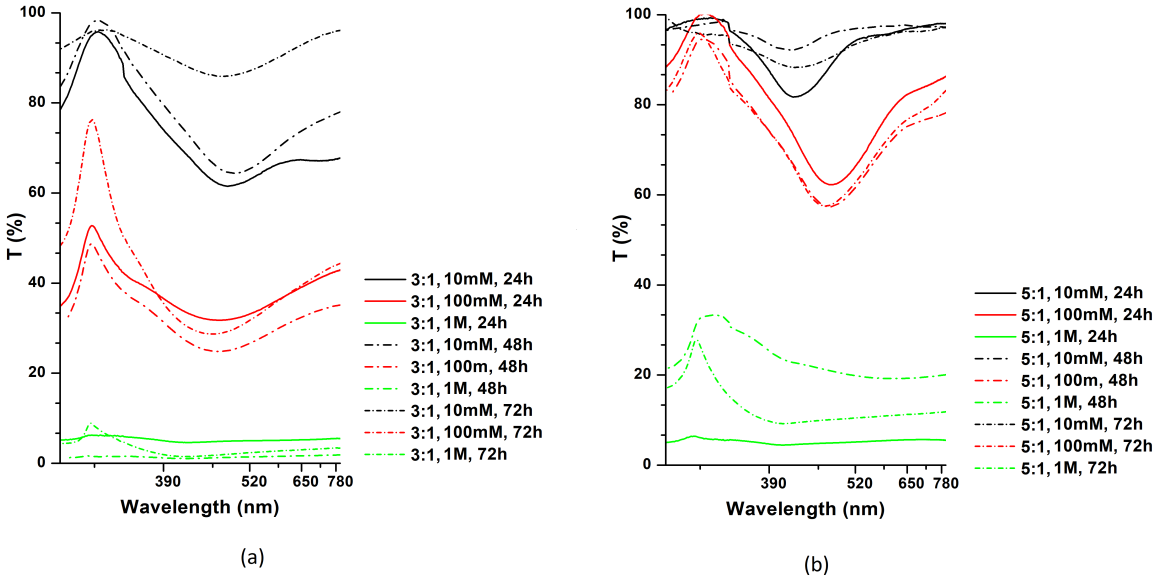

Fig. 6.22 UV-Vis in Air for 3:1, 30°C, totally cross-linked (a), UV-Vis in Air for 5:1, 30°C, totally cross-linked (b).

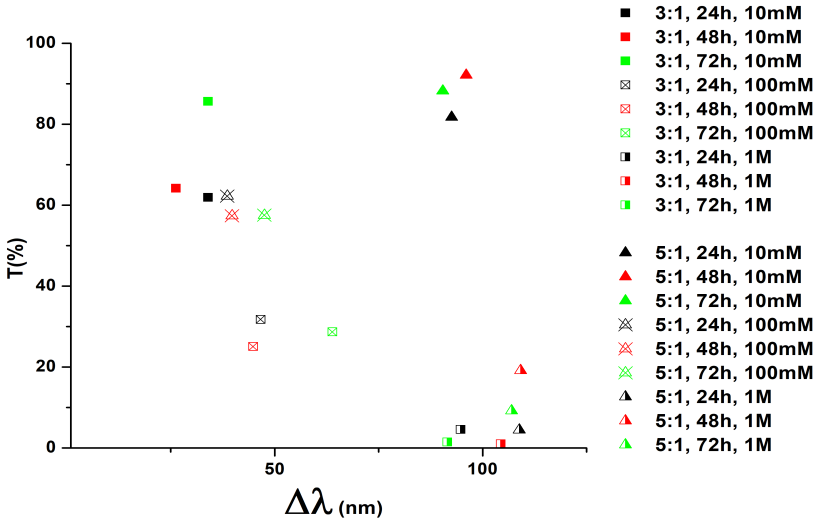

Fig. 6.23 Dip transmittance vs. $\Delta\lambda$ for samples with different concentrations of precursor.

an anomalous behaviour with respect to the previous cases is obtained. In fact, if in the previous experiments it was always found that 5:1 samples are more tuned with the 514.5 *nm* wavelength, the same can't be stated for this case. In fact, looking at the FESEM images (see Appendix A.6) it can be noticed that 5:1 samples have very small particles, while 3:1 substrates present Ag-NPs with a dimension comparable to the required one. In fact, the lower concentration of silver nitrate in the solution gives origin to smaller nanoparticles, but in the case of 5:1 samples, these are too small (i.e., causing the tuning out of the nanostructure), whereas those of the 3:1 samples are comparable to the 5:1 samples of other experiments with a concentration of $AgNO_3$ of *100 mM*.

Nevertheless, PDMS membranes immersed in a 1 *mM* silver nitrate solution show very high transmittances, which make them unsuitable for the SERS application. On the contrary, samples immersed in a 1 *M* silver nitrate solution show a $\Delta\lambda$ which is too high to result useful for plasmonic applications. In conclusion, further analysis is unnecessary, making the samples immersed in 100 *mM* the best suited for the SERS activity.

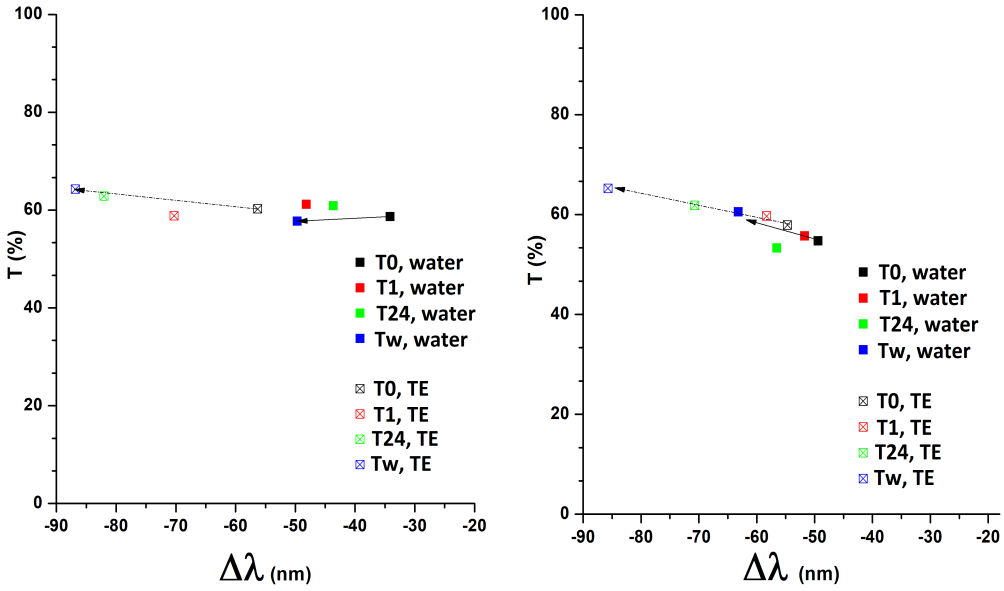

(a) (b)

Fig. 6.24 Graph of the dip transmittance vs. relative $\Delta\lambda$ for different samples and solutions (water and TE): (a) *3:1, 0.5 mm, 20 °C, 72 h*, (b) *3:1, 1 mm, 40 °C, 24 h*

6.3.6 Stability tests

To study the stability, the samples were incubated in TE-NaCl solution and measured at the beginning of the test (T0) and after *1 h* (T1), *24 h* (T24) and *1 week* (Tw). The appendices collect the UV-Vis spectra of all the produced samples.

It was also chosen to plot the dip transmittance vs. $\Delta\lambda$ to have a fast way to study the stability. In this case the $\Delta\lambda$ is represented with its sign, in order to show the direction of the shift with respect to the source wavelength: when its value is negative, a blue-shift is registered, when positive, a red-shift is registered instead. As an example, in Figure 6.24 the graphs are shown for two samples: the first (a) with NPs synthesized at the conditions of *3:1, 0.5 mm, 20 °C, 72 h* incubation time, while the second (b) fabricated at the conditions *3:1, 1 mm, 40 °C, 24 h*.
The stability tests on the incubated samples showed that they generally exhibit a limited blue shift of the minimum of the dip after the incubation. This variation to lower wavelength could be explained by the detachment of some of the nanoparticles, which increases the inter-particle gap size. In particular, samples with 5:1 monomer-to-curing ratio membranes usually show smaller shifts when incubated in TE-NaCl solution (compared to the ones with 3:1 PDMS membranes), that makes them better candidates for the integration in the microfluidic chip.

6.3.7 Integration of the best Ag-coated PDMS substrate in all-PDMS optofluidic chip

In the previous sub-sections, the results obtained from the different samples fabricated for each experiment were separately analysed, to draw a special attention to the links between the variation of the synthesis parameters and the characteristics of the substrate. As final step, a comparison between all the incubated samples was carried out, and the chosen sample was selected for the application of the bioassay.

6.3.7.1 Comparison of results and choice of the best sample

During the fabrication of the samples, various synthesis parameters were changed. For this reason, in order to efficiently compare all the samples, it is important to choose: i) a method for the comparison of all the sample (for example, which parameters to fix and which to use to group the samples for the comparison), ii) which are the characteristics of the nanostructures that are required for SERS applications. As already said, a good SERS substrate must show

high sensitivity (i.e., high enhancement) and uniformity within the same sample and different replicates, so high reproducibility and of course high stability. For what concerns point i), it was chosen to divide all the samples by their incubation temperature and their cross-linking degree (partial or total).
For sake of completeness, it was chosen to fabricate some replicates of some particular conditions. In fact, in some cases only single samples were available, thus making impossible the evaluation of inter-sample reproducibility, necessary for the comparison.
Finally, to compare the samples it was chosen to follow the following steps: first of all, the samples with the highest Raman efficiency were chosen, with a particular attention to take only the ones with high reproducibility; secondly, their uniformity was taken into account and, as final step, the stability was checked, to be sure that the sample can be used for the bioassays.

Raman efficiency and reproducibility

The Raman efficiency of the samples is analysed as first step. Results of all the other comparisons are shown in the Appendix B, where the results have been subdivided by incubation temperature. Some of the conditions for the synthesis were fixed for all the samples that are compared: the thickness of the PDMS membranes is fixed at the value of $1\,mm$ and the concentration of silver nitrate in the incubation solution (with 0% of ethanol) is chosen of $100\,mM$. These decisions are based on the experiments that were carried out – and previously analysed – that showed that these conditions are the ones that give better performances.

Figure 6.25 contains all the histograms, subdivided by incubation temperature and cross-linking degree, showing the Raman average intensities of all the samples. Columns with same colour correspond to samples produced under the same conditions, but fabricated for different experiments. This means that, in order to have a high inter-samples repeatability (i.e., reproducibility of the sample), same-colour columns should show similar values of the average intensity.

By looking at Figure 6.25, it can be noticed that the highest efficiencies are obtained for samples incubated at $30\,^{\circ}C$, both totally and partially cross-linked. In particular, the highest intensities have been obtained for the samples at $30\,^{\circ}C$ at $72\,h$ incubation time. However, in spite of these high Raman signals, the samples incubated at the temperature of $30\,^{\circ}C$ also show very low reproducibility. As it can be seen, all the samples fabricated under the same conditions of synthesis (same colour columns of Figures 6.25b and 6.25.d) show very different values of intensity if compared on to each other.
On the other hand, substrates prepared at $40^{\circ}C$, with $24\,h$ and $48\,h$ incubation time show

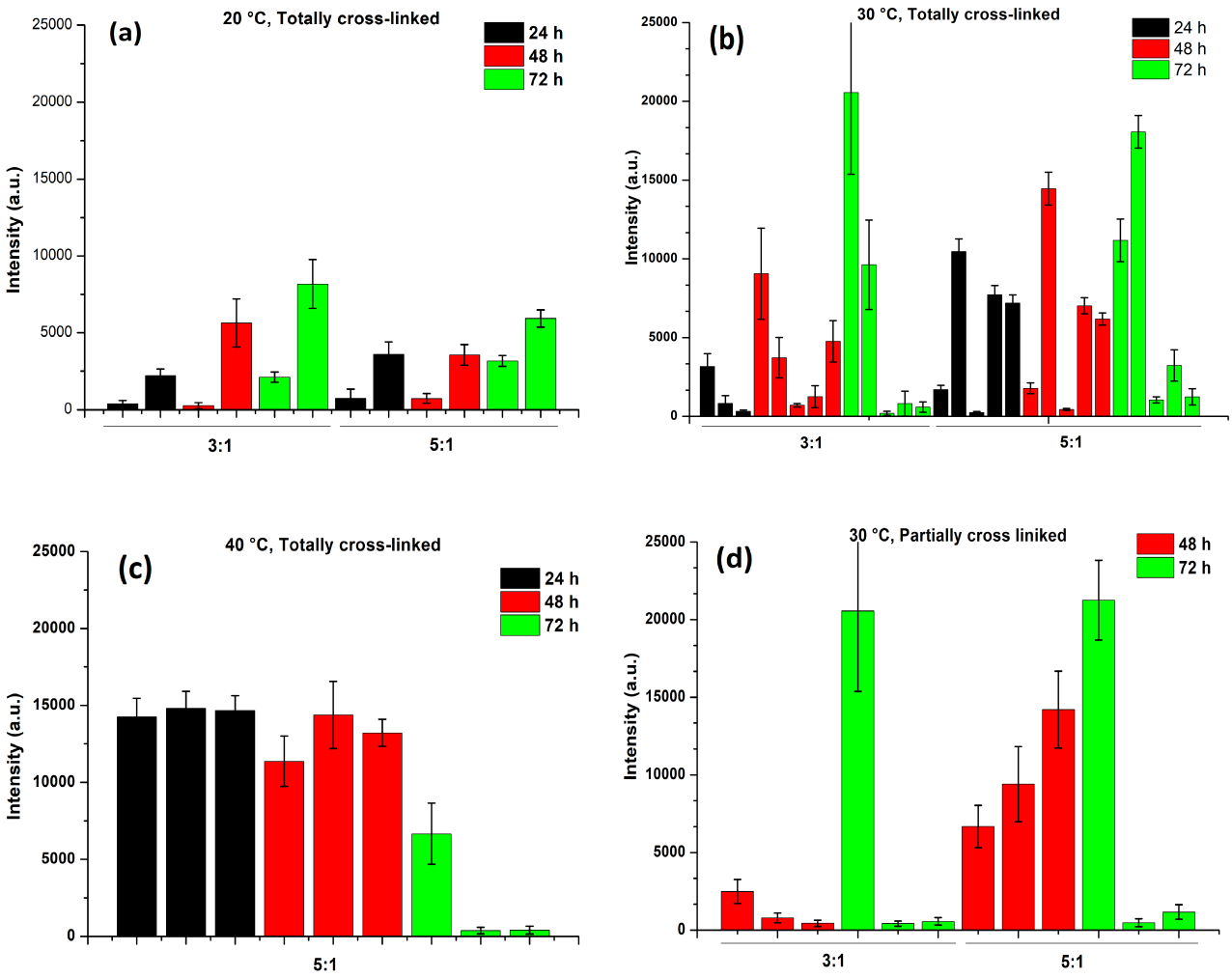

Fig. 6.25 Raman intensities for samples totally cross-linked at incubation temperature of *20 °C* (a), *30 °C* (b) and *40 °C* (c) and for partially cross-linked at incubation temperature of *30 °C* (d).

good Raman intensities too, but differently from the samples synthesized at *30 °C*, they also have high inter-sample repeatability. In addition to this, the performances are almost equal for both incubation times at 40°*C*, so that the sample which is fabricated at lower incubation time is the one which best meets the requirements. Therefore, the most efficient synthesis conditions are: 5:1, *1 mm*, *40 °C*, totally cross-linked and *24 h* incubation time.

Raman uniformity

As already said, the sample chosen from the previous step (5:1, *1 mm*, *40 °C*, totally cross-linked and *24 h* incubation time) shows good Raman efficiency and high inter-sample

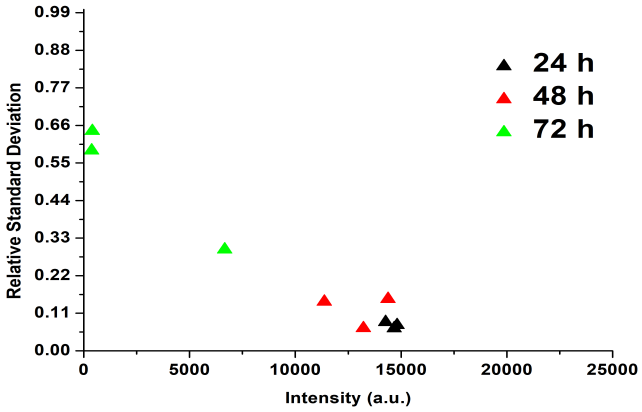

Fig. 6.26 Relative standard deviation vs. Raman intensities, for samples with 5:1 monomer-to curing agent ratio, at incubation temperature of *40 °C*, totally cross-linked.

repeatability. To have a complete picture of the properties of the chosen sample, also the RSD must be studied. Figure 6.26 gives information about the RSD of the sample incubated at 40 °*C*. As it can be seen, the 5:1 samples incubated for *24 h* (black triangles) not only show high intensities, but also the lowest RSD (6.6 %), that remains almost equal for all the replicates. This result highlights the good uniformity of all the synthesised samples under the chosen conditions.

Stability in solution

The pivotal check on the chosen sample (5:1, *1 mm*, *40 °C*, totally cross-linked and *24 h* incubation time) is represented by the study of the stability of the substrate after the incubation in water and TE-NaCl buffer solution. Figures 6.27a and 6.27b show the UV-Vis transmittance spectra for the chosen sample, respectively in water and TE. Figure 6.27c shows the dip transmittance vs. $\Delta\lambda$, with the sign that indicates the direction of the shift. As usual, a limited blue shift of the wavelength of the dip to lower values, along with a weak increase of the transmittance is recorded.

A further check on the stability was performed by comparing the average intensity of the Raman signals of MBA, before and after the incubation in TE-NaCl solution for *24 h* (T24) and *1 week* (Tw). The results are shown in Figure 6.28. It can be noticed that, after the incubation the intensity decreases, almost halving its value, after *24 h*, with another mild decrease after *1 week* in TE-NaCl solution. In addition to this, also a small increase of the RSD is registered (*0.16*) after *24 h*. After *1 week* the RSD decreases with respect to the sample incubated for *24 h*, but it still remains higher than the sample not incubated.

In Figure 6.29 the FESEM images of the substrate are shown, before (a-b) and after the incubation in TE-NaCl solution for *1 week* (c-d). As it can be seen, the NPs after the week

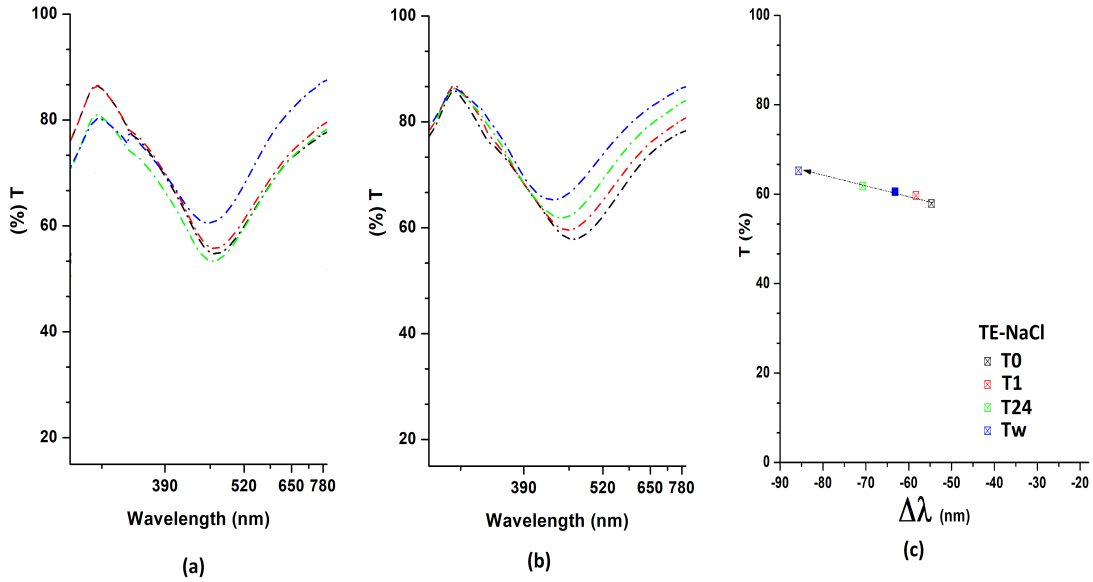

Fig. 6.27 UV-Vis measurements after the incubation in water (a) and TE-NaCl buffer (b) for synthesis conditions of 5:1, *1 mm*, totally cross-linked, *24 h* incubation time. (c) Graph of the dip transmittance vs relative $\Delta\lambda$.

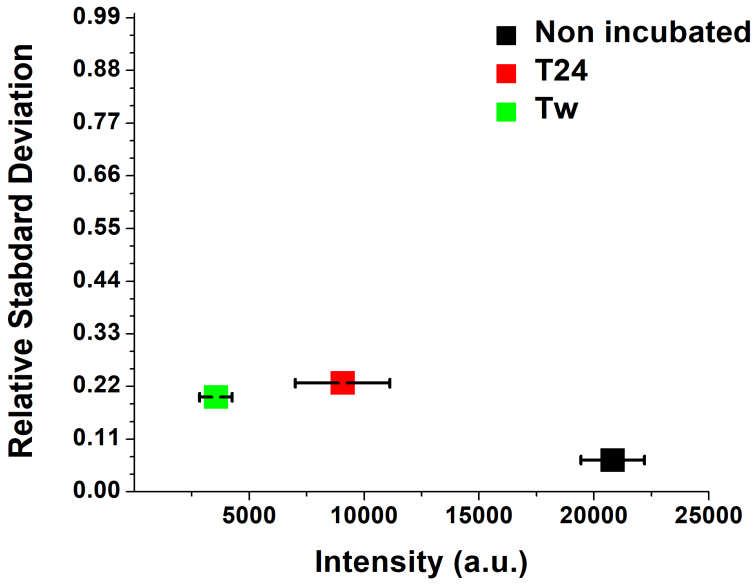

Fig. 6.28 Relative Standard Deviation vs. average intensity of MBA measurements before (black point) and after the incubation in TE-NaCl buffer for *24 h* (red point) and for *1 week* (green point) (bars are the SD of the intensities). The sample was synthesised in the following conditions: 5:1, *1 mm*, totally cross-linked, *24 h* incubation time.

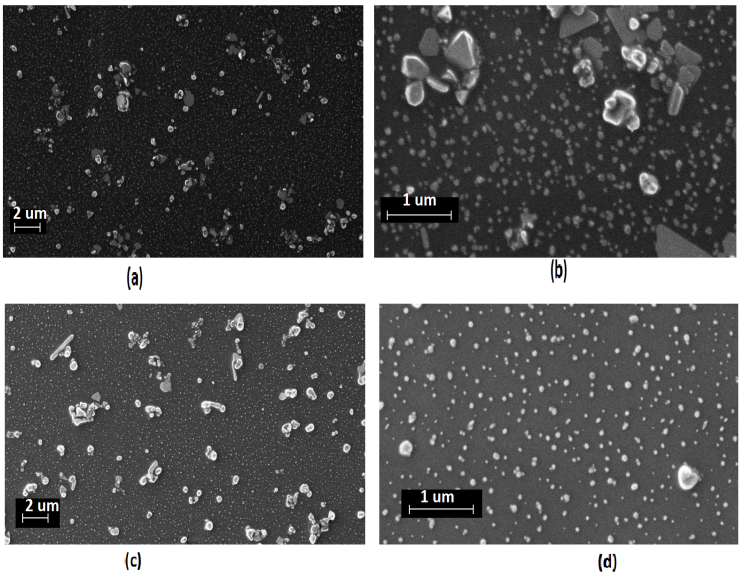

Fig. 6.29 FESEM images of the best sample (5:1, 1 mm, totally cross-linked, 24 h incubation time) before (a-b) and after (c-d) the incubation in TE-NaCl buffer for *1 week*. The images are taken with *10 kx* magnification (a,c) and *50 kx* magnification (b,d)

in TE-NaCl solution are sparser and smaller. In addition to this, also the clusters have a different morphology: indeed, they revealed less sharp Ag-NPs, that are also bigger and fewer per cluster. This last phenomenon can be attributed to the fact that, the Ag that is removed from the Ag-NPs because of the action of the TE-NaCl buffer, agglomerate with the previously-formed clusters, which work as nucleation points. These results justify the blue-shift of the dip wavelength and the increase of the dip transmittance (due to the decrease of the Ag-NPs size and to the increase of the inter-particle gap). Moreover, the decease of the Raman efficiency agrees with the decrease of the gap-size, which leads also to a lower hot-spots density.

6.3.8 Conclusions

In conclusion, the different synthesis parameters in the case of a static incubation synthesis of Ag-NPs on PDMS substrates were analysed. All the variations in the optical response, as well as the morphology and the Raman behaviour were registered and linked to the variation of the synthesis parameter. These substrates generally reported higher intensities of the Raman signals if compared to the samples with sputtered Ag-NPs. Along with this, also a good stability in solution was observed that makes these substrates good candidates for bioapplications. For this reason, a comparison of all the incubated samples was made, in order to select a sample for the application of the bioassay. After the comparison, it

was found that the best sample (i.e., with high SERS enhancement, high intra- and inter-sample reproducibility and good stability in solution) is the one with the following synthesis conditions: 5:1, *1 mm*, *40 °C*, totally cross-linked and *24 h* incubation time.

6.4 Bioassay for miRNA222 detection

This last section deals with the use of the PDMS-supported Ag-NPs SERS substrates in biosensing applications. To this aim, it was chosen to perform a bioassay for the detection of miRNA tumour biomarkers for all the different types of synthesized substrates: i) Ag-coated PDMS substrates, ii) APTES and MPTMS functionalised Ag-coated PDMS substrates and ii) Ag-coated silver nitrate incubated PDMS membranes. The synthesized substrates were tested in the bioassay for the detection of miRNA222, a tumour biomarker connected to various neoplastic diseases, such as renal and pancreatic cancer [151].
The metal-dielectric nanostructures were first functionalised, using a protocol already optimized for PDMS-supported silver-coated porous silicon membranes [134]. The immobilization of a DNA probe, used to capture the specific miRNA target, was performed on the Ag-NPs that coat the substrates. A labelled miRNA-R6G was employed. First of all, (5×5) *mm* pieces are taken out from the best samples for each type of synthesis (sputtered PDMS, functionalised PDMS and incubated PDMS). These pieces are then prepared using the protocol for the bioassay, in the view of performing the SERS analysis. Moreover, an Enzyme-Linked ImmunoSorbent Assay (ELISA) was eventually used for a cross-check analysis. In a successive phase, the sample, which showed the best results from the previous bioassay, was integrated in a multi-chamber microfluidic chip. Finally, the SERS analysis was tested also in the chip. Results of the bioassays are shown in the following.

6.4.1 Immobilization of the probe on PDMS-supported Ag-NPs

Figure 6.30 shows the steps that were followed both for the miRNA222 detection by means of SERS (from (a) to (c)) and through ELISA (from (a) to (e)). The miRNA222 undergoes a hybridization with the DNA probe, modified at the 5' end with a C6 alkyl-thiol group and immobilized on the surface of the substrates (Figure 6.30.(b)) [134], to trigger the target to the SERS-active nanostructured substrate. Unfortunately, other interactions between the miRNA oligonucleotides and the Ag-NPs substrates can occur in cases that don't correspond to a recognition event with the probe [50], like for example due to electrostatic interactions. For this reason, following previous works of Novara et al. [94, 134], a preliminary surface blocking was performed on the SERS substrates (see Figure 6.30.(a)) to reduce this phenomenon, known as nonspecific binding.
Here, a focus on the pre-treatment of the substrate (to reduce the nonspecific binding) and on the immobilization of the probe is reported.

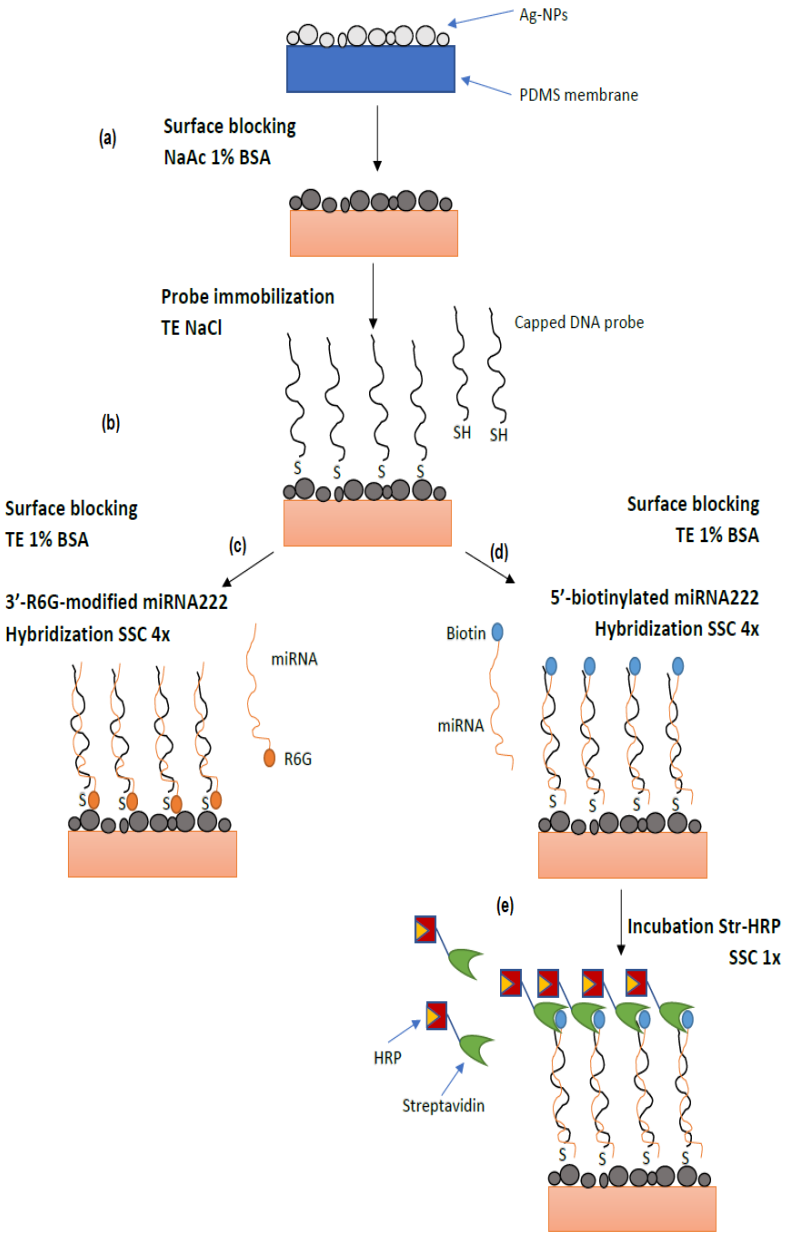

Fig. 6.30 Scheme of the functionalisation protocol. First of all, the PDMS substrates are passivated with BSA (a). The overnight immobilization of the DNA probe in TE-NaCl buffer is performed (b). Incubation of the 3'-R6G-modified miRNA222 target for one hour in SSC 4x, for the hybridization for SERS assay (c). Incubation of the 5'-biotinylated miRNA222 target for one hour in SSC 4x, for the hybridization for ELISA (d). Final incubation with Str-HRP in SCC 1x before the development of the colorimetric ELISA (e).

6.4.1.1 Surface blocking and probe immobilization

As already explained a pretreatment of the SERS substrates is necessary before the probe immobilization step, to reduce the effects of the nonspecific binding. Binding of the target to the Ag-NPs, due to other interactions different from the probe-target trigger event, can lead to false positive results. A high nonspecific binding causes the increase of the limit of detection (LOD), defined as the minimum value below which no relevant interaction between the target and the probe can be considered. This is the reason why a negative control was performed for all the following bioassays. This corresponds to the incubation of the target on a substrate with no immobilized probe, in order to allow the quantification of the nonspecific binding on that particular substrate.
For the synthesised SERS substrates, an optimized protocol was used, following the results found by previous researches (see for example [50, 94, 134]). A passivation pre-treatment was performed through the application of Bovine Serum Albumin (BSA), already largely used as blocking reagent for various immunoassays [152]. Previous works of Novara et al. [94, 134] on silver nanostructures on porous silicon substrates have shown the efficacy of passivation by means of BSA, leading to a reduction of the nonspecific signal. Following the obtained results, BSA in sodium acetate (NaAc) at *pH 4.0* was used, in order to maximize the adsorption on the substrate surface (Figure 6.30.(a)).

Immobilization of the DNA-probe on the Ag-NPs is ensured by the sulphur-silver bond. For this reason, following previous works, the reduction of the alkylthiol-capped DNA probe was performed in DTT solution, to maximize the probability of having free -SH groups. A desalting process was finally performed on the solution to separate the probe from the DTT molecules, by means of size exclusion microcolumns. Finally, probe immobilization was performed using a TE NaCl buffer (see Figure 6.30.(b)).

6.4.2 miRNA222 detection

In this section the results obtained from the bioassays are presented and discussed.
The scheme of the functionalisation protocol for miRNA222 detection is shown in Figure 6.30, both for the ELISA assay and the SERS assay. As first approach a labelled-miRNA222-R6G assay (see Figure. 6.30c) is used. For this purpose, the miRNA222 is modified at the 3' end with a R6G molecule. This is required since through the SERS analysis it is not possible to sense the interaction between the unlabelled miRNA and the probe. In fact, the R6G works as a "label": when the miRNA222 interacts with the probe, the R6G gives high SERS signals thanks to the enhancement due to the SERS substrate, thus to have an indirect measure of

the specific interaction between the miRNA and the probe. In addition to this, the choice of modifying the miRNA222 at the 3' end is justified by the position of the probe on the SERS substrate. In fact, when the miRNA binds to the probe immobilized on the substrate, the miRNA 3' end is the one that is nearer to the SERS substrate. This ensures a higher proximity of the R6G molecule to the Ag-NPs, increasing the probability of R6G to be in the vicinity of a hot-spot region and thus to have high SERS enhancement. Moreover, it must also be reminded that the EM enhancement rapidly decreases with the distance from the metal NPs surface, so that the farer the R6G molecule from the Ag-NPs, the smaller the SERS enhancement.
An ELISA assay is then performed to check the success of the protocol. The protocol for the application of the ELISA technique was optimized in previous studies on metal-dielectric nanostructures and applied also in this particular case for the fabricated metal-PDMS nanostructures [94]. Differently from the previous assay, a 5'-biotinylated miRNA222 is used as target (Figure 6.30.(d)). The substrate is then incubated in a solution of Streptavidin protein covalently conjugated to the Horse Radish Peroxidase enzyme (Str-HRP) (Figure 6.30.(e)). The Streptavidin binds to the biotin, whereas the HRP guarantees an enzyme activity that is exploited for the detection, with the use of an appropriate substrate system. A TMB substrate was used for the initiation of the colorimetric reaction, which is stopped after *3 min* by the addition of H_2SO_4. This explains why the biotin molecule is conjugated to the 5' end of the miRNA222: indeed, in this way the maximum exposure to the Str-HRP is guaranteed. The measured Optical Density (OD) gives information about the hybridization state of the miRNA222. In fact, with low nonspecific binding and with fine control over the time of the colorimetric reaction, the OD values will depend only on the number of miRNA222 bound to the DNA probe on the substrate.

6.4.2.1 Labelled miRNA222-R6G detection

First of all, the results obtained by SERS analysis are presented. The SERS spectra collected after miRNA222-R6G hybridization are shown in Figure 6.31. The spectra were derived for sputtered Ag-NPs on PDMS, for functionalised APTES and MPTMS Ag-coated PDMS and for the SERS substrate obtained by incubation. Each spectrum was obtained by averaging the SERS signal acquired at the different spots of the Raman map for each sample and for different miRNA222-R6G concentrations (*100 nM*, *10 nM* and *1 nM*), including also the control samples. The control spectra were obtained using two different conditions: in the first case no probe immobilization was actuated and *1* μM of labelled miRNA222-R6G was incubated (no probe/miRNA), in the second case the immobilization was performed, but no miRNA222 incubated (probe/no miRNA).

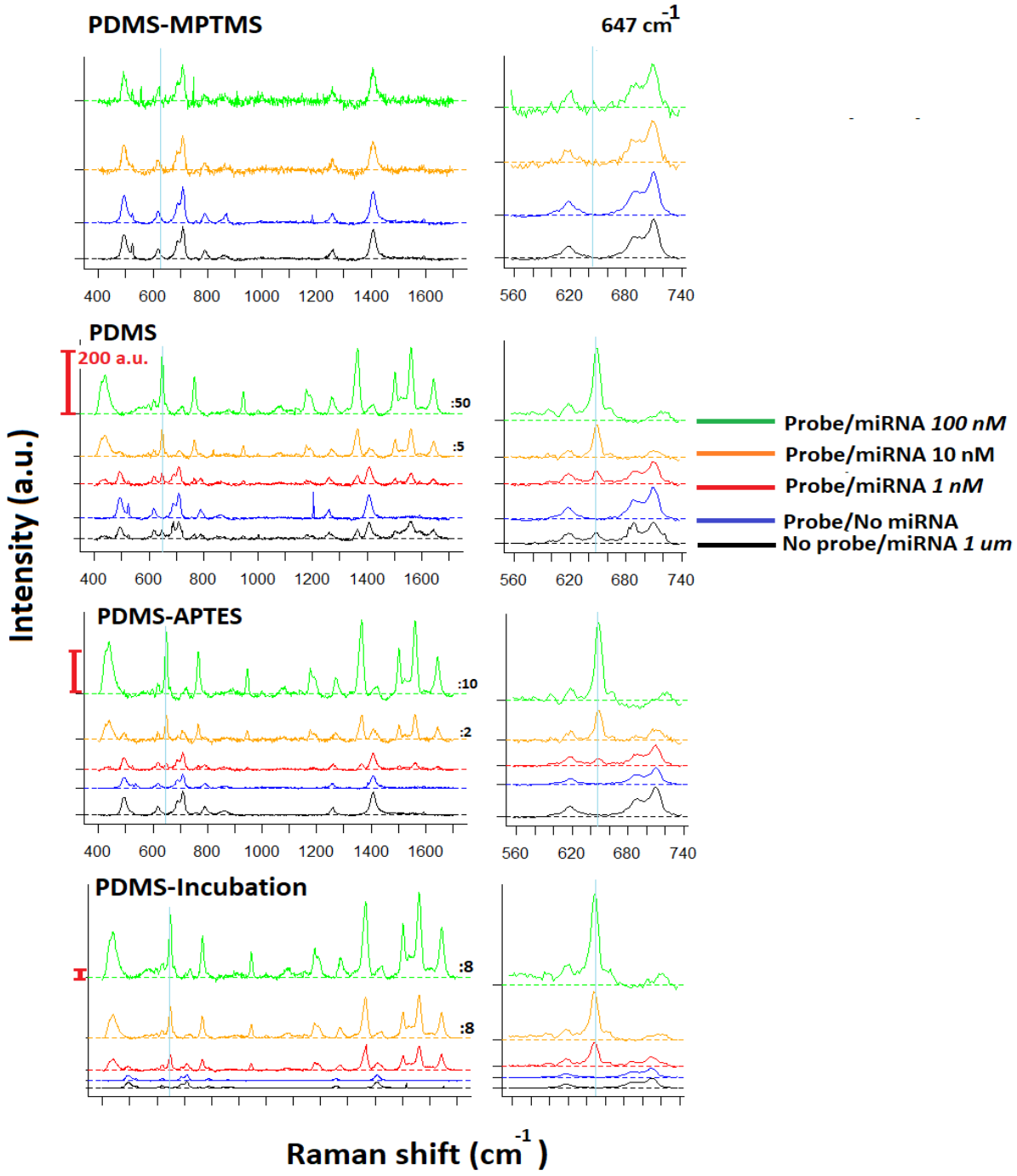

Fig. 6.31 SERS mean spectra of the labelled miRNA222-R6G, acquired on the functionalised MPTMS and APTES Ag-coated PDMS, Ag-coated PDMS and incubated Ag-coated PDMS. Smaller graphs show the miRNS222-R6G peak at 647 cm^{-1}. The black and blue curves represent the negative controls. The blue straight line highlights one of the main vibrational bands of miRNA22-R6G.

Firstly, the MPTMS sample is analysed. As it can be seen from Figure 6.31, the two controls show similar spectra one to each other, characterized by the typical vibrational bands of PDMS. In fact, control samples don't exhibit peaks of the miRNA222-R6G vibrational pattern, agreeing with the fact that for the so-called "negative control" samples, no miRNA molecules interact with the probe or with the nanostructures. This suggests that nonspecific interaction is not occurring and that BSA passivation actually works also for this substrate.

Despite this, miRNA222-R6G is weakly detected by this substrate, that shows a very weak spectrum that is mixed up with the background noise, also for the highest miRNA222-R6G concentration.

On the other side, the Ag-coated PDMS substrate (PDMS) exhibit a quite high nonspecific signal. As it can be seen looking at the Figure 6.31, the spectrum obtained for the no probe/miRNA case (black line) shows quite intense Raman bands related to the miRNA222-R6G, whose intensity is almost comparable to the one obtained in the case of the sample with the immobilized probe incubated with *1 nM* solution of target miRNA (red curve). This means that it is impossible to use this SERS substrate for miRNA222-R6G concentration lower than *1 nM*.

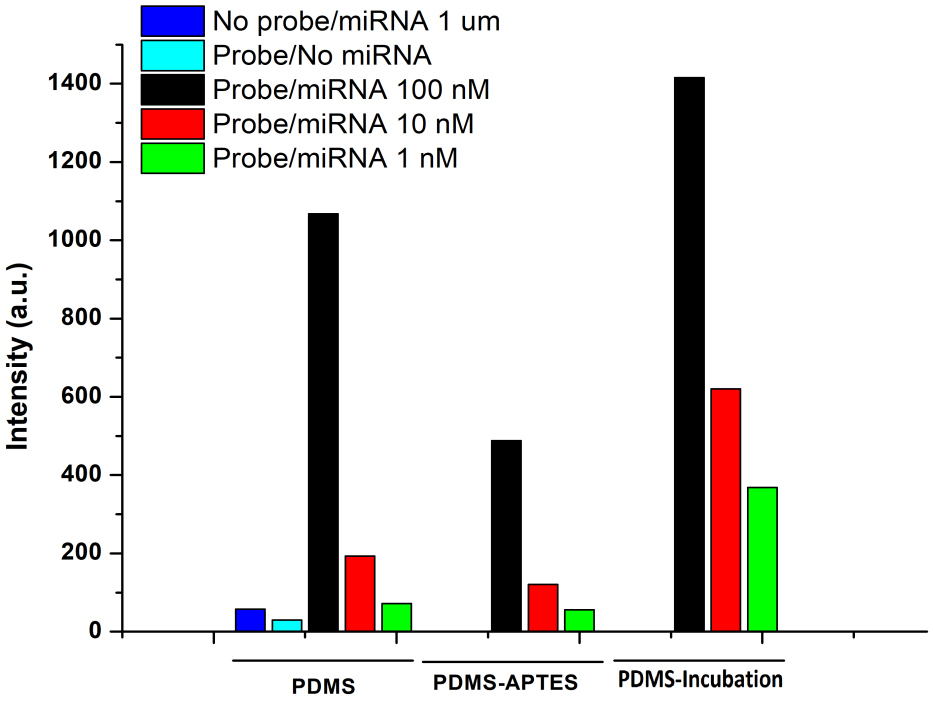

Fig. 6.32 Average SERS intensities obtained by the integration of the area of the miRNA-R6G band at $647\ cm^{-1}$ for the different Ag-coated substrates, at different concentrations of miRNA222-R6G for SERS bioassay

The functionalised APTES PDMS substrate (PDMS-APTES) and the SERS substrate obtained by incubation procedure (PMDS-Incubation) show instead extremely low nonspecific signal. Moreover, PDMS-APTES and PDMS-Incubation substrates both show intense miRNA222-R6G spectra for all the concentrations, along with low nonspecific binding.

To compare all the substrates, it was chosen to integrate the area of the characteristic miRNA222-R6G vibrational peak found at $647\,cm^{-1}$ for all the collected spectra per sample, followed by an average of the calculated intensities. All the results are collected and compared in the histogram of Figure 6.32. The results show that the PDMS-Incubation substrate exhibits the best performances. The PDMS substrates provide high intensities, too, but also a high nonspecific binding. On the contrary, even if PDMS-APTES shows a lower sensitivity, it can be used for lower miRNA222-R6G concentrations.

The cross-check through ELISA was performed for the same concentrations of miRNA222. In Figure 6.33 the results are shown. Very low nonspecific binding is exhibited by all the samples, along with high concentration of miRNA222, guaranteeing the detection of miRNA222 for the complete range of used concentrations.

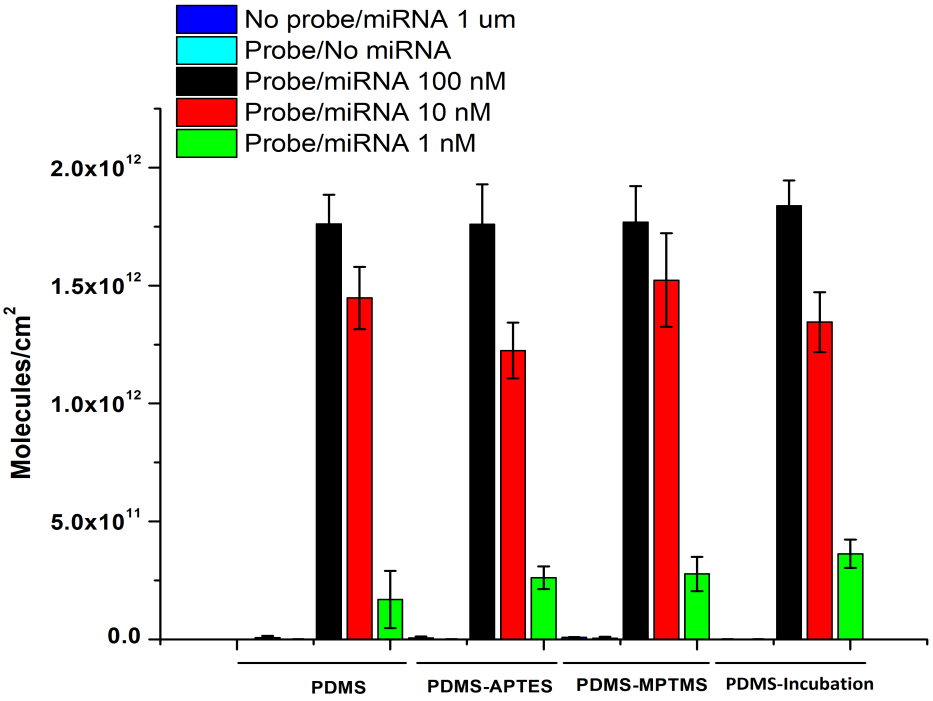

Fig. 6.33 Detection of different concentrations of miRNA by means of metal-PDMS substrates. The vertical bar for each sample represent the correspondent Standard Deviation of the measurement.

In general, all the samples showed similar performances in the case of the ELISA bioassay. Nevertheless, PDMS-Incubation substrate showed slightly better performances if compared to the other samples, confirming the results obtained by means of the SERS analysis. However, the most interesting result is given by the PDMS-MPTMS sample, which showed in this case performances comparable to the ones obtained from the other samples. This result an be justified by the morphology of the substrate. In fact, ELISA bioassay gives mostly information about the success of the protocol regarding the passivation, the immobilization of the probe and of the hybridization of the miRNA. On the other side, the SERS analysis, which takes advantage of the plasmonic effects that are given by the nanostructured surface, points out that the nanostructures obtained on the PDMS-MPTMS substrates do not allow a high enhancement of the Raman signal, confirming the outcomes of the SERS efficiency tests performed with 4-MBA.

6.4.2.2 Chip fabrication

The sample synthesised by static incubation (5:1, *1 mm*, *40 °C*, totally cross-linked and *24 h* incubation time) showed the best performances for the bioassays. For this reason, it was chosen to be integrated in a multi-chamber all-PDMS optofluidic chip. Such a device gives the advantage of an improved handling of the sensors, along with transparency in the Vis-NIR range, that makes it ready to be used under Raman microscope for SERS spectroscopy. In this paragraph the fabrication and integration of the sample in the chip is briefly discussed, while in the next section the results obtained from the bioassay are presented.
The fabrication process consists mainly of three steps. The first one corresponds to the synthesis of the silver NPs on the PDMS membrane, in the synthesis conditions (5:1, *1 mm*,

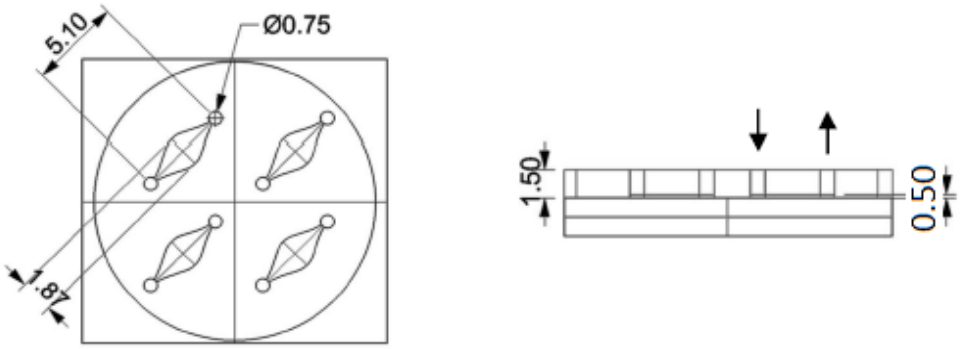

Fig. 6.34 Schematic top view and cross section of the cover mould. Dimensions are expressed in millimetres [50]

40 °C, totally cross-linked and *24 h* incubation time) for the chosen sample. Secondly, the cover of the chip is fabricated with the use of a mould (see Figure. 6.34). A 10:1 monomer-to-curing agent ratio of PDMS is poured into the mould and cross-linked at the temperature of 60°*C* for 1 *h*. The cross-linked PDMS is finally stripped out from the mould and bounded by stamp and stick technique [134] to the silvered PDMS membrane.
Finally, the chip is put in an oven at the temperature of 60°*C* for 60 *min*, in order to achieve the bonding of the sample to the cover.

6.4.2.3 Labelled miRNA222-R6G detection in chip

The same procedure for the SERS analysis was also used for the multichamber chip, in which the best sample, obtained by means of static incubation (5:1, *1 mm*, *40 °C*, totally cross-linked and *24 h* incubation time), was integrated. The mean spectra are obtained

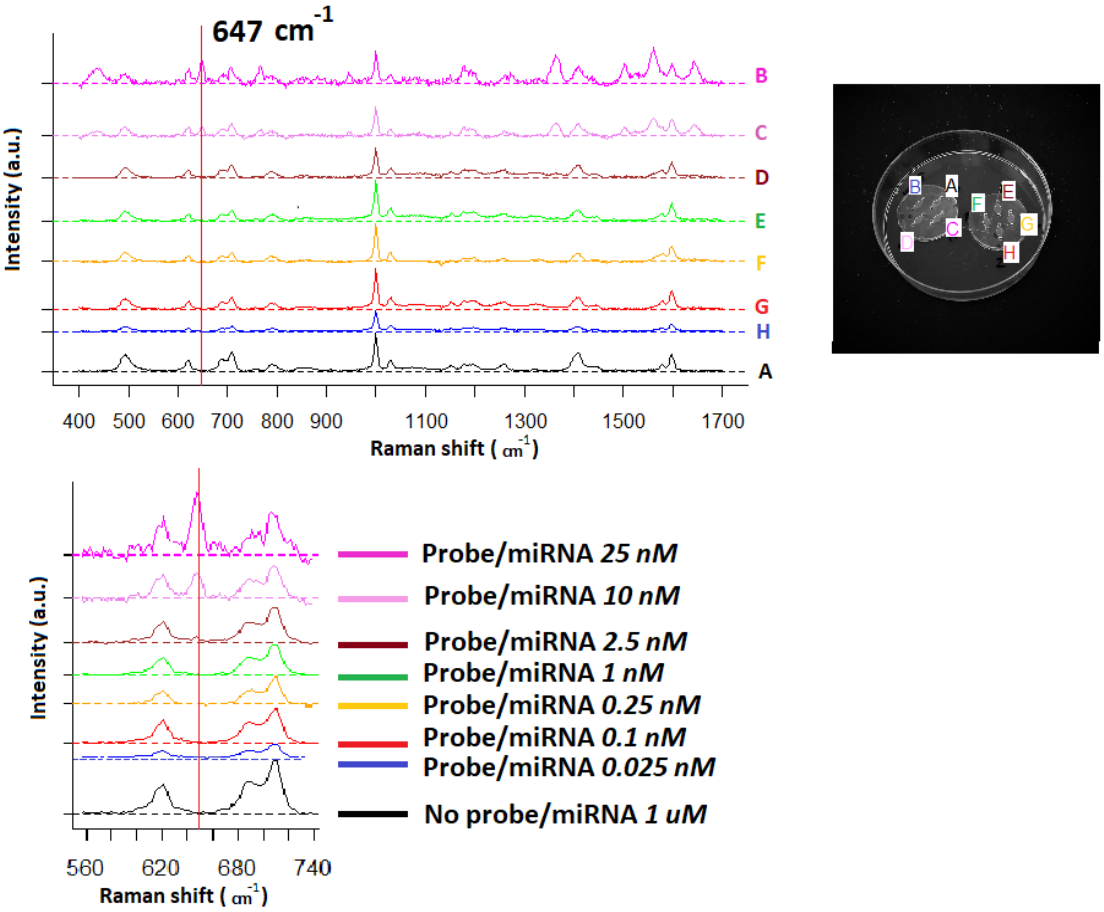

Fig. 6.35 SERS mean spectra of the labelled miRNA222-R6G incubated in the chip for different miRNA222-R6G concentrations and negative control (no Probe/miRNA *1* μM).

for different concentrations of the target, apart from the usual no probe/miRNA control to measure the nonspecific binding. Figure 6.35 collects the mean spectra and the conditions in which they have been obtained.

As it can be seen, the passivation protocol seems to work also for the multichamber chip. Indeed, the negative control spectrum (black line) doesn't show any relevant miRNA222-R6G peak. In addition to this, it can be seen that the miRNA222-R6G is detected for the highest concentrations (*25 nM*, *10 nM* and *2.5 nM*), but the SERS signal is already too weak for the *1 nM* concentration. Moreover, the detected signals are weaker than the ones obtained from the samples synthesized under the same conditions, but non integrated in the chip. This could be attributed to the smaller volume of miRNA222-R6G that is contained in the chip chambers, but this effect would be overcome by the full integration of the device with the proper microfluidics, allowing the interaction of the SERS-active area with a higher volume of sample.

6.4.3 Conclusions

In conclusion, the protocol for the miRNA222 bioassay, both through SERS and ELISA, was tested on the Ag-coated PDMS substrates (PDMS, PDMS-APTES, PDMS-MPTMS and PDMS-Incubation). It was found that the protocol for the passivation works well for all the substrates, apart from the PDMS one, for which a high nonspecific signal was detected by the SERS analysis. The SERS analysis showed the best results in the case of PDMS-Incubation and good results also for PDMS-APTES membranes, compared to the initial PDMS membranes. On the contrary, PDMS-MPTMS samples didn't allow the detection of miRNA222-R6G, even at the highest concentrations. However, the bioassay, performed by means of ELISA, showed comparable results for all the samples.
For what concerns the SERS analysis applied to the multi-chamber chip, it was found that the passivation process works also in this case, reducing the nonspecific binding. At the same time, the highest miRNA222-R6G concentrations were efficiently detected, but with lower SERS intensities than the ones obtained by the bioassay carried out on the non-integrated corresponding sample (PDMS-Incubation). This behaviour could be related to the smaller volume of solution containing the target miRNA, that is incubated in the chip chambers, if compared to the one used for the non-integrated samples. This means that, an optimization of the fabricated chip could guarantee better performances, for instance by integrating a proper microfluidic system. Moreover, the chip could be further optimized for a label-free detection of miRNA222.

Chapter 7

Conclusions

The main aim of this work was to investigate low-cost methods for the synthesis of sensitive and stable substrates, based on Ag-NPs immobilized on PDMS membranes. The optimization of this SERS substrate was ultimately aimed to the development of a flexible multi-chamber microfluidic chip, for fast and low-cost detection, oriented to biosensing applications.
As first attempt, the optimization of Ag-coated PDMS membranes, obtained by means of DC-sputtering, was performed by varying the synthesis parameters (current, deposition time and distance from target). The analysis of these substrates showed very low reproducibility and very low stability. For this reason, two main approaches have been followed in order to increase the stability of the NPs on the PDMS substrates.
In the first case the PDMS membranes were activated with a piranha-like solution or with a plasma treatment and finally functionalized by means of (3-mercaptopropyl)trimethoxysilane (MPTMS) and (3-Aminopropyl)triethoxysilane (APTES), in order to promote the adhesion between the sputtered-Ag and the PDMS. The second strategy was, instead, based on the static incubation of the PDMS samples in a AgNO3 solution in different conditions

For what concerns the functionalized PDMS substrates, the stability tests showed that the best performances where attained in the case of the MPTMS-functionalized Ag-coated PDMS membrane. However, despite of the high stability, these substrates also showed the lowest Raman efficiency and intra-sample repeatability, compared to Ag-coated PDMS and APTES functionalized Ag-PDMS. For what concerns the APTES functionalized sample, it was found a higher Raman efficiency with respect to both the other two specimens, but still a lower stability compared to the MPTMS sample typology. For this reason, we have investigated a different method for the synthesis of the Ag-NPs based on the static incubation of the sample in silver nitrate: the synthesis parameters (monomer to curing ratio, thickness of the substrate, incubation temperature, cross-linking degree, precursor concentration,

presence of ethanol in the solution) have been deeply analysed one-by-one to find the best conditions. The incubated SERS samples showed better properties (high Raman efficiency, high intra-sample repeatability and high stability) than the Ag-sputtered PDMS substrates. A comparison among all the samples synthesised by static incubation was also carried out, to choose the best conditions for the application of the miRNA cancer biomarker bioassay.

Finally, an assay for the detection of miRNA222, a known cancer biomarker, was performed both by SERS and Enzyme-Linked ImmunoSorbent assay (ELISA) on the best sample obtained from each fabrication technique. The bioassay was implemented using different concentrations of miRNA222-R6G, along with two "negative control" to measure the nonspecific binding. The results revealed that the best performances (high sensitivity, low nonspecific binding) are obtained in the case of the SERS substrate synthesised by means of static incubation. As a consequence, the best sample obtained by static incubation (5:1 monomer to curing-agent ratio, totally cross-linked 1 mm thick PDMS membranes, incubated at 40 °C for 24 h), were chosen for the development of an all-PDMS multi-chamber microfluidic chip. This revealed that the SERS analysis works also in the case of the multi-chamber chip, showing a good sensitivity for the highest concentrations, along with a low non specific binding. In conclusion, these results suggest that the fabricated chip is a good candidate in the view of an effective implementation for biosensing applications, such as label-free detection of cancer biomarkers.

References

[1] P. J. Hendra M. Fleischmann and A. J. McQuillan. Raman spectra of pyridine adsorbed at a silver electrode. *Chem. Phys. Lett.*, pages 26:163–66, 1974.

[2] Pablo Etchegoin Eric Le Rue. *Principles of Surface Enhanced Raman Spectroscopy and related Plasmonic Effects*. Elsevier, 2009.

[3] Evanthia Papadopoulou and Steven Bell. Label-free detection of nanomolar unmodified single- and double-stranded dna by using surface-enhanced raman spectroscopy on ag and au colloids. 18:5394–400, 04 2012.

[4] Izabella Hidi, Olga Zukovskaja, Xiao-Shan Zheng, Karina Weber, Thomas Bocklitz, Dana Cialla-May, and Juergen Popp. Surface-enhanced raman spectroscopy and microfluidic platforms: Challenges, solutions and potential applications. 142, 03 2017.

[5] Federica Felicetti, M Cristina Errico, Patrizia Segnalini, Gianfranco Mattia, and Alessandra Carè. Microrna-221 and -222 pathway controls melanoma progression. *Expert Review of Anticancer Therapy*, 8(11):1759–1765, 2008.

[6] Alois Bonifacio, Silvia Dalla Marta, Riccardo Spizzo, Silvia Cervo, Agostino Steffan, Alfonso Colombatti, and Valter Sergo. Surface-enhanced raman spectroscopy of blood plasma and serum using ag and au nanoparticles: A systematic study. 406, 02 2014.

[7] Lucas Lane, Ximei Qian, and Shuming Nie. Sers nanoparticles in medicine: From label-free detection to spectroscopic tagging. 115, 08 2015.

[8] Jing Yang, Zhuyuan Wang, Shenfei Zong, H L Chen, Ruohu Zhang, and Yiping Cui. Dual-mode tracking of tumor-cell-specific drug delivery using fluorescence and label-free sers techniques. *Biosensors and bioelectronics*, 51:82–9, 2014.

[9] C. W. Brown J. R. Ferrao, K. Nakamoto. *Introductory Raman Spectroscopy*. Elsevier, 2003.

[10] P. B. Johnson and R. W. Christy. Optical constants of noble metals. *Phys. Rev. B*, pages 6:4370–79, 1972.

[11] D. Pines. Collective energy losses in solids. *Rev. Mod. Phys.*, pages 28:184–99, 1956.

[12] Thibault Brulé. PhD thesis, UNIVERSITE DE BOURGOGNE FACULTE DES SCIENCES Laboratoire - Interdisciplinaire Carnot de Bourgogne - Departement Nanoscience, 10 2014.

[13] Darya Radziuk and Helmuth Moehwald. Prospects for plasmonic hot spots in single molecule sers towards chemical imaging of live cells. 17, 01 2015.

[14] D. Cialla-May, X.-S. Zheng, K. Weber, and J. Popp. Recent progress in surface-enhanced raman spectroscopy for biological and biomedical applications: from cells to clinics. *Chem. Soc. Rev.*, 46:3945–3961, 2017.

[15] Marco Musiani, Liu Jun-yang, and Zhong-Qun Tian. Applications of electrochemical surface-enhanced raman spectroscopy (ec-sers), 06 2014.

[16] Yuanjie Teng, Wenhan Liu, Minbo Lan, Suzhen Ma, and Chunan Ma. Porous and dendritic structure of screen-printed electrode for in-situ electrochemical surface-enhanced raman scattering. *Analytical Letters*, 49(2):299–306, 2016.

[17] Pamela A. Mosier-Boss. Review of sers substrates for chemical sensing. *Nanomaterials*, 7(6), 2017.

[18] John Neddersen, George Chumanov, and Therese M. Cotton. Laser ablation of metals: A new method for preparing sers active colloids. *Applied Spectroscopy*, 47(12): 1959–1964, 1993.

[19] Josef Štěpánek Blanka Vlčková Marek Procházka, Peter Mojzeš and Pierre-Yves Turpin. Probing applications of laser-ablated ag colloids in sers spectroscopy: Improvement of ablation procedure and sers spectral testing. *Anal. Chem.*, 69(24): 5103–5108, 1997.

[20] John Neddersen, George Chumanov, and Therese M. Cotton. Laser ablation of metals: A new method for preparing sers active colloids. *Appl. Spectrosc.*, 47(12):1959–1964, Dec 1993.

[21] P. C. Lee and D. Meisel. Adsorption and surface-enhanced raman of dyes on silver and gold sols. *The Journal of Physical Chemistry*, 86(17):3391–3395, 1982.

[22] Rares Stiufiuc, Cristian Iacovita, Constantin M. Lucaciu, Gabriela Stiufiuc, Alina G. Dutu, Cristiana Braescu, and Nicolae Leopold. Sers-active silver colloids prepared by reduction of silver nitrate with short-chain polyethylene glycol. *Nanoscale Research Letters*, 8(1):47, Jan 2013.

[23] C. G. Blatchford J. A. Creighton and M. G. Albrecht. Plasma resonance enhancement of raman scattering by pyridine adsorbed on silver or gold sol particles of size comparable to the excitation wavelength. *Chem. Soc.: Faraday Trans.*, pages 2:790–98, 1979.

[24] Furong Tian, Franck Bonnier, Alan Casey, Anne E. Shanahan, and Hugh J. Byrne. Surface enhanced raman scattering with gold nanoparticles: effect of particle shape. *Anal. Methods*, 6:9116–9123, 2014.

[25] Catherine J. Murphy, Tapan K. Sau, Anand M. Gole, Christopher J. Orendorff, Jinxin Gao, Linfeng Gou, Simona E. Hunyadi, and Tan Li. Anisotropic metal nanoparticles: Synthesis, assembly, and optical applications. *Journal of Physical Chemistry B*, 109 (29):13857–13870, 7 2005.

[26] B. Lim Y. Xia, Y. Xiong and S. E. Skrabalak. Shape-controlled synthesis of metal nanocrystals: simple chemistry meets complex physics? *Angew. Chem.*, 48:13857–13870, 2009.

[27] Benjamin J Wiley, Sang Hyuk Im, Zhi-Yuan Li, Joeseph McLellan, Andrew R Siekkinen, and Younan Xia. Maneuvering the surface plasmon resonance of silver nanostructures through shape-controlled synthesis. *The journal of physical chemistry. B*, 110 32:15666–75, 2006.

[28] E.-B. Ying X.-Q. Zou and S.-J. Dong. Seed-mediated synthesis of branched gold nanoparticles with the assistance of citrate and their surface-enhanced raman scattering properties. *Nanotechnology*, 17:4758, 2006.

[29] Xiangqin Zou and Shaojun Dong. Surface-enhanced raman scattering studies on aggregated silver nanoplates in aqueous solution. *The Journal of Physical Chemistry B*, 110(43):21545–21550, 2006.

[30] Pedro H. C. Camargo Claire Cobley Zhi-Yuan Li Matthew Rycenga, Moon Ho Kim and Younan Xia. Surface-enhanced raman scattering: Comparison of three different molecules on single-crystal nanocubes and nanospheres of silver. *J Phys Chem A*, 113, 2009.

[31] H. Grau S. Schneider, P. Halbig and Ulrich Nickel. Reproducible preparation of silver sols with uniform particle size for applications in surface-enhanced raman spectroscopy. *Photochem. Photobiol.*, pages 60:605–10, 1994.

[32] Wei Meng, Fang Hu, Xiaohong Jiang, and Lude Lu. Preparation of silver colloids with improved uniformity and stable surface-enhanced raman scattering. In *Nanoscale research letters*, 2015.

[33] Yuling Wang and Sebastian Schlücker. Rational design and synthesis of sers labels. 138, 02 2013.

[34] Brown R J C Milton M J T Tantra, R. Strategy to improve the reproducibility of colloidal sers. *J. Raman Spectrosc.*, 38, 2007.

[35] Juan Fraire, Valeria N. Sueldo Ocello, Leandro G. Allende, Alicia Veglia, and Eduardo Coronado. Toward the design of highly stable small colloidal sers substrates with supramolecular host-guest interactions for ultrasensitive detection. *The Journal of Physical Chemistry C*, 2015.

[36] Martin Jahn, Sophie Patze, Izabella J. Hidi, Richard Knipper, Andreea I. Radu, Anna Mühlig, Sezin Yüksel, Vlastimil Peksa, Karina Weber, Thomas Mayerhöfer, Dana Cialla-May, and Jürgen Popp. Plasmonic nanostructures for surface enhanced spectroscopic methods. *Analyst*, 141:756–793, 2016.

[37] Anuj Dhawan, Michael Gerhold, and Tuan Vo-Dinh. Theoretical simulation and focused ion beam fabrication of gold nanostructures for surface-enhanced raman scattering (sers). 3:164–171, 12 2007.

[38] G Giallongo, Christian Dr, Roberto Pilot, Denis Garoli, Renato Bozio, Filippo Romanato, Armando Gennaro, Gian Rizzi, and Gaetano Granozzi. Growth and optical properties of silver nanostructures obtained on connected anodic aluminum oxide templates. 23:325604, 07 2012.

[39] Allison KJ Bright RM Davis JA Guthrie AP-Hommer MB Jackson MA Smith PC Walter DG Natan MJ. Freeman RG, Grabar KC. Self-assembled metal colloid monolayers: An approach to sers substrates. *Science*, 267(5204):1629–32, 1995.

[40] Maximilien Cottat, Nathalie Lidgi-Guigui, Inga Tijunelyte, Grégory Barbillon, Frédéric Hamouda, Philippe Gogol, Abdelhanin Aassime, jean-michel Lourtioz, Bernard Bartenlian, and Marc Lamy de la Chapelle. Soft uv nanoimprint lithography designed highly sensitive substrates for sers detection. 9:623, 11 2014.

[41] M. Kahl, E. Voges, S. Kostrewa, C. Viets, and W. Hill. Periodically structured metallic substrates for sers. *Sensors and Actuators B: Chemical*, 51(1):285 – 291, 1998.

[42] Weisheng Yue, Zhihong Wang, Yang Yang, Longqing Chen, Ahad Syed, Kimchong Wong, and Xianbin Wang. Electron-beam lithography of gold nanostructures for surface-enhanced raman scattering. 22:125007, 10 2012.

[43] Cai W Jun YC White JS Brongersma ML Schuller JA, Barnard ES. Plasmonics for extreme light concentration and manipulation. 9:193–204, 02 2010.

[44] M Dubiel, M Heinz, V V Srabionyan, V V Pryadchenko, L A Avakyan, Ya V Zubavichus, J Meinertz, J Ihlemann, and L A Bugaev. Silver nanoparticles in silicate glass prepared by uv laser irradiation: dependences of size and atomic structure of particles upon irradiation parameters. *Journal of Physics: Conference Series*, 712(1): 012110, 2016.

[45] Maximilian Heinz, Vasiliy Srabionyan, Aram Bugaev, Vasiliy Pryadchenko, Egor V. Ishenko, Leon Avakyan, Ya Zubavichus, Jürgen Ihlemann, Jörg Meinertz, Eckhard Pippel, Manfred Dubiel, and Lusegen Bugaev. Formation of silver nanoparticles in silicate glass using excimer laser radiation: Structural characterization by hrtem, xrd, exafs and optical absorption spectra. 681, 04 2016.

[46] Dominique Decanini Jian Shi Andrea Cattoni, Jing Chen and Anne-Marie Haghiri-Gosnet. Soft uv nanoimprint lithography: A versatile tool for nano structuration at the 20nm scale, recent advances in nanofabrication techniques and applications. ISBN: 978-953-307-602-7, InTech, 2011.

[47] Maximilien Cottat, Nathalie Lidgi-Guigui, Inga Tijunelyte, Grégory Barbillon, Frédéric Hamouda, Philippe Gogol, Abdelhanin Aassime, jean-michel Lourtioz, Bernard Bartenlian, and Marc Lamy de la Chapelle. Soft uv nanoimprint lithography designed highly sensitive substrates for sers detection. 9:623, 11 2014.

[48] Dean J. Campbell, Katie J. Beckman, Camilo E. Calderon, Patrick W. Doolan, Rebecca M. Ottosen, Arthur B. Ellis, and George C. Lisensky. Replication and compression of surface structures with polydimethylsiloxane elastomer. 76:537–, 04 1999.

[49] Meikun Fan, Gustavo Fernandes Souza Andrade, and Alexandre Guimarães Brolo. A review on the fabrication of substrates for surface enhanced raman spectroscopy and their applications in analytical chemistry. *Analytica chimica acta*, 693 1-2:7–25, 2011.

[50] C. Novara. *Silver nanostructures on porous silicon for multiplexed Surface Enhanched Raman Scattering biosensing platforms*. PhD thesis, Politecnico di Torino, Department of Applied Science and Technology, 2016.

[51] Catherine Henrist Pierre Colson and Rudi Cloots. Nanosphere lithography: A powerful method for the controlled manufacturing of nanomaterials. Journal of Nanomaterials, Volume 2013, Article ID 948510, 2013.

[52] John C. Hulteen and Richard P. Van Duyne. Nanosphere lithography: A materials general fabrication process for periodic particle array surfaces. 13:1553 – 1558, 06 1995.

[53] Christy L. Haynes and Richard P. Van Duyne. Nanosphere litography: A versatile nanofabrication tool for studies of size-dependent nanoparticle optics. *The Journal of Physical Chemistry B*, 105(24):5599–5611, 2001.

[54] Maritoni Litorja, Christy L. Haynes, Amanda J. Haes, Traci R. Jensen, and Richard P. Van Duyne. Surface-enhanced raman scattering detected temperature programmed desorption: Optical properties, nanostructure, and stability of silver film over sio2 nanosphere surfaces. *The Journal of Physical Chemistry B*, 105(29):6907–6915, 2001.

[55] Jon P. Camden, Jon A. Dieringer, Jing Zhao, and Richard P. Van Duyne. Controlled plasmonic nanostructures for surface-enhanced spectroscopy and sensing. *Accounts of Chemical Research*, 41(12):1653–1661, 2008.

[56] M. T. Smith J. C. Hulteen C. L. Haynes, A. D. McFarland and R. P. Van Duyne. Angle-resolved nanosphere lithography: manipulation of nanoparticle size, shape, and interparticle spacing. *Journal of Physical Chemistry B, vol. 106, no. 8*, page 1898–1902, 2002.

[57] Elin M Larsson, Joan Alegret, Mikael Käll, and Duncan Sutherland. Sensing characteristics of nir localized surface plasmon resonances in gold nanorings for application as ultrasensitive biosensors. 7:1256–63, 05 2007.

[58] Si Hoon Lee, Kyle C. Bantz, Nathan C. Lindquist, Sang-Hyun Oh, and Christy L. Haynes. Self-assembled plasmonic nanohole arrays. *Langmuir*, 25(23):13685–13693, 2009.

[59] R. Chen H. Yang X. Peng Q. Yu, H. Huang and Z. Ye. Filtration-assembling colloidal crystal templates for ordered macroporous nanoparticle films. *Journal of Materials Chemistry, vol. 21, no. 44*, page 18089–18094, 2011.

[60] Yandong Wang, Mengyuan Zhang, Yuekun Lai, and Lifeng Chi. Advanced colloidal lithography: From patterning to applications. *Nano Today*, 2018.

[61] I. Zorić C. Langhammer, Z. Yuan and B. Kasemo. Plasmonic properties of supported pt and pd nanostructures. *Nano Letters, vol. 6, no. 4*, page 833–838, 2006.

[62] Frank Schreiber. Structure and growth of self-assembling monolayers. 65, 11 2000.

[63] Olivier Péron, Emmanuel Rinnert, Michel Lehaitre, Philippe Crassous, and Chantal Compère. Detection of polycyclic aromatic hydrocarbon (pah) compounds in artificial sea-water using surface-enhanced raman scattering (sers). *Talanta*, 79(2):199 – 204, 2009.

[64] J. Christopher Love, Lara A. Estroff, Jennah K. Kriebel, Ralph G. Nuzzo, and George M. Whitesides. Self-assembled monolayers of thiolates on metals as a form of nanotechnology. *Chemical Reviews*, 105(4):1103–1170, 2005.

[65] Han-Wen Cheng, Shuang-Yan Huan, Hai-Long Wu, Guo-Li Shen, and Ru-Qin Yu. Surface-enhanced raman spectroscopic detection of a bacteria biomarker using gold nanoparticle immobilized substrates. *Analytical Chemistry*, 81(24):9902–9912, 2009.

[66] Maung Kyaw Khaing Oo, Yun Han, Jiri Kanka, Svetlana Sukhishvili, and Henry Du. Structure fits the purpose: photonic crystal fibers for evanescent-field surface-enhanced raman spectroscopy. *Opt. Lett.*, 35(4):466–468, Feb 2010.

[67] Yun Han, Svetlana Sukhishvili, Henry Du, John Cefaloni, and Benjamin Smolinski. Layer-by-layer self-assembly of oppositely charged ag nanoparticles on silica microspheres for trace analysis of aqueous solutions using surface-enhanced raman scattering. 8:5791–5800, 11 2008.

[68] Ricardo F. Aroca, Paul J. G. Goulet, David S. dos Santos, Ramón A. Alvarez-Puebla, and Osvaldo N. Oliveira. Silver nanowire layer-by-layer films as substrates for surface-enhanced raman scattering. *Analytical Chemistry*, 77(2):378–382, 2005.

[69] Chongyang Peng, Yonghai Song, Gang Wei, Wanxi Zhang, Zhuang Li, and Wenfei Dong. Self-assembly of lambda-dna networks/ag nanoparticles: Hybrid architecture and active-sers substrate. 317:183–190, 01 2008.

[70] Sun L Guo C Yang T Liu Z-Xu F Li Z. Sun Y, Wang L. Fabrication, characterization, and application in surface-enhanced raman spectrum of assembled type-i collagen-silver nanoparticle multilayered films. 128:074704, 02 2008.

[71] Hui Wang, Janardan Kundu, and Naomi Halas. Plasmonic nanoshell arrays combine surface-enhanced vibrational spectroscopies on a single substrate. 46:9040–4, 12 2007.

[72] Aline Cerf, Gábor Molnár, and Christophe Vieu. Novel approach for the assembly of highly efficient sers substrates. *ACS Applied Materials & Interfaces*, 1(11):2544–2550, 2009.

[73] Mehmet Kahraman, M. Müge Yazıcı, Fikrettin Şahin, and Mustafa Çulha. Convective assembly of bacteria for surface-enhanced raman scattering. *Langmuir*, 24(3):894–901, 2008.

[74] Thiago S. Rezende, George Andrade, Ledjane Barreto, Nivan Da Costa Jr, Iara F. Gimenez, and L.E. Almeida. Facile preparation of catalytically active gold nanoparticles on a thiolated chitosan. 64:882–884, 04 2010.

[75] Syed Rahin Ahmed, Jeonghyo Kim, Van Tan Tran, Tetsuro Suzuki, Suresh Neethirajan, Jaewook Lee, and Enoch Y. Park. In situ self-assembly of gold nanoparticles on hydrophilic and hydrophobic substrates for influenza virus-sensing platform. 2017.

[76] Scott M Tabakman, Zhuo Chen, Hernan Sanchez Casalongue, Hailiang Wang, and Hongjie Dai. A new approach to solution-phase gold seeding for sers substrates. 7: 499–505, 02 2011.

[77] Benjamin Wiley, Yugang Sun, Brian Mayers, and Younan Xia. Shape-controlled synthesis of metal nanostructures: The case of silver. 11:454–63, 01 2006.

[78] Andrea Tao, Prasert Sinsermsuksakul, and Peidong Yang. Polyhedral silver nanocrystals with distinct scattering signatures. *Angewandte Chemie (International ed. in English)*, 45(28):4597—4601, July 2006.

[79] Chiara Novara, Silvia Dalla Marta, Alessandro Virga, Andrea Lamberti, Angelo Angelini, Alessandro Chiadò, Paola Rivolo, Francesco Geobaldo, Valter Sergo, Alois Bonifacio, and Fabrizio Giorgis. Sers-active ag nanoparticles on porous silicon and pdms substrates: A comparative study of uniformity and raman efficiency. 120, 07 2016.

[80] Martin Molberg, Daniel Crespy, Patrick Rupper, Frank Nüesch, Jan-Anders E. Månson, Christiane Löwe, and Dorina M. Opris. High breakdown field dielectric elastomer actuators using encapsulated polyaniline as high dielectric constant filler. *Advanced Functional Materials*, 20(19):3280–3291.

[81] Andrea Zanardi, Dario Bandiera, Francesco Bertolini, Chiara Antonia Corsini, Giuliana Gregato, Paolo Milani, Emanuele Barborini, and Roberta Carbone. Miniaturized fish for screening of onco-hematological malignancies. *BioTechniques*, 49 1:497–504, 2010.

[82] John A. Rogers, Takao Someya, and Yonggang Huang. Materials and mechanics for stretchable electronics. *Science*, 327 5973:1603–7, 2010.

[83] A. Lamberti, S. L. Marasso, and M. Cocuzza. Pdms membranes with tunable gas permeability for microfluidic applications. *RSC Adv.*, 4:61415–61419, 2014.

[84] Andrea Lamberti, Alessandro Virga, Paola Rivolo, Angelo Angelini, and Giorgis Fabrizio. Easy tuning of surface and optical properties of pdms decorated by ag nanoparticles. *The Journal of Physical Chemistry B*, 119(25):8194–8200, 2015.

[85] Keun Soo Kim, Yue Zhao, Houk Jang, Sang Yoon Lee, Jong Min Kim, Kwang S. Kim, Jong Hyun Ahn, Philip Kim, Jae Young Choi, and Byung Hee Hong. Large-scale pattern growth of graphene films for stretchable transparent electrodes. *Nature*, 457 (7230):706–710, 2 2009.

[86] Fernando Carrillo, Shikha Gupta, Mehdi Balooch, Sally J. Marshall, Grayson W. Marshall, Lisa Pruitt, and Christian M. Puttlitz. Nanoindentation of polydimethylsiloxane elastomers: Effect of crosslinking, work of adhesion, and fluid environment on elastic modulus. *Journal of Materials Research*, 20(10):2820–2830, 2005. doi: 10.1557/JMR.2005.0354.

[87] Andrea Lamberti, Alessandro Virga, Angelo Angelini, Alessandro Ricci, Emiliano Descrovi, Matteo Cocuzza, and Fabrizio Giorgis. Metal–elastomer nanostructures for tunable sers and easy microfluidic integration. *RSC Adv.*, 5:4404–4410, 2015.

[88] Anubha Goyal, Ashavani Kumar, Prabir K. Patra, Shaily Mahendra, Salomeh Tabatabaei, Pedro J. J. Alvarez, George John, and Pulickel M. Ajayan. In situ synthesis of metal nanoparticle embedded free standing multifunctional pdms films. *Macromolecular Rapid Communications*, 30(13):1116–1122.

[89] Bo Wang, Ke Chen, Shan Jiang, François Reincke, Weijun Tong, Dayang Wang, and Changyou Gao. Chitosan-mediated synthesis of gold nanoparticles on patterned poly(dimethylsiloxane) surfaces. *Biomacromolecules*, 7(4):1203–1209, 2006.

[90] Qing Zhang, Jing-Juan Xu, Yan Liu, and Hong-Yuan Chen. In-situ synthesis of poly(dimethylsiloxane)–gold nanoparticles composite films and its application in microfluidic systems. 8:352–7, 03 2008.

[91] A. Paulina de la Mata, Aaron J. Fleischman, and Shuvo Roy. Characterization of polydimethylsiloxane (pdms) properties for biomedical micro/nanosystems. *Biomedical microdevices*, 7 4:281–93, 2005.

[92] Andrea Lamberti, Simone Marasso, and Matteo Cocuzza. Pdms membranes with tunable gas permeability for microfluidic applications. 4, 11 2014.

[93] Ju Yeoul Baek, Han Gu, Soo-Il Kwon, Jeongyun Kim, Jin Ho Cho, Seung Ha Lee, Kyung Sun, and Sang Hoon Lee. Stable deposition and patterning of metal layers on the pdms substrate and characterization for the development of the flexible and implantable micro electrode. 124-126:124–126, 06 2007.

[94] Alessandro Chiadò, Chiara Novara, Andrea Lamberti, Francesco Geobaldo, Fabrizio Giorgis, and Paola Rivolo. Immobilization of oligonucleotides on metal-dielectric nanostructures for mirna detection. *Analytical Chemistry*, 88(19):9554–9563, 2016.

[95] *Fabrication of Silver Nanoparticles Immobilzed Microfluidic Chip for Chemiluminescence based Analytical Application*, Nürnberg/Nuremberg, Germany, 2012. AMA.

[96] Guodong Sui, Jinyi Wang, Chung-Cheng Lee, Weixing Lu, Stephanie P. Lee, Jeffrey V. Leyton, Anna M. Wu, and Hsian-Rong Tseng. Solution-phase surface modification in intact poly(dimethylsiloxane) microfluidic channels. *Analytical Chemistry*, 78(15): 5543–5551, 2006.

[97] Bin Wang, Lu Chen, Zamin Abdulali-Kanji, J. Hugh Horton, and Richard D. leschuk. Aging effects on oxidized and amine-modified poly(dimethylsiloxane) surfaces studied with chemical force titrations: Effects on electroosmotic flow rate in microfluidic channels. *Langmuir*, 19(23):9792–9798, 2003.

[98] Cristina Potrich, Valentina Vaghi, Lorenzo Lunelli, Laura Pasquardini, Gaia Santini, Chiara Ottone, Marzia Quaglio, Matteo Cocuzza, Fabrizio Candido Pirri, Manuela Ferracin, Massimo Negrini, Paola Tiberio, Veronica De Sanctis, Roberto Bertorelli, and Cecilia Pederzolli. Oncomir detection in circulating body fluids: A pdms microdevice perspective. 14, 08 2014.

[99] Christine Séguin, Jessica M. McLachlan, Peter R. Norton, and François Lagugné-Labarthet. Surface modification of poly(dimethylsiloxane) for microfluidic assay applications. 256:2524–2531, 02 2010.

[100] Daojun Liu, Robbyn K Perdue, li Sun, and Richard M Crooks. Immobilization of dna onto poly(dimethylsiloxane) surfaces and application to a microelectrochemical enzyme-amplified dna hybridization assay. 20:5905–10, 08 2004.

[101] Ralph A. Tripp, Richard A. Dluhy, and Yiping Zhao. Novel nanostructures for sers biosensing. *Nano Today*, 3(3):31 – 37, 2008.

[102] Kyle C. Bantz, Audrey F. Meyer, Nathan J. Wittenberg, Hyungsoon Im, Özge Kurtuluş, Si Hoon Lee, Nathan C. Lindquist, Sang-Hyun Oh, and Christy L. Haynes. Recent progress in sers biosensing. *Phys. Chem. Chem. Phys.*, 13:11551–11567, 2011.

[103] M. Procházka. Raman and surface-enhanced raman scattering (sers) biosensing, 2013.

[104] Agnieszka Kamińska, Tomasz Szymborski, Tomasz Jaroch, Adam Zmysłowski, and Arkadiusz Szterk. Gold-capped silicon for ultrasensitive sers-biosensing: Towards human biofluids analysis. 84, 12 2017.

[105] Terence Moore, Amber S Moody, Taylor D Payne, Grace Sarabia, Alyssa Daniel, and Bhavya Sharma. In vitro and in vivo sers biosensing for disease diagnosis. 8, 05 2018.

[106] Tuan Vo-Dinh, Hsin-Neng Wang, and Jonathan Scaffidi. Plasmonic nanoprobes for sers biosensing and bioimaging. 3:89–102, 11 2009.

[107] Cuicui Fu, Lijia Liang, Guohua Qi, Shuping Xu, and W Xu. Biomolecule-assisted surface-enhanced raman scattering(sers) technology and sers biosensing. 36:2134–2147, 11 2015.

[108] Dinish U. S and Malini Olivo. Sers for sensitive biosensing and imaging, 01 2015.

[109] Nikolay N. Durmanov, Rustam R. Guliev, Arkady V. Eremenko, Irina A. Boginskaya, Ilya A. Ryzhikov, Ekaterina A. Trifonova, Egor V. Putlyaev, Aleksei N. Mukhin, Sergey L. Kalnov, Marina V. Balandina, Artem P. Tkachuk, Vladimir A. Gushchin, Andrey K. Sarychev, Andrey N. Lagarkov, Ilya A. Rodionov, Aidar R. Gabidullin, and Ilya N. Kurochkin. Non-labeled selective virus detection with novel sers-active porous silver nanofilms fabricated by electron beam physical vapor deposition. *Sensors and Actuators B: Chemical*, 257:37 – 47, 2018.

[110] Hyun Ji Park, Sung Chul Yang, and Jaebum Choo. Early diagnosis of influenza virus a using surface-enhanced raman scattering-based lateral flow assay. *Bulletin of the Korean Chemical Society*, 37(12):2019–2024.

[111] Roger M. Jarvis, Alan Brooker, and Royston Goodacre. Surface-enhanced raman spectroscopy for bacterial discrimination utilizing a scanning electron microscope with a raman spectroscopy interface. *Analytical Chemistry*, 76(17):5198–5202, 2004.

[112] I. S. Patel, W. R. Premasiri, D. T. Moir, and L. D. Ziegler. Barcoding bacterial cells: a sers-based methodology for pathogen identification. *Journal of Raman Spectroscopy*, 39(11):1660–1672.

[113] Lei Chen, Linjun Cai, Weidong Ruan, and Bing Zhao. *Surface-enhanced Raman Spectroscopy (SERS): Protein Application*, pages 1–23. American Cancer Society, 2014.

[114] Neus Feliu, Moustapha Hassan, Eduardo Garcia Rico, Daxiang Cui, Wolfgang Parak, and Ramon Alvarez-Puebla. Sers quantification and characterization of proteins and other biomolecules. *Langmuir*, 33(38):9711–9730, 2017.

[115] Wenbo Lu, Ying Wang, Xiaowei Cao, Li Li, Jian Dong, and Weiping Qian. Multiplexing determination of lung cancer biomarkers using electrochemical and surface-enhanced raman spectroscopic techniques. *New J. Chem.*, 39:5420–5430, 2015.

[116] Jie Chao, Wenfang Cao, Shao Su, Lixing Weng, Shiping Song, Chunhai Fan, and Lianhui Wang. Nanostructure-based surface-enhanced raman scattering biosensors for nucleic acids and proteins. *J. Mater. Chem. B*, 4:1757–1769, 2016.

[117] Aoune Barhoumi, Dongmao Zhang, Felicia Tam, and Naomi J. Halas. Surface-enhanced raman spectroscopy of dna. *Journal of the American Chemical Society*, 130 16:5523–9, 2008.

[118] Aoune Barhoumi, Dongmao Zhang, and Naomi J. Halas. Correlation of molecular orientation and packing density in a dsdna self-assembled monolayer observable with surface-enhanced raman spectroscopy. *Journal of the American Chemical Society*, 130(43):14040–14041, 2008.

[119] Liyan Bi, Yanying Rao, Qin Tao, Jian Dong, Ting Su, Fangjing Liu, and Weiping Qian. Fabrication of large-scale gold nanoplate films as highly active sers substrates for label-free dna detection. 43C:193–199, 12 2012.

[120] J.D. Driskell, A.G. Seto, L.P. Jones, S. Jokela, R.A. Dluhy, Y.-P. Zhao, and R.A. Tripp. Rapid microrna (mirna) detection and classification via surface-enhanced raman spectroscopy (sers). *Biosensors and Bioelectronics*, 24(4):917 – 922, 2008.

[121] Silvia Catuogno, Carla Lucia Esposito, Cristina Quintavalle, Laura Cerchia, Gerolama Condorelli, and Vittorio de Franciscis. Recent advance in biosensors for micrornas detection in cancer. In *Cancers*, 2011.

[122] Edith S. Grabbe and Richard P. Buck. Surface-enhanced raman-spectroscopic investigation of human immunoglobulin-g adsorbed on a silver electrode. 111, 10 1989.

[123] Jung Mo Ahn and Je Yoel Cho. Current serum lung cancer biomarkers. s4, 01 2013.

[124] Teng Xu, Xinle Jia, Xia Chen, and Zhanfang Ma. Simultaneous electrochemical detection of multiple tumor markers using metal ions tagged immunocolloidal gold. *Biosensors and Bioelectronics*, 56:174 – 179, 2014.

[125] Vladimir P. Drachev, Mark D. Thoreson, Vishal Nashine, Eldar N. Khaliullin, Dor Ben-Amotz, V. Jo Davisson, and Vladimir M. Shalaev. Adaptive silver films for surface-enhanced raman spectroscopy of biomolecules. *Journal of Raman Spectroscopy*, 36 (6-7):648–656.

[126] Vladimir P. Drachev, Mark D. Thoreson, and Vladimir M. Shalaev. Sensing proteins with adaptive metal nanostructures. 2006.

[127] Vladimir Drachev, Mark Thoreson, Eldar N. Khaliullin, Andrey Sarychev, Dongmao Zhang, Dor Ben-Amotz, and Vladimir M. Shalaev. Semicontinuous silver films for protein sensing with sers. 5221, 11 2003.

[128] Vladimir Drachev and Vladimir M. Shalaev. Biomolecule sensing with adaptive plasmonic nanostructures, 09 2006.

[129] mirnas in the biology of cancers and viral infections. *Current Medicinal Chemistry*, 14(2), 2007.

[130] Sophia Cammaerts, Mojca Strazisar, Peter De Rijk, and Jurgen Del Favero. Genetic variants in microrna genes: impact on microrna expression, function, and disease. *Frontiers in Genetics*, 6:186, 2015.

[131] Lanlan Sun, Yonghai Song, Li Wang, Cunlan Guo, Yujing Sun, Zhelin Liu, and Zhuang Li. Ethanol-induced formation of silver nanoparticle aggregates for highly active sers substrates and application in dna detection. *The Journal of Physical Chemistry C*, 112 (5):1415–1422, 2008.

[132] Latha A. Gearheart, Harry J. Ploehn, and Catherine J. Murphy. Oligonucleotide adsorption to gold nanoparticles: A surface-enhanced raman spectroscopy study of intrinsically bent dna. *The Journal of Physical Chemistry B*, 105(50):12609–12615, 2001.

[133] Mino Green, Feng-Ming Liu, Lesley Cohen, Peter Köllensperger, and Tony Cass. Sers platforms for high density dna arrays. *Faraday Discuss.*, 132:269–280, 2006.

[134] Chiara Novara, Alessandro Chiadò, Niccolò Paccotti, Silvia Catuogno, Carla Lucia Esposito, Gerolama Condorelli, Vittorio De Franciscis, Francesco Geobaldo, Paola Rivolo, and Fabrizio Giorgis. Sers-active metal-dielectric nanostructures integrated in microfluidic devices for label-free quantitative detection of mirna. *Faraday Discuss.*, 205:271–289, 2017.

[135] Harsh Sharma and Raj Mutharasan. Review of biosensors for foodborne pathogens and toxins. *Sensors and Actuators B: Chemical*, 183:535 – 549, 2013.

[136] Shalini Prasad. Nanobiosensors: the future for diagnosis of disease? 3:1, 08 2014.

[137] Ruth Hall Sedlak and Keith R. Jerome. Viral diagnostics in the era of digital polymerase chain reaction. *Diagnostic Microbiology and Infectious Disease*, 75(1):1 – 4, 2013.

[138] Judith H. Henkel, Stephan W. Aberle, Michael Kundi, and Therese Popow-Kraupp. Improved detection of respiratory syncytial virus in nasal aspirates by seminested rt-pcr. *Journal of Medical Virology*, 53(4):366–371.

[139] Jinghui Wang, M. Josephine Morton, Christopher T. Elliott, Nitsara Karoonuthaisiri, Laura Segatori, and Sibani Lisa Biswal. Rapid detection of pathogenic bacteria and screening of phage-derived peptides using microcantilevers. *Analytical Chemistry*, 86 (3):1671–1678, 2014.

[140] B Ilic, Y Yang, and H.G. Craighead. Virus detection using nanoelectromechanical devices. 85:2604–2606, 09 2004.

[141] Kim A Donaldson, Marianne F Kramer, and Daniel V Lim. A rapid detection method for vaccinia virus, the surrogate for smallpox virus. *Biosensors and Bioelectronics*, 20 (2):322 – 327, 2004.

[142] Chris Rowe Taitt, George P. Anderson, and Frances S. Ligler. Evanescent wave fluorescence biosensors. *Biosensors and Bioelectronics*, 20(12):2470 – 2487, 2005.

[143] Yurii G. Kuznetsov, Sarah Daijogo, Jiashu Zhou, Bert L. Semler, and A. McPherson. Atomic force microscopy analysis of icosahedral virus rna. *Journal of Molecular Biology*, 347(1):41 – 52, 2005.

[144] Nicholas E. Kurland, Zouheir Drira, and Vamsi K. Yadavalli. Measurement of nanomechanical properties of biomolecules using atomic force microscopy. *Micron*, 43(2): 116 – 128, 2012.

[145] M.S. Ibelings, K. Maquelin, H. Ph. Endtz, H.A. Bruining, and G.J. Puppels. Rapid identification of candida spp. in peritonitis patients by raman spectroscopy. *Clinical Microbiology and Infection*, 11(5):353 – 358, 2005.

[146] Didier Hutsebaut, K Maquelin, Paul De Vos, Peter Vandenabeele, Luc Moens, and Gerwin Puppels. Effect of culture conditions on the achievable taxonomic resolution of raman spectroscopy disclosed by three bacillus species. 76:6274–81, 12 2004.

[147] W. R. Premasiri, D. T. Moir, M. S. Klempner, N. Krieger, G. Jones, and L. D. Ziegler. Characterization of the surface enhanced raman scattering (sers) of bacteria. *The Journal of Physical Chemistry B*, 109(1):312–320, 2005.

[148] W R. Premasiri, Donald Moir, M S. Klempner, and L Ziegler. Surface-enhanced raman scattering of microorganisms, 08 2007.

[149] Alessandro Virga Paola Rivolo Sergio Ferrero Alessandro Chiolerio-Francesco Geobaldo Samuele Porro Novara Chiara, Francesco Petracca and Fabrizio Giorgis. Sers active silver nanoparticles synthesized by inkjet printing on mesoporous silicon. *Nanoscale Research Letters*, pages 9–527, 2014.

[150] Arnab Bhattacharyya, S Kumar, S Jana, Parameshwar Yadav, Kumar Gaurav, S Prabha, Vidya Kujur, and Prachurya Bharadwaj. Sputtering based epitaxial growth and modeling of cu/si thin films. 08 2015.

[151] Yingying Zhao, Yuqiong Wang, Yuefeng Yang, Jingqi Liu, Yang Song, Yan Cao, Xiaoyu Chen, Wenzhuo Yang, Fei Wang, Jun Gao, Zhaoshen Li, and Changqing Yang. Microrna-222 controls human pancreatic cancer cell line capan-2 proliferation by p57 targeting. *Journal of Cancer*, 6(12):1230—1235, 2015.

[152] Rao Fu, Can Wang, Jiaqi Zhuang, and Wensheng Yang. Adsorption and desorption of dna on bovine serum albumin modified gold nanoparticles. *Colloids and Surfaces A: Physicochemical and Engineering Aspects*, 444:326 – 329, 2014.

Appendices

Appendix A

Results of experiments

A.1 PDMS SERS substrates with sputtered Ag-NPs

UV-Vis in air

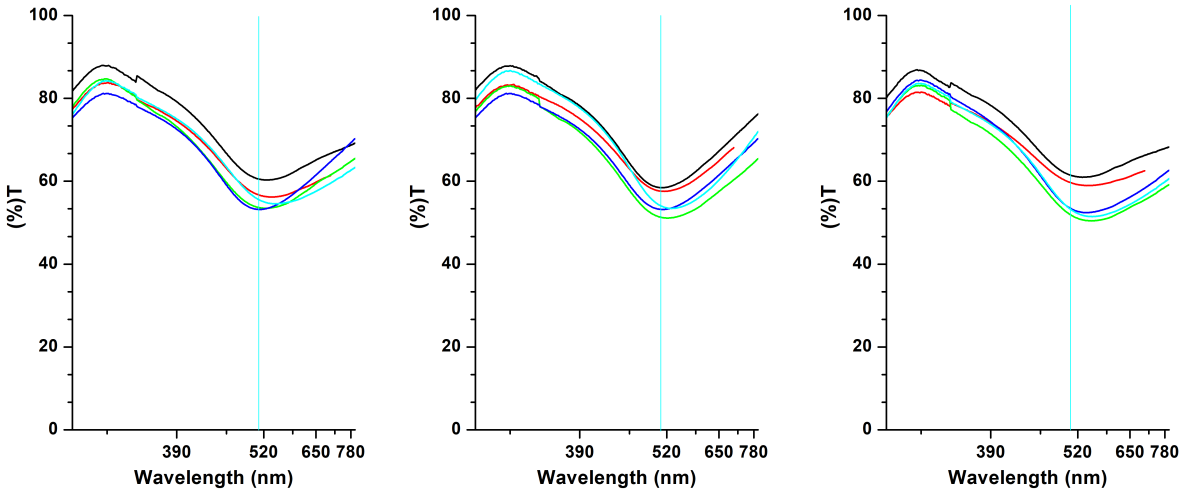

(a) UV-Vis in Air at the conditions of 40 mA, 3 s, 4 cm

(b) UV-Vis in Air at the conditions of 40 mA, 3 s, 4.5 cm

(c) UV-Vis in Air at the conditions of 40 mA, 4 s, 4.5 cm

Fig. A.1 UV-Vis measurements in air for 1 mm PDMS membranes (10:1 curing ratio) with sputtered Ag-NPs at different synthesis conditions. Different curves for the same condition correspond to different samples, fabricated at same synthesis parameters.

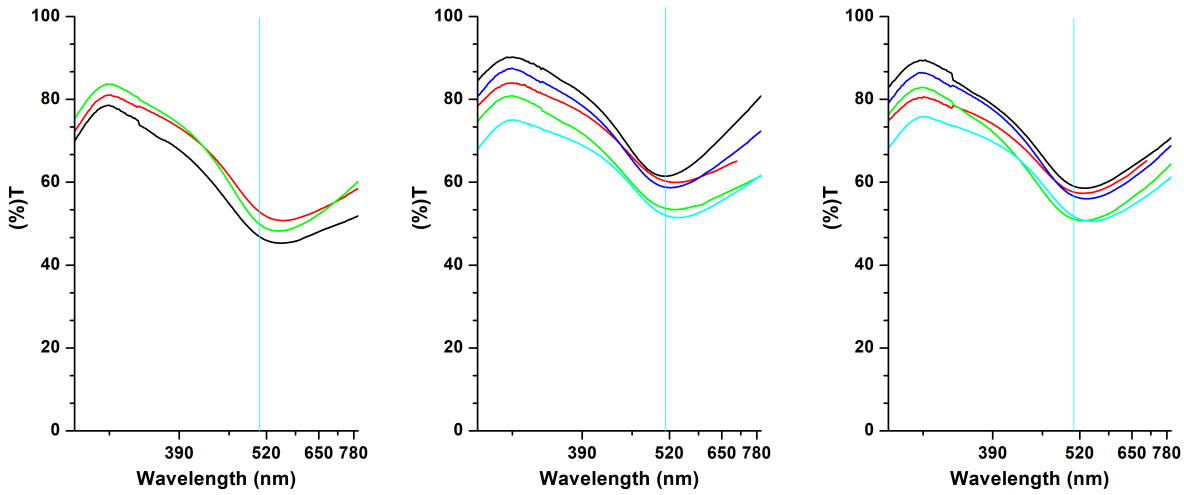

(a) UV-Vis in Air at the conditions of 40 mA, 5 s, 5 cm

(b) UV-Vis in Air at the conditions of 50 mA, 2s, 4 cm

(c) UV-Vis in Air at the conditions of 50 mA, 3s, 5 cm

Fig. A.2 UV-Vis measurements in air for 1 mm PDMS membranes (10:1 curing ratio) with sputtered Ag-NPs at different synthesis conditions. Different curves for the same condition correspond to different samples, fabricated at same synthesis parameters.

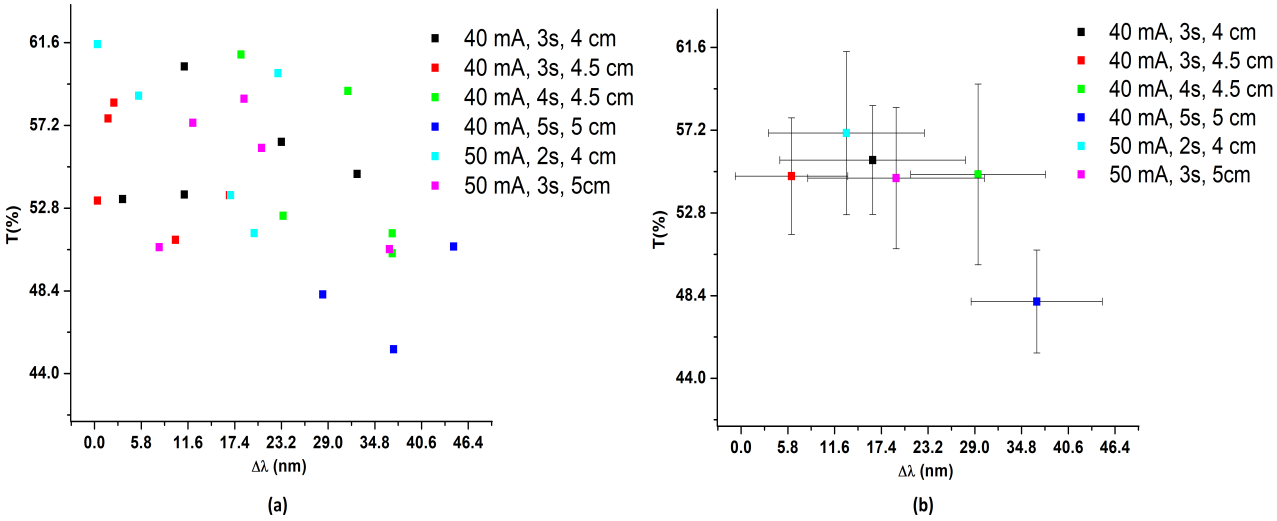

Fig. A.3 Dip transmittance vs. $\Delta\lambda$ for samples with different sputtering conditions. Different points at same colours (a) represent different samples at same synthesis conditions.
In the figure (b) the different points represent mean points of all the samples. The bars are standard deviation of the transmittance (vertical bar) and of the difference from the wavelength of the lase (horizontal bars).

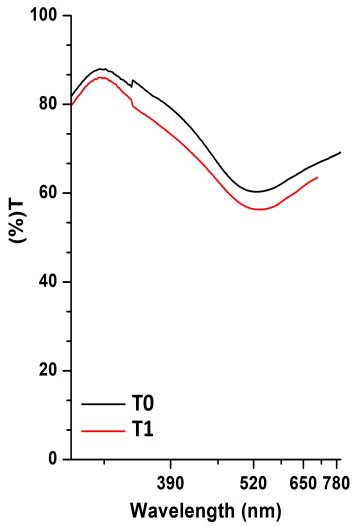

(a) UV-Vis in Air at the conditions of 40 mA, 3 s, 4 cm

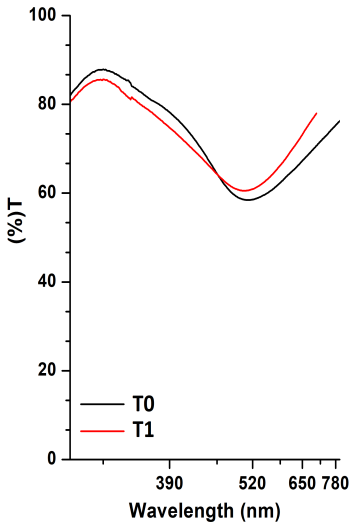

(b) UV-Vis in Air at the conditions of 40 mA, 3 s, 4.5 cm

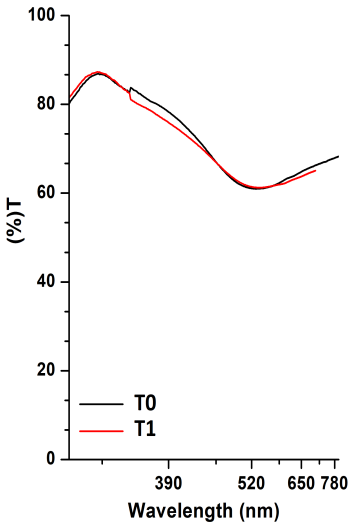

(c) UV-Vis in Air at the conditions of 40 mA, 4 s, 4.5 cm

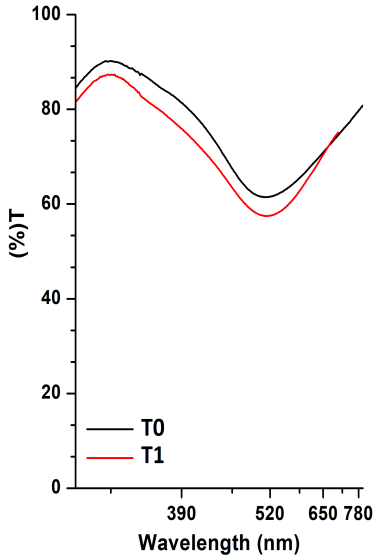

(d) UV-Vis in Air at the conditions of 50 mA, 2 s, 4 cm

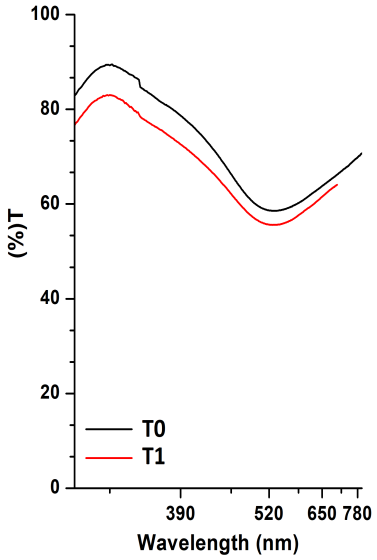

(e) UV-Vis in Air at the conditions of 50 mA, 3 s, 5 cm

Fig. A.4 UV-Vis measurements in air for 1 mm PDMS membranes (10:1 curing ratio) with sputtered Ag-NPs at different synthesis conditions, for the sample (black line) and the same sample after one week (red line) in air.

FESEM images

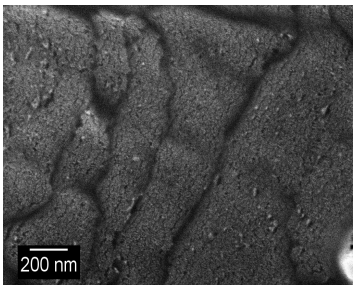

(a) FESEM image of sample with deposition conditions of 40 mA, 3 s, 4 cm

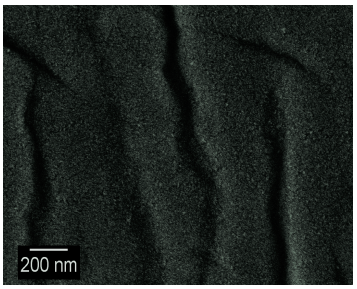

(b) FESEM image of sample with deposition conditions of 40 mA, 3 s, 4.5 cm

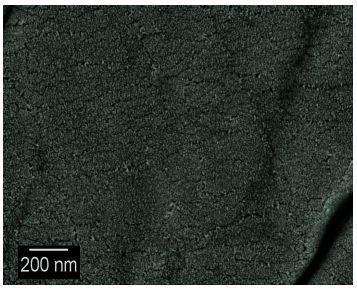

(c) FESEM image of sample with deposition conditions of 40 mA, 4s, 4.5 cm

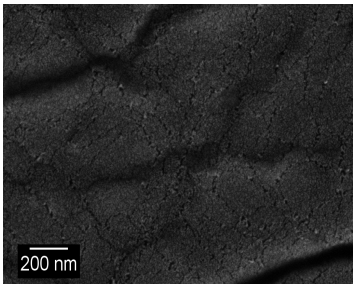

(d) FESEM image of sample with deposition conditions of 40 mA, 5 s, 5 cm

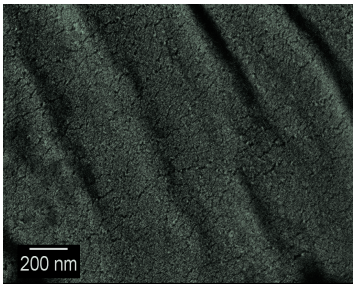

(e) FESEM image of sample with deposition conditions of 50 mA, 2 s, 4 cm

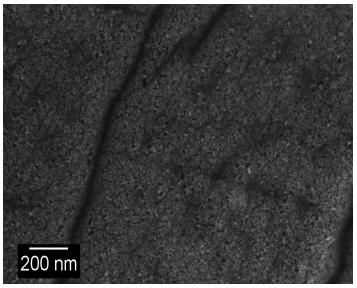

(f) FESEM image of sample with deposition conditions of 50 mA, 3s, 5 cm

Fig. A.5 FESEM images of samples with 1 mm PDMS membranes (10:1 curing ratio) and sputtered Ag-NPs at different synthesis conditions.

A.2 Thickness of the PDMS membranes

UV-Vis in air

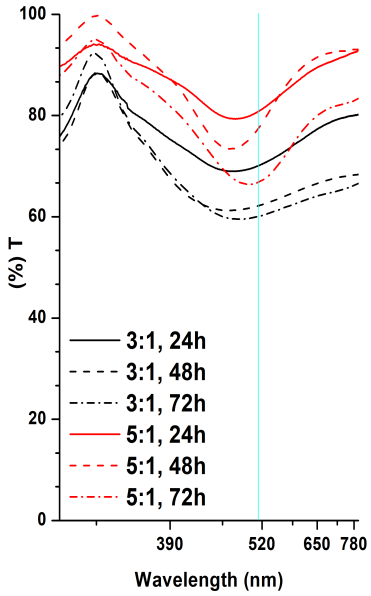

(a) UV-Vis in Air for 0.5mm, 20°C, Totally cross-linked

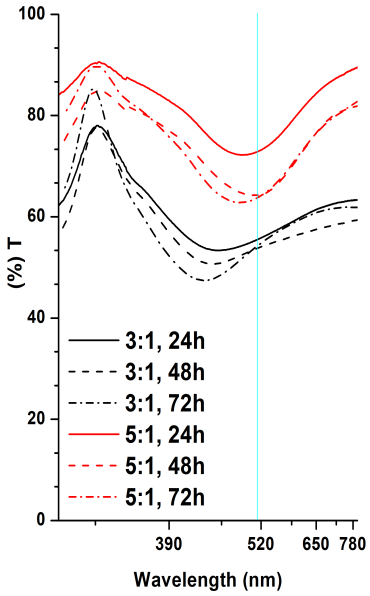

(b) UV-Vis in Air for 1mm, 20°C, Totally cross-linked

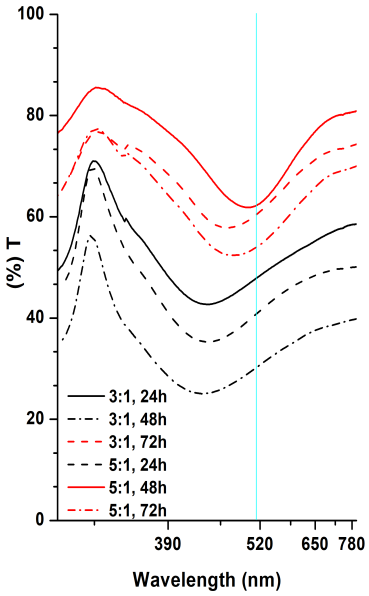

(c) UV-Vis in Air for 2mm, 20°C, Totally cross-linked

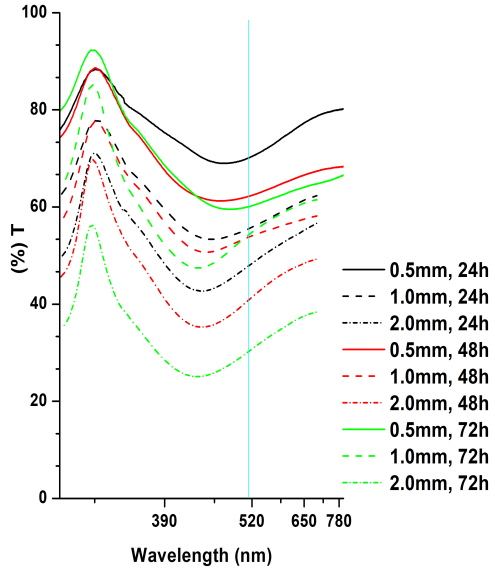

(d) UV-Vis in Air for 3:1, 20°C, Totally cross-linked

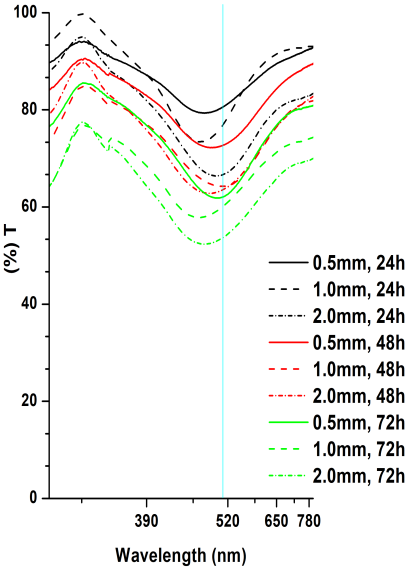

(e) UV-Vis in Air for 5:1, 20°C, Totally cross-linked

Fig. A.6 UV-Vis measurements in air for PDMS thickness of 0.5*mm* (a), 1*mm* (b) and 2*mm* (c). UV-Vis measurements in air for curing ratio of 3:1 (d) and 5:1 (e) at different substrate thickness

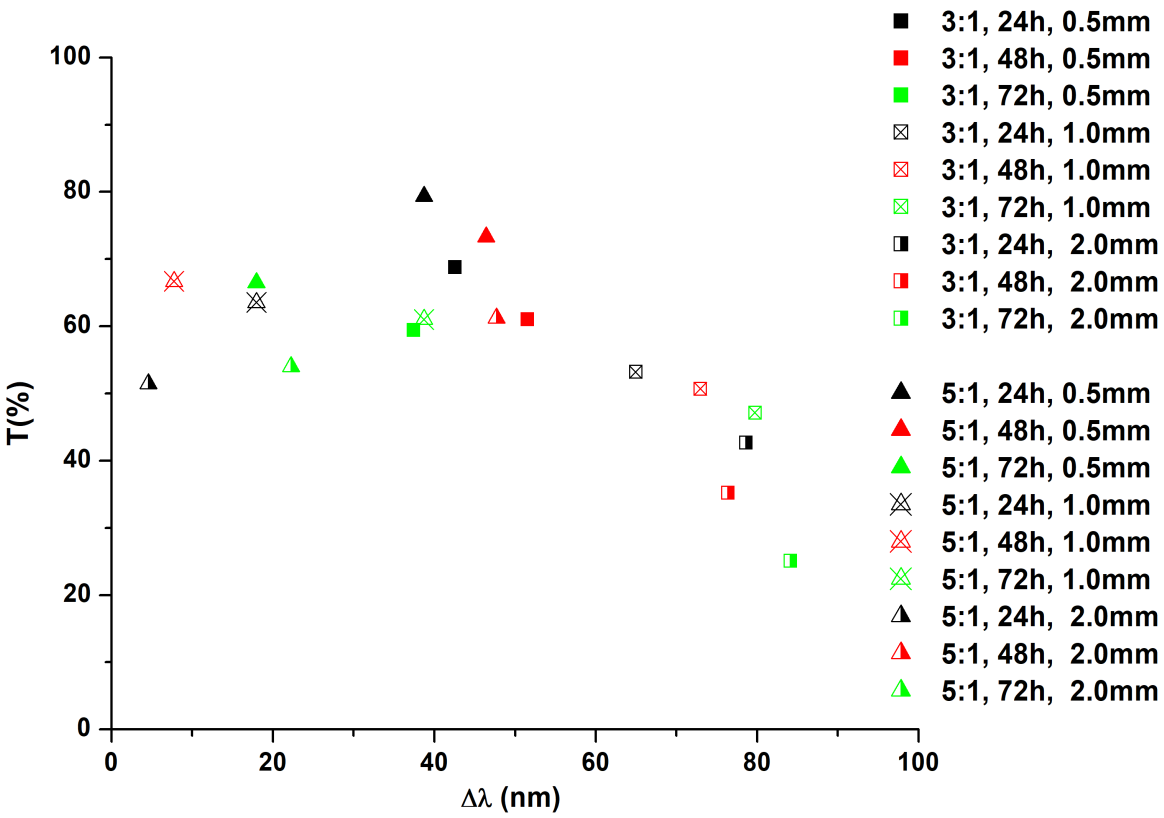

Fig. A.7 Dip transmittance vs. $\Delta\lambda$ for samples with different substrate thickness.

UV-Vis in water

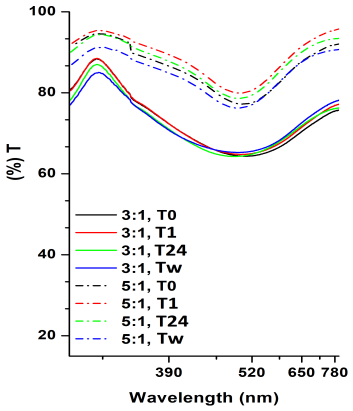

(a) UV-Vis in Water for 24h, 20°C, 0.5mm

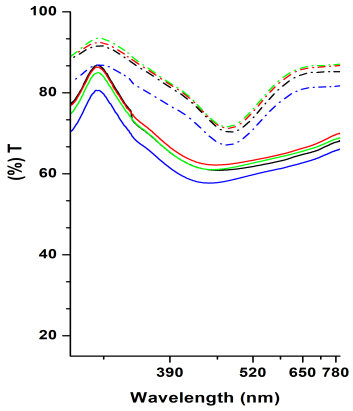

(b) UV-Vis in Water for 48h, 20°C, 0.5mm

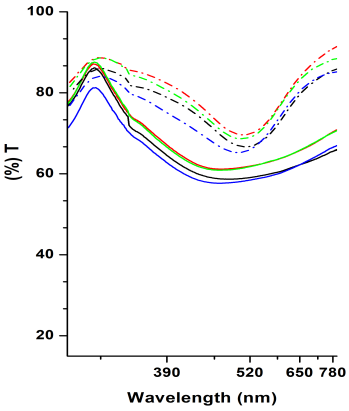

(c) UV-Vis in Water for 72h, 20°C, 0.5mm

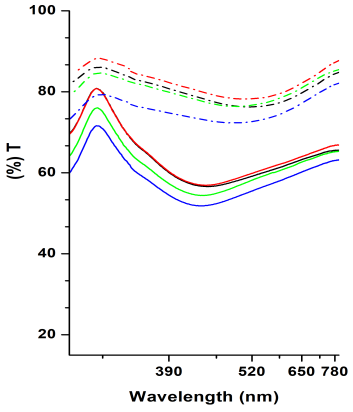

(d) UV-Vis in Water for 24h, 20°C, 1mm

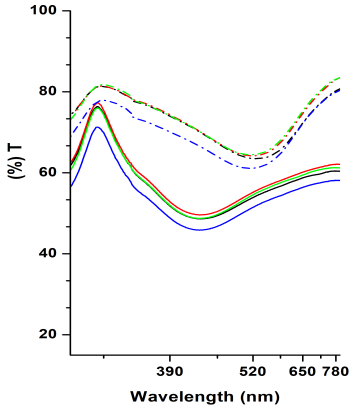

(e) UV-Vis in Water for 48h, 20°C, 1mm

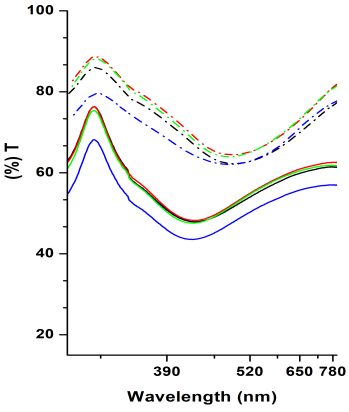

(f) UV-Vis in Water for 72h, 20°C, 1mm

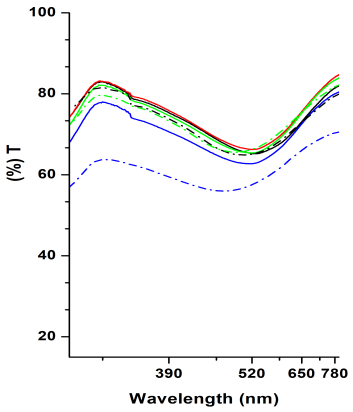

(g) UV-Vis in Water for 24h, 20°C, 2mm

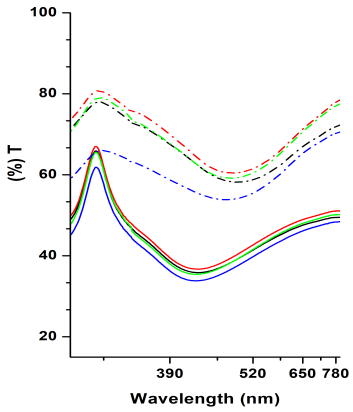

(h) UV-Vis in Water for 48h, 20°C, 2mm

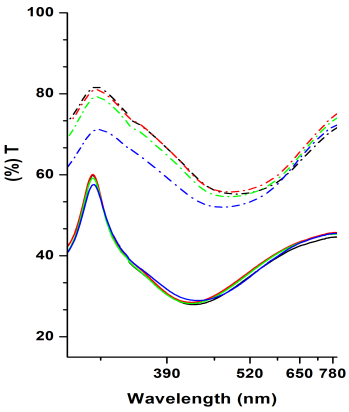

(i) UV-Vis in Water for 72h, 20°C, 2mm

Fig. A.8 UV-Vis measurements in water for different substrate thickness at different time intervals

UV-Vis in TE-NaCl solution

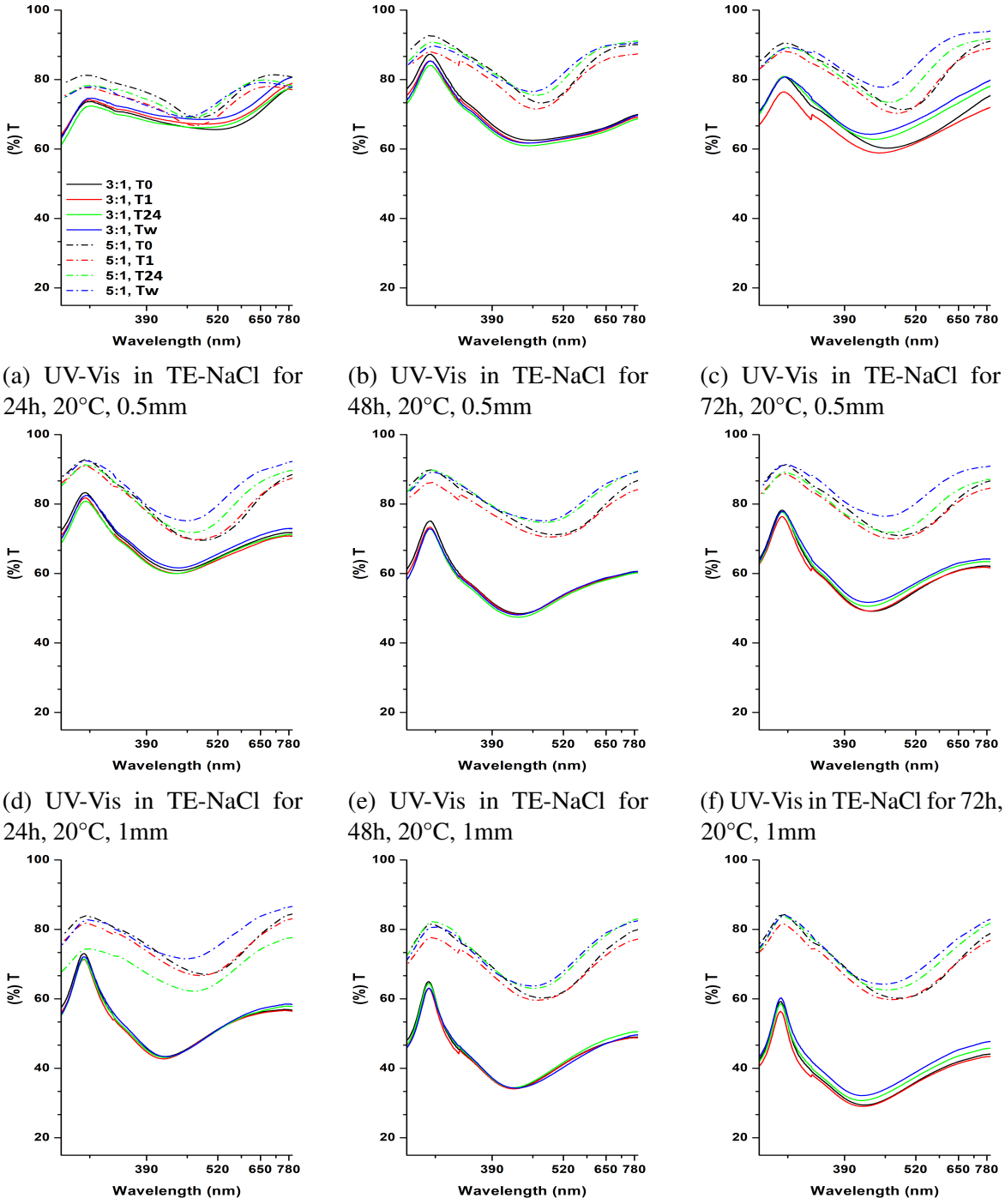

(a) UV-Vis in TE-NaCl for 24h, 20°C, 0.5mm

(b) UV-Vis in TE-NaCl for 48h, 20°C, 0.5mm

(c) UV-Vis in TE-NaCl for 72h, 20°C, 0.5mm

(d) UV-Vis in TE-NaCl for 24h, 20°C, 1mm

(e) UV-Vis in TE-NaCl for 48h, 20°C, 1mm

(f) UV-Vis in TE-NaCl for 72h, 20°C, 1mm

(g) UV-Vis in TE-NaCl for 24h, 20°C, 2mm

(h) UV-Vis in TE-NaCl for 48h, 20°C, 2mm

(i) UV-Vis in TE-NaCl for 72h, 20°C, 2mm

Fig. A.9 UV-Vis measurements in TE-NaCl solution for different substrate thickness at different time intervals

FESEM Images

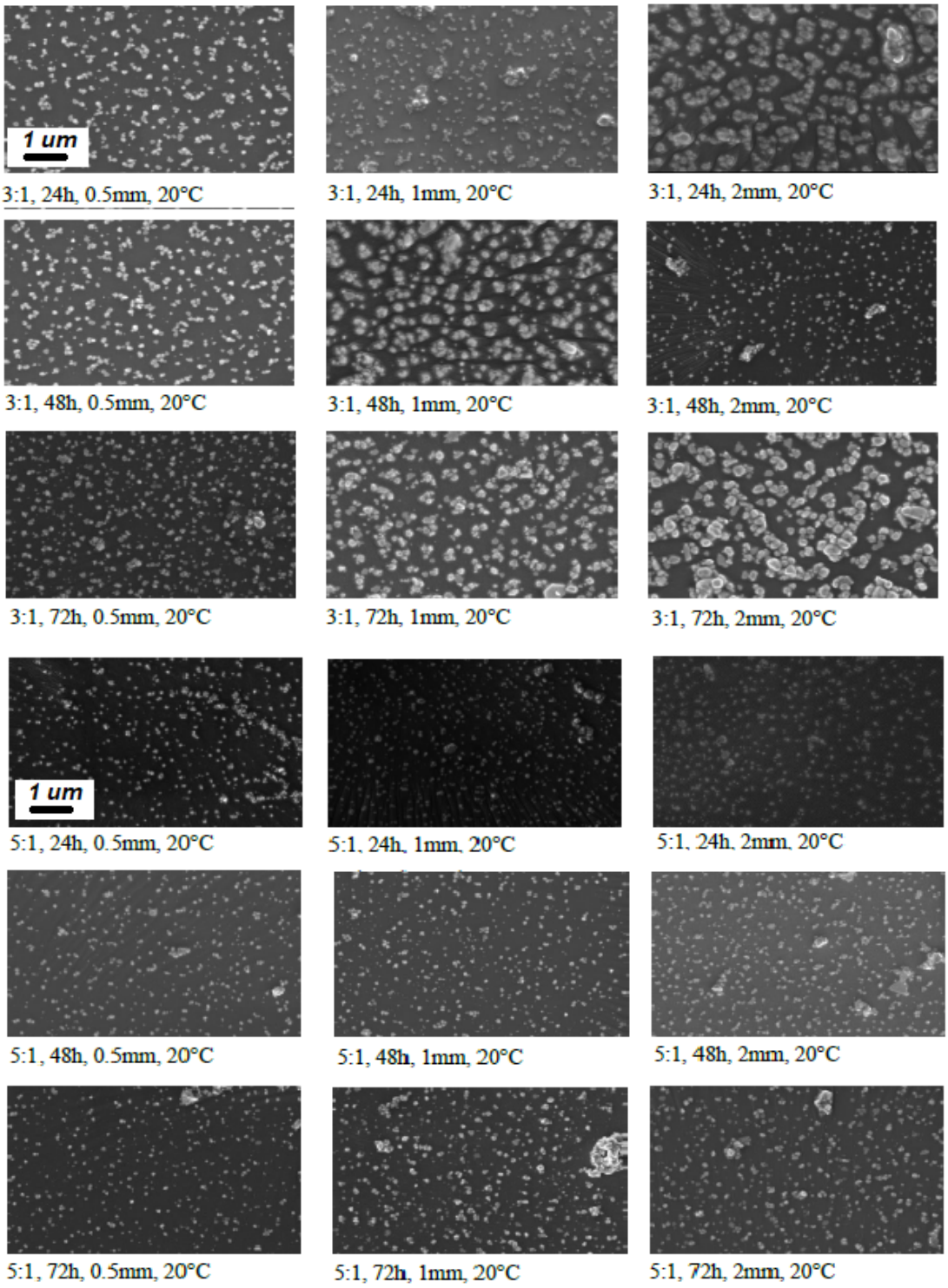

Fig. A.10 FESEM images of samples for different thickness at 50kx magnification

Raman efficiency and uniformity

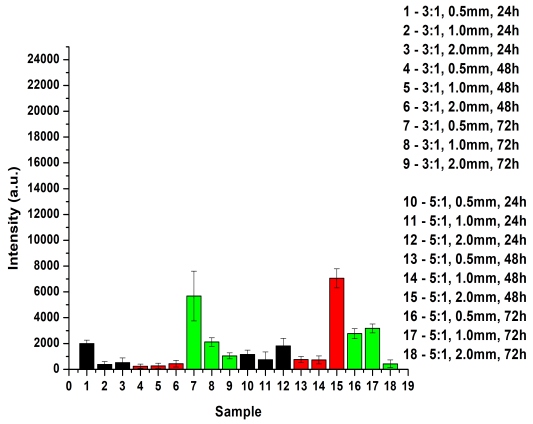

(a) Average intensities of the SERS substrates synthesised for different thickness of the PDMS membranes

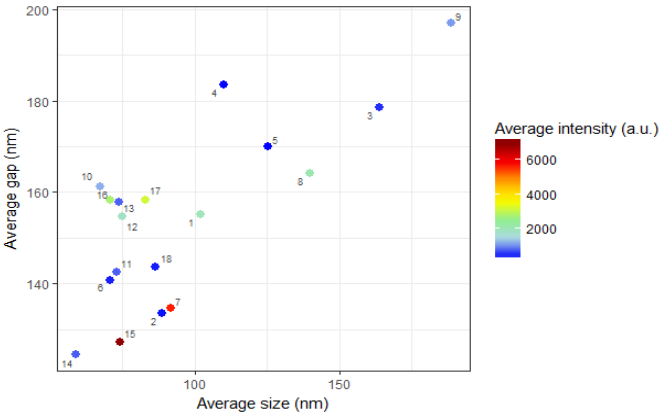

(b) Each point represents a sample: the colour represents the Average intensity in arbitrary unit, while in the y- and x-axis, the average size of the Ag-NPs and their Average inter-gap distance are used respectively.

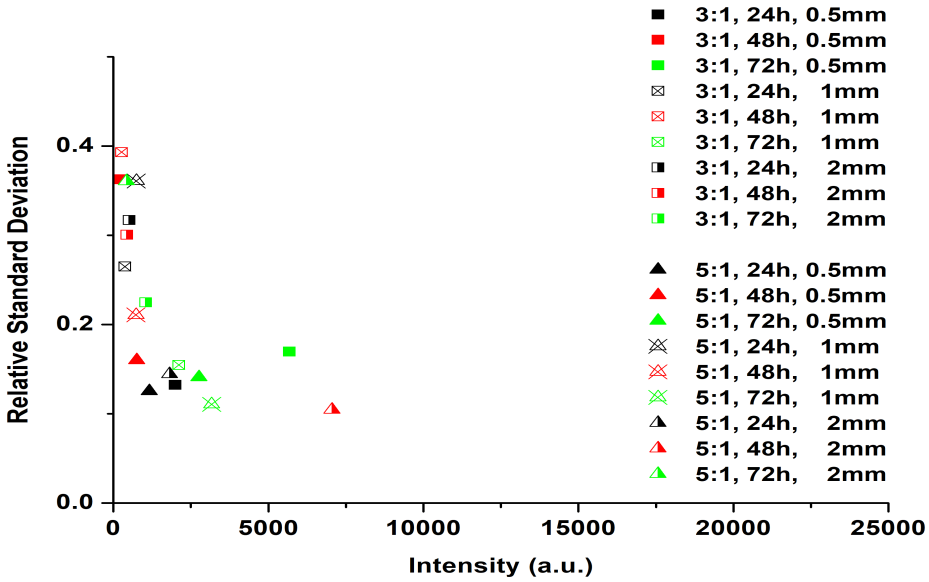

(c) Relative Standard Deviation vs. average intensity of the SERS substrates synthesised for different thickness of the PDMS membranes.

Fig. A.11 Raman efficiency and uniformity of SERS substrates synthesised for different thickness of the PDMS membranes

A.3 Incubation temperature of PDMS membranes

UV-Vis in air

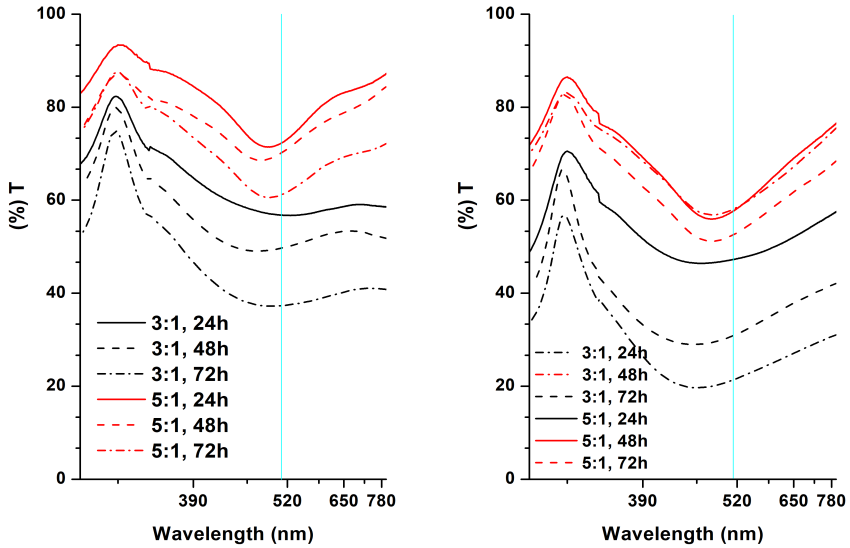

(a) UV-Vis in Air for 20°C, 1mm, Totally cross-linked

(b) UV-Vis in Air for 40°C, 1mm, Totally cross-linked

Fig. A.12 UV-Vis measurements in air for incubation temperature of 20°*C* (a) and 40°*C* (b)

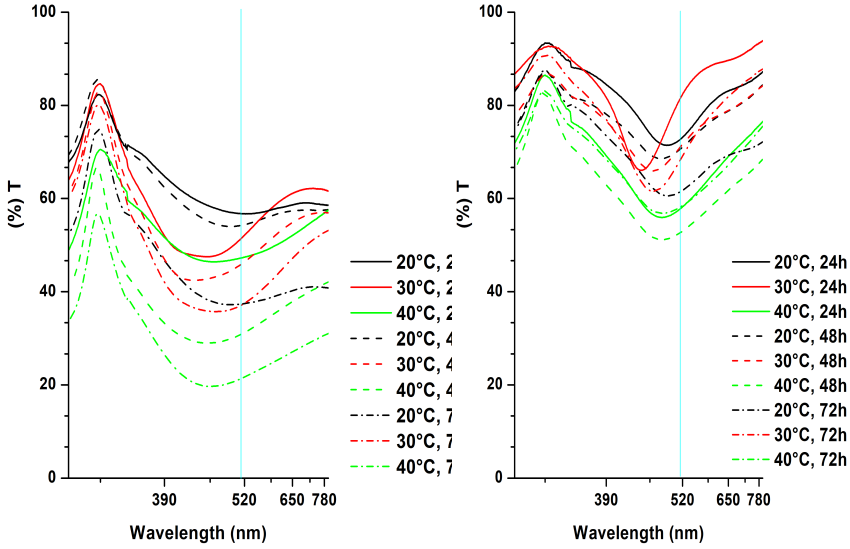

(a) UV-Vis in Air for 3:1, 1mm, Totally cross-linked

(b) UV-Vis in Air for 5:1, 1mm, Totally cross-linked

Fig. A.13 UV-Vis measurements in air for curing ratio of 3:1 (a) and 5:1 (b) at different incubation temperature

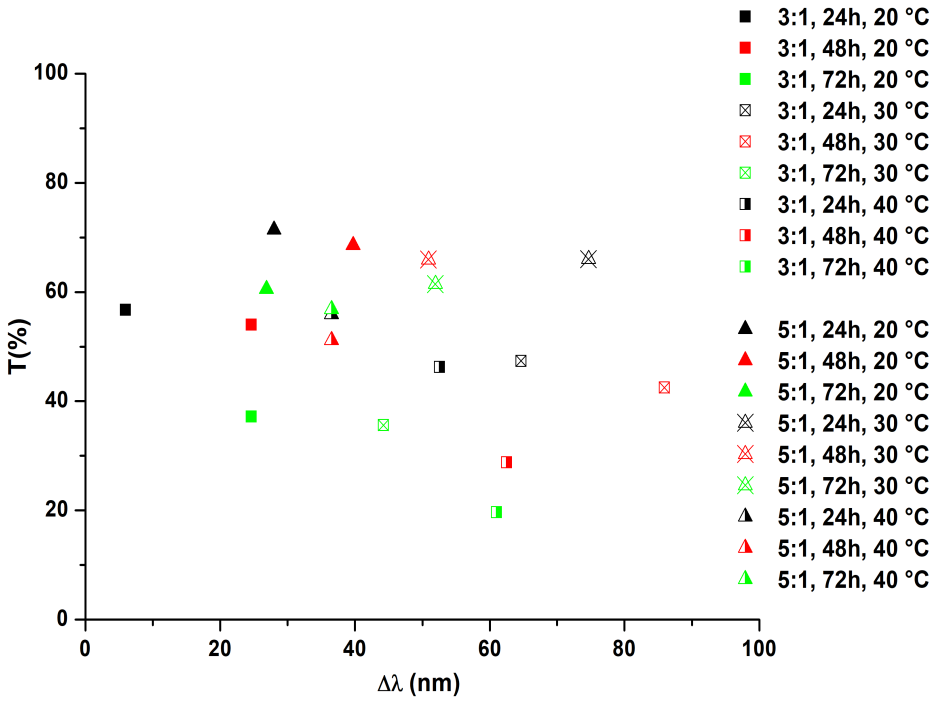

Fig. A.14 Dip transmittance vs. $\Delta\lambda$ for samples at different incubation temperatures.

UV-Vis in water

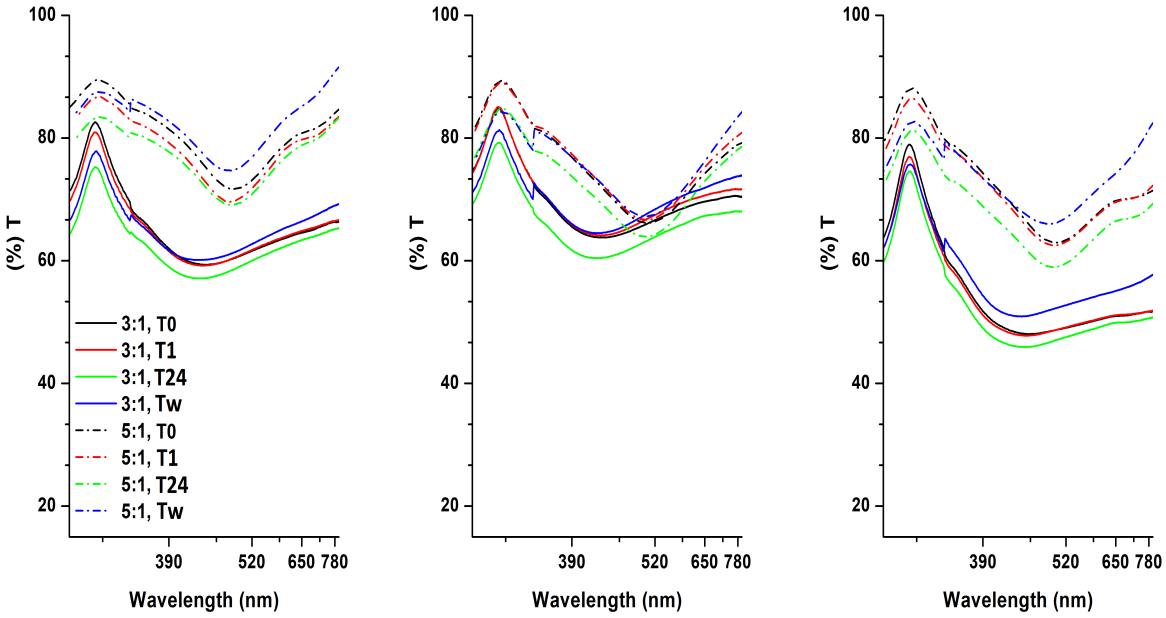

(a) UV-Vis in Water for 24h 20°C, Totally cross-linked

(b) UV-Vis in Water for 48h 20°C, Totally cross-linked

(c) UV-Vis in Water for 72h 20°C, Totally cross-linked

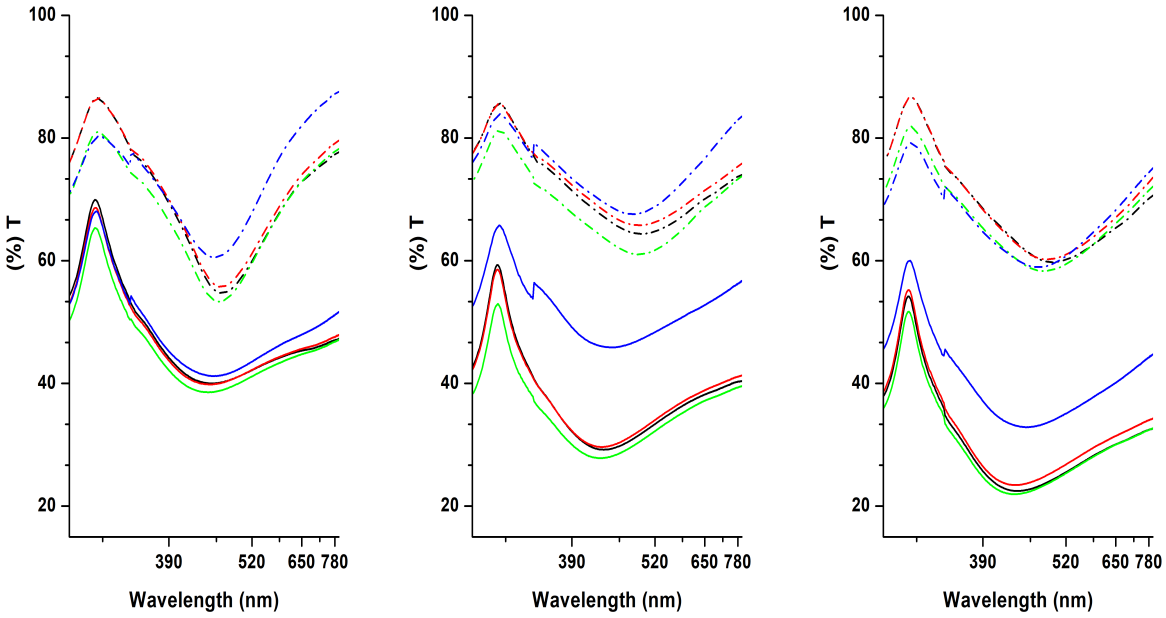

(d) UV-Vis in Water for 24h 40°C, Totally cross-linked

(e) UV-Vis in Water for 48h 40°C, Totally cross-linked

(f) UV-Vis in Water for 72h 40°C, Totally cross-linked

Fig. A.15 UV-Vis measurements in water for different incubation temperature at different time intervals

UV-Vis in TE-NaCl solution

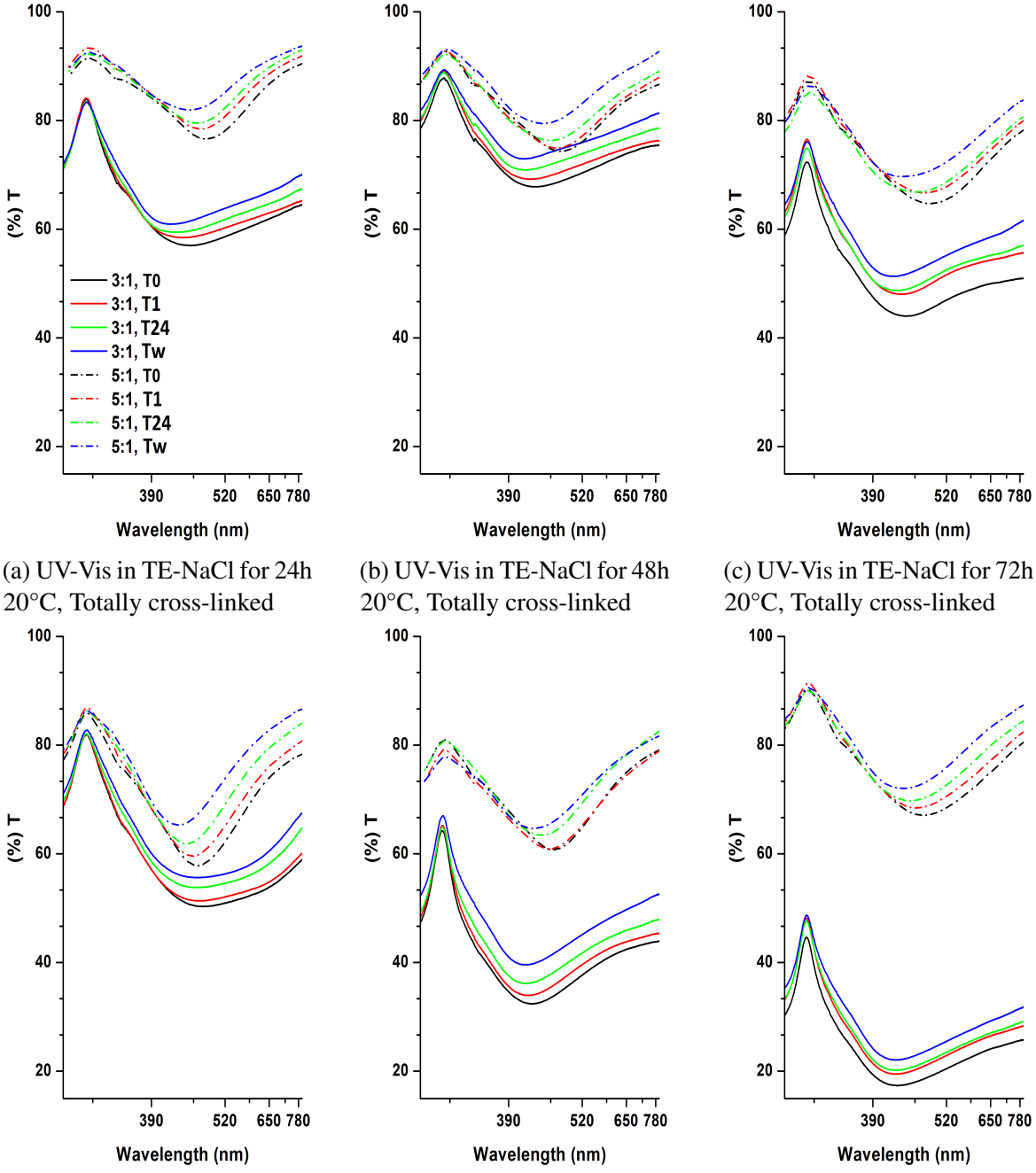

(a) UV-Vis in TE-NaCl for 24h 20°C, Totally cross-linked

(b) UV-Vis in TE-NaCl for 48h 20°C, Totally cross-linked

(c) UV-Vis in TE-NaCl for 72h 20°C, Totally cross-linked

(d) UV-Vis in TE-NaCl for 24h 40°C, Totally cross-linked

(e) UV-Vis in TE-NaCl for 48h 40°C, Totally cross-linked

(f) UV-Vis in TE-NaCl for 72h 40°C, Totally cross-linked

Fig. A.16 UV-Vis measurements in TE-NaCl solution for different incubation temperature at different time intervals

FESEM Images

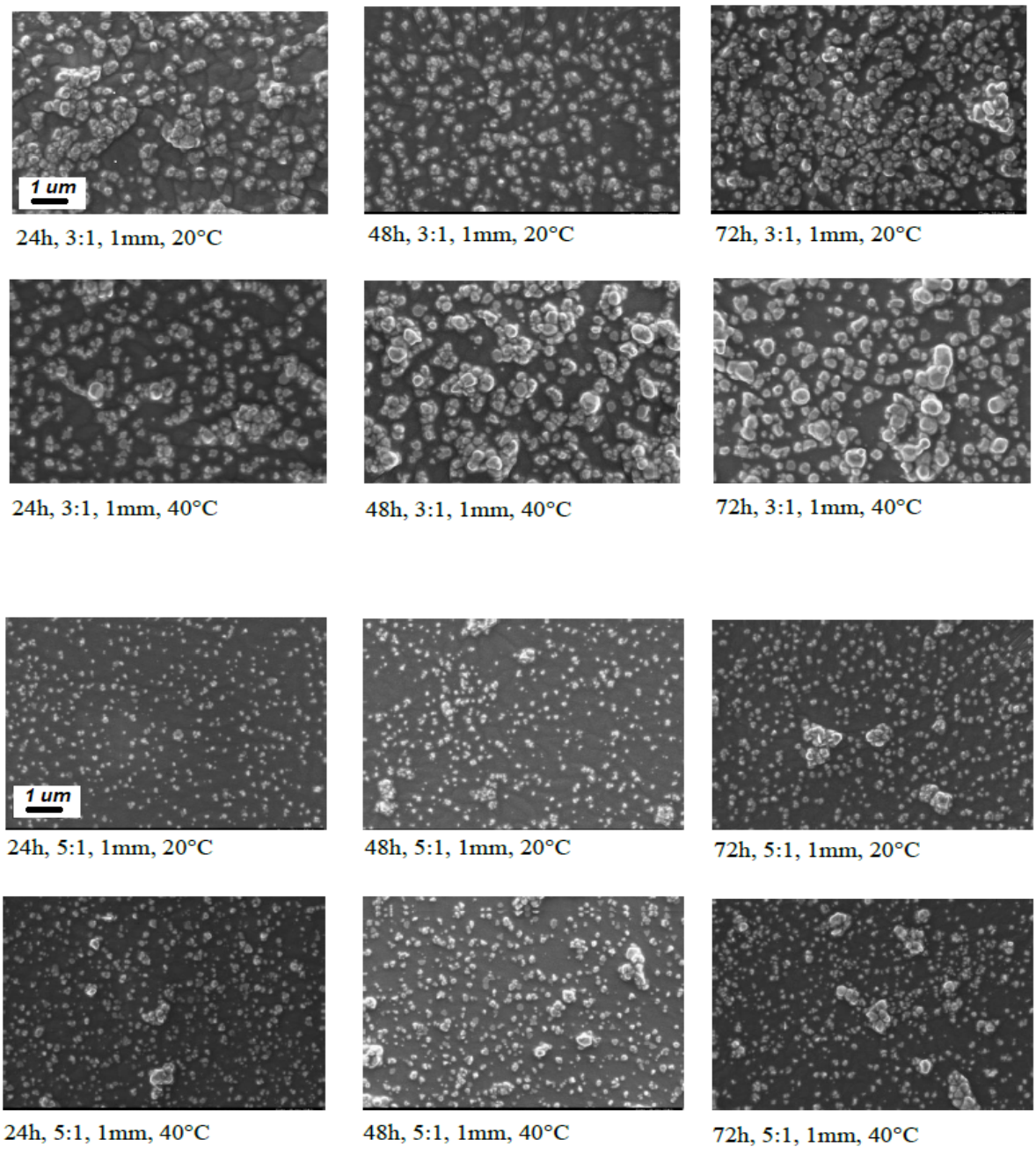

Fig. A.17 FESEM images of samples for different incubation temperature at 50kx magnification

Raman efficiency and uniformity

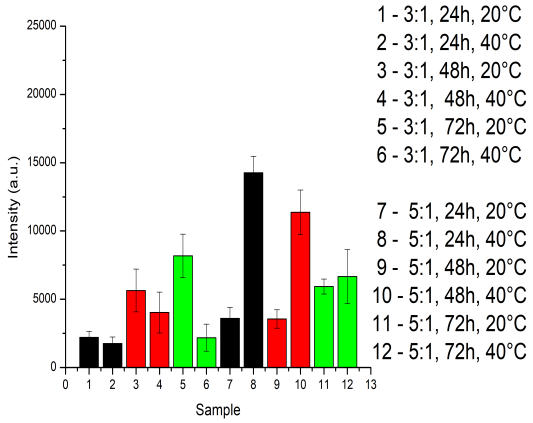

(a) Average intensities of the SERS substrates synthesised for different incubation temperatures of the PDMS membranes

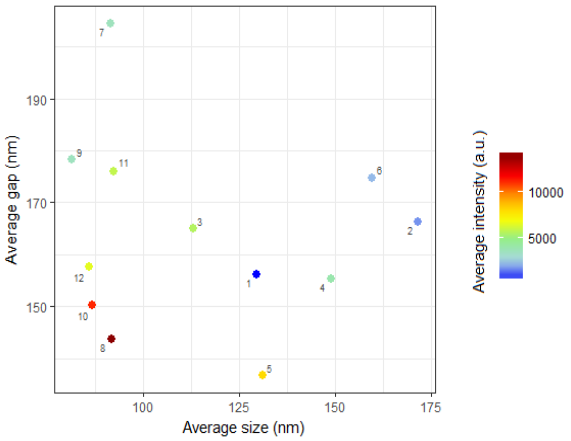

(b) Each point represents a sample: the colour represents the Average intensity in arbitrary unit, while in the y- and x-axis, the average size of the Ag-NPs and their Average inter-gap distance are used respectively.

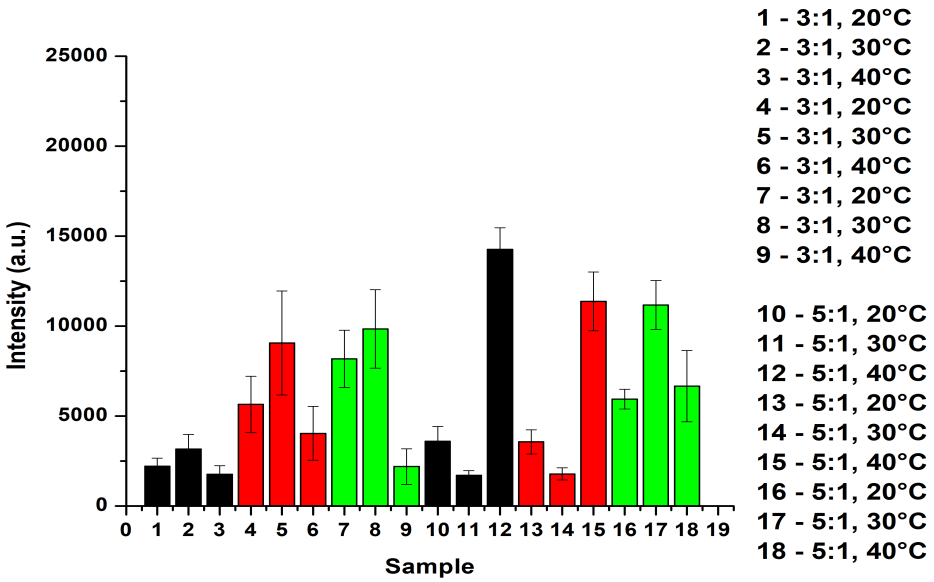

(c) Relative Standard Deviation vs. average intensity of the SERS substrates synthesised for different incubation temperatures of the PDMS membranes.

Fig. A.18 Raman efficiency and uniformity of SERS substrates synthesised for different temperatures of incubation of the PDMS membranes

A.4 Cross-linking degree

UV-Vis in air

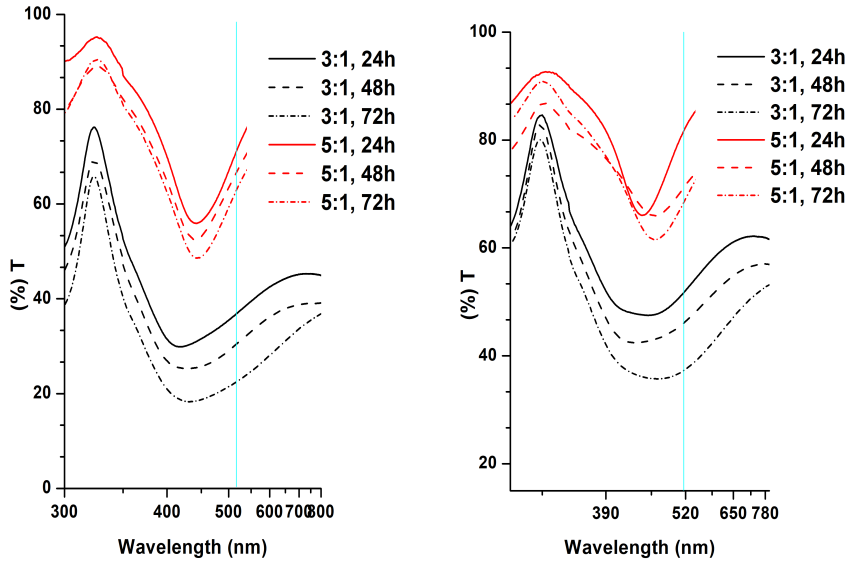

(a) UV-Vis in Air for 30°C, 1mm, Partially cross-linked

(b) UV-Vis in Air for 30°C, 1mm, Totally cross-linked

Fig. A.19 UV-Vis measurements in air for partially cross-linked (a) and totally cross-linked (b) PDMS substrate

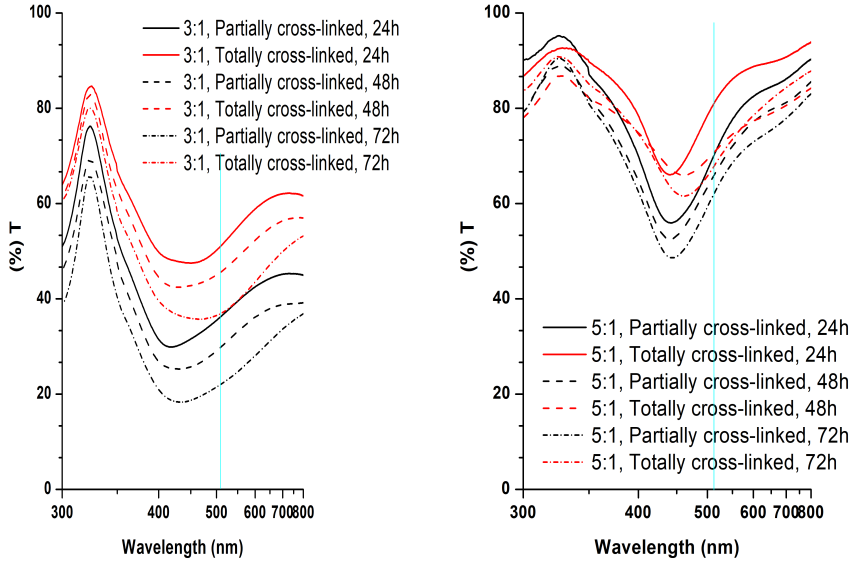

(a) UV-Vis in Air for 3:1, 1mm, 30°C

(b) UV-Vis in Air for 5:1, 1mm, 30°C

Fig. A.20 UV-Vis measurements in air for curing ratio of 3:1 (a) and 5:1 (b) at different PDMS cross-linking degree

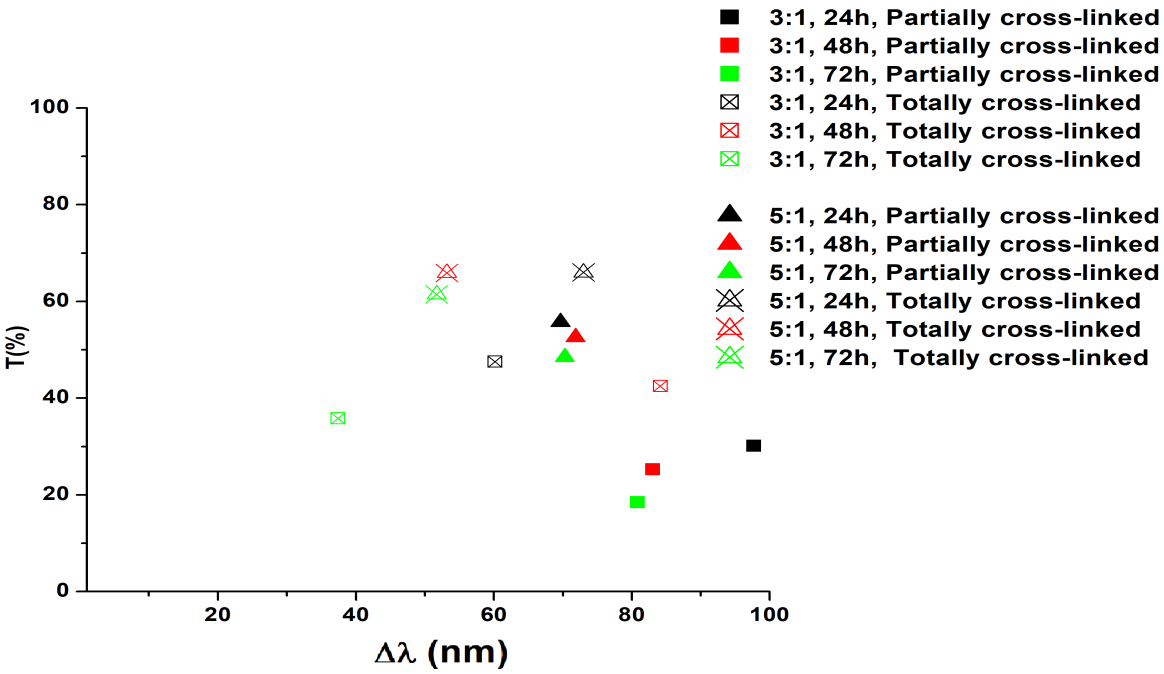

Fig. A.21 Dip transmittance vs. $\Delta\lambda$ for samples with different cross-linking degree.

UV-Vis in water

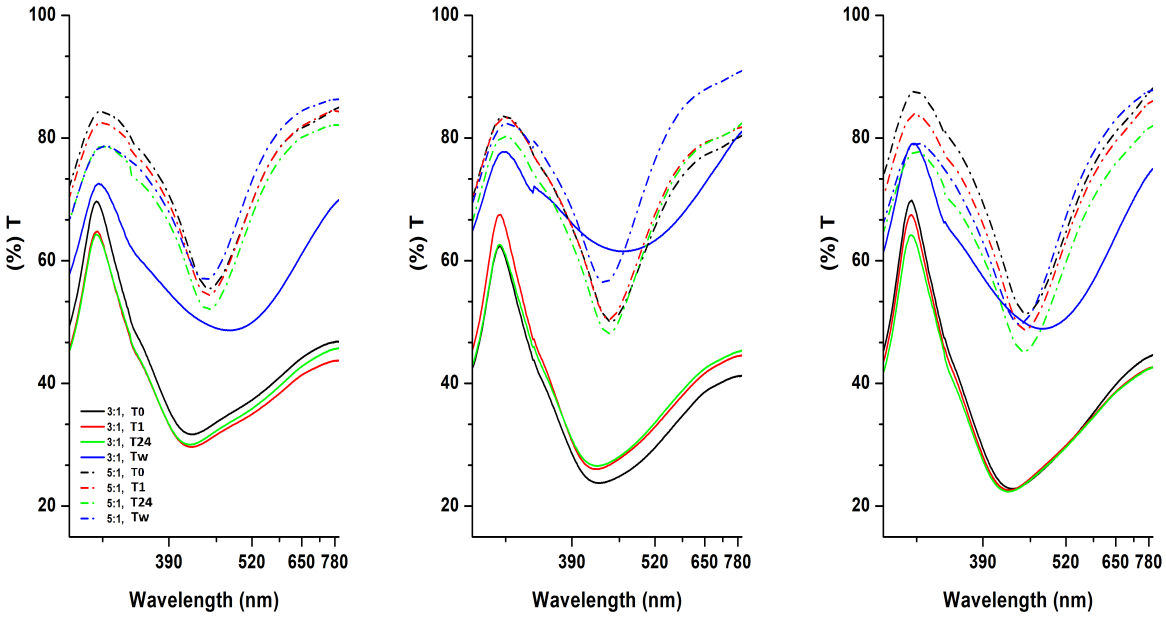

(a) UV-Vis in Water for 24h 30°C, Partially cross-linked

(b) UV-Vis in Water for 48h 30°C, Partially cross-linked

(c) UV-Vis in Water for 72h 30°C, Partially cross-linked

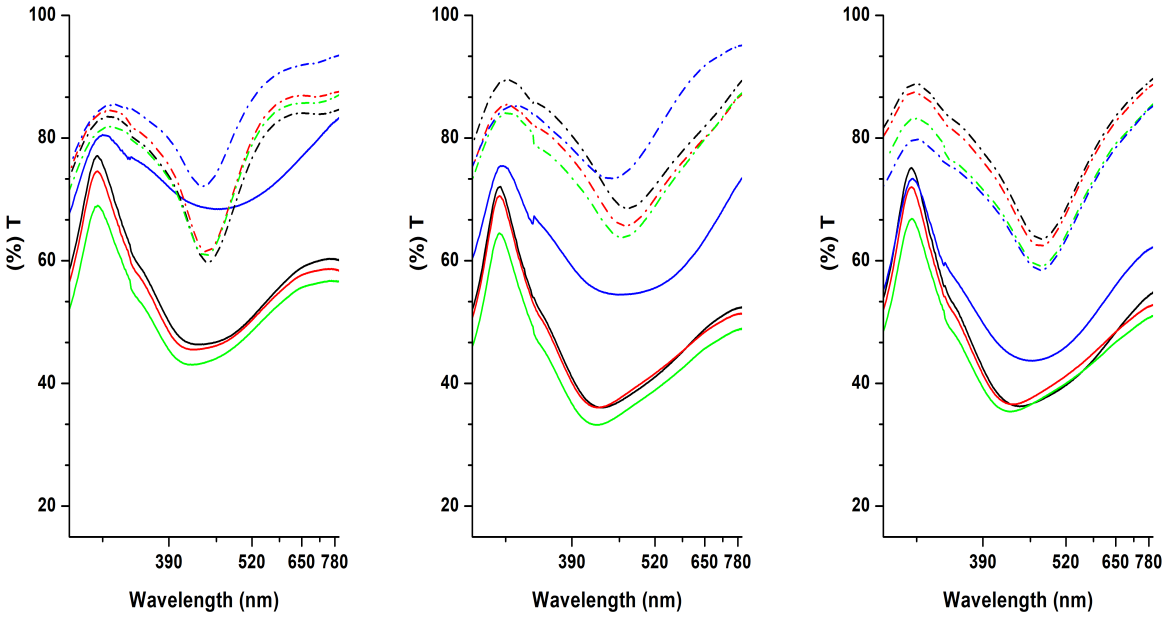

(d) UV-Vis in Water for 24h 30°C, Totally cross-linked

(e) UV-Vis in Water for 48h 30°C, Totally cross-linked

(f) UV-Vis in Water for 72h 30°C, Totally cross-linked

Fig. A.22 UV-Vis measurements in water for different cross-linking degrees at different time intervals

UV-Vis in TE-NaCl solution

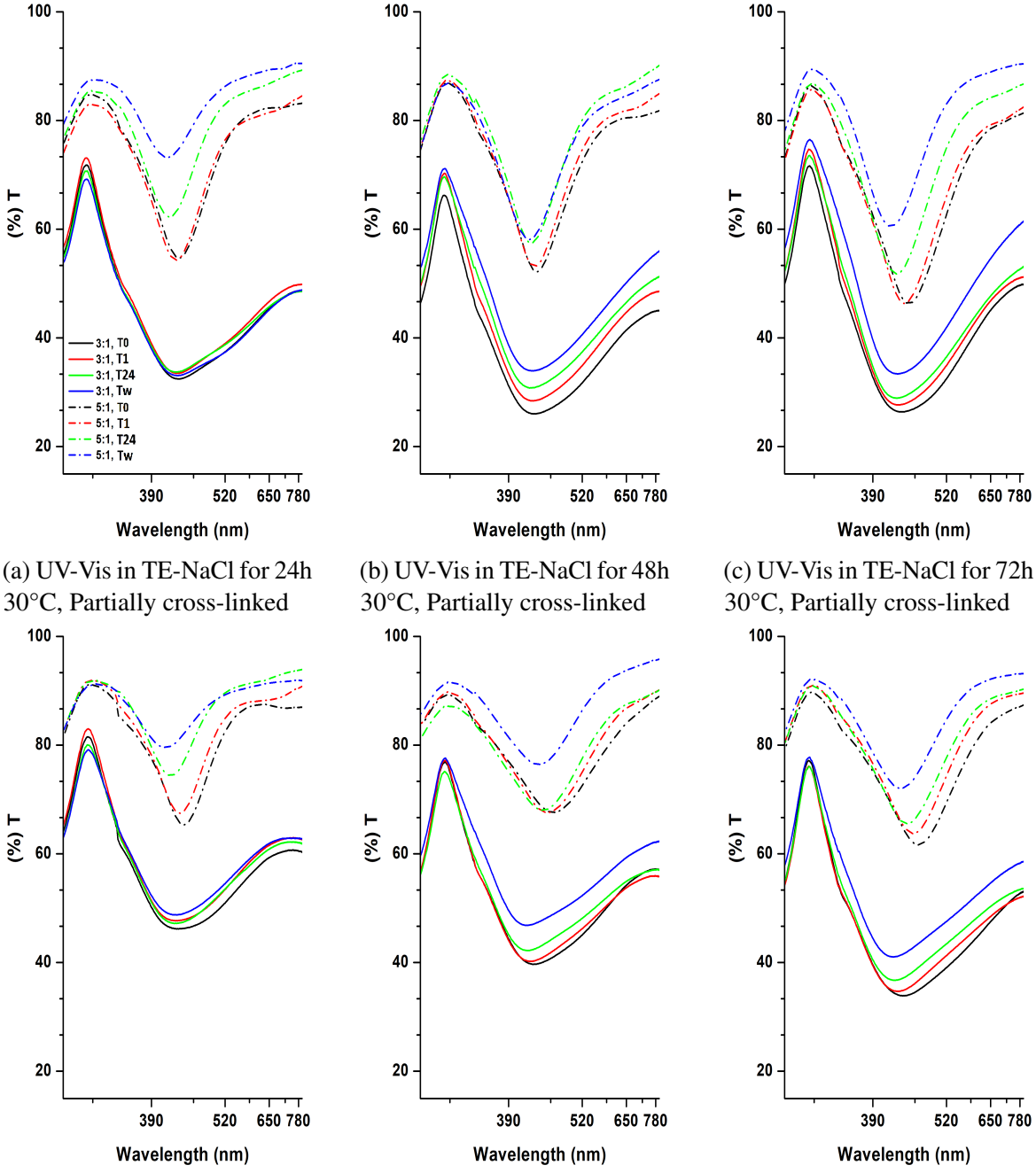

(a) UV-Vis in TE-NaCl for 24h 30°C, Partially cross-linked

(b) UV-Vis in TE-NaCl for 48h 30°C, Partially cross-linked

(c) UV-Vis in TE-NaCl for 72h 30°C, Partially cross-linked

(d) UV-Vis in TE-NaCl for 24h 30°C, Totally cross-linked

(e) UV-Vis in TE-NaCl for 48h 30°C, Totally cross-linked

(f) UV-Vis in TE-NaCl for 72h 30°C, Totally cross-linked

Fig. A.23 UV-Vis measurements in TE-NaCl solution for different cross-linking degrees at different time intervals

FESEM Images

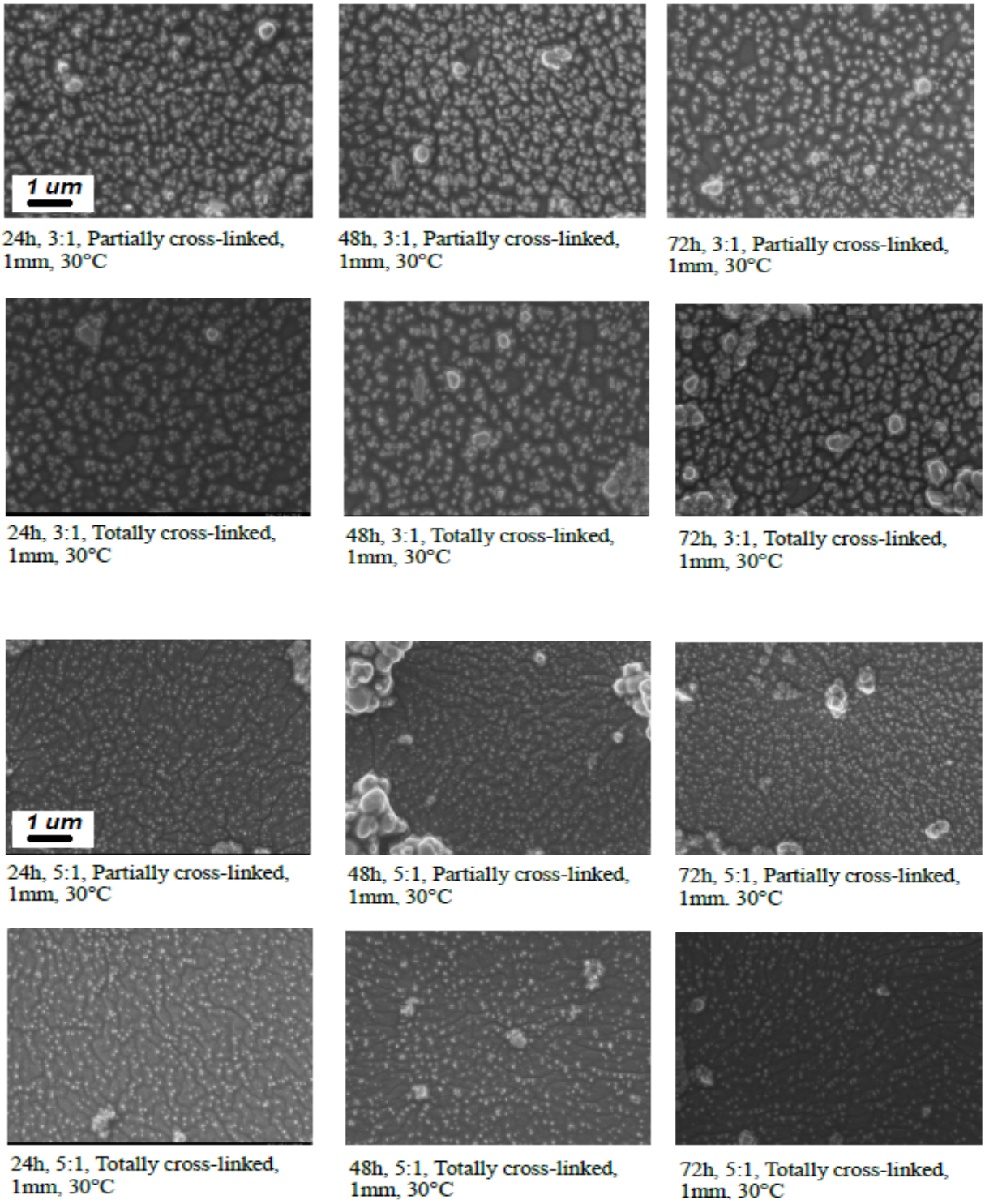

Fig. A.24 FESEM images of samples for different cross linking-degree at 50kx magnification

Raman efficiency and uniformity

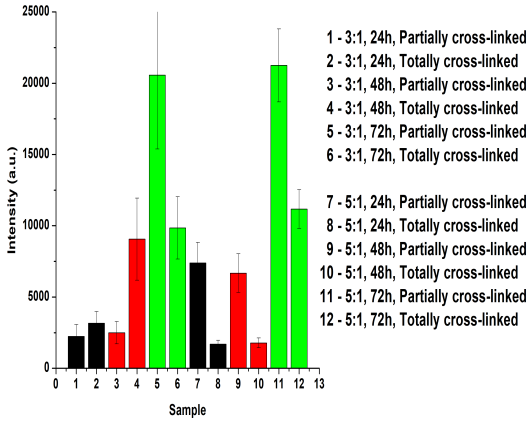

(a) Average intensities of the SERS substrates synthesised for different cross-linking degrees of the PDMS membranes

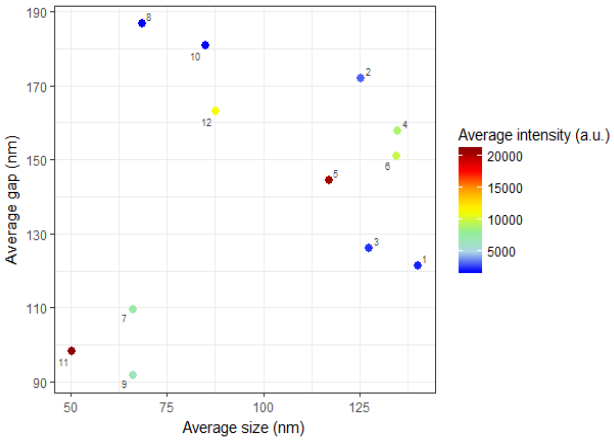

(b) Each point represents a sample: the colour represents the Average intensity in arbitrary unit, while in the y- and x-axis, the average size of the Ag-NPs and their Average inter-gap distance are used respectively.

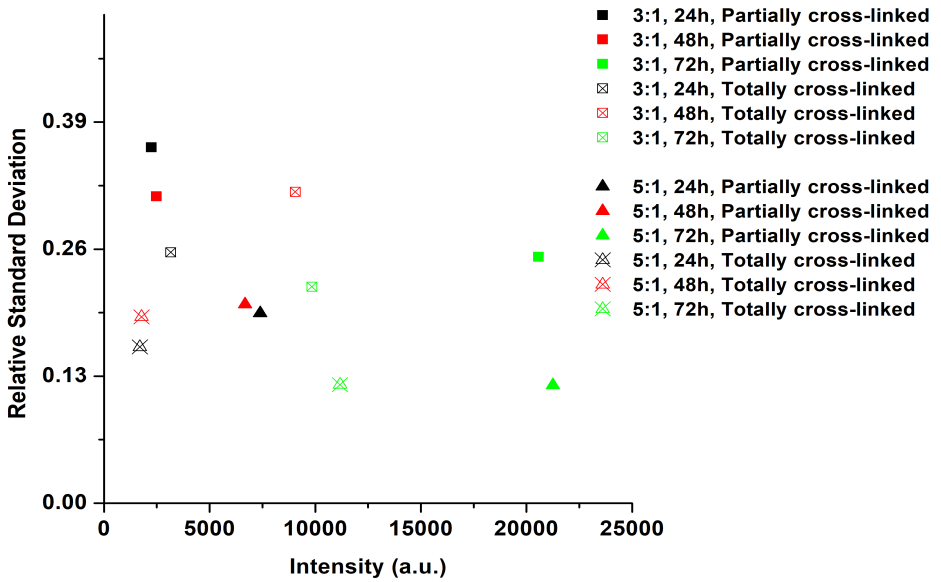

(c) Relative Standard Deviation vs. average intensity of the SERS substrates synthesised for different cross-linking degrees of the PDMS membranes.

Fig. A.25 Raman efficiency and uniformity of SERS substrates synthesised for different cross-linking degrees of the PDMS membranes

A.5 Concentration of ethanol in incubation solution

UV-Vis in air

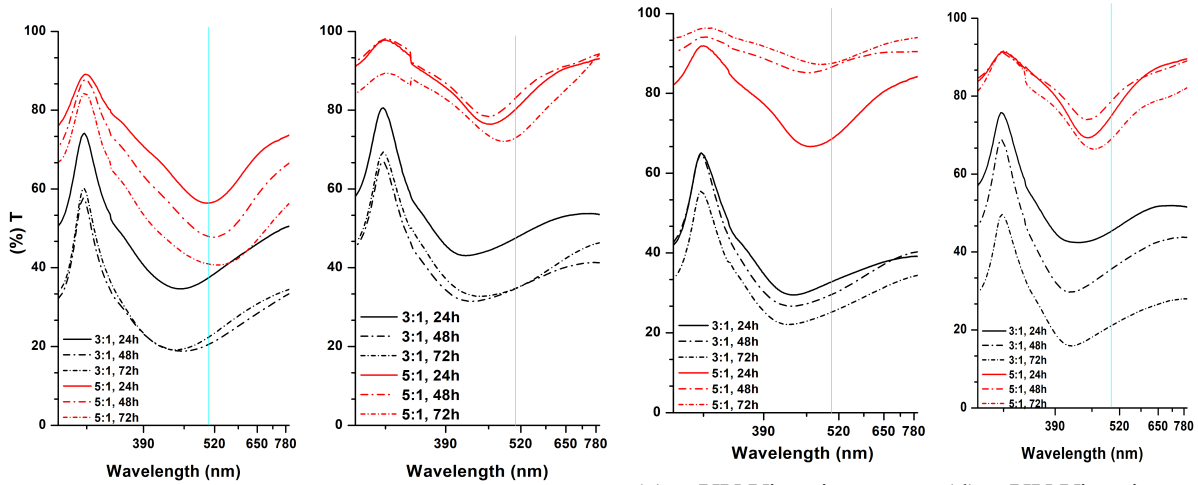

(a) UV-Vis in Air for 0% of ethanol, 30°C, Totally cross-linked

(b) UV-Vis in Air for 5% of ethanol, 30°C, Totally cross-linked

(c) UV-Vis in Air for 10% of ethanol, 30°C, Totally cross-linked

(d) UV-Vis in Air for 20% of ethanol, 30°C, Totally cross-linked

Fig. A.26 UV-Vis measurements in air for 0% concentration (a), 5% (b), 10% (c) and 20% (d) of ethanol in incubation solution

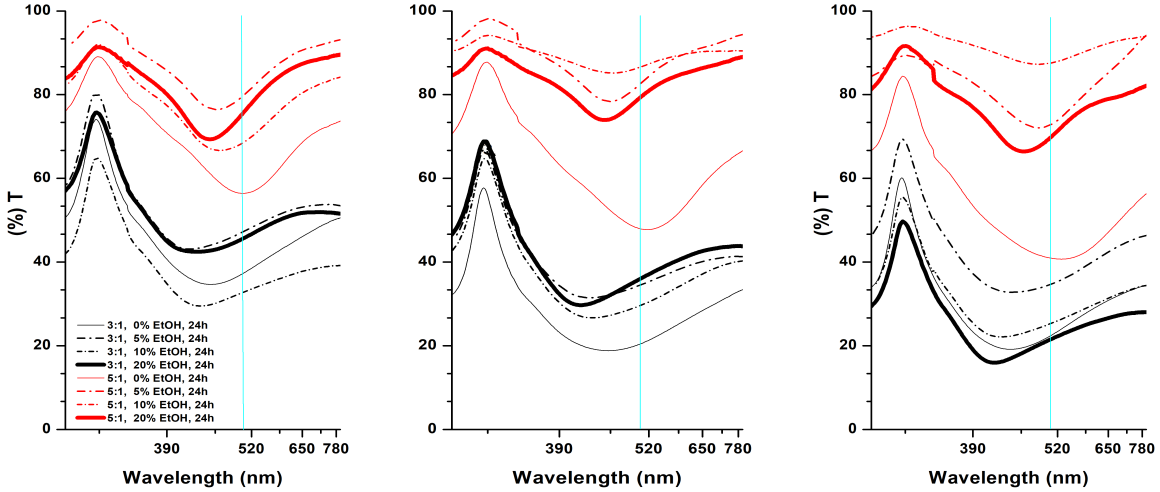

(a) UV-Vis in Air for 3:1 and 5:1, 24h

(b) UV-Vis in Air for 3:1 and 5:1, 48h

(c) UV-Vis in Air for 3:1 and 5:1, 72h

Fig. A.27 UV-Vis measurements in air for different incubation time periods and concentration of ethanol in the incubation solution

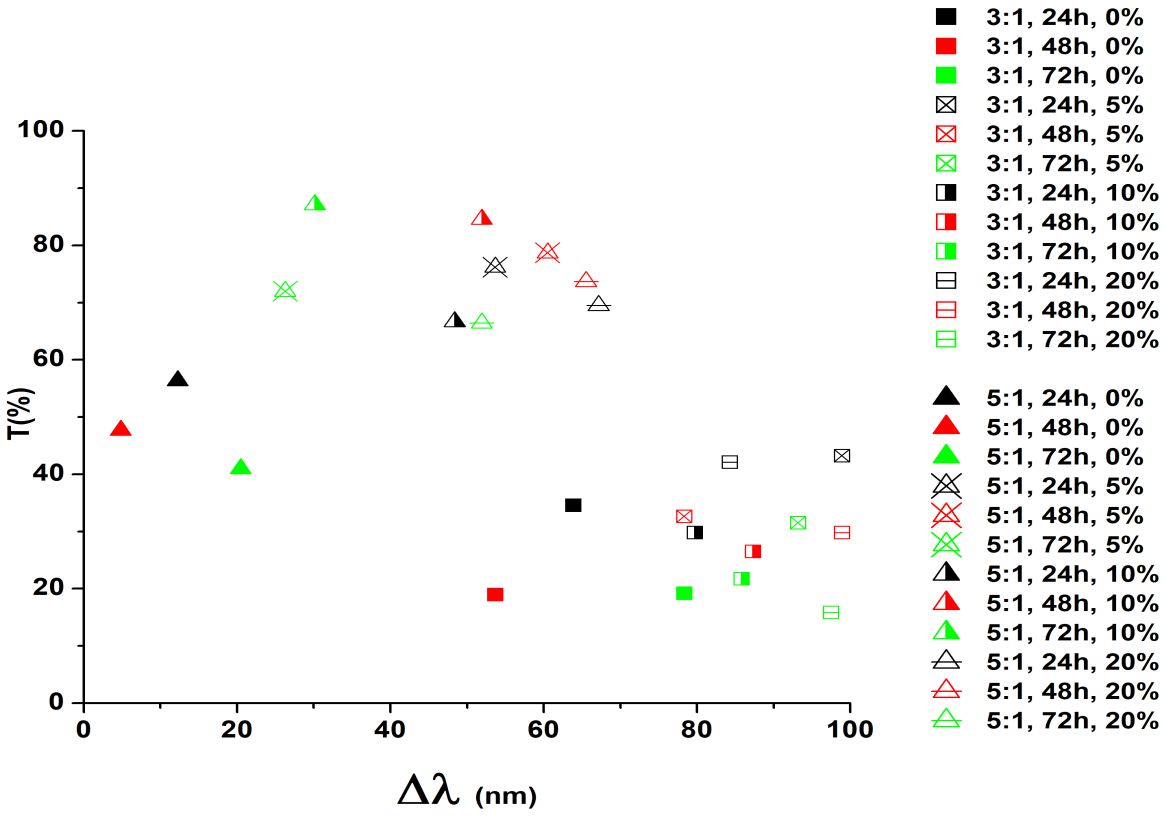

Fig. A.28 Dip transmittance vs. $\Delta\lambda$ for samples with different concentration of ethanol – Low transmittance and displacement means high probability of Raman resonance

UV-Vis in water

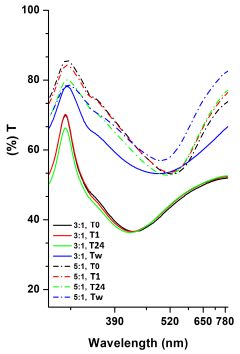

(a) UV-Vis in Water for 24h, 0% of EtOH

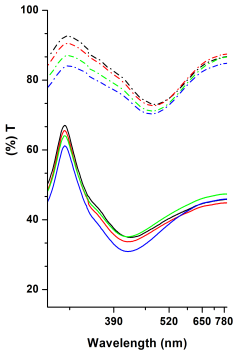

(b) UV-Vis in Water for 24h, 5% of EtOH

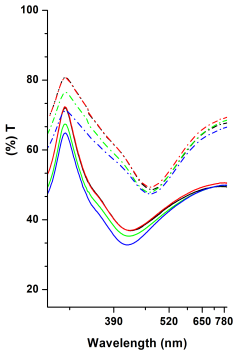

(c) UV-Vis in Water for 24h, 10% of EtOH

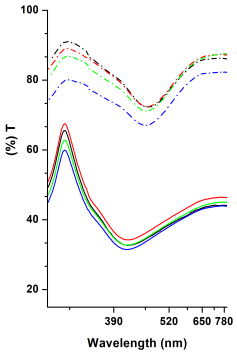

(d) UV-Vis in Water for 24h, 20% of EtOH

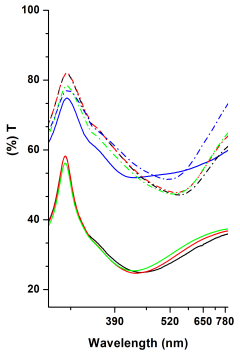

(e) UV-Vis in Water for 48h, 0% of EtOH

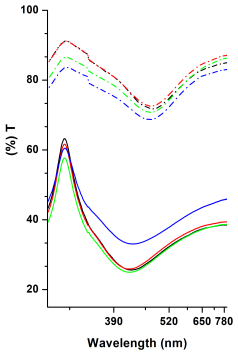

(f) UV-Vis in Water for 48h, 5% of EtOH

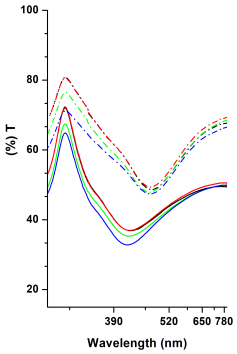

(g) UV-Vis in Water for 48h, 10% of EtOH

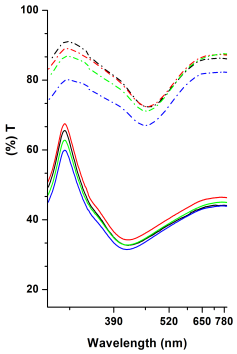

(h) UV-Vis in Water for 48h, 20% of EtOH

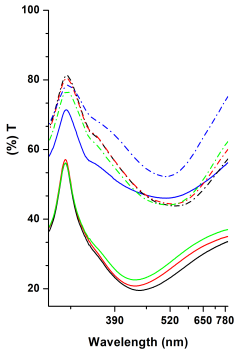

(i) UV-Vis in Water for 72h, 0% of EtOH

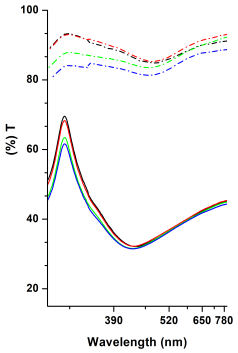

(j) UV-Vis in Water for 72h, 5% of EtOH

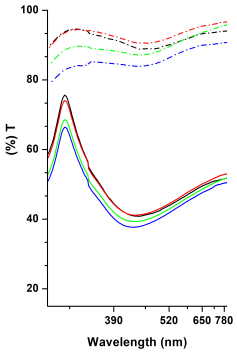

(k) UV-Vis in Water for 72h, 10% of EtOH

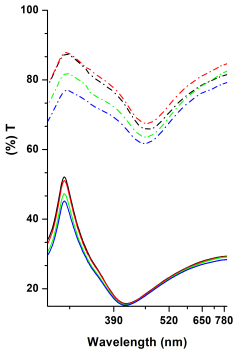

(l) UV-Vis in Water for 72h, 20% of EtOH

Fig. A.29 UV-Vis measurements in water for different concentrations of ethanol at different time interval

UV-Vis in TE-NaCl solution

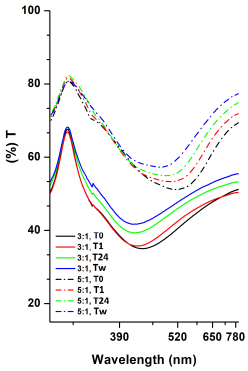

(a) UV-Vis in TE-NaCl for 24h, 0% of EtOH

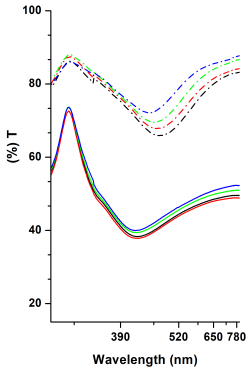

(b) UV-Vis in TE-NaCl for 24h, 5% of EtOH

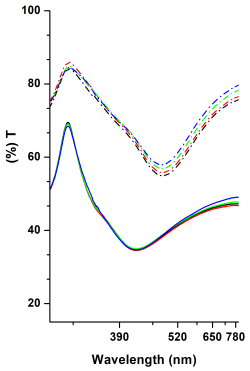

(c) UV-Vis in TE-NaCl for 24h, 10% of EtOH

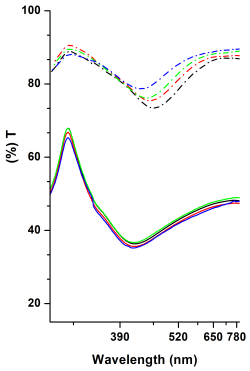

(d) UV-Vis in TE-NaCl for 24h, 20% of EtOH

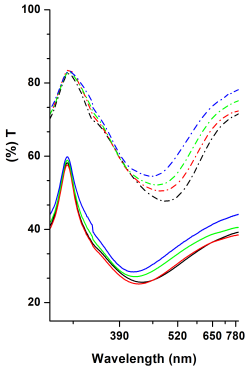

(e) UV-Vis in TE-NaCl for 48h, 0% of EtOH

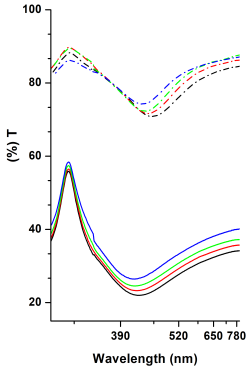

(f) UV-Vis in TE-NaCl for 48h, 5% of EtOH

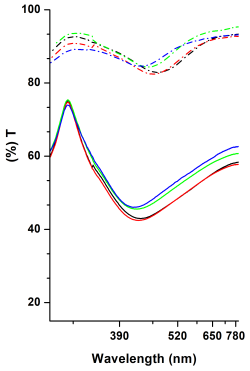

(g) UV-Vis in TE-NaCl for 48h, 10% of EtOH

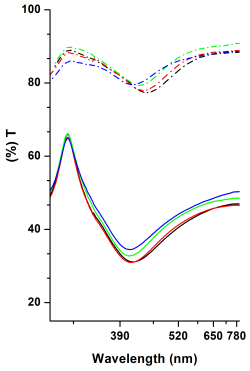

(h) UV-Vis in TE-NaCl for 48h, 20% of EtOH

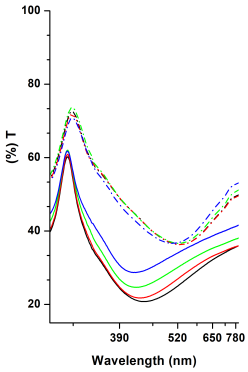

(i) UV-Vis in TE-NaCl for 72h, 0% of EtOH

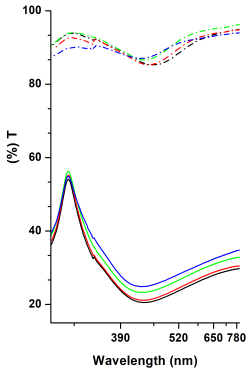

(j) UV-Vis in TE-NaCl for 72h, 5% of EtOH

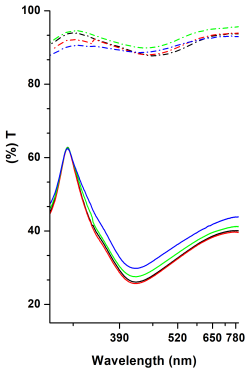

(k) UV-Vis in TE-NaCl for 72h, 10% of EtOH

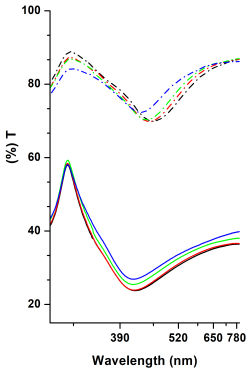

(l) UV-Vis in TE-NaCl for 72h, 20% of EtOH

Fig. A.30 UV-Vis measurements in TE-NaCl solution for different concentrations of ethanol at different time interval

FESEM Images

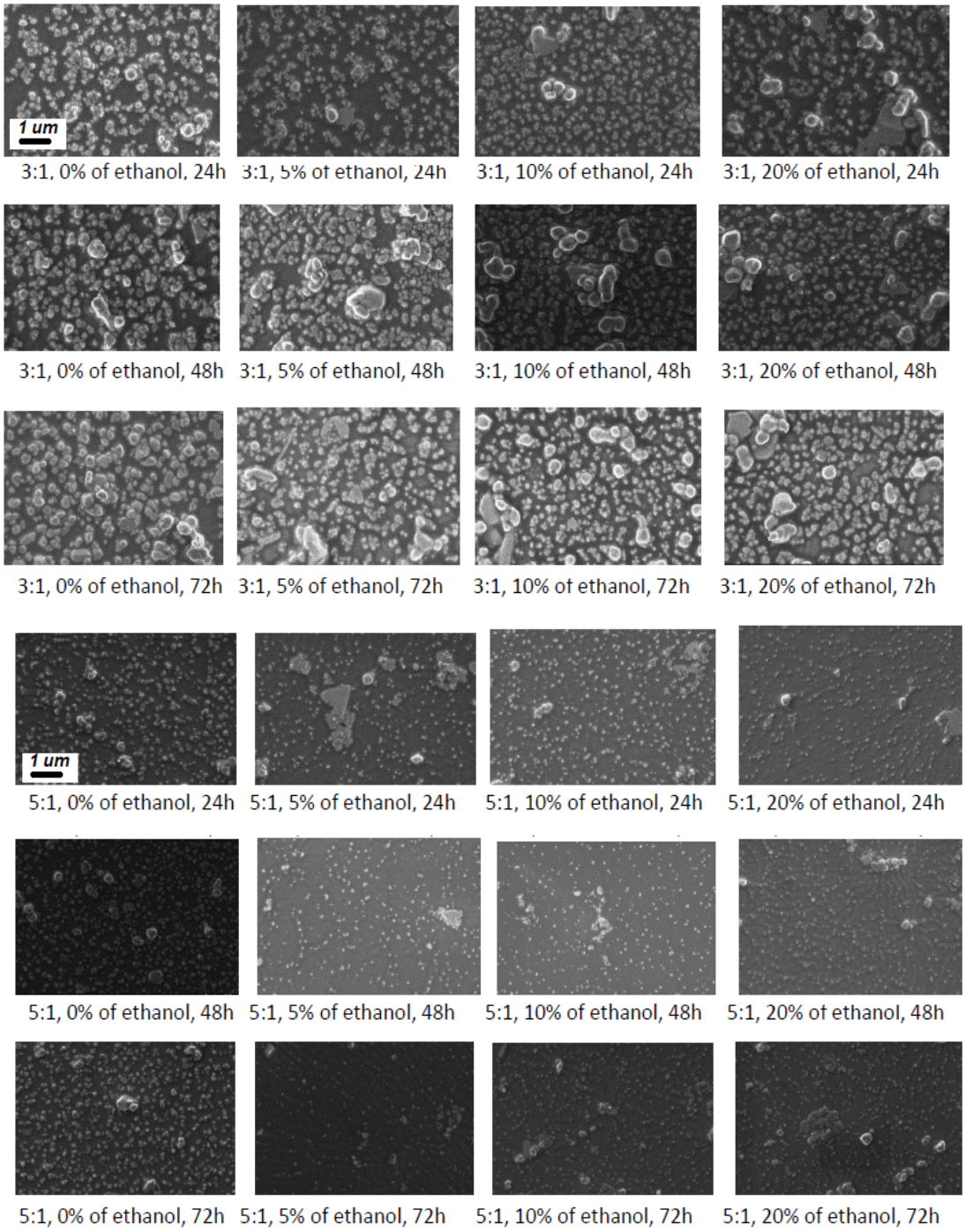

Fig. A.31 FESEM images of samples for different percentage of ethanol in the incubation solution at 50kx magnification

Raman efficiency and uniformity

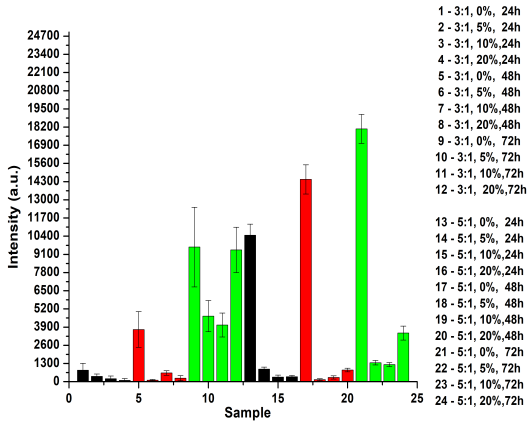

(a) Average intensities of the SERS substrates synthesised for different percentage of ethanol in incubation solution

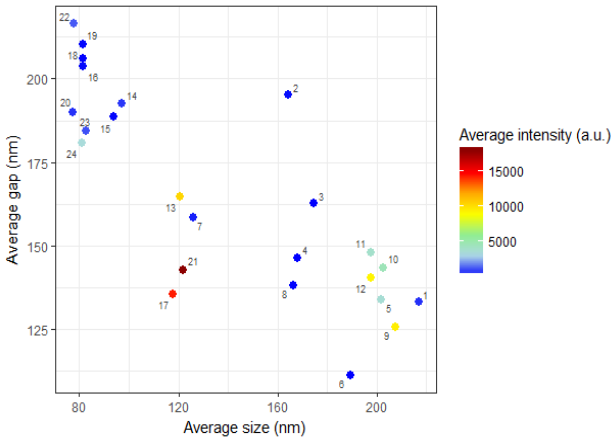

(b) Each point represents a sample: the colour represents the Average intensity in arbitrary unit, while in the y- and x-axis, the average size of the Ag-NPs and their Average inter-gap distance are used respectively.

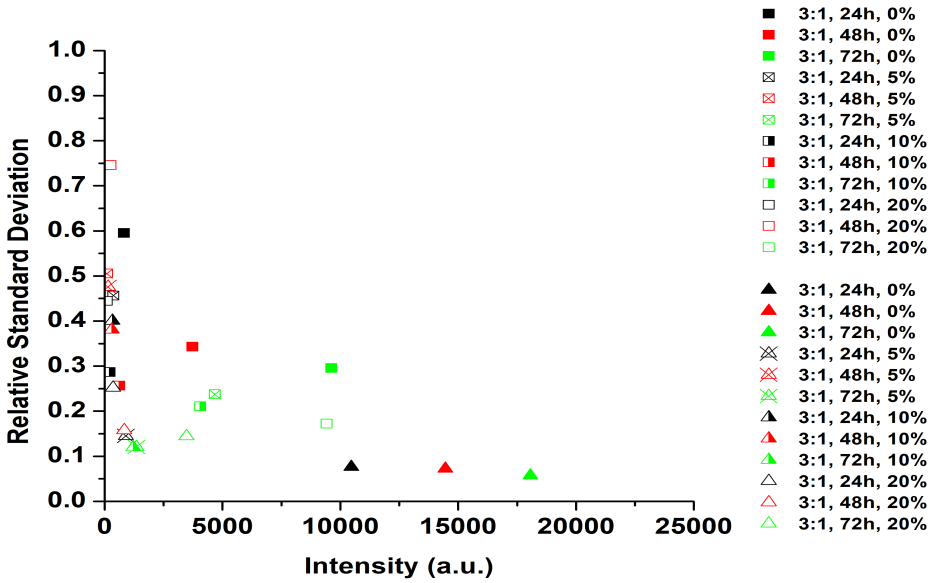

(c) Relative Standard Deviation vs. average intensity of the SERS substrates synthesised for different percentage of ethanol in incubation solution.

Fig. A.32 Raman efficiency and uniformity of SERS substrates synthesised for different percentage of ethanol in incubation solution

A.6 Precursor concentration

UV-Vis in air

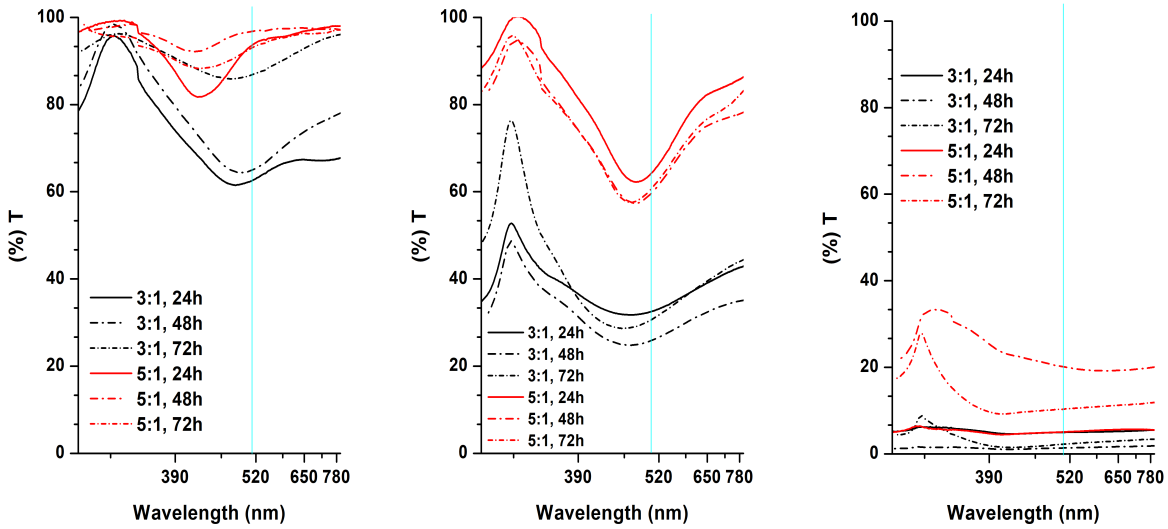

(a) UV-Vis in Air for 10mM of $AgNO_3$, 30°C, Totally cross-linked

(b) UV-Vis in Air for 100mM of $AgNO_3$, 30°C, Totally cross-linked

(c) UV-Vis in Air for 1M of $AgNO_3$, 30°C, Totally cross-linked

Fig. A.33 UV-Vis measurements in air for concentration of the precursor of 10mM (a), 100mM (b) and 1M (c)

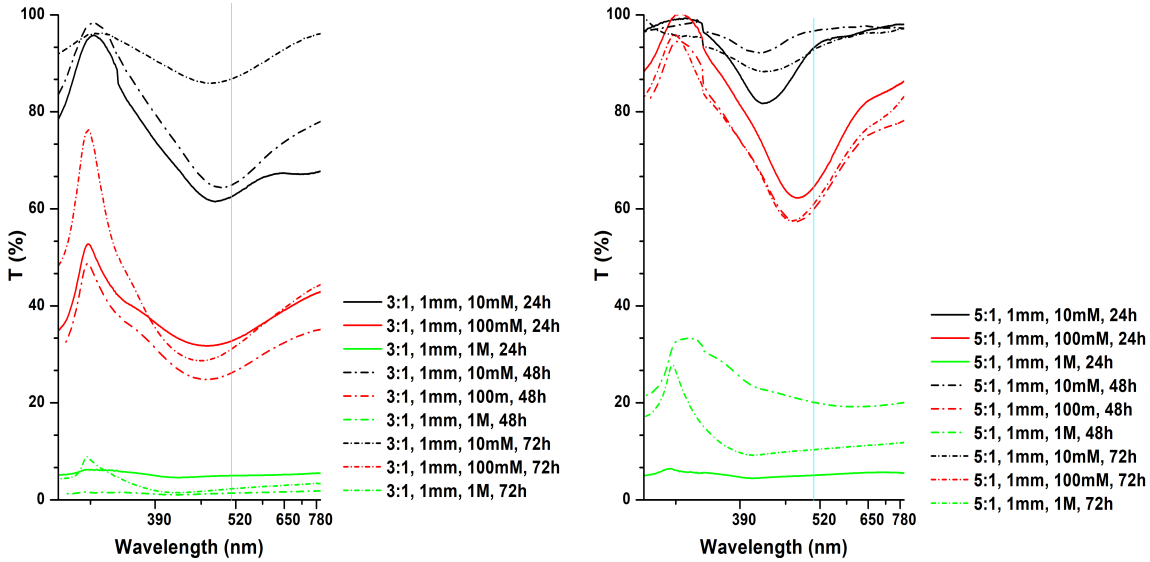

(a) UV-Vis in Air for 3:1, 30°C, Totally cross-linked

(b) UV-Vis in Air for 5:1, 30°C, Totally cross-linked

Fig. A.34 UV-Vis measurements in air for curing ratio of 3:1 (a) and 5:1 (b) at different concentrations of precursor in the incubation solution

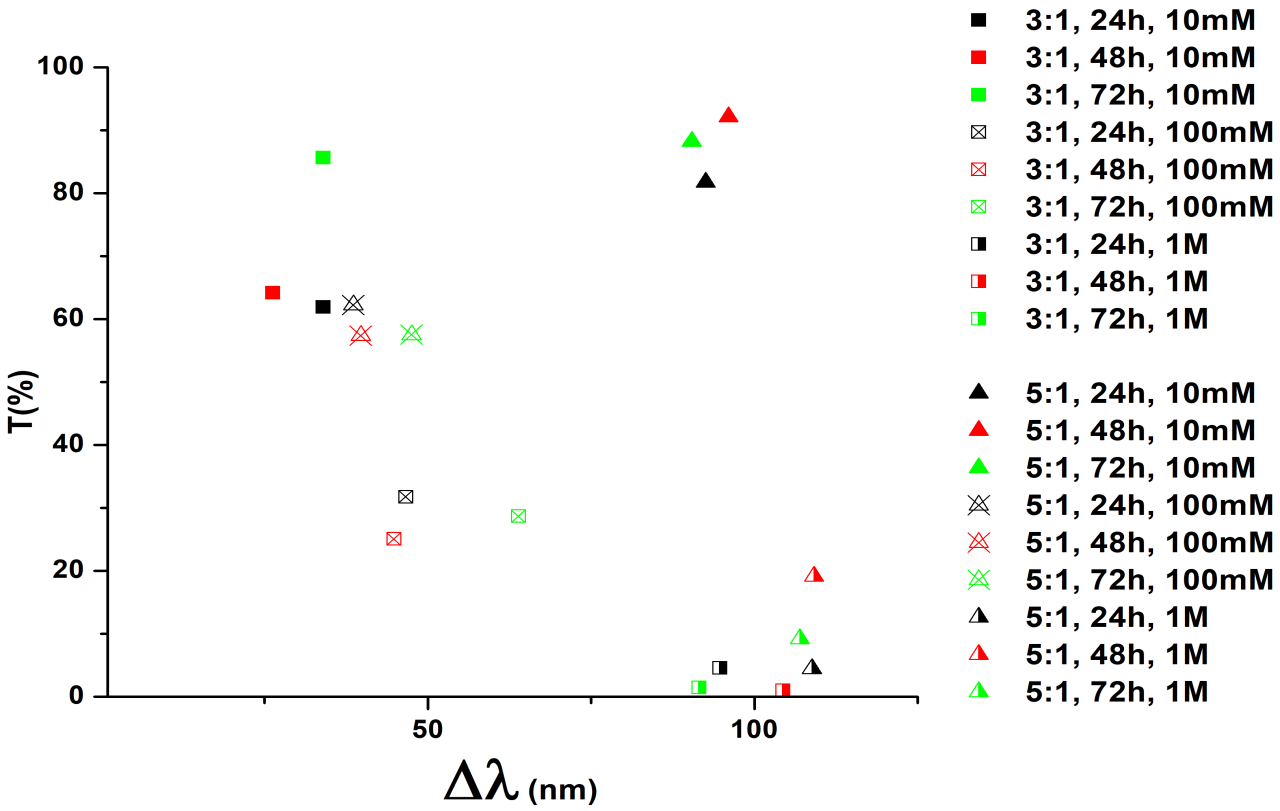

Fig. A.35 Dip transmittance vs. $\Delta\lambda$ for samples with different concentrations of precursor.

UV-Vis in water

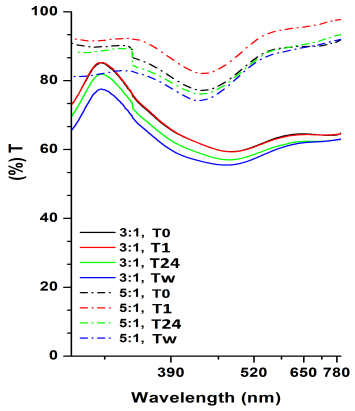

(a) UV-Vis in Water for 24h 30°C, 10mM of $AgNO_3$

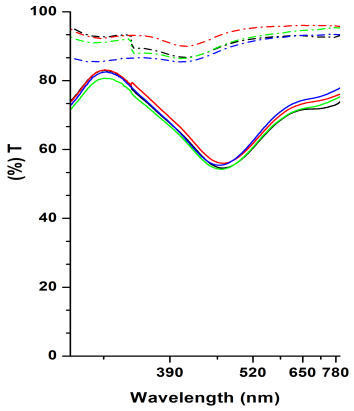

(b) UV-Vis in Water for 48h 30°C, 10mM of $AgNO_3$

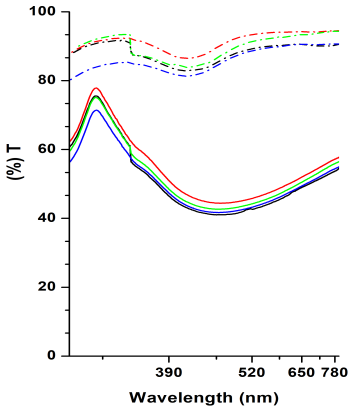

(c) UV-Vis in Water for 72h 30°C, 10mM of $AgNO_3$

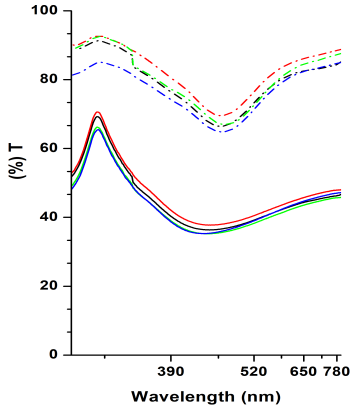

(d) UV-Vis in Water for 24h 30°C, 100mM of $AgNO_3$

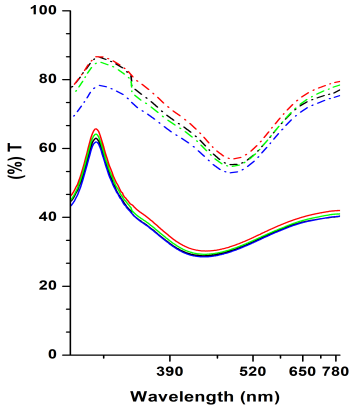

(e) UV-Vis in Water for 48h 30°C, 100mM of $AgNO_3$

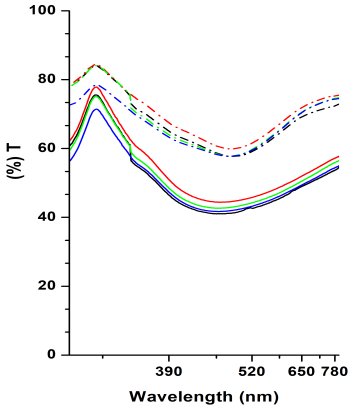

(f) UV-Vis in Water for 72h 30°C, 100mM of $AgNO_3$

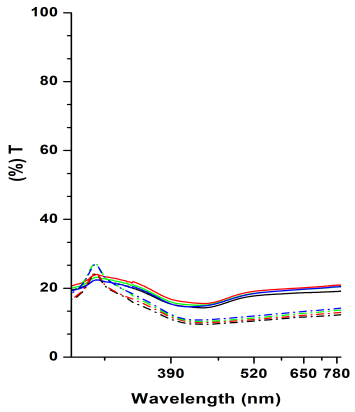

(g) UV-Vis in Water for 24h 30°C, 1M of $AgNO_3$

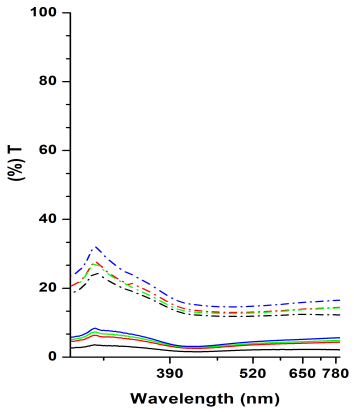

(h) UV-Vis in Water for 48h 30°C, 1M of $AgNO_3$

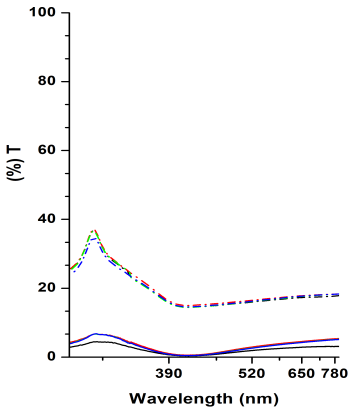

(i) UV-Vis in Water for 72h 30°C, 1M of $AgNO_3$

Fig. A.36 UV-Vis measurements in water for different concentrations of precursor at different time intervals

UV-Vis in TE

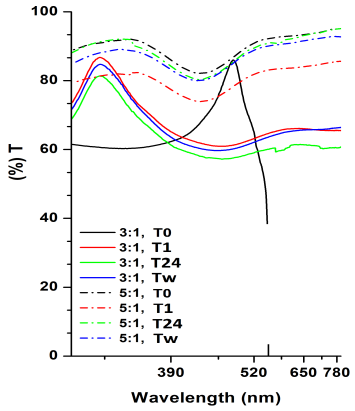

(a) UV-Vis in TE-NaCl for 24h 30°C, 10mM of $AgNO_3$

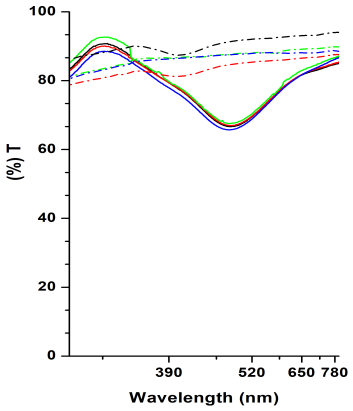

(b) UV-Vis in TE-NaCl for 48h 30°C, 10mM of $AgNO_3$

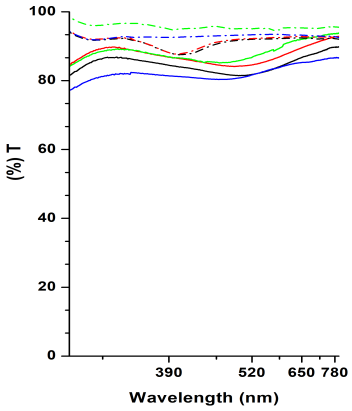

(c) UV-Vis in TE-NaCl for 72h 30°C, 10mM of $AgNO_3$

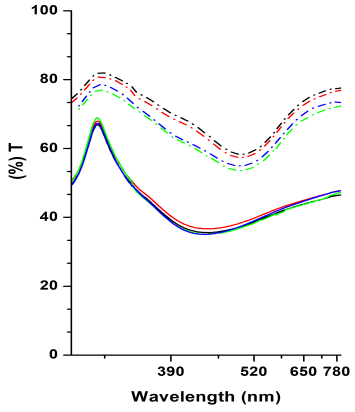

(d) UV-Vis in TE-NaCl for 24h 30°C, 100mM of $AgNO_3$

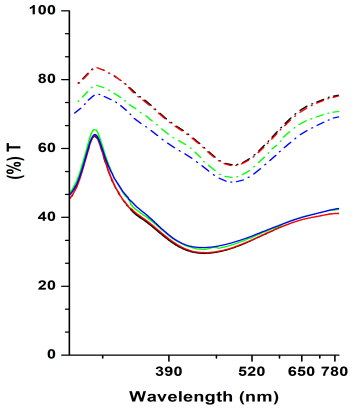

(e) UV-Vis in TE-NaCl for 48h 30°C, 100mM of $AgNO_3$

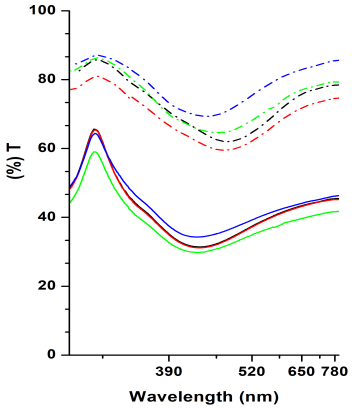

(f) UV-Vis in TE-NaCl for 72h 30°C, 100mM of $AgNO_3$

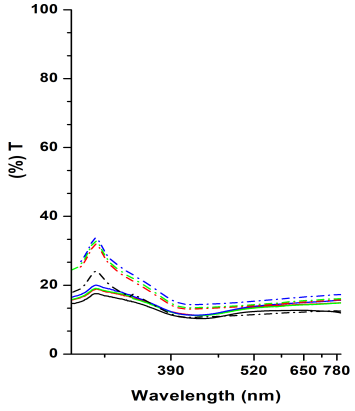

(g) UV-Vis in TE-NaCl for 24h 30°C, 1M of $AgNO_3$

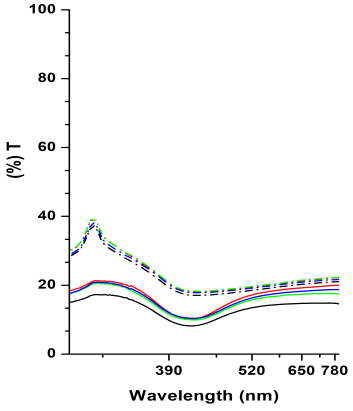

(h) UV-Vis in TE-NaCl for 48h 30°C, 1M of $AgNO_3$

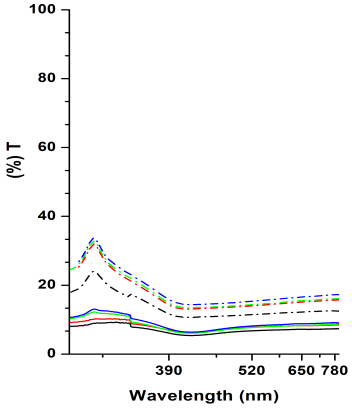

(i) UV-Vis in TE-NaCl for 72h 30°C, 1M of $AgNO_3$

Fig. A.37 UV-Vis measurements in TE-NaCl solution for different concentrations of precursor at different time intervals

FESEM Images

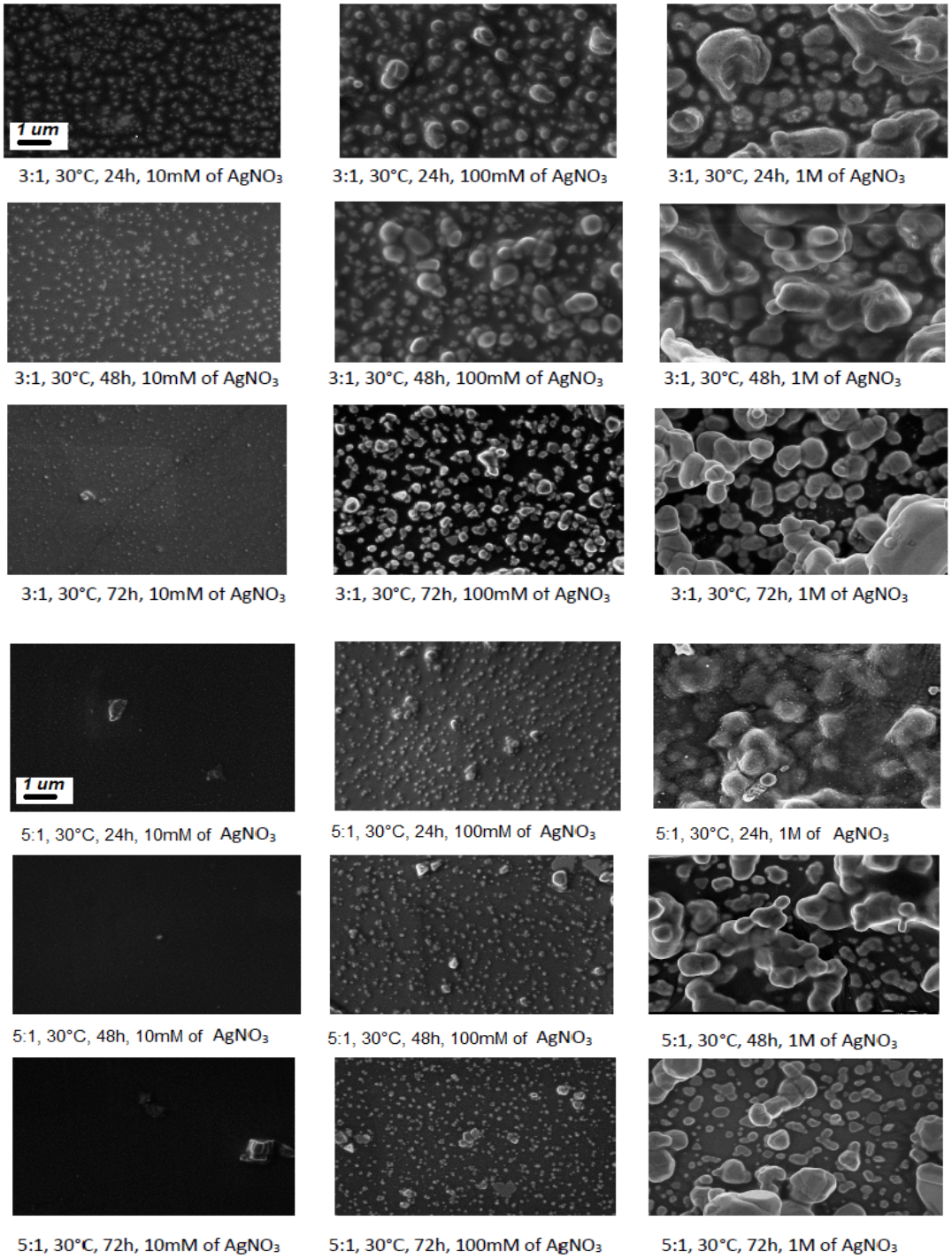

Fig. A.38 FESEM images of samples for different concentration of silver nitrate in the aqueous incubation solution at 50kx magnification

Appendix B

Comparison of results of static incubation synthesis

B.1 Comparison for samples at 20°C

Raman efficiency and uniformity

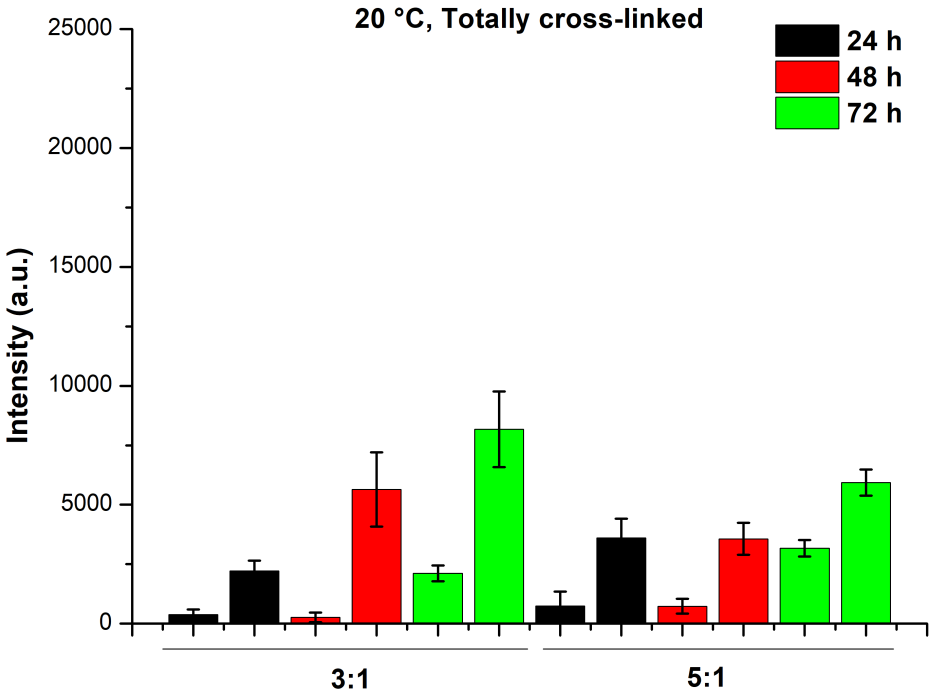

Fig. B.1 Raman intensities (at arbitrary unit) for samples at same incubation temperature of 20°C, totally cross-linked

B.2 Comparison for samples at 30°C

Raman efficiency and uniformity

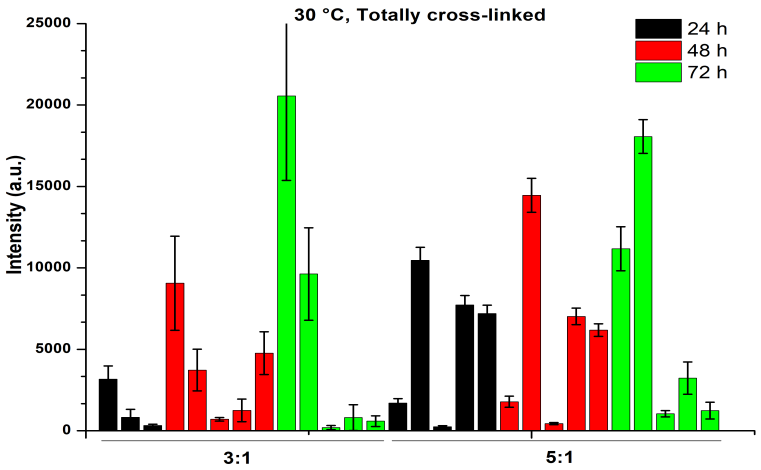

Fig. B.2 Raman intensities (at arbitrary unit) for samples at same incubation temperature of *30 °C*, for totally cross-linked substrate

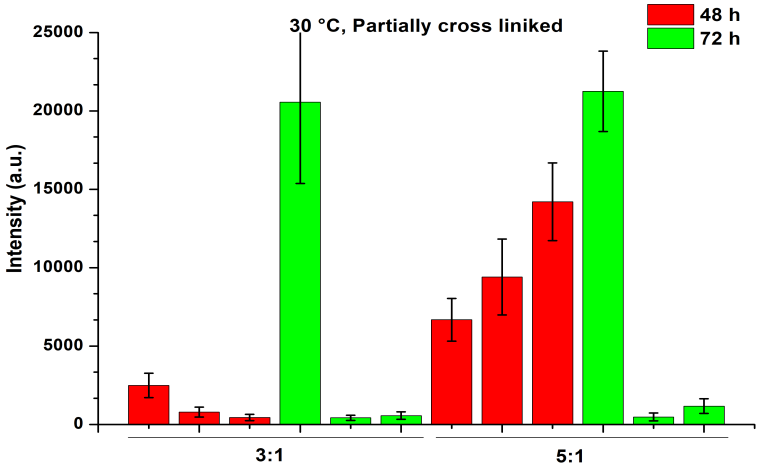

Fig. B.3 Raman intensities (at arbitrary unit) for samples at same incubation temperature of *30 °C*, for partially cross-linked substrate

B.3 Comparison for samples at 40°C

Raman efficiency and uniformity

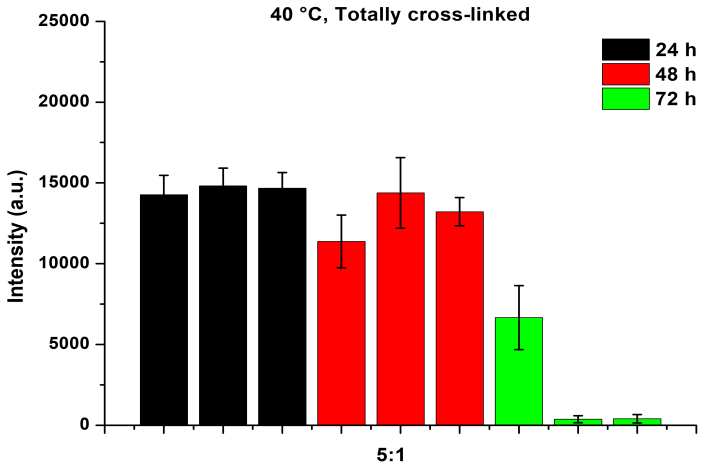

Fig. B.4 Raman intensities (at arbitrary unit) for samples at same incubation temperature of 40°C, for totally cross-linked substrate